Aus der

Radiologischen Universitätsklinik Tübingen

Abteilung Bildgebung und Radiopharmazie

The Study of Brain Function at Rest and Under Activation Using Simultaneous PET/MRI Imaging

Inaugural-Dissertation
zur Erlangung des Doktorgrades
der Humanwissenschaften

der Medizinischen Fakultät
der Eberhard Karls Universität
zu Tübingen

vorgelegt von

Ionescu, Tudor Mihai

2023

Dekan: Professor Dr. B. Pichler

1. Berichterstatter: Professorin Dr. K. Herfert
2. Berichterstatter: Professor Dr. K. Scheffler
3. Berichterstatter: Professor Dr. V. Riedl

Tag der Disputation: 08.11.2023

TABLE OF CONTENTS

Abbreviations

Table 1: List of Abbreviations.

Abbreviation	Full Name
6-PG	6-Phosphogluconate
6-PGDH	6-Phosphogluconate Dehydrogenase
6-PGL	6-Phosphoglucono-δ-lactone
APD	Avalanche Photodiode
ASL	Arterial Spin Labelling
ATP	Adenosine Triphosphate
BD	Bipolar Disorder
bdPET-rsFC	Bolus Dynamic PET-derived Resting-State Functional Connectivity
BGO	Bismuth-Germanate
BOLD	Blood-Oxygenation-Level-Dependent
BOLD-rsFC	BOLD-derived Resting-State Functional Connectivity
BP_{ND}	Non-displaceable Binding Potential
CBF	Cerebral Blood Flow
CBV	Cerebral Blood Volume
CMRGlu	Cerebral Metabolic Rate of Glucose
$CMRO_2$	Cerebral Metabolic Rate of Oxygen
CNS	Central Nervous System
CT	Computer Tomography
D2R	D_2 Receptor
DASB	3-amino-4-(2-dimethylaminomethylphenylsulfanyl)-benzonitrile
DHAP	Diyhdroxyacetone Phosphate
DMN	Default-Mode Network
DVR	Distribution Volume Ratio
EEG	Electroencephalography
EPSP	Excitatory Post-synaptic Potential
Erythrose-4P	Erythrose-4-phosphate
FC	Functional Connectivity
FDG	Fluorodeoxyglucose
FID	Free Induciton Decay

fMRI	Functional Magnetic Resonance Imaging
FOV	Field Of View
fPET	Functional Positron Emission Tomography
Fructose-1,6-P_2	Fructose-1,6-biphosphate
G protein	Guanine nucleotide-binding protein
G6PDH	Glucose-6-Phosphate Dehydrogenase
GABA	Gamma-aminobutyric Acid
GLUT	Glucose Transporter
GMV	Gray Matter Volume
GPI	Glucose-6-phosphate Isomerase
HRF	Hemodynamic Response Function
ICA	Independent Component Analysis
idPET-rsFC	Infusion Dynamic PET-derived Resting-State Functional Connectivity
IPSP	Inhibitory Post-synaptic Potential
LOR	Line-Of-Response
LSD	Lysergic Acid Diethylamide
LSO	Lutetium Oxyorthosilicate
MDD	Major Depressive Disorder
MDMA	3,4-Methylenedioxymethamphetamine
MEG	Magnetoencephalography
MIBG	Meta-iodobenzylguanidine
mPFC	Medial Prefrontal Cortex
MRI	Magnetic Resonance Imaging
NADPH	Nicotinamide Adenine Dinucleotide Phosphate
OSEM	Ordered-Subsets Expectation Maximization
PD	Parkinson's Disease
PET	Positron Emission Tomography
PFK	Phosphofructokinase-1
Ph-fMRI	Pharmacological Functional Magnetic Resonance Imaging
PMT	Photomultiplier Tube
PPP	Pentose Phosphate Pathway

RF	Radiofrequency
Ribose-5P	Ribose-5-phosphate
Ribulose-5P	Ribulose-5-phosphate
ROI	Region Of Interest
rsFC	Resting-State Functional Connectivity
Rs-fMRI	Resting-state Functional Magnetic Resonance Imaging
RSN	Resting-State Network
Sedoheptulose-7P	Sedoheptulose-7-phosphate
SERT	Serotonin Transporter
SiPM	Silicate Photomultiplier
SMN	Sensorimotor Network
SN	Salience Network
sPET-rsFC	Static PET-derived Resting-State Functional Connectivity
SRTM	Simple Reference Tissue Model
St-fMRI	Stimulus Functional Magnetic Resonance Imaging
T	Tesla
TA	Transaldolase
TAC	Time-Activity Curve
TCA	Tricarobxylic Acid Cycle
TE	Echo Time
TK	Transketolase
TOF	Time-Of-Flight
TPI	Triose Phosphate Isomerase
TR	Relaxation Time
VOI	Volume-Of-Interest
VTA	Ventral Tegmental Area
Xylulose-5P	Xylulose-5-Phosphate

1. Introduction

The brain plays a decisive role in animals due to its control over large parts of their organisms. It represents the central interface of interaction with the environment, integrating external cues and generating appropriate responses on several physiological levels. The complex and manifold roles of the brain require similarly complex molecular, cellular and systemic architectures, enabling its functionality and adaptability.

In the human brain, around 10^{11} neurons (Azevedo et al., 2009), interconnected by up to 10^{14} synapses (Drachman, 2005), facilitate the transfer of information via activation or inhibition processes. In a simple model, neuronal activation can be split between intracellular and extracellular processes. At the synapse, the space between two neurons, information is transmitted by the release of molecules called neurotransmitters from the pre-synaptic neuron, which can bind to receptors of the post-synaptic neuron. This binding can then generate changes of electrical potential in the cellular membrane of the post-synaptic neuron called action potentials, which are propagated along the neuronal membrane, thus facilitating the transfer of information to other nearby or distant areas of the brain (Kandel et al., 2013).

Today, it is established that activity generated across the brain does not function independently but in a coherent, well-orchestrated manner in systems called functional networks (Petersen and Sporns, 2015). Functional networks represent populations of neurons exhibiting temporally correlated activation patterns. It is assumed that, independently or through their interplay, these networks mediate different brain functions (Petersen and Sporns, 2015). To perform its manifold processes, the brain requires, compared to its weight, a disproportionately high amount of energy delivered by its vascular system in the form of glucose (Raichle and Gusnard, 2002). Hence, not only neurons are essential for brain function but also, among others, the neurovascular system. Moreover, the brain is a highly dynamic system - action potentials, neurotransmitter-receptor processes, changes in synaptic distributions, metabolism and network architectures all occur over time spans ranging from seconds to years. To fully understand how the brain works, it therefore appears necessary to not merely examine each phenomenon in isolation but to elucidate the links between them *in vivo*. The tremendous complexity of the brain has been accompanied until the latter part of the 20^{th} century by an almost complete lack of quantifiable *in vivo* methods, neuroscience relying on either *in vitro, ex vivo,* or behavioral studies. Therefore, perhaps to a greater extent than for any other organ, truly grasping brain function as a system and finding reliable, quantitative biomarkers for its evaluation have largely eluded science and medicine.

Brain functional processes from molecules to networks will be explained in the next subchapters. Then, magnetic resonance imaging (MRI) and positron emission tomography (PET) will be introduced, and their significance as methods for the examination of brain physiology *in vivo* will be presented. Finally, the potential of simultaneous imaging in linking different layers of brain function will be presented.

1.1 Neuronal Activity: from Synapse to Neuron to Synapse

The central nervous system (CNS) comprises two types of cells: glial cells and neurons (Purves et al., 2018). Glial cells can be separated in further subtypes taking on different roles. For instance, microglia represent the main actors of the brain's immune system (Filiano et al., 2015). Oligodendrocytes, which insulate neurons, facilitate faster signal transduction along the neuronal membrane. Finally, astrocytes are postulated to perform different functions, such as the delivery of nutrients to the neurons (Kandel et al., 2013).

While glial cells play essential supporting roles, neurons are responsible for conducting information across the brain. Neurons propagate information via synapses, the neuron transmitting a signal being called pre-synaptic neuron and the neuron receiving it post-synaptic neuron. The synaptic cleft is a narrow space between both neurons (Kandel et al., 2013). Upon a stimulus, induced for instance by a sensory input, molecules called neurotransmitters are released from the pre-synaptic neuron into the synaptic cleft. Neurotransmitters are molecules that can bind to receptors expressed on neurons and induce a signal (Lodish et al., 2021). Several classifications exist, but depending on the type of signal induced, neurotransmitters can be grouped into excitatory, inhibitory, or modulatory neurotransmitters (Boto and Tomchik, 2019). The primary excitatory neurotransmitter in the brain is glutamate, while gamma-aminobutyric acid (GABA) is the principal inhibitory neurotransmitter (Kandel et al., 2013). Modulatory neurotransmitters also affect brain function in other ways. In addition to transmitting a signal, the effects exerted by such neurotransmitters can be longer-lasting and alter multiple properties of the neuron, such as its firing activity, membrane potential or synaptic configuration (Kupfermann, 1979; Marder, 2012). The main modulatory neurotransmitters in the brain are acetylcholine and a class of neurotransmitters called monoamines, including serotonin, dopamine and norepinephrine.

After being released into the synaptic cleft following a stimulus, the neurotransmitters can bind to different receptor subtypes on the pre-synaptic or post-synaptic membrane. Multiple subtypes of receptors exist, each having high specificity for one type of neurotransmitter

(Kandel et al., 2013). Additionally, receptors can be grouped into two classes. For ionotropic receptors, the binding of the neurotransmitter to the receptor directly leads to the opening of ion channels and either an influx of ions from the extracellular space into the neuron or an efflux from the neuron into the extracellular space. The second class is represented by metabotropic receptors. These receptors are connected by a guanine nucleotide-binding protein (G protein) to ion channels. Therefore, neurotransmitter binding to these receptors triggers conformational changes in the G proteins, which in turn lead to the opening of ion channels, although they can also initiate additional, longer-lasting processes within the cell, such as synaptic potentiation (Kandel et al., 2013). For excitatory binding processes, Na^+ channels open, and Na^+ ions enter the cell, leading to a decrease in membrane potential called depolarization. This process is also termed excitatory post-synaptic potential (EPSP). Inhibitory processes, such as those induced by GABA, trigger the influx of Cl^- ions through corresponding channels. This process increases the membrane potential, causing a hyperpolarization, an effect also termed inhibitory post-synaptic potential (IPSP). If the magnitude of a depolarization reaches a specific threshold, it leads to the opening of numerous Na^+ channels across the neuron and the depolarization is transmitted throughout the entire neuron as an electrical impulse called action potential. The action potential can then lead to the release of neurotransmitters from the neuron into the synaptic cleft and then to another neuron - the illustrated process can repeat itself between this new pair of neurons. After the transduction of the signal is completed between two neurons, several processes occur to prepare both the pre-synaptic and the post-synaptic neuron for the next stimulus. At the synapse, the released neurotransmitters are metabolized or restored to the pre-synaptic neuron through reuptake via transporter proteins expressed in the pre-synaptic membrane. In the post-synaptic neuron, the pre-stimulus intracellular and extracellular ion concentrations are restored to allow the generation of new EPSPs or IPSPs (Kandel et al., 2013). A graphical illustration of the architectures of neurons and synapses is presented in Figure 1.

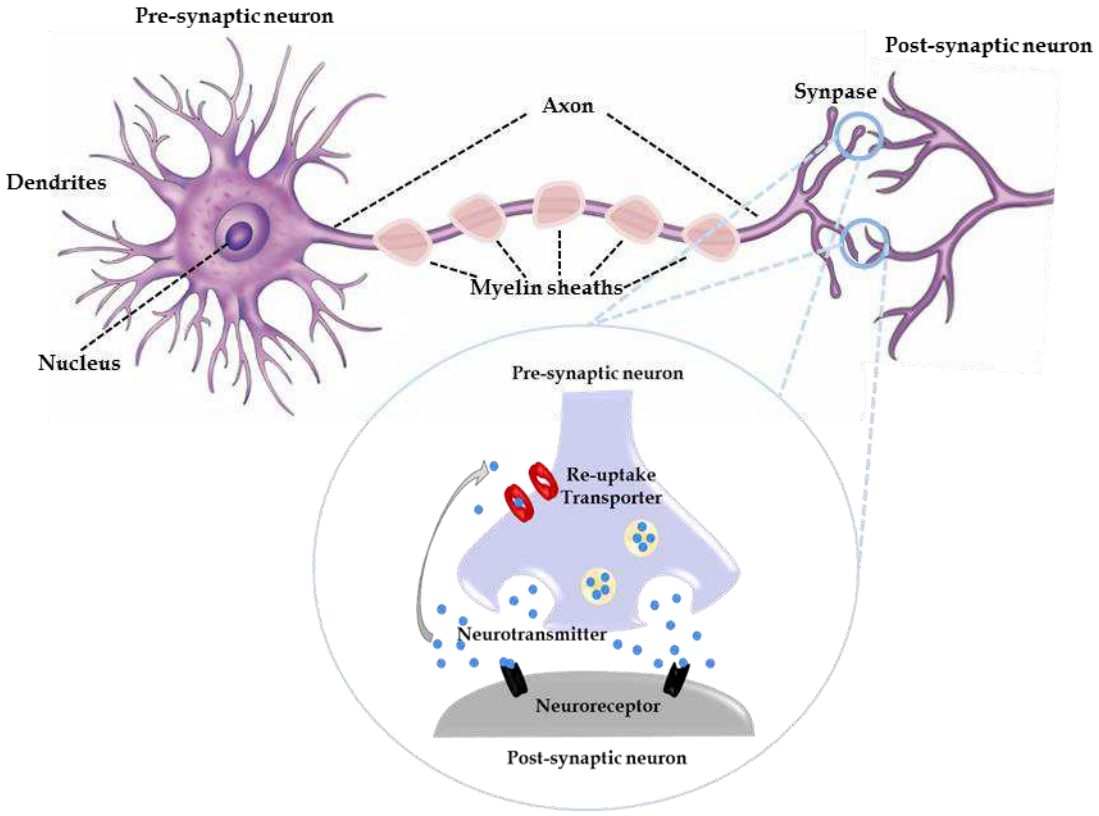

Figure 1: Architecture of neurons and synapses. Like every cell, the neuron is composed of a nucleus, cytoplasm and different organelles. Dendrites emerge from the cell body and are used to receive stimuli from other neurons. The axon transmits information as electrical impulses and is coated by myelin sheaths produced by oligodendrocytes, accelerating signal transduction. At the synapse, neurotransmitters are released and bind to receptors of the post-synaptic neuron. Pre-synaptic transporters enable their reuptake into the pre-synaptic neuron, thereby ending their synaptic action. Reprinted with permission from (Amend, 2019).

1.2 Neurovascular Coupling: The Link between Activity and Metabolism

The processes described in the previous subchapter, along with other maintenance processes ensuring proper brain function, require a high amount of energy. Although the brain represents only about 2% of the body mass, it spends up to 25% of the body's energy. The highest portion of the brain's energy budget is spent on post-synaptic processes, up to 50% of the signaling energy being used at glutamate receptors and approximately 21% for the generation of action potentials. Just 10% of the energy budget is used at the pre-synapse for processes such as neurotransmitter release (~5%) and reuptake (~4%). Around 20% of the energy is spent on maintaining resting potentials (Howarth et al., 2012).

To generate energy, cells need to produce adenosine triphosphate (ATP) using a chain of chemical reactions requiring glucose and oxygen (Bélanger et al., 2011) (Figure 2). These nutrients are delivered to sites where energy is required via blood vessels. To this extent, a

continuous cerebral blood flow (CBF) ensured by the brain's vascular system is necessary. The largest vessels of the brain are the arteries and veins at its surface. The arteries deliver oxygenated blood to the brain and are further divided into arterioles and fine capillaries. Nutrient exchange occurs at the capillaries, which receive extensive signaling from nearby cells such as neurons, thus being able to generate adaptive responses to neuronal activity. After the oxygen delivery from the capillaries to the cells, the blood is drained by venules and larger veins towards the lungs for re-oxygenation. The difference in oxygenation between capillaries and draining venules indicates oxygen consumption and is defined as the metabolic rate of oxygen ($CMRO_2$). To match the energy requirements of neuronal activity, CBF is enhanced at the activation site by the effect of vasoactive substances, which can increase the diameters of blood vessels. The link between increased neuronal activity and CBF in order to supply the necessary nutrients is termed neurovascular coupling (Iadecola, 2004).

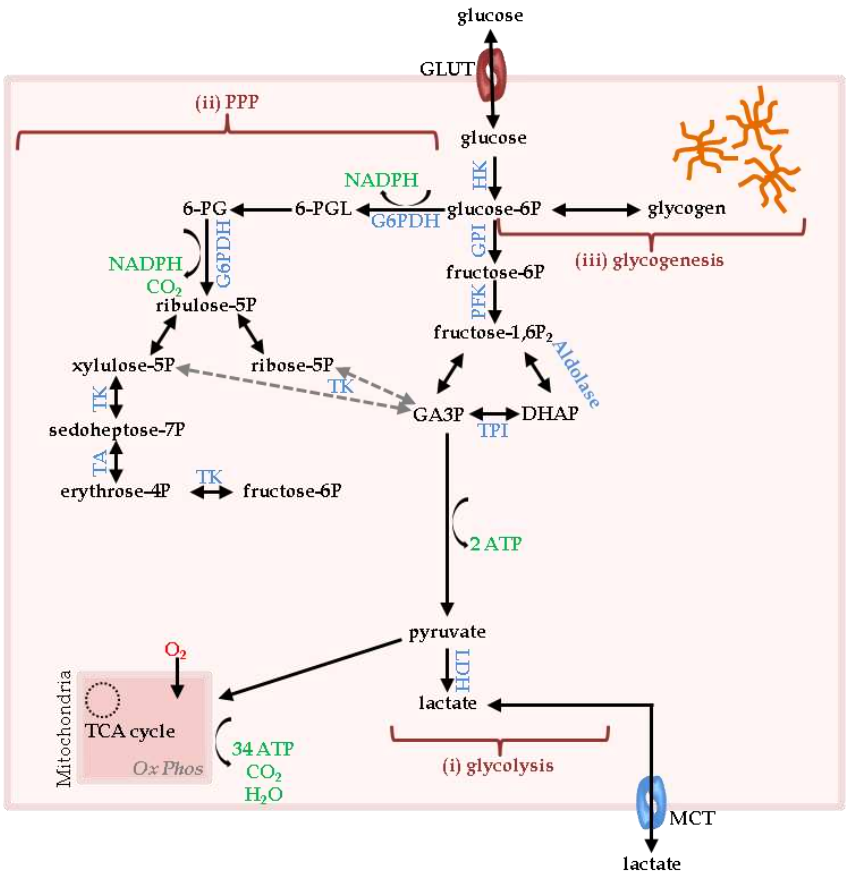

Figure 2: Pathways of glucose metabolism. Upon delivery, glucose enters the cells via glucose transporters (GLUTs). In the cell, glucose undergoes phosphorylation to glucose-6-phosphate through an enzymatic reaction. Three different pathways are then available for further metabolization of glucose-6-phosphate: glycolysis, the pentose phosphate pathway and glycogenesis. Glycolysis requires O_2 and leads to the production of 34 molecules of ATP, along with CO_2. The glucose analogue [^{18}F]flulorodeoxyglucose (FDG) undergoes phosphorylation after entering the cell via GLUTs, however does not go through further metabolization steps

afterwards. Abbreviations: 6-PG: 6-phosphogluconate 6-PGDH: 6-phosphogluconate dehydrogenase, 6-PGL, 6-phosphoglucono-δ-lactone, ATP: adenosine triphosphate, DHAP: dihydroxyacetone phosphate, erythrose-4P: erythrose-4-phosphate, fructose-1,6-P_2: fructose-1,6-bisphosphate, G6PDH: glucose-6-phosphate dehydrogenase, GPI: glucose-6-phosphate isomerase, GLUT: glucose transporter, NADPH: nicotinamide adenine dinucleotide phosphate, PFK: phosphofructokinase-1, PPP: pentose phosphate pathway, ribose-5P: ribose-5-phosphate, ribulose-5P: ribulose-5-phosphate, sedoheptulose-7P: sedoheptulose-7-phosphate, TA: transaldolase, TCA: tricarboxylic acid cycle, TK: transketolase, TPI, triose phosphate isomerase, xylulose-5P: xylulose-5-phosphate. Adapted from (Amend, 2019; Bélanger et al., 2011).

While research has elucidated many properties of this phenomenon, some remain elusive. For instance, the shape of the CBF response following neuronal activation is well-established, with a peak in CBF increase occurring 4 to 6 seconds after neuronal activity (Rangaprakash et al., 2021). Secondly, although the relationship between the amplitudes of neuronal activation and CBF increase is assumed to be primarily linear (Logothetis et al., 2001), evidence of non-linear vascular responses exists (Sheth et al., 2004).

Neurovascular coupling is of particular relevance for functional magnetic resonance imaging (fMRI), a method used in the present work and described in detail in the following subchapters.

1.3 Brain Architecture: Functional Networks and Neurotransmitter Systems

The molecular and cellular-level processes presented in the previous subchapters are ultimately organized into a system of pathways and networks enabling the various functions of the brain. Classically, to explain brain architecture, the field of neuroscience has aimed to separate the brain into different well-defined areas and assign one or several functions to each. Brain areas can be delineated using various approaches. For instance, the human cortex was divided into different regions by Korbinian Brodmann in 1909 based on its cytoarchitecture (Brodmann, 1909). The resulting areas have since been reevaluated and refined but are still of relevance presently. They are named after Brodmann, numbered and are mostly assigned one or several functions, as determined in later studies. For instance, Brodmann area 4 is also known as the primary motor cortex due to its importance in motor processing.

Nonetheless, while it still holds true that certain areas are more involved in specific functions than others, the approach of segregating the brain into separate areas which only perform one function is nowadays regarded as outdated, since it cannot explain the tremendous variability in brain functionality. In contrast, currently neuroscience attempts to assign different

functions to networks of regions working in conjunction by investigating the brain's connectivity (Pessoa, 2013; van den Heuvel and Sporns, 2013). Two types of connectivity can be defined between brain regions. First, structural connectivity represents the anatomical link between areas via neuronal tracts (Huang and Ding, 2016). As a rule of thumb, it is established that the brain is organized to maximize efficiency and minimize energy expenditure (Tomasi et al., 2013). Hence, both local connections in the form of synapses and long-path connections in the form of neuronal tracts are only maintained if they are sufficiently used (Kandel et al., 2013). Therefore, if regions are structurally connected, they are mostly also functionally connected, according to Hebb's rule ("neurons that fire together, wire together") (Hebb, 1950; Löwel and Singer, 1992). Regions are defined as functionally connected if they share the execution of a brain function. Although the two types of connectivity overlap partly, structural connectivity is not a prerequisite for regions being functionally connected (Honey et al., 2009; Uddin, 2013). For instance, if region A is structurally connected to region B and region B is structurally connected to region C, however there is no direct structural connection between regions A and C, they can still be defined as functionally connected if they both function in conjunction for the execution of a specific function.

The most widespread approach to track structural connectivity *in vivo* is using tractography with diffusion MRI (Basser et al., 2000). Functional connectivity, a concept introduced over the last decades, is defined as the temporal correlation between the activities of separate brain regions (Biswal et al., 1995b). Hence, functional connectivity can only be assessed *in vivo*, using methods able to dynamically provide either direct or indirect measures of neuronal activity over a period of time. Functional connectivity relies on the notion that neurons or neuronal populations firing in conjunction over longer periods of time indicate a transfer of information (Bowyer, 2016). The phenomenon of coherent firing has been observed *in vitro* (Scarpetta and de Candia, 2014), where cultures of neurons have been shown to fire in concerted fashion without external stimuli, as well as *in vivo* (Biswal et al., 1995b). In the living brain, coherent activity patterns occur both locally, between neurons of the same region, and at the level of entire populations, between pairs and ultimately arrays of distinct brain areas, termed as functional brain networks. Importantly, although they can be enhanced by specific stimuli, evoked neuronal activation is not a prerequisite for the function of brain networks (Smith et al., 2009). In contrast, functionally connected areas show coherent activity patterns even at rest, when no external stimulus is being processed and, remarkably, during

sleep or even during coma (Achard et al., 2012). Therefore, they are also termed resting-state networks (RSNs) (Fox et al., 2005b).

1.4 Resting-State Networks

Several functional brain networks have been defined (Figure 3), and, as their name suggest, functions have been assigned to most. One of the most prominent examples is the default-mode network (DMN), comprised of a collection of regions along the midline of the cortex and parts of the parietal cortex (Buckner et al., 2008). In the human brain, the medial prefrontal cortex, the precuneus, the posterior cingulate cortex, and the posterior parietal cortex are postulated to comprise the DMN. One of the most intriguing properties of the DMN is its enhanced activation during rest or the absence of a task (Raichle et al., 2001). Therefore, it is assumed to be involved in introspective processes, such as mind-wandering, remembering the past, and planning the future, but also memory consolidation. Its counterpart is deemed to be the sensorimotor network (SMN), comprising an array of regions involved in extrospective processing, such as the integration of sensory information and generation of subsequent motor responses (Conio et al., 2019). The regions comprising this network are, among others, the somatosensory and motor cortices, as well as the striatum and thalamus, two regions working as relay areas between the cortex and the periphery. The salience network (SN) is assumed to ensure the balance between the DMN and SMN and, thus, between introspective and extrospective processing (Conio et al., 2019; Seeley, 2019; Seeley et al., 2007). This network is coordinated by the insula, a main hub of emotional processing, and the anterior cingulate cortex. Finally, several networks integrating different types of stimuli, such as the visual or auditory network, have been reported (Smith et al., 2009). The first publication part of this thesis is centered around the detection of RSNs from simultaneously acquired fMRI and [^{18}F]FDG PET datasets.

The RSNs investigated in the second publication comprising this thesis, the DMN (Andrews-Hanna, 2012), SN (Seeley, 2019; Seeley et al., 2007) and SMN (Göttlich et al., 2013), were selected due to their roles in various diseases. A number of pathologies have been suggested to be dominated by dysfunctions of one single network. For instance, in Parkinson's Disease (PD) alterations of the SMN have been reported by most studies (Göttlich et al., 2013). In contrast, for certain pathologies, including psychiatric diseases such as major depressive disorder (MDD) or bipolar disorder (BD), changes have not only been detected in the function of single networks, but also in the interactions between them (Conio et al., 2019). In the case of the mentioned psychiatric disorders, a recent study has proposed that the interactions

between DMN, SN and SMN mediate different psychiatric phenotypes (Conio et al., 2019). The physiological background behind the importance of the balance between these three networks is the following. The DMN is postulated to be involved in introspective processing, such as mind-wandering and rumination (Andrews-Hanna, 2012; Conio et al., 2019; Lu et al., 2012). By contrast, the SMN network is responsible for extrospective processing, comprised by integrating external stimuli and generating appropriate responses to the outer world (Conio et al., 2019; Göttlich et al., 2013). Preserving the balance between these two types of processing appears mandatory, a loss of balance towards either side leading to behavioral dysfunctions (Conio et al., 2019). The SN is believed to ensure the balance between internal and external processing by, among others, selecting relevant external or internal stimuli and modulating emotion (Conio et al., 2019).

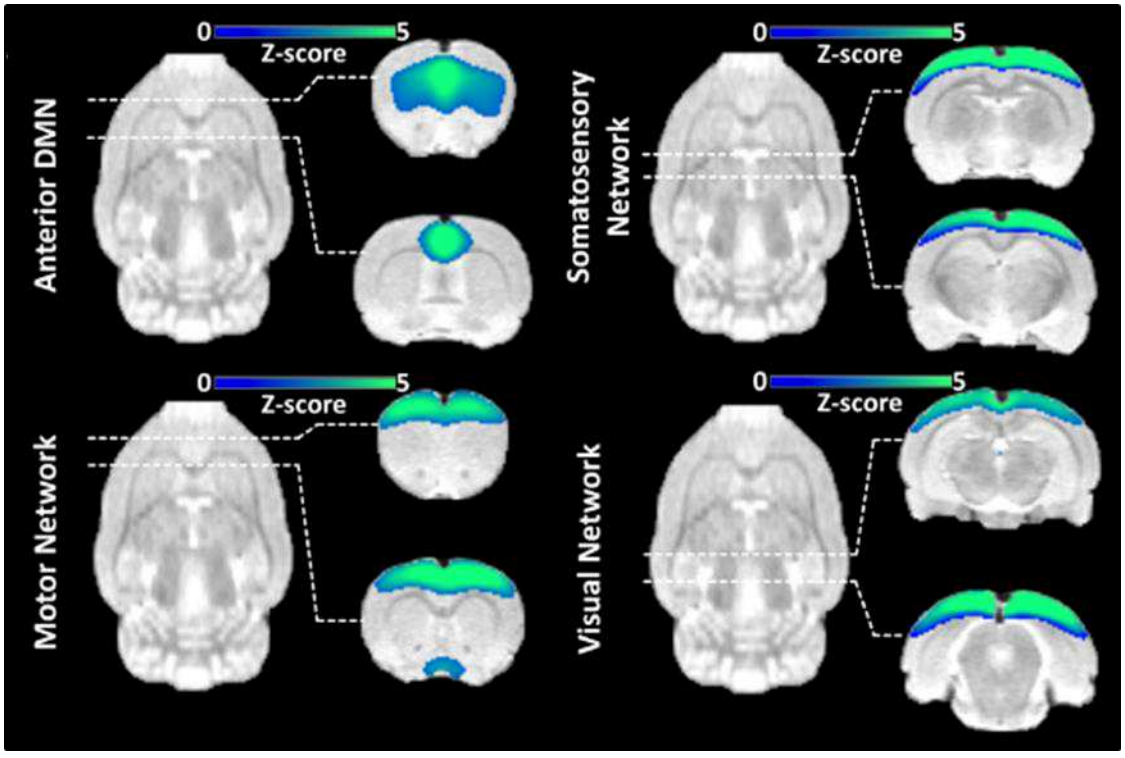

Figure 3: Examples of common resting state networks in the rat brain (adapted from (Ionescu et al., 2021b)). Using independent component analysis, robust RSNs such as the default-mode network (DMN), motor network, somatosensory network or visual network can be derived.

1.5 Neurotransmitter Systems

Neuronal pathways are also characterized by the primary neurotransmitter involved in their functions. Pathways defined in this fashion partly overlap with functional networks described above. For instance, dopamine, a monoaminergic modulatory neurotransmitter, acts via four separate pathways, each purported to play a separate role. One of the dopaminergic pathways

emerges from the substantia nigra pars compacta and projects prominently to the striatum across the nigrostriatal pathway. The nigrostriatal pathway has been associated with motor function and anatomically it overlaps to a high extent with the sensorimotor network described above. Next, the mesolimbic pathway, involved in reward processing, involves projections from the ventral tegmental area (VTA) to the nucleus accumbens. The mesocortical pathway, playing a role in cognition, also arises from the VTA, yet its projections reach the frontal cortex. Finally, the tuberoinfundibular pathway regulates hormone secretion via the hypothalamus and pituitary gland (Kandel et al., 2013). Serotonin, another main modulatory neurotransmitter, is produced at the raphé nuclei, which project to a more widespread array of brain regions than dopamine. However, serotonergic pathways are also somewhat more diffuse, their functions being much more elusive than those of dopamine (Andrews et al., 2015; Hornung, 2010). Nonetheless, serotonin is assumed to play a role in various psychiatric diseases, such as MDD or BD (Conio et al., 2019). Generally, the monoaminergic innervation of prominent projection areas appears to be of particular importance for brain health (Bhagwagar et al., 2018; Conio et al., 2019; Roussakis et al., 2016). The nigrostriatal pathway appears to modulate striato-thalamo-cortico-striatal loops important for various functions in the healthy brain and its dysfunction is associated with PD (Silkis, 2001). A further essential region postulated to exert significant top-down control is the medial prefrontal cortex (mPFC) (Avery and Krichmar, 2015; Celada et al., 2013). Dopaminergic and serotonergic innervations of the mPFC have been shown to be changed in both schizophrenia (Avery and Krichmar, 2015) and MDD (Celada et al., 2013; Lanzenberger et al., 2012).

1.6 From Single Molecules to Entire Networks: Imaging the Brain *In Vivo*

The emergence of imaging methods allowing the *in vivo* examination of the brain during the last century has provided a whole new dimension to research and medicine. Until then, neuroscience had a relatively narrow methodology for studying brain function *in vivo*, being largely limited to relating normal or abnormal behavioral traits to the respective post-mortem findings. Therefore, the ability to image the processes in such a complex and rapidly changing organ represents a major advance. Figure 4 shows the main processes associated with neuronal activation and methods to map them *in vivo*.

Today, various methods enable the *in vivo* tracking of numerous processes occurring in the brain. The entire neuronal activity mechanism, but also adjacent processes, such as the

delivery of oxygen and glucose via blood vessels, can be observed in both animals and humans. The first non-invasive method to record neuronal activity *in vivo* was electroencephalography (EEG). EEG uses electrodes placed on the scalp to record the electrical activity of neuronal populations in the cortex (Niedermeyer and da Silva, 2005). As described above, information is transported post-synaptically across the bodies of neurons in the form of action potentials. The action potential of a single neuron is not of sufficient magnitude to be captured by non-invasive methods. Yet, since neuronal populations exhibit coherent spontaneous activity patterns, they amount to a signal of sufficient magnitude to be recorded as changes in voltage by EEG electrodes. While advantageous due to its simple use and direct recording of neuronal activity at a very high temporal resolution in the range of milliseconds, EEG suffers from poor spatial resolution and the fact that it misses activity from subcortical areas. Moreover, it only illuminates part of the neuronal activation process, namely the propagation of electrical signals across neurons, but does not reveal anything about synaptic mechanisms (Niedermeyer and da Silva, 2005).

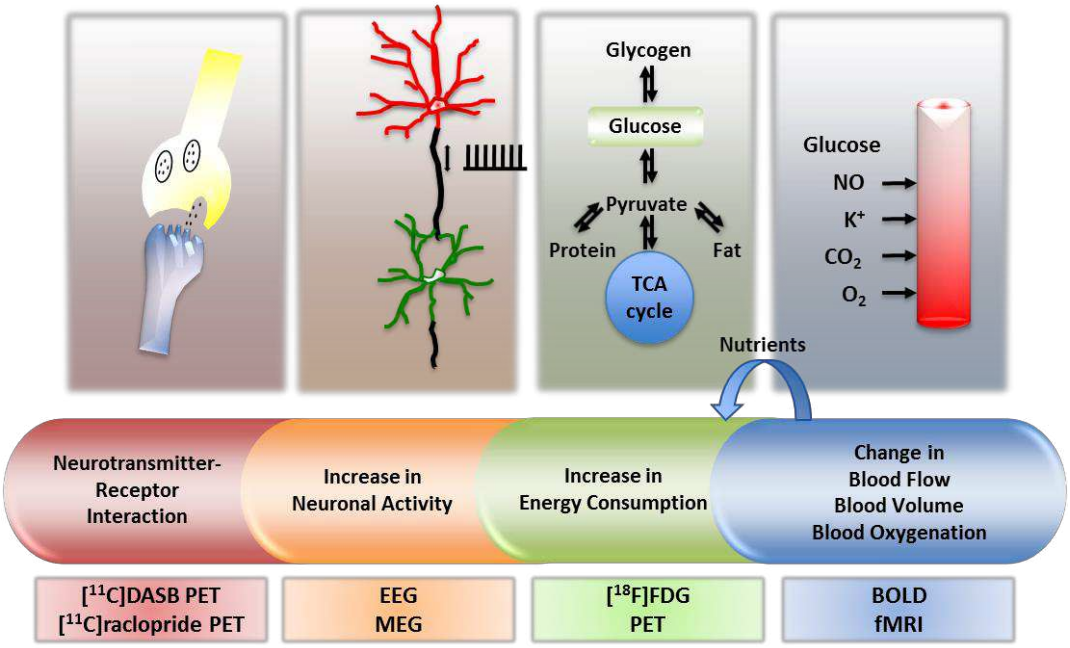

Figure 4: Physiological processes comprising or accompanying neuronal activity and imaging methods used to track them. Starting at the synapse, neuronal activation involves the release of neurotransmitters into the synaptic cleft and their binding to post-synaptic receptors. PET ligands targeting receptors or transporters such as [^{11}C]raclopride can track such processes. Large enough post-synaptic signals can generate action potentials which can be captured by EEG or magnetoencephalography (MEG). To meet the energy demand of these processes, glucose is delivered to the brain, the consumption of which can be quantified using [^{18}F]FDG-PET. Nutrient intake is associated with hemodynamic changes that can be measured with BOLD-fMRI. Abbreviations: TCA: tricarboxylic acid cycle, DASB: 3-amino-4-(2-dimethylaminomethylphenylsulfanyl)-benzonitrile, PET: positron emission tomography, EEG: electroencephalography, MEG:

magnetoencephalography, FDG: fluorodeoxyglucose, BOLD fMRI: blood-oxygenation-level-dependent functional magnetic resonance imaging. Adapted from (Amend, 2019; Wehrl, 2013; Wehrl et al., 2014).

1.6.1 Magnetic Resonance Imaging

Magnetic resonance imaging exhibits several advantageous technical capabilities for depicting the anatomy and monitoring the function of the brain, including excellent spatial resolution and temporal resolution, along with high soft-tissue contrast (Pichler et al., 2008). Additionally, the MR images are generated using contrasts emerging from the intrinsic magnetic properties of the tissues imaged. Therefore, although substances improving the contrast of MR images, so-called contrast agents, can be applied, these are not a prerequisite for performing MR scans. Importantly, whether executed with or without contrast agents, MR offers the advantage of not requiring the delivery of radiation for the generation of images, as opposed to PET or computer tomography (CT).

Principles of MRI: Quantum Physics

The concept of MRI relies on the properties of atoms to spin around their own axes and was first used for producing images in 1973 (Lauterbur, 1973). Each nucleus with an uneven number of neutrons or protons produces a spin, which in turn generates a magnetic moment. The factor connecting the spin ($\vec{J}$) and the magnetic moment $\overrightarrow{\mu_m}$ is the gyromagnetic ratio γ:

$$\overrightarrow{\mu_m} = \gamma \vec{J}$$

MRI, even though other types of atoms can be investigated, most commonly records the magnetic properties of hydrogen (H^+) atoms, which are comprised of one proton and have the spin $\frac{1}{2}$. Hydrogen atoms are available in abundance in the organism as part of water (H_2O) or fat molecules. Outside an external magnetic field, the spins of different nuclei are aligned in random directions. Once placed into a strong magnetic field, as generated by an MRI scanner, the spins align either parallel or anti-parallel to the external magnetic field, taking up one of two states, either $\frac{1}{2}$ or $-\frac{1}{2}$ (Haken and Wolf, 2003). The energy required for crossing between the two states is dependent on the so-called Larmor frequency, which in turn is determined by the static magnetic field the spin is placed in:

$\Delta E = \frac{h}{2\pi}\omega_0$, where:

- h is the Planck constant
- ω_0 is the Larmor frequency

- $\omega_0 = \gamma B_0$, where B_0 is the magnetic field

The Larmor frequency is highly significant for MR images since the state of the spins can be changed when applying a radiofrequency (RF) pulse at the corresponding Larmor frequency. Importantly, since it is energetically more favorable, slightly more spins align parallel to the magnetic field than antiparallel. This difference between the probability of a spin being parallel or antiparallel to the direction of the magnetic field depends on the energy difference between both spin states and the temperature:

$P_p - P_a = \frac{\Delta E}{2k_B T}$, where

- P_p is the probability of a spin being aligned parallel to the magnetic field
- P_a is the probability of a spin being aligned antiparallel to the magnetic field
- ΔE is the energy difference between the two states
- k_B is the Boltzmann constant
- T is the temperature

Therefore, at room temperature, per Tesla approximately 0.0003% more spins align parallel than antiparallel, generating a net magnetization which is ultimately at the root of the signal in MR images (Huettel et al., 2004b).

Principles of MRI: Traditional Physics

To understand the generation of images, the net magnetization described above can be further contemplated using a mixture of quantum and traditional physics.

While the net magnetization is at the root of the MRI signal, further steps are required to generate images based on this effect. To this end, the net magnetization needs to be manipulated. By convention, the net magnetization $\vec{M}$ is directed along the main magnetic field $\vec{B}_0$. A second important aspect regarding the spins in a static magnetic field is their angular momentum, which by its slight tilt causes them to rotate in a precession movement around the z-direction, by convention the direction of the main magnetic field, at the Larmor frequency. The manipulation of the spins and the generated net magnetization occurs via an RF pulse, referred to as $\vec{B}_1$, applied at the Larmor frequency perpendicular to the static magnetic field. By convention, the RF pulse is applied in x-direction. On quantum level, the RF pulse has two effects. First, while the precession of the spins continues, they are tilted by the angle θ. Second, directly after the application of the RF pulse, the spins are in the same

phase. On macroscopic level, this generates a net magnetization rotating at Larmor frequency and an angle θ to the z-axis. The angle θ depends on the duration of $\vec{B}_1$, t_{B_1}, its amplitude, as well as the gyromagnetic ratio γ (Huettel et al., 2004b):

$$\theta = \gamma B_1 t_{B_1}$$

The rotating magnetization induces a voltage in a metallic receiver coil, which represents the MR signal. However, after application of a single RF pulse, its effect on the net magnetization only lasts for a short time, $\vec{M}$ quickly returning to its initial state. The signal induced into the receiving coil between the RF pulse and the return to its original state is called free induction decay (FID). The return to the initial magnetization state occurs due to two processes called relaxation, the T_1 and T_2 relaxations. Different substances and, for *in vivo* measurements, tissues, have different T_1 and T_2 relaxation rates, a fact which is at the origin of the contrast in MR images (Huettel et al., 2004b). T_1 relaxation, or longitudinal relaxation, describes the return of the net magnetization from the x-y plane, in the case of a tilt angle of 90°, to the z-axis. This process is driven by the release of energy induced by the RF pulse from the spins, during which they return to their initial state of lower energy. During relaxation, the net magnetization is composed of a component along the z-axis, called $\vec{M}_z$, which increases over time, and the x-y plane component, $\vec{M}_{xy}$, which simultaneously decreases. The magnitude of $\vec{M}_z$ in relation to the time following the RF pulse is described by the following equation (Huettel et al., 2004b):

$M_Z = M_0(1 - e^{-\frac{t}{T_1}})$, where

- M_0 represents the net magnetization
- t represents the time after the RF pulse
- T_1 is the longitudinal relaxation rate of the volume

The second relaxation process, T_2, also called transversal relaxation, represents the loss of phase coherence between the phases of the precessing spins. In turn, the loss of coherence is due to two separate processes. First, the interactions between spins lead to a loss of coherence due to the effects their own magnetic fields have on neighbouring spins. Therefore, T_2 relaxation is also called spin-spin relaxation. Over time, this leads to an additional decay of the transversal magnetization, depending on the T_2 relaxation constant (Weishaupt et al., 2013):

$$M_{xy} = M_0 e^{-\frac{t}{T_2}}$$

A second factor leading to the loss of coherence between the spins is represented by the local magnetic inhomogeneities. These can be either of technical nature or due to the distortions in the magnetic field caused by the magnetic properties of the tissues, a phenomenon called magnetic susceptibility. The relaxation induced by magnetic inhomogeneities is termed T_2' and together with the T_2 relaxation can be summarized to a single constant T_2* (Huettel et al., 2004b):

$$\frac{1}{T_2^*} = \frac{1}{T_2} + \frac{1}{T_2'}$$

T_2^*-relaxation induces the decay of the transverse magnetization M_{xy}:

$$M_{xy} = M_0 e^{-\frac{t}{T_2^*}}$$

Signal Localization

When applying an RF pulse in a homogeneous magnetic field, the entire volume is affected, since the Larmor frequency applied to manipulate the spins corresponds the magnitude of the static magnetic field. Therefore, it would not be possible to determine from which location the signal measured by the receiving coil originates. Thus, when performing MR imaging, only a specific slice of the volume is manipulated at a time. To achieve this, additional coils generate so-called gradient magnetic fields. These are gradually increasing magnetic fields in each direction. The gradient fields are in the range of mT and their respective magnitudes are added at each location onto the main magnetic field. In contrast to the main magnetic field, the gradient fields can be switched on and off during image acquisition (Brown et al., 2014; Weishaupt et al., 2013).

First, the slice-encoding gradient, $\vec{G}_z$, is turned on to select single slices in z-direction. The linearly increasing field overlapped onto the static field ensures different Larmor frequencies of the spins depending on the respective spatial location of the slice. Therefore, only the slice containing spins precessing with the appropriate Larmor frequency can be stimulated by the RF pulse. Using the bandwidth and slope of the gradient the widths of slices can be adjusted. To localize signals within a slice, two additional gradients, $\vec{G}_X$ and $\vec{G}_y$ are used. When switching both gradients on, the spins within the slice precess with location-dependent frequencies and phases. Therefore, each volume in x-y direction has a unique combination of

phase and frequency, allowing the localization of the signal. The direction along which the magnetizations have different frequencies is termed frequency-encoding direction. In the phase-encoding direction, the corresponding gradient is only shortly switched on, accelerating spins in accordance to the gradient magnitude. After switching this gradient off, the spins in this direction are slightly dephased. The matrix describing the phase and frequency-encoding directions in a slice is called k-space (Huettel et al., 2004a).

MRI Sequences

MRI sequences are different protocols to manipulate the magnetization of the volume of interest and generate images based on the different relaxation properties of tissues contained within the respective volume. Based on the type of contrast they generate, they can be classed as T_1 or T_2-weighted sequences. In Figure 5 the two types of relaxation and the sequences allowing their manipulation are illustrated.

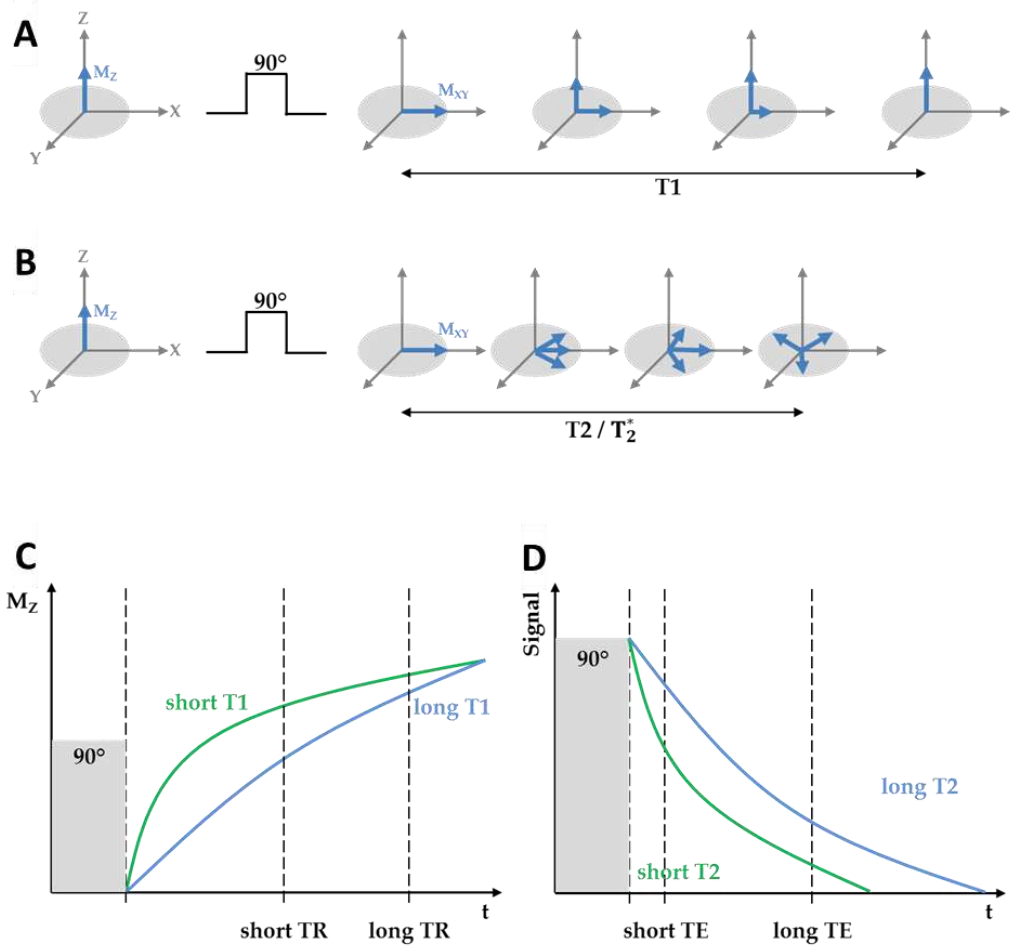

Figure 5: Types of relaxation and their impact on the acquired signals and contrasts. Adapted from (Amend, 2019; Weishaupt et al., 2013).

The main method to manipulate tissue magnetizations based on the T_1 relaxation is using RF pulses. As described above, following an RF pulse the tilted magnetization immediately undergoes the T_1 relaxation process. If a second RF pulse is applied before the relaxation process is concluded, only the $\vec{M}_z$ component available at the moment of the second RF pulse can be manipulated. Hence, since different tissues have different T_1 relaxation constants, the magnitudes of their respective $\vec{M}_z$ components at the time subsequent RF pulses are applied will differ, generating a contrast between them. The duration between two RF pulses is called relaxation time and is abbreviated as TR (Brown et al., 2014).

To take advantage of the T_2 relaxation two approaches exist. As mentioned above, T_2 relaxation refers to the loss of coherence between different spins in x-y plane. The loss of coherence due to magnetic inhomogeneities (T_2') can be reverted. The first method to achieve this is, after a period of time following the first RF pulse of 90°, to apply a second RF pulse of 180°. The second pulse inverts the phases of the spins relative to each other. This leads the spins with the fastest precession frequencies to be trailing and vice-versa. Since the respective spins maintain their frequencies after the RF pulse, they catch up und rephase in relation to the slower-precessing spins, leading to an increase in $\vec{M}_{xy}$ magnetization called echo. The time between the first RF pulse of 90° and the echo is called echo-time (TE). Sequences using a second RF pulse to restore the phase of the spins are called spin-echo sequences (Brown et al., 2014).

A second approach to restore the phase of the precessing spins is by consecutively applying two additional gradient fields. The first gradient, called dephasing gradient, accelerates the phase loss, or FID. The second gradient is applied in the opposite direction, cancelling out the effects of the first gradient applied and refocusing the spins, thereby generating an echo. In contrast to spin-echo sequences, gradient echo sequences do not reverse T_2' relaxation effects. Therefore, they can be used to generate contrasts between areas of the volume with differing T_2' constants, caused for example by differing magnetic susceptibilities (Brown et al., 2014). While all types of relaxation impact the contrast in each generated image, each combination of TR and TE can generate contrasts which are dominated by T_1, T_2 or T_2* effects respectively. Accordingly, the sequences used to generate these images are termed T_1, T_2 or T_2*-weighted (Brown et al., 2014).

MRI Scanners

MRI scanners are comprised of several components. First, a superconductive main magnet generates the main magnetic field. For human scanners used in clinics the field strengths are standardly 1.5 or 3T, while higher field strengths can be employed for research. Animal scanners are usually conducted at higher field strengths ranging from 4.7 to 15.1T (Wehrl et al., 2014). The main magnet is cooled using liquid helium. Additionally, scanners consist of gradient coils, shim coils to correct for inhomogeneities of the main field and RF coils which can be used to generate RF pulses, receive signals, or both (Weishaupt et al., 2013).

Functional MRI

Initially, MRI scans were performed to merely provide morphological information of the imaged volumes. In 1990, based on earlier work performed on the magnetic properties of blood oxygenation (Thulborn et al., 1982), functional magnetic resonance imaging was introduced, allowing the imaging of function through the hemodynamic properties of tissues, a breakthrough which proved to be of particular significance for brain research (Ogawa et al., 1990a). The method was named blood oxygenation level dependent fMRI (BOLD-fMRI) and took advantage of the differing magnetic properties of deoxygenated and oxygenated hemoglobin to generate contrasts between different regional blood oxygenation levels. It relies on the fact that deoxygenated hemoglobin is strongly paramagnetic, while oxygenated hemoglobin is weakly diamagnetic. Therefore, deoxygenated hemoglobin has a 20% higher magnetic susceptibility compared to oxygenated hemoglobin, causing a faster dephasing of the nearby spins due to T_2* effects (Pauling and Coryell, 1936). The BOLD effect can be generated using both gradient-echo and spin-echo sequences (Ogawa et al., 1990a; Thulborn et al., 1982).

Through its ability to provide contrasts depending on blood oxygenation, BOLD-fMRI is therefore purported to be an indirect method of recording neuronal activity, which is coupled to hemodynamics via the neurovascular coupling (Buxton, 2012). Significant research has been performed to decompose the hemodynamic factors contributing to the BOLD signal. While not completely elucidated, the current notion is that the $CMRO_2$, CBF and cerebral blood volume (CBV) all contribute to the BOLD signal to different extents (Buxton, 2012). Upon neuronal stimulation, a typical shape in the BOLD signal relative to the baseline value can be observed, termed hemodynamic response function (HRF). First, an initial dip occurs in the signal, believed to be driven by an increase in oxygen extraction after neuronal activation (Menon et al., 1995). To provide the necessary nutrients to cover the energy demands elicited

by the activation, oxygenated hemoglobin is transported by a massive increase in CBF corroborated with smaller increase in CBV. This effect leads to an increase in the BOLD signal, which reaches a peak 4-6 seconds after neuronal activation (Buxton, 2012; Mandeville et al., 1999). If a singular stimulus is applied, after the peak the BOLD signal decreases below the initial value after several seconds, a phenomenon called post-stimulus undershoot. The post-stimulus undershoot is believed to be induced by the different dynamics of CBF and CBV leading to a higher proportion of deoxygenated hemoglobin compared to oxygenated hemoglobin (Mandeville et al., 1999). After an additional couple of seconds, the BOLD signal returns to pre-stimulus levels. The described process is illustrated in Figure 6.

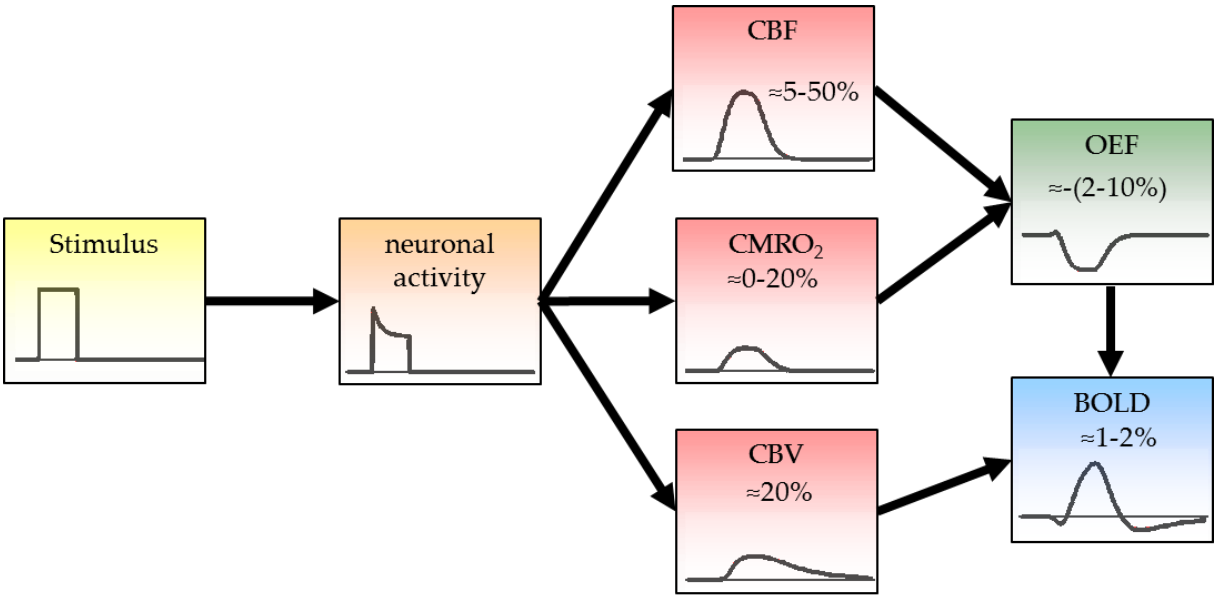

Figure 6: Neurovascular coupling detected using BOLD-fMRI. When a stimulus is applied, neuronal activation takes place. Via neurovascular coupling, it is accompanied by changes in CBF, $CMRO_2$ and CBV of different magnitudes and temporal characteristics. Together, they result in changes of the BOLD signal characterized by the HRF. Abbreviations: CBF: cerebral blood flow, $CMRO_2$: cerebral metabolic rate of oxygen, CBV: cerebral blood volume, OEF: oxygen extraction fraction, BOLD: blood oxygenation level dependent, HRF: hemodynamic response function. Adapted from (Amend, 2019; Buxton, 2009).

Accordingly, the BOLD effect can be used to indirectly detect neuronal stimulation. To this extent, two types of applications exist. Stimulus-evoked fMRI (st-fMRI) describes the study of brain activation patterns following tasks or non-pharmacological stimuli. For st-fMRI, a stimulus such as a visual or auditory cue can be delivered directly or the subject can actively perform a task, such as finger-tapping, leading to neuronal activation in corresponding brain regions. Secondly, the effect of pharmacological agents can be investigated by delivering a pharmacological challenge during the scan using pharmacological fMRI (ph-fMRI) (Jonckers et al., 2015). Finally, functional connectivity can be derived from the fluctuations of the

BOLD signal reflecting the coherence of spontaneous fluctuations of underlying neurons (Biswal et al., 1995a). When acquired at rest, the generated readout is called resting-state functional connectivity (rsFC) (Fox et al., 2005a). FC can however also be acquired and compared to the resting-state condition during pharmacological or non-pharmacological stimulations, generating task-modulated FC (Cole et al., 2021). Spatially, both activation and connectivity measures can be calculated at either voxel or regional level. To this extent, the BOLD signal in the voxels or regions of interest is extracted and undergoes specific analytical steps. To detect activation, the BOLD signal during stimulation must be statistically tested against the BOLD signal during the baseline phase. Based on a significance threshold, a statistical test can indicate the activation, or deactivation in case of a signal decrease, induced by the applied stimulation paradigm.

Functional connectivity readouts can be generated using different approaches (Figure 7). To calculate the functional connectivity between two regions-of-interest (ROIs), the BOLD signal must be extracted from both. Their functional connectivity is then calculated as the temporal correlation between their BOLD signals, for instance using Pearson's correlation coefficient. Thus, when calculating correlating coefficients between each pair of regions defined for instance by a brain atlas, a correlation matrix can be generated. A functional connectivity matrix indicates the functional connectivity between all pairs of ROIs investigated. Using the same mathematical approach, FC can be calculated between an ROI and each voxel in the brain or even between two voxels. Pearson's correlation coefficients can be calculated using the following equation:

$$r = \frac{\sum_{i=1}^{n}(u_i - \bar{u})\,(v_i - \bar{v})}{\sqrt{\sum_{i=1}^{n}(u_i - \bar{u})^2}\sqrt{\sum_{i=1}^{n}(v_i - \bar{v})^2}}$$

where:

- n is the number of samples (time-points)
- u and v are the BOLD values of two regions over a period of time
- u_i and v_i are the single samples (BOLD values at time-point i)
- $\bar{u}$ and $\bar{v}$ are the arithmetical sample means of the respective values at all time-points

Furthermore, functional networks can be extracted using independent component analysis (ICA). ICA is based on the assumption that neurons belonging to the same network fluctuate

in temporally similar patterns, which is also reflected in the BOLD signal. Hence, ICA is able to extract different functional networks based on their temporal characteristics (Figure 7). More advanced analysis can further characterize the properties of the extracted networks or of the entire connectome. For instance, graph theory can be applied to determine parameters describing the global or local organization of the connectome (Bullmore and Sporns, 2009).

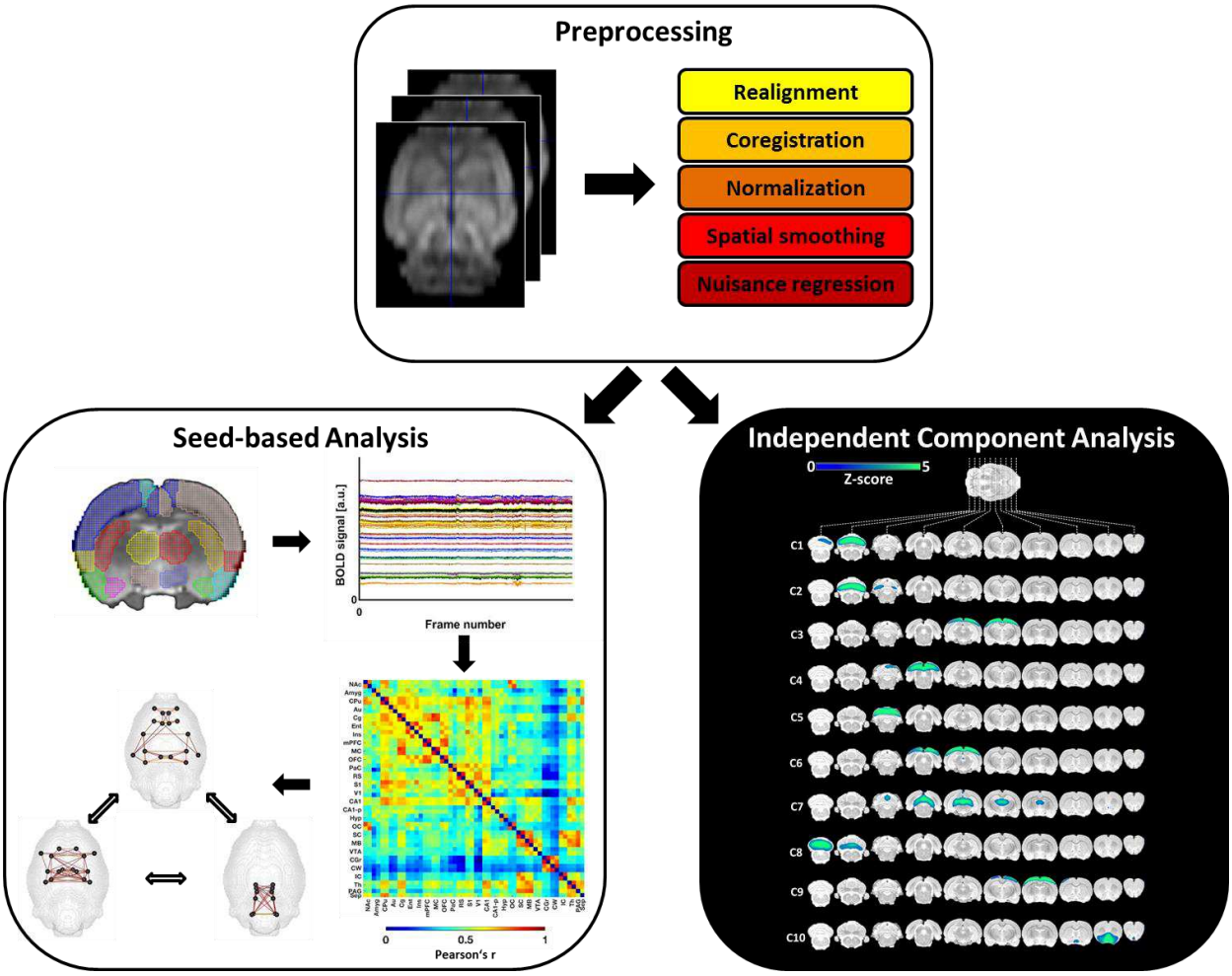

Figure 7: Methods of inferring functional connectivity. Prior to analysis, the acquired fMRI images undergo preprocessing, including realignment, coregistration to anatomical reference, normalization to a standard template, spatial smoothing and nuisance regression. Seed-based analysis and independent component analysis are among the most widespread methods to infer functional connectivity. For seed-based analysis, regional time-courses are first extracted after parcelation based on an atlas. By computing pair-wise correlations between all time-courses, a whole-brain connectivity matrix is generated, indicating the connectivity between for every pair of regions. Based on the whole-brain readout, resting-state networks can be extracted and their interplays analyzed. For independent component analysis, no a-priori parcelation is required. As a data-driven approach, the whole-brain signal can be analytically separated into a pre-defined number of independent components and the voxelwise contribution of each voxel to every component can yield resting-state networks (Scheinost et al., 2017).

1.6.2 Positron Emission Tomography

For neuroscience, the emergence of PET (Ter-Pogossian et al., 1975) enabled the tracking of neurotransmitter-receptor interactions in the synaptic cleft, along with various other molecular-level processes. Based on the radioactive tracer concept introduced by de Hevesy in 1923 (Hevesy, 1923), the first clinical PET scanner was introduced in the 1970s (Ter-Pogossian et al., 1975). The principle by which PET allows the imaging of a process in an organism is by injecting a molecule with analogous physiological properties to the molecule involved in the process of interest, but labelled with a radioactive isotope. Such molecules are called PET tracers.

Radioactive Isotopes and Decay

Different types of radioactive decay exist. PET is based on β^+ decay, the isotopes used for labelling being called positron emitters. For a list of several isotopes used for PET tracer labeling, please refer to Table 2.

Table 2: List of isotopes with different half-lives used for PET imaging (Phelps, 2004), along with examples of tracers for which the isotopes are used. Abbreviations: DASB: 3-amino-4-(2-dimethylaminomethylphenylsulfanyl)-benzonitrile, FDG: fluorodeoxyglucose, MIBG: Meta-iodobenzylguanidine.

Isotope	Half-life	Positron range in tissue [mm]	Exemplary tracer	Application
^{15}O	2 min	1.5	[^{15}O]H_2O	Blood perfusion
^{11}C	20.3 min	0.3	[^{11}C]raclopride [^{11}C]DASB	D2/D3 receptors and serotonin transporters
^{18}F	109.8 min	0.2	[^{18}F]FDG	Glucose metabolism
^{64}Cu	12.7 h	0.65	[^{64}Cu]Dotatate	Cancer: somatostatin receptors
^{124}I	4.18 days	2.8	[^{124}I]MIBG	Cancer: Neuroblastoma

β^+ decay occurs in unstable, proton-rich nuclei. In such nuclei, a proton decays to a neutron, simultaneously emitting a positron and an electron-neutrino (Phelps, 2004):

$$p \rightarrow n + e^+ + v_e,$$

where:

- p is a proton
- e^+ is a positron
- v_e is a electron-neutrino

The same phenomenon can be described on atomic level using the following equation (Phelps, 2004):

$$^A_Z X \rightarrow {}^A_{Z-1}X' + e^+ + v_e,$$

where:

- A is the mass number
- Z is the atomic number
- $^A_Z X$ is the mother nuclide
- $^A_{Z-1}X'$ is the daughter nuclide

After injection, the PET tracer accumulates in areas where the process of interest occurs. For instance, the glucose analogue [^{18}F]FDG preferentially accumulates in areas with high glucose consumption. At the same time, the isotope labelling the tracer emits positrons during radioactive decay. Shortly after being emitted, the positron loses energy upon interaction with other particles causing its deceleration. After traveling a distance in the range of a few millimeters, depending on the isotope, it interacts with an electron (e^-), taking part in a so-called annihilation process (Phelps, 2004). The distance travelled by a positron until the annihilation process is called positron range and limits the spatial resolution of a PET scan (Table 2). The result of this annihilation is the generation two γ-quants of equal energies, 511 keV, traveling in opposite directions at an angle of roughly 180°:

$$\beta^+ + e^- \rightarrow 2\gamma$$

In this work, two reversible PET tracers were used. [^{11}C]3-amino-4-(2-dimethylaminomethylphenylsulfanyl)-benzonitrile ([^{11}C]DASB) is a PET tracer trageting the serotonin transporter (SERT) (Houle et al., 2000). The function of SERT is the reuptake of

serotonin from the synaptic cleft into the pre-synaptic neuron, thereby ending its action at the synapse. Regionally, the highest [^{11}C]DASB uptake occurs in regions with high SERT availability, such as the brain stem, midbrain and other subcortical areas (Ionescu et al., 2022; Reimold et al., 2007). The second tracer used was [^{11}C]raclopride, an antagonist tracer binding to dopamine D_2 and D_3 receptors, with higher affinity to D_2 receptors (D2Rs) over D_3 receptors (D3Rs) (Farde et al., 1995; Köhler et al., 1985). D_2 receptors are involved in the so-called indirect striatal pathway, which, in contrast to its counterpart, the direct pathway, inhibits the cortico-striato-thalamo-cortical pathways responsible for several motor and cognitive functions in the brain (Gerfen and Surmeier, 2011).

In addition to tracers that image direct neuronal processes, PET tracers exist to study adjacent processes linked to neuronal activity, such as energy consumption. In this work, one of the most widely applied PET tracers was used, the glucose analogue [^{18}F]FDG. This tracer is composed of a glucose molecule labeled with a radioactive ^{18}F isotope. After tracer application, the tracer is delivered to cells according to their metabolic rates of glucose. After passing the membrane the cell [^{18}F]FDG enters glucose metabolism, yet only goes through the first step, namely the phosphorylation (Phelps, 2004). For an overview of the metabolic pathways of glucose please refer to Figure 2. After phosphorylation it cannot exit the cell and return to the blood pool, a phenomenon termed trapping. Hence, based on availability in the blood compartment, [^{18}F]FDG accumulates in the cells according to their respective metabolisms, with regions of higher metabolic activity showing increased [^{18}F]FDG uptake.

PET Scanners

A PET scanner is used to detect the pairs of photons generated the annihilation process described above. It mostly consists of a circular array of detectors able to record pairs of photons. To this extent, PET detectors need to be able to convert the γ-quants into a measurable signal. Therefore, they are largely composed of two units serving distinct purposes: first, the γ-quants need to be transformed into visible light in a process called scintillation. Scintillators are able to absorb particles such as γ rays and generate light. Thus, the γ-quants generated in an annihilation process reach two opposed PET detectors where they are transformed into visible light by scintillators. Scintillator materials used for PET are mostly crystals and include, among others, bismuth-germanate (BGO) and lutetium oxyorthosilicate (LSO). The second part of a detector converts the light into an electrical signal and amplifies the generated signal (Phelps, 2004). In standard PET scanners, this is achieved using photomultiplier tubes (PMTs), although other types of amplifier systems with

improved technical specifications such as avalanche photodiodes (APDs) (Judenhofer et al., 2008) or silicate photomultipliers (SiPMs) (Yoon et al., 2012) have emerged more recently and are employed, among others, in simultaneous PET/MRI (Phelps, 2004; Pichler et al., 2008) and PET/CT scanners (van Sluis et al., 2019). An illustration of a PET scanner is presented in Figure 8.

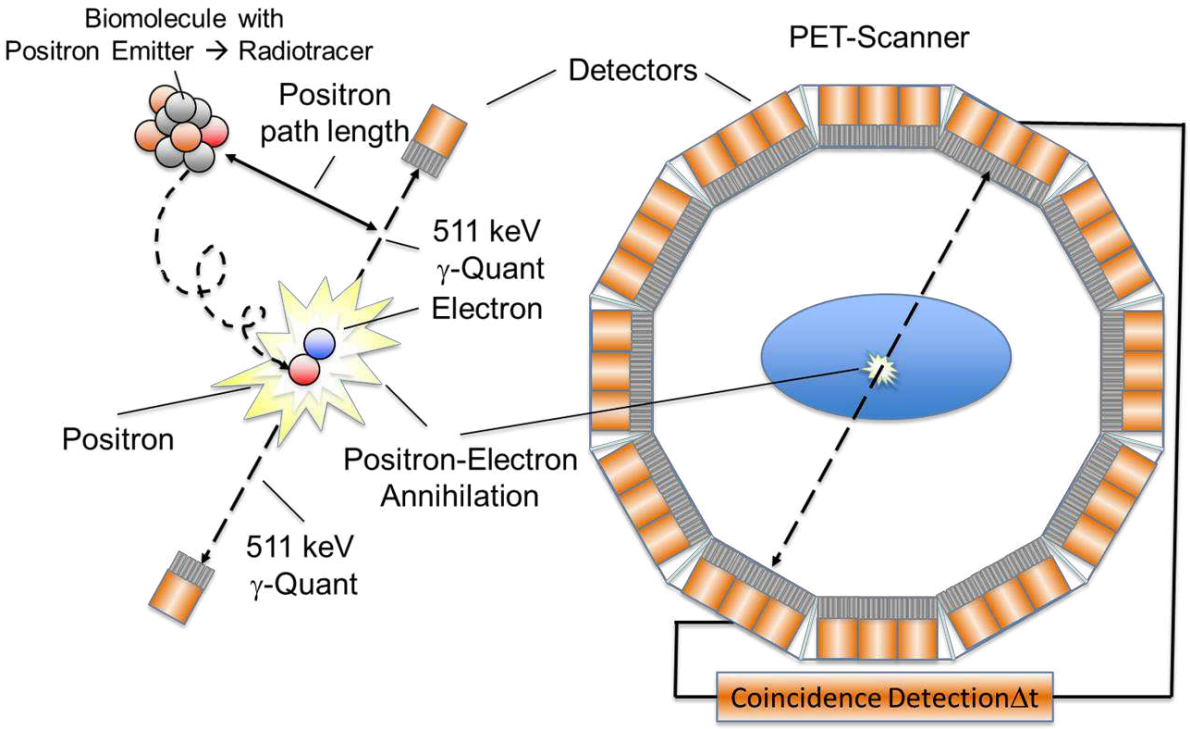

Figure 8: Principle of positron emission tomography (PET). After injection, the PET tracer accumulates in target areas rich in proteins it has high affinity to or tissue it can get trapped in. The PET tracer emits positrons, which, through annihilation with nearby electrons, produce two gamma rays travelling in different directions. These gamma rays can be detected along a line-of-response (LOR) by the PET detectors. Adapted from (Amend, 2019; Wehrl, 2013).

PET Image Generation

For an annihilation event to be recorded, the generated photons must reach a pair of detectors within a certain time-window of each other in the range of nanoseconds, or even picoseconds for scanners with time-of-flight (TOF) capabilities (Phelps, 2004). A recorded event is called a coincidence. Importantly however, PET cannot determine the exact location where a coincidence occurs, but merely a so-called line of response (LOR), the imaginary line between the two detectors having recorded the coincidence. Newer generation scanners with improved temporal resolution are able to derive the TOF of the photons. Using TOF, a PET scanner can limit the range where the annihilation took place to just a segment of the LOR, thereby improving spatial resolution (Pichler et al., 2008).

The LORs of all recorded annihilations during a PET scan are stored in list-mode files. List-mode files include the energies of the detected coincidences, the distance of each LOR in relation to the center of the FOV, the angle of the LOR and the time of the event. From the list-mode information a sinogram can be generated containing data on the coincidences generated along each LOR. Using different algorithms, the sinogram can then be reconstructed to an image. A PET image is composed of voxels, each voxel representing a volume in space. A value is assigned to each voxel, indicating the amount of radioactivity recorded in the respective volume over the duration the image was acquired. Two types of reconstruction algorithms exist. First, analytical reconstruction methods, such as the filtered back-projection, are fast, but have drawbacks in terms of image quality. Second, iterative reconstruction methods, such as the ordered-subsets expectation maximization (OSEM) algorithm, are more time-consuming but yield images of better quality through the implementation of additional factors such as the positron ranges or the sizes of the detectors (Phelps, 2004; Tong et al., 2010).

In addition, a number of correction methods are standardly applied to optimize the images generated from the reconstruction algorithm. The corrections include attenuation, scatter, random, or dead-time correction and account for interactions between the γ-quants and the matter they are traveling through or for technological limitations of the scanners. For instance, dead-time correction takes into account the period of time required for the detector to be able to detect a new coincidence after having recorded one before (Phelps, 2004).

PET Quantification

For most PET studies, the experimental design, including the type of tracer, the type of reconstruction and the quantification of the acquired images, depends on the investigated physiological process. A large array of tracers exists to image various aspects of brain function. For imaging neuronal activity, PET tracers can be grouped into two types. The first group of tracers investigates synaptic properties, such as the distribution of certain types of receptors or transporters. The second type of tracers can be used to indirectly derive neuronal activity from adjacent processes such as glucose metabolism or blood perfusion.

Temporally, PET scans can be acquired in two different ways. If the temporal component of the process observed is not of interest, typically one image is generated and the acquisition is called a static scan. A static scan reveals the summed distribution (e.g. in the form of a mean value) of the injected radiolabeled molecules over the period of the acquisition. The second option is a so-called dynamic acquisition, for which the data are separated in different time

periods. The lengths of the time periods, also called frames, are determined *a priori* to the reconstruction depending on the aim of the study. While a better time-resolution is achieved by choosing shorter frames, the trade-off is that also fewer counts, and therefore less signal, are acquired (Herfert et al., 2020). The average uptake in an ROI can be extracted from each time-frame of a dynamic PET scan, generating a time-activity curve (TAC) (Herfert et al., 2020).

To quantify the target distribution of a bolus-injected PET tracer, a dynamic acquisition is required. This is due to the fact that the signal extracted does not only originate from specific ligand-target interactions, but also from other compartments. Compartments define the possible states of a tracer in tissue and plasma during a scan. The number of compartments depends on the type of tracer. Since tracers are usually injected intravenously, one compartment defined for all types of tracers is the blood plasma. If the injected tracer is delivered from the blood to tissues, one or several tissue compartments can be distinguished. First, the tracer can be found freely available in the tissue. Second, it can bind unspecifically to the tissue. Finally, it can bind specifically to its target. Additionally, the manner in which a tracer transitions between compartments can be quantified by so-called kinetic rate constants. The rate constant describing the transport of tracer from the plasma to the tissue is called K_1. The transport back from the tissue to the plasma is defined by the constant k_2. Constants describing further interactions between the tracer and the tissue are defined by the constants k_3 to k_6. Depending on their ability to detach after binding to the target, tracers are further defined as reversible or irreversible. In the case of irreversible binding, the tracer cannot detach from the target after binding or gets trapped within the tissue, in which case the k_4 constant, used to quantify this process, is assumed to equal zero. Within this work, both an irreversible tracer, [^{18}F]FDG, which gets trapped within the cell after phosphorylation, as well as two reversible tracers, [^{11}C]DASB and [^{11}C]raclopride, were employed. To summarize, full quantification of a PET scan involves not only determining the distributions of the ligand in the image volume but defining the kinetics between the different compartments using kinetic modeling approaches (Gunn et al., 2002).

Two types of approaches are available to model the kinetics of tracers after a bolus injection. First, plasma input-derived models are considered the gold standard, since radioactivity in the plasma compartment is directly measured. The dynamic assessment of plasma radioactivity can be performed invasively, by drawing arterial blood at short intervals and measuring the radioactivity in a gamma counter. Alternatively, the PET images themselves can be used to

extract an image-derived input function if the heart or the carotid artery in the field of view. To this extent, a VOI is placed in the carotid artery or the left heart ventricle and the plasma radioactivity is assessed over time. In small animals, both approaches are challenging. While the former is highly invasive, the latter is complicated by the difficulty to parcelate small structures such as an artery (Herfert et al., 2020).

Therefore, the second approach for PET quantification, the reference tissue model, is a viable alternative. Reference tissue models are based on the assumption that a reference region exists, void of specific targets for the injected tracer. Thus, the signal extracted from the reference region is assumed to be unspecific. Additionally, the ratio of the rate constants K1 and k2 (K1/k2), defining the transfer from plasma to tissue and back, is assumed to be equal for both the reference region and the region of interest. Several models and graphical approaches have been developed to quantify tracer binding to a target region using a reference tissue, including the Logan graphical approach or the simplified reference tissue model (SRTM) (Gunn et al., 2002; Lammertsma and Hume, 1996; Logan et al., 1990). These models are able to quantify the specific binding of the applied tracer for each voxel or ROI as non-displaceable binding potentials (BP_{ND}) (Innis et al., 2007).

Another approach that does not require kinetic modeling is to reach true tracer equilibrium between a target and reference region. This can be achieved by a constant infusion of the PET tracer, which may also be preceded by a bolus (Carson et al., 1993; Rischka et al., 2018; Villien et al., 2014). The constant infusion of the tracer ensures constant concentrations in plasma and tissue, a state called equilibrium or steady-state. Under steady-state conditions, the specific binding in a region can be estimated as a ratio between the uptake in the respective region and the reference region (Innis et al., 2007):

$BP_{ND} = \frac{C_T - C_R}{C_R} = \frac{C_T}{C_R} - 1$, where

- BP_{ND} is the binding potential
- C_T is the concentration of the tracer in the tissue of interest
- C_R is the concentration of the tracer in the reference region

$\frac{C_T}{C_R}$ is also referred to as distribution volume ratio (DVR), hence the above equation can be written as

$BP_{ND} = DVR - 1$

The BP_{ND} can be calculated using the above equation as soon as the steady-state condition is met. A hybrid between bolus and infusion protocols exists in the form of a smaller bolus followed by a constant infusion. The advantage of a bolus-plus-constant-infusion protocol is that tracer concentrations reach equilibrium earlier compared to infusion protocols (Rischka et al., 2018). For instance, a BP_{ND} value of 0 indicates no specific binding, since the uptake is of equal magnitude to the reference region which is void of the target, while a BP_{ND} value of 1 indicates the total uptake in the region investigated is twice as high compared to the unspecific uptake in reference region. BP_{ND} values can be calculated for each frame and plotted over time similarly to a TAC. Under baseline conditions, after reaching a tracer-dependent equilibrium, the BP_{ND} curves are constant. From this point on, dynamic changes, induced for instance by a pharmacological challenge, can be observed in the bindings. For example, if a pharmacological agent competing for the same target as the PET tracer is injected during the scan after equilibrium is reached, the binding is expected to decrease, since competition would lead to a decreased availability of the target. A similar effect would be expected if the pharmacological agent does not compete itself for the same target, but its action would lead to increased concentrations of endogenous molecules acting as competitors.

The Resurgence of [^{18}F]FDG PET for the Research of Neuronal Activity

Tracer uptake or cerebral metabolic rate of glucose (CMRGlu) distributions computed using from [^{18}F]FDG PET scans can provide important insights into brain function. On single-subject level, [^{18}F]FDG scans are for example standardly used in epilepsy, where areas of decreased metabolism compared to the contralateral hemisphere, so-called hypometabolisms, can reveal the extent of an epileptogenic focus (Tang et al., 2019). In group level research, it has been shown to robustly delineate disease-induced alterations (Perani, 2013; Schroeter et al., 2009).

Since glucose is consumed across the brain, no reference region is available for [^{18}F]FDG. Therefore, an input function is required for full quantification. An alternative approach to assess relative changes in [^{18}F]FDG scans is by performing a whole brain normalization. To this extent, the dynamic or static uptake in each ROI or voxel is normalized by dividing its value through the whole-brain average uptake. The whole-brain average uptake is calculated as a mean of the tracer uptake in all voxels or regions of the brain. Nonetheless, whole-brain normalization also bears several drawbacks and has been shown to be outperformed by normalizing to the cerebellum or by data-driven normalization approaches (López-González et al., 2020). Several analytical approaches have emerged over the last decade to improve the

evaluation of [^{18}F]FDG PET data. Intriguingly, the concept of using imaging data to calculate interregional correlations has been first introduced through [^{18}F]FDG PET, although currently known as a method mostly used in fMRI. In 1984, Horwitz et al. computed interregional correlations in [^{18}F]FDG uptakes, postulating that regions with high correlations may be functionally connected (Horwitz et al., 1984). Importantly, and in contrast to the later-introduced fMRI-derived rsFC, the correlations in [^{18}F]FDG PET were calculated between subjects, rather within-subject and between time-series. The postulated biological background for both approaches is however comparable: if two regions correlate over a subject-series with regard to metabolic demand or over time with regard to hemodynamics, it is assumed that they do so because they are functionally connected.

However, static measurements do not provide information on dynamic processes occurring in the brain. Dynamic [^{18}F]FDG PET scans can reveal spontaneous or induced changes in glucose metabolism over the course of the scan and thereby, indirectly, changes in neuronal activity. Despite at a first glance merely offering a different angle to neuronal activity by calculating metabolism instead of hemodynamics, as is the case for BOLD-fMRI, the two readouts have been shown to overlap only partially. Using a simple task such as whisker stimulation during dynamic simultaneous [^{18}F]FDG PET/fMRI scans, Wehrl et al. have shown that the spatial extents of activation revealed by fMRI and [^{18}F]FDG PET are strikingly different (Wehrl et al., 2013). Intriguingly, hemodynamic changes elicited by whisker stimulation were restricted to the barrel-field cortex and the thalamus, the areas expected to be directly targeted by the stimulation. In addition to strong signal in the barrel-field cortex, PET indicated further areas of activation. These included the amygdala and insula, involved in emotional processing, and the hippocampus, relevant for memory formation. The findings may indicate that even such a simple stimulation is not only processed locally, but involves different regions across the brain, being possibly integrated into higher cognitive processes.

The recent development of constant infusion paradigms for [^{18}F]FDG PET, termed functional PET (fPET), adds the possibility of evaluating dynamic changes in glucose following activation. In 2014, Villien et al. demonstrated the use of [^{18}F]FDG fPET to detect task-induced activations (Villien et al., 2014). While the temporal resolution for the detection of activations is still poorer compared to fMRI, more recent work has shown the potential for improvement through optimized protocols. In 2018, Rischka et al. demonstrated that 2-minute tasks could be detected using [^{18}F]FDG fPET (Rischka et al., 2018). Further developments

could enable [^{18}F]FDG fPET to further close the gap to fMRI in terms of temporal resolution for activation studies. When simultaneously combined with fMRI, using dynamic [^{18}F]FDG fPET data enables the possibility of a more direct and possibly more viable comparison between hemodynamic and metabolic parameters.

1.6.3 Simultaneous PET/MRI Brain Imaging

PET and MRI exhibit strongly complementary attributes. PET has picomolar sensitivity and, through the high variety of available tracers, can offer molecular-level readout on a multitude of targets and physiological processes. MRI has lower sensitivity compared to PET, but profits from higher temporal and spatial resolutions, excellent soft-tissue contrast and can also serve various applications through the array of available MR sequences (Pichler et al., 2008). To this end, MRI is not only able to offer morphological information, but also functional information through sequences such as BOLD-fMRI. Hence, for any type of study, the combination of PET and MRI is of interest due to the ability of MRI to deliver information on the underlying morphology for a physiological process depicted by PET, similarly to PET/CT. However, particularly for brain studies, PET/MRI is able to not only generate simultaneous readout on morphology and one function but, with the addition of fMRI, two different functional processes in the brain.

The first simultaneous PET/MRI body scanner for humans emerged in 2010 (Delso et al., 2011), while human brain MR-compatible PET inserts were introduced in 2008 (Schlemmer et al., 2008). To develop a functioning hybrid between the two different types of scanner several types of challenges had to be overcome (Judenhofer et al., 2008). Using their respective traditional builds, combining PET and MRI would not have been feasible due to the influences the two systems would have on each other (Wehrl et al., 2011). One of the main reasons for this incompatibility is the strong magnetic field generated by the MR scanner and its effect on the traditional PMT detectors. Briefly, the strong magnetic field would deflect the electrons from their pathways between the dynodes of a PMT and thereby prevent the amplification and detection of the PET signal. In addition, the magnetic field would affect the function of other metallic components of PET scanners, which in turn, would cause, via their susceptibility, large distortions in the magnetic field, ultimately compromising the function of both systems (Judenhofer et al., 2008). Such technical issues had to be solved, for instance, by the development of novel detector designs, such as APDs (Judenhofer et al., 2008) or SiPMs (Yoon et al., 2012), as described in previous sections. Today, several

solutions for simultaneous PET/MR imaging are available both for humans and animals (Vandenberghe and Marsden, 2015).

As apparent from previous paragraphs, simultaneous PET/MRI opens tremendous possibilities of generating strongly complementary *in vivo* data on a rapidly-changing and highly complex organ. In combination with BOLD-fMRI, an indirect and convoluted method of inferring neuronal activity (Buxton, 2012), molecular data provided by PET can be used for validation and cross-correlation (Sander et al., 2013). For studies on neuronal activation, the PET readout can validate hemodynamic changes yielded by BOLD by providing data on other processes potentially indicating neuronal activity more directly (Villien et al., 2014; Wehrl et al., 2013). For instance, measuring glucose consumption using [^{18}F]FDG PET, arguably a more direct method to detect neuronal activity, has been shown to deliver spatially strongly complementary input to BOLD-fMRI (Wehrl et al., 2013). In terms of rsFC, while the research of RSNs has taken flight over the last decades, little is known on their molecular substrate (Roffman et al., 2016). Including simultaneously acquired information using PET can contribute to closing this particular gap and understanding how certain molecular properties impact macroscopic brain organization (Roffman et al., 2016).

1.6.4 Small Animal Imaging: Challenges and Opportunities

Although bearing several advantages, a number of challenging aspects must be considered for small animal imaging compared to human studies. The first relevant factor for PET/fMRI studies in small animals is that in contrast to humans, they are usually performed under anesthesia. The impact of anesthesia is of manifold relevance, since it can directly impact neuronal activation, along with neurovascular coupling and metabolism, which can alter both PET and BOLD-fMRI readouts (Gao et al., 2017). Different anesthetics are available for animal imaging, each having different mechanism of action and thereby variable, mostly dose-dependent effects (Grandjean et al., 2014; Paasonen et al., 2018). These effects need to be taken into account when interpreting readouts from both modalities. Importantly, when performing scans under anesthesia, a constant monitoring of physiological parameters such as heartbeat, respiration or temperature is essential, since they can indicate the depth and anesthesia, which could impact the acquired data.

A further challenge is represented by the smaller sizes of the brains of small animals compared to humans (Figure 9). This difference results in a poorer relative spatial resolution of the acquired data when taking into account the total volume of the brain. Therefore, small animal experiments are generally acquired at higher field and gradient strengths and using

smaller scanner bores (Jakob, 2011; Mandino et al., 2020). The PET detectors employed are normally also composed of smaller crystal blocks, enabling an improved spatial resolution (Kiessling and Pichler, 2011). Nonetheless, especially for PET, spatial resolution of current small-animal scanners is still limited to approximately 1.5 mm in the center of the FOV (Cherry and Gambhir, 2001; Wehrl et al., 2013; Wehrl et al., 2011). Depending on the size of the imaged brain, potential partial volume effects must therefore be taken into consideration when defining ROIs and extracting signal from neighboring sources.

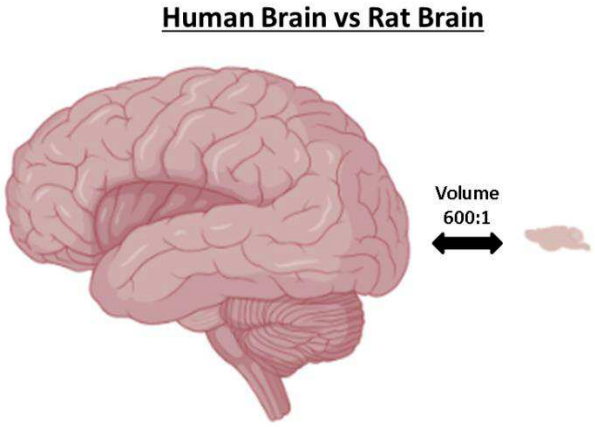

Figure 9: Comparison between human and rat brain volumes. The human brain is approximately 600 times larger than the rat brain. Adapted from (Herfert et al., 2020)**.**

Having mentioned several of its challenges, it must be stated that small-animal imaging also opens up tremendous opportunities for research. First, the homogeneity of cohorts in small-animal studies can be optimized to an extent which cannot be achieved for human studies. The subjects themselves are standardly matched regarding age, gender, strain, yet also their housing conditions, including temperature, humidity, day-night cycle, and the nutrition are identical for the entire cohort. Therefore, variability in the readout can be strongly reduced, which can enhance and optimize the detection of a studied effect.

In addition, methods incompatible with human studies can be applied in rats under the approval of animal use and care authorities. For instance, genetic manipulations can be performed to study their effects on brain function (Marciano et al., 2021). Additionally, invasive methods of stimulation or acquisition can be used to generate readouts on specific processes in the brain (Bernal-Casas et al., 2017; Thanos et al., 2013). Finally, cross-correlation can be performed after *in vivo* scans using *ex vivo* analyses, yielding readout on cellular level to complement the acquired imaging data (Thanos et al., 2013).

1.7 Research of Psychedelic Compounds

Recent years have brought a strong resurgence in psychedelic research, mainly due to their promise as treatment for psychiatric diseases (Andersen et al., 2021; Carhart-Harris and Goodwin, 2017). Psychedelic drugs, such as psilocybin, ayahuasca, lysergic acid diethylamine (LSD) and methylenedioxymethamphetamine (MDMA), induce altered states of consciousness by affecting monoaminergic systems and especially serotonergic neurotransmission (Millière et al., 2018). While molecular mechanisms of psychedelic compounds are fairly well understood, the serotonin 2A ($5HT_{2A}$) receptor being known for instance to be one of their main targets, the way they affect brain function at network level to affect consciousness is still somewhat elusive (Millière et al., 2018). To better understand psychedelic mechanisms, several imaging studies have been conducted in recent years (Andersen et al., 2021). To a large extent, the methodology employed to image the effects of these compounds relied on hemodynamics measured by MRI through either BOLD, arterial spin labelling (ASL) or both. While advantageous due to their high temporal resolution, enabling the imaging of acute pharmacological challenges, their reliance on hemodynamics to infer neuronal activity may be problematic. This aspect is even more important for compounds with direct vascular effects. Generally, studies measuring neuronal activity through neurovascular coupling have indicated inhibitory effects induced by psychedelics, such as psilocybin (Carhart-Harris et al., 2012) or MDMA (Carhart-Harris et al., 2015). The authors in these publications have interpreted the decreased signals as originating from reduced neuronal activity. Evidence on the acute neuronal effects of psychedelics from other *in vivo* imaging modalities mapping neuronal activity more directly than methods based on hemodynamics is sparse. For instance, a PET study from 1997 evaluating the effects of psilocybin on CMRGlu indicated increases in the cortex and the cerebellum (Vollenweider et al., 1997). However, as rightly noted by the authors of the study on psilocybin mentioned above (Carhart-Harris et al., 2012), the readouts are only partially comparable. This is due to two reasons: first, while in the fMRI study (Carhart-Harris et al., 2012), the effects measured can be classified as truly acute, i.e. the changes were measured on the same day and directly after the challenge, the effects in earlier PET studies (Vollenweider et al., 1997) were reported as differences between baseline and challenge scans acquired one or two months apart. Second, the scans were acquired only 90 minutes after the challenge. Therefore, it could be argued that the imaged effects were not entirely acute.

1.8 Aim of the Project

The present thesis is comprised of three different projects aiming to shed light on brain function in terms of both functional connectivity and activation processes by integrating molecular information yielded by PET and the hemodynamic readout provided by BOLD-fMRI.

The first project involved the simultaneous acquisition of rsFC data in healthy rats using hemodynamic and metabolic readouts from [^{18}F]FDG PET/fMRI experiments (Ionescu et al., 2021b). While traditionally acquired using BOLD-fMRI data, rsFC can also be derived from fluctuations in glucose metabolism using [^{18}F]FDG PET. Recent studies have indicated the potential of this readout to outperform BOLD-fMRI in the detection of RSN alterations in pathological cohorts (Ripp et al., 2020). The aim of the study was the detection of common and complementary RSNs using the two modalities in healthy rats, which could serve as biomarkers in future studies.

The second project aimed to decipher the link between D2R and SERT distributions and established RSNs (Ionescu et al., 2021a). Both D2R and SERT are postulated to play essential roles in various pathologies. Similarly, the three RSNs investigated, as well as their interplay, have been shown to impact several psychopathologies (Conio et al., 2019). The direct connection between D2R and SERT distributions, on one side, and rsFC, on the other, is however poorly elucidated. Since many therapeutic approaches directly affect monoaminergic systems with the aim to normalize brain function, elucidating the link between monoamines and RSNs is of importance.

Finally, the third project aimed to decipher the acute effects of MDMA on the brain. To this extent, the data were acquired in two different cohorts reflecting changes in hemodynamics, glucose consumption, and SERT availability, one of the main targets of MDMA. Although the interest in psychedelics has surged tremendously in recent years for their therapeutic potential in psychiatric diseases (Andersen et al., 2021; Carhart-Harris and Goodwin, 2017), in addition to their societal relevance as illegal drugs, their mechanisms are not entirely understood. Using the present study, the potential of simultaneous PET/MRI to delineate effects of psychedelic drugs both spatially and temporally was evaluated. Therefore, as mentioned above, the generated readout and corresponding conclusions are of tremendous interest for future research of psychedelics in both therapy and abuse.

2. Results

The thesis consists of three original publications for the three projects mentioned above.

Publication 1: Ionescu TM, Amend M, Hafiz R, Biswal BB, Wehrl HF, Herfert K, et al. Elucidating the complementarity of resting-state networks derived from dynamic [^{18}F]FDG and hemodynamic fluctuations using simultaneous small-animal PET/MRI. (NeuroImage, 2021) (Ionescu et al., 2021b)

The first publication indicates common and complementary properties of rsFC acquired from BOLD-fMRI and [^{18}F]FDG uptake fluctuations in healthy rats. The study demonstrates that the two readouts partly overlap, yet at the same time yield several complementary aspects at both whole-brain and network level.

Publication 2: Ionescu TM, Amend M, Hafiz R, Biswal BB, Maurer A, Pichler BJ, et al. Striatal and prefrontal D2R and SERT distributions contrastingly correlate with default-mode connectivity. (NeuroImage, 2021) (Ionescu et al., 2021a)

The second publication deciphers direct correlations between availabilities of D2R and SERT in two essential dopaminergic and serotonergic projection areas, the striatum and medial prefrontal cortex, on one side, and three RSNs, the DMN, SN and SMN, on the other side. The study shows strong negative correlations between striatal D2R availability and all RSNs investigated. Additionally, the data reveal that prefrontal SERT availability correlates in a differentiated fashion with short-path and long-path frontal functional connectivity.

Publication 3: Ionescu TM, Amend M, Watabe T, Hatazawa J, Maurer A, Reischl G, et al. Neurovascular Uncoupling: Multimodal Imaging Delineates the Acute Effects of MDMA. (Journal of Nuclear Medicine, 2022)(Ionescu et al., 2022)

The third publication delineates the spatial and temporal effect of MDMA, indicating the dominance of peripheral vascular effects in the readout produced by BOLD-fMRI. It demonstrates that MDMA induces neuronal activation accompanied by decreased hemodynamics, a phenomenon defined in the publication as neurovascular uncoupling.

The three original publications are included in the present document. The first two publications have been accepted and published in NeuroImage (Ionescu et al., 2021a; Ionescu et al., 2021b), the third publication is currently available ahead of print in the Journal of Nuclear Medicine (Ionescu et al., 2022).

2.1 Elucidating the Complementarity of Resting-State Networks Derived from Dynamic [^{18}F]FDG and Hemodynamic Fluctuations Using Simultaneous Small-Animal PET/MRI

The article included in this chapter was published in (Ionescu et al., 2021b):

NeuroImage, Volume 236, 2021, 118045, ISSN 1053-8119
https://doi.org/10.1016/j.neuroimage.2021.118045.
"Elucidating the complementarity of resting-state networks derived from dynamic [^{18}F]FDG and hemodynamic fluctuations using simultaneous small-animal PET/MRI"
Tudor M. Ionescu, Mario Amend, Rakibul Hafiz, Bharat B. Biswal, Hans F. Wehrl, Kristina Herfert, Bernd J. Pichler

NeuroImage 236 (2021) 118045

Contents lists available at ScienceDirect

NeuroImage

journal homepage: www.elsevier.com/locate/neuroimage

Elucidating the complementarity of resting-state networks derived from dynamic [^{18}F]FDG and hemodynamic fluctuations using simultaneous small-animal PET/MRI

Tudor M. Ionescu[a], Mario Amend[a], Rakibul Hafiz[b], Bharat B. Biswal[b], Hans F. Wehrl[a], Kristina Herfert[a], Bernd J. Pichler[a,*]

[a] Werner Siemens Imaging Center, Department of Preclinical Imaging and Radiopharmacy, Eberhard Karls University Tuebingen, Tuebingen, Germany
[b] Department of Biomedical Engineering, New Jersey Institute of Technology, University Heights, Newark, NJ, United States

ARTICLE INFO

Keywords:
Resting-state networks
Functional connectivity
Dynamic [^{18}F]FDG correlations
Connectomics
simultaneous PET/MRI

ABSTRACT

Functional connectivity (FC) and resting-state network (RSN) analyses using functional magnetic resonance imaging (fMRI) have evolved into a growing field of research and have provided useful biomarkers for the assessment of brain function in neurological disorders. However, the underlying mechanisms of the blood oxygen level-dependant (BOLD) signal are not fully resolved due to its inherent complexity. In contrast, [^{18}F]fluorodeoxyglucose positron emission tomography ([^{18}F]FDG-PET) has been shown to provide a more direct measure of local synaptic activity and may have additional value for the readout and interpretation of brain connectivity. We performed an RSN analysis from simultaneously acquired PET/fMRI data on a single-subject level to directly compare fMRI and [^{18}F]FDG-PET-derived networks during the resting state. Simultaneous [^{18}F]FDG-PET/fMRI scans were performed in 30 rats. Pairwise correlation analysis, as well as independent component analysis (ICA), were used to compare the readouts of both methods. We identified three RSNs with a high degree of similarity between PET and fMRI-derived readouts: the default-mode-like network (DMN), the basal ganglia network and the cerebellar-midbrain network. Overall, [^{18}F]FDG connectivity indicated increased integration between different, often distant, brain areas compared to the results indicated by the more segregated fMRI-derived FC. Additionally, several networks exclusive to either modality were observed using ICA. These networks included mainly bilateral cortical networks of a limited spatial extent for fMRI and more spatially widespread networks for [^{18}F]FDG-PET, often involving several subcortical areas.

This is the first study using simultaneous PET/fMRI to report RSNs subject-wise from dynamic [^{18}F]FDG tracer delivery and BOLD fluctuations with both independent component analysis (ICA) and pairwise correlation analysis in small animals. Our findings support previous studies, which show a close link between local synaptic glucose consumption and BOLD-fMRI-derived FC. However, several brain regions were exclusively attributed to either [^{18}F]FDG or BOLD-derived networks underlining the complementarity of this hybrid imaging approach, which may contribute to the understanding of brain functional organization and could be of interest for future clinical applications.

1. Introduction

Although the understanding of brain function has taken major leaps over the past several decades due to the development of novel imaging and computational modelling techniques, functional brain organization and its dysfunctions continue to be incompletely understood. Functional connectivity (FC) describes synchronous oscillations of brain activity in different parts of the brain and can be used to study its functional organization. Ogawa et al. introduced functional magnetic resonance imaging (fMRI), making use of the blood oxygenation level dependant (BOLD) signal to derive neural activity (Ogawa et al., 1990). This technique opened the possibility of acquiring FC using MRI (Biswal et al., 1995). FMRI-derived FC studies focus on characterizing functional resting-state networks (RSN) through temporal correlations of the BOLD signal between different brain regions (Fox et al., 2005; Greicius et al., 2003).

The default-mode network (DMN) is the most widely reported resting-state network (Raichle et al., 2001). The DMN is composed of a number of medial and lateral cortical regions characterized by decreased connectivity during tasks compared to the resting state. Hence, the DMN appears to be related to a certain default state of the brain during rest. The DMN is believed to play an essential role in brain organization, recollection, self-awareness and imagination (Raichle et al.,

* Corresponding author.
E-mail address: bernd.pichler@med.uni-tuebingen.de (B.J. Pichler).

https://doi.org/10.1016/j.neuroimage.2021.118045.
Received 19 January 2021; Received in revised form 15 March 2021; Accepted 4 April 2021
Available online 10 April 2021.

2001). The function of the DMN has been shown to be disrupted in several clinical populations, including Alzheimer's disease and schizophrenia (Badhwar et al., 2017; Bluhm et al., 2007; Greicius et al., 2004; Mwansisya et al., 2017). In addition to the DMN, several other RSNs have been reported to involve other cortical areas (Damoiseaux et al., 2006). Additionally, RSNs have been identified in other brain regions, including the cerebellum and brainstem and subcortical areas such as the basal ganglia (Joel and Weiner, 1994). These networks encompass a variety of different structures and are therefore thought to be involved in a number of integrative processes, including perception, memory, attention, seizure suppression, executive control and emotion (Becerra et al., 2011; Cole et al., 2010). Due to their manifold roles, such networks are of interest for various clinical and research applications, such as diagnostics or drug development.

Although networks such as the DMN were initially assumed to be exclusive to the human brain, analogues of human RSNs have been observed in other species, including rats (Hutchison et al., 2010; Lu et al., 2012; Majeed et al., 2011; Zhang et al., 2010). The interpretation of the significance of the RSN continues to be a topic of scientific interest. However, it is widely established that numerous such networks are not only reproducible across species, individuals and ages but can also play a role as biomarkers, as they are disrupted in neurological disorders or by certain drugs (Barkhof et al., 2014). The field of research investigating disruptions of whole-brain or network-level FC has profited from the emergence of connectomics, which focus on defining the properties of the brain as a network (Bullmore and Sporns, 2009; Sporns et al., 2005). The framework of connectomics includes measures defining the functional organization of the brain to enable the analysis and detection of alterations to brain functionality (Sporns, 2010).

Although better established through BOLD-fMRI studies, the concept of functional connectivity between different brain regions first emerged using [^{18}F]fluorodeoxyglucose positron emission tomography ([^{18}]FDG-PET). Horwitz et al. showed relationships between the metabolism of different brain regions by computing correlations between regional subject series derived from static [^{18}F]FDG-PET scans (Horwitz et al., 1984). Compared to the BOLD signal, which is driven by a still incompletely understood convolution of cerebral blood flow (CBF), cerebral blood volume (CBV) and cerebral metabolic rate of oxygen ($CMRO_2$) (Buxton, 2012), [^{18}F]FDG-PET may represent a more direct reflection of neural activity (Hahn et al., 2016; Lanzenberger et al., 2012). By operating on a different neurophysiological level, [^{18}F]FDG correlations could potentially provide complementary information to BOLD-derived FC and thereby further help decipher the substrate of brain connectivity.

More recent studies focusing on [^{18}F]FDG correlations have derived networks similar to those revealed by BOLD-fMRI (Di and Biswal, 2012). Upon further investigation by other groups, these networks acquired using [^{18}F]FDG-PET have been shown to exhibit comparable organizational properties to BOLD-derived RSNs (Sanabria-Diaz et al., 2013; Seo et al., 2013b). Importantly, Savio and colleagues described several similar networks from simultaneously acquired FC and [^{18}F]FDG-PET-derived connectivity in humans, suggesting the presence of a common substrate between both outputs (Savio et al., 2017). Recently, the same group has applied a similar methodology to investigate the effects of Alzheimer's Disease on both metabolic and hemodynamic RSNs (Ripp et al., 2020). The authors showed that connectivity acquired using [^{18}F]FDG-PET not only depicted partly complementary aspects of RSNs, but also exhibited increased specificity for Alzheimer's Disease compared to FC derived from simultaneously acquired BOLD-fMRI, thereby emphasizing the value of [^{18}F]FDG correlation analysis for diagnostics of neurodegenerative diseases.

All the studies mentioned above derived [^{18}F]FDG correlations at inter-subject level from static PET scans. To enable subject-level computation of connectivity from [^{18}F]FDG scans, dynamic PET acquisitions are employed to compute correlations between dynamic regional [^{18}F]FDG tracer delivery fluctuations. Studies computing correlations between regional [^{18}F]FDG dynamic PET time-courses are however few and the majority did not acquire PET simultaneously to BOLD-fMRI (Passow et al., 2015a; Tomasi et al., 2017). To the best of our knowledge, only two studies have reported the simultaneous acquisition of dynamic PET scans and fMRI to investigate correlations of dynamic [^{18}F]FDG tracer delivery and BOLD fluctuations (Amend et al., 2019; Wehrl et al., 2013). These studies indicated a significant amount of complementary data by the two methods for both rest and task conditions.

The aim of the present study was to compare the resting-state outputs of dynamic [^{18}F]FDG-PET and BOLD-fMRI by analysing different RSNs derived from [^{18}F]FDG correlations and FC at the single-subject level using both pairwise correlation analysis and independent component analysis (ICA). This study builds on our prior work focused on analysing and comparing the effects indicated by BOLD-fMRI and [^{18}F]FDG-PET following brain stimulation (Wehrl et al., 2013) and on defining the dynamics of tracer delivery driving [^{18}F]FDG correlations (Amend et al., 2019) by elucidating the complementarity of the [^{18}F]FDG correlations and FC readouts on a physiological level. We hypothesized that the common substrate of both outputs will enable the observation of similar organizational properties; however, we also expect a complementary input to be provided by [^{18}F]FDG correlations. To the best of our knowledge, this is the first study investigating RSNs of both FC and subject-wise [^{18}F]FDG correlations using simultaneous PET/MRI and employing both independent component analysis (ICA) and pairwise correlation analysis in small animals.

2. Materials and methods

2.1. Animals

Healthy male Lewis rats (n = 30) were ordered from Charles Rivers Laboratories (Sulzfeld, Germany). The animals used in the experiments had bodyweights of 292.2 ± 22.1 g, corresponding to an age of approximately 11 weeks. Rats were kept on a 12 h day-night cycle at a room temperature of 22 °C and 40–60% humidity. The rats received a standard diet and tap water *ad libitum* before and during the experimental period. All animals were fasted for 6 h prior to the scans. A separate cohort of three rats was used for determining physiological parameters over the course of the scans using pulse oximetry (please refer to *Supplementary Information* for details). All experiments were performed in accordance with the German federal regulations regarding the use and care of experimental animals and under approval by the local research administration.

Fifteen of the datasets were used in our previous study on the methodology of acquiring [^{18}F]FDG and BOLD-fMRI resting-state functional connectivity using simultaneous acquisitions in rats (Amend et al., 2019).

2.2. Simultaneous PET/MRI experiments

The rats were placed into a knock-out box and 3% isoflurane in regular air was delivered to induce anaesthesia. The isoflurane concentration was then reduced to 2% for all subsequent preparation steps. First, the baseline capillary blood glucose levels were measured by puncturing the tail vein and the weights of the animals were examined. Subsequently, an intravenous catheter was placed into a tail vein using a 30 G needle for [^{18}F]FDG administration. Finally, the animals were positioned onto a dedicated small-animal bed and introduced inside a PET/MRI scanner. The temperature was monitored and maintained at 36.5 °C using a rectal temperature probe and a feedback-controlled system, and the respiration rate was observed during the experiments. For the resting-state measurements, the isoflurane concentration was reduced to 1.3% in regular air over the course of the scan. At the end of each scan, the capillary blood glucose concentrations were re-evaluated. For additional data on the physiology of the animals under these experimental conditions, including heart rate, breathing rate and blood oxygenation, please refer to *Supplementary Information.*

Simultaneous PET/MRI measurements were performed over the course of 60 min. Magnetic resonance imaging was performed using a small-animal 7 T ClinScan system (Bruker BioSpin MRI, Ettlingen, Germany). A linearly polarized RF coil (Bruker) with a diameter of 72 cm was employed for transmission and a four-channel rat brain coil (Bruker) was used for reception. First, localizer scans were acquired to adjust the position of the rat brains to the centre of the PET/MRI field of view (FoV). Before performing further sequences, local field maps were acquired to optimize the local magnetic field homogeneity. Subsequently, T2 sequences were acquired as anatomical references (TR: 1800 ms, TE: 67.11 ms, 0.25 mm^3 isotropic resolution, FoV: 40 × 32 × 32 mm, image size: 160 × 128 × 128 px, Rare factor: 28, averages: 1). Functional MRI scans were performed using a T2*-weighted gradient echo EPI sequence (TE: 18 ms, TR: 2500 ms, 0.27 mm isotropic resolution, FoV 25 × 23 mm, image size: 92 × 85 × 20 px, slice thickness: 0.8 mm, 20 slices, 0.2 mm separation between slices). The fMRI scans were performed over the same 60 min time interval as the PET scans described below.

[^{18}F]FDG-PET acquisitions were performed using a small-animal PET insert developed in cooperation with Bruker, a second generation with similar performance parameters as our in-house developed PET insert (Wehrl et al., 2013). Additionally, 31.6 ± 0.9 MBq of [^{18}F]FDG diluted in NaCl was administered over a period of 30 s as a bolus shortly after the start of the PET/MRI acquisition. PET data were stored as list-mode files and reconstructed in 60 1-minute frames employing an in-house written ordered-subsets expectation maximization 2 (OSEM-2D) algorithm including random, decay, time-delay corrections and normalization. For a detailed description of [^{18}F]FDG production, see the *Supplementary Information*.

The original raw dataset will be made available on Mendeley.

2.3. Data processing and analysis

Both the PET scans and the anatomical and functional MRI data were first realigned using Statistical Parametric Mapping 12 (SPM 12, Wellcome Trust Centre for Neuroimaging, University College London, London, United Kingdom) and checked for motion. The motion parameters were stored for fMRI denoising. Mean images of each data set were created and used to generate binary brain masks for the fMRI and PET scans using Analysis of Functional NeuroImages (AFNI, National Institute of Mental Health (NIMH), Bethesda, Maryland, USA). Additionally, brain masks were generated for the T2-weighted anatomical MRI scans. The respective masks were used to remove outer-cerebral tissues from all the PET, fMRI and T2-weighted anatomical MRI datasets. The remaining pre-processing steps were performed using SPM 12. First, all the realigned and skull-stripped fMRI and PET datasets were co-registered to their respective anatomical reference scans. Subsequently, using the anatomical images as a reference, all the datasets were normalized to the Schiffer rat brain atlas (Schiffer et al., 2006). Motion regression was applied to the normalized datasets using an in-house written script by regressing out the motion parameters acquired during the realignment step at the beginning of the pre-processing pipeline. Additionally, fMRI signal drifts were removed voxel-wise using linear and quadratic fits. Following motion regression, both the fMRI and PET datasets were smoothed using a 1.5 × 1.5 × 1.5 mm^3 full-width-half-maximum (FWHM) Gaussian kernel as described previously (Wehrl et al., 2013), which is equivalent to the physical spatial resolution of the PET system used.

Fifty-two regions of the Schiffer rat brain atlas were selected for region of interest (ROI)-based analysis (Schiffer et al., 2006) (for a list of regions of the Schiffer rat brain atlas, see the *Supplementary Methods*). The fMRI and [^{18}F]FDG-PET time courses from these ROIs were extracted using the SPM toolbox Marseille Boîte À Région d'Intérêt (MarsBaR) (Matthew Brett, June 2–6, 2002). Prior to analysis, the extracted time courses underwent whole-brain normalization to account for global effects. Therefore, the values of each ROI at every time-point were divided by the whole-brain mean of the signal at the respective time-points. For each dataset, Pearson's r correlation coefficients were computed between the normalized time courses of each pair of regions, resulting in correlation matrices of 52 × 52 entries for each dataset. Since the 52 self-correlations were set to zero, 2652 correlation coefficients were computed for each individual scan. Due to the findings in our previous study (Amend et al., 2019) on the inability to ensure temporal stability of the [^{18}F]FDG correlation readout when applying a bolus protocol and the lack of a gold standard to determine the most suited period for the analysis, correlations were performed over the course of the entire scan to avoid potential bias by choosing a specific period.

For group-level analysis, Pearson's r values were transformed into Fischer's z-scores, and mean correlation matrices were generated for both fMRI and PET datasets (for a detailed description, please refer to the *Supplementary Methods*). Additionally, a second-level analysis was performed to test every edge for significance (one-sample *t*-test, $p \leq 0.05$, corrected for multiple comparisons). All multiple comparison corrections presented in the manuscript were performed using Bonferroni-Holm.

To investigate the whole-brain organization of FC and [^{18}F]FDG connectivity, three network measures were applied to the PET and fMRI-derived correlation matrices of each subject using the Brain Connectivity Toolbox (Rubinov and Sporns, 2010). First, for each individual correlation matrix, 500 randomized matrices with the same average degree were generated by rewiring each of the edges of the respective matrix. Ideal modularity (Reichardt and Bornholdt, 2006) and clustering coefficients (Onnela et al., 2005) were then computed for both the individual correlation matrices and all randomized matrices. To derive values representative of a null distribution the network metrics of the random matrices were averaged over the 500 iterations. Finally, small-world coefficients were derived for each matrix using the averaged randomized network metrics (for detailed descriptions of these methods, see the *Supplementary Methods*). As described previously, networks were defined as exhibiting small-world properties when the small-world coefficients were higher than 1 (Humphries and Gurney, 2008). To define the nodes and edges of the generated correlation matrices for further network analysis, a threshold was applied to achieve a sparsity value of 20%. Di et al. investigated metabolic connectivity matrices using thresholds between 4% and 18% sparsity (Di et al., 2017). For this application, a slightly more liberal threshold was chosen to avoid missing relevant edges since the data were acquired from anaesthetized animals, as opposed to humans in the mentioned study. Elsewhere, thresholds up to 40% sparsity have been reported for metabolic connectivity studies (Seo et al., 2013a).

To assess the similarity between group-averaged [^{18}F]FDG correlations and FC readouts on whole-brain and RSN levels the correlation coefficients between the respective outputs were computed (Di et al., 2017). Therefore the Pearson's correlation coefficient between the two sets of connectivity values was employed. The same calculations were also repeated for [^{18}F]FDG correlations and FC readouts of each subject at whole-brain level, as well as and for the DMN, basal ganglia network and cerebellar-midbrain network. To report group-level mean correlation values between the [^{18}F]FDG connectivity and FC of single subjects, the correlation coefficients were transformed to Fischer's z-scores before averaging over all subjects.

Independent component analysis (ICA) was performed using Group ICA of the fMRI Toolbox (GIFT, MIALAB, University of New Mexico, Albuquerque, NM, USA). As described previously for small-animal datasets, 20 components were chosen for the ICA algorithm (Wehrl et al., 2013). The maps of the generated components were thresholded ($z \geq 1.96$, corresponding to $p \leq 0.05$) (Di et al., 2012). Voxel-wise Dice-Sörensen coefficients (DSCs) were computed between the components generated from the fMRI and PET datasets. Furthermore, DSCs were computed between each component and the 52 regions under consideration from the Schiffer brain atlas to determine the voxel-wise percentage contribution of each region to the respective components. By combining these measures with a visual inspection, similar components

of the fMRI and PET datasets, as well as components exclusive to either one of the two datasets, were determined and quantified.

For the defined networks common to both BOLD-fMRI and [^{18}F]FDG-PET, specific sets of nodes were isolated based on previous rat FC studies describing the regions contributing to each of these RSNs (Becerra et al., 2011). Using these nodes, unthresholded and thresholded (20%) mean correlation matrices were generated. The similarity of these RSNs for [^{18}F]FDG and BOLD-fMRI using ROI-based methods was visualized through scatter plots and quantified using Pearson's r. Additionally, common edges between FC and [^{18}F]FDG correlations were derived from the thresholded matrices and illustrated using the BrainNet Viewer toolbox (Xia et al., 2013). For information on the regions included in each network, please refer to the *Supplementary Methods*. For the thresholded correlation matrices of each RSN, please refer to the *Supplementary Results*.

3. Results

3.1. Whole-brain connectivity assessment

First, the properties of the whole-brain [^{18}F]FDG correlations and FC were assessed (Fig. 1). The analysis of an exemplary single subject is first depicted (Fig. 1A-F). The [^{18}F]FDG and BOLD-fMRI correlation matrices were compared by computing their similarity using Pearson's r. Additionally, clustering, modularity and small-worldness were quantified to derive the network properties of the investigated matrices. In the second part of the figure (Fig. 1G-L), the same analysis measures on the group level are shown.

The whole-brain correlation matrix of the exemplary single-subject analysis (Fig. 1A) indicates its PET-derived interregional [^{18}F]FDG correlations (upper half above the diagonal) and its fMRI-derived FC (lower half below the diagonal). This matrix was thresholded at 20% (Fig. 1B) to depict the common areas of [^{18}F]FDG correlations and FC. The correlation between [^{18}F]FDG connectivity and FC was also calculated and is shown as a scatter plot (Fig. 1C). For this exemplary subject, the correlation between the [^{18}F]FDG and BOLD-fMRI readouts on the whole-brain level was $r = 0.38$ ($p \leq 0.001$), and thus, it was highly significant ($p \leq 0.001$). In addition, graph theory measures, including modularity (Fig. 1D), clustering (Fig. 1E) and small-worldness (Fig. 1F), were calculated for the exemplary subject, as well as for all other subjects. For this subject, both [^{18}F]FDG correlations (small-world coefficient = 1.73) and FC (small-world coefficient = 1.91) exhibited small-world properties.

The whole-brain connectivity matrix (Fig. 1G) reveals the connectivity patterns of [^{18}F]FDG-PET (above diagonal) and BOLD-fMRI (below diagonal) data on the group-mean level. All correlations were tested on group level for significance using multiple comparison correction ($p \leq 0.05$, Bonferroni-Holm) and significant edges are indicated by asterisks. For an additional comparison between [^{18}F]FDG correlations and FC involving only significant edges, please refer to *Supplementary Figure 9*. Here, a sparsity threshold of 20% was applied across all correlations to further compare the distribution of the strongest edges between [^{18}F]FDG connectivity and FC (Fig. 1H). A number of similarities could be assessed visually from the whole-brain connectivity matrices. First, two large clusters with high densities of connections could be observed for both [^{18}F]FDG connectivity and FC. The first cluster (indicated by green box (1) in Fig. 1I) was mainly composed of cortical regions, such as the auditory (Au), cingulate (Cg), entorhinal (Ent), motor (M1), orbitofrontal (OFC), parietal (PaC), retrosplenial (RS), primary sensory (S1) or visual (V1) cortices. Other regions included in this cluster were anterior subcortical areas, such as the nucleus accumbens (NAc), amygdala (Amyg) or caudate putamen (CPu). The remaining regions in the subcortical and posterior brain areas, including the superior and inferior colliculi (SC and IC, respectively), the midbrain (MB), the cerebellum white and grey matter (CW and CG), the thalamus (Th), the hypothalamus (Hyp), the periaquaeductal grey (PAG) and the septum (Sep), formed a separate cluster (indicated by the blue box (2) in Fig. 1H) with sparse connections to the anterior cluster mentioned above. The anterodorsal and posterior hippocampus (CA1 and CA1-p) exhibited connectivity to both clusters in the FC matrix; however, they were much less connected in the [^{18}F]FDG readout. Observing the two separate clusters in more detail, further smaller clusters of dense and intense correlations could be observed for both outputs, including one composed of posterior cortical regions (RS, PaC, S1 and V1) and another of the cerebellum (CG and CW).

Quantitatively, the observed similarities translated into a Pearson's r coefficient of 0.45 ($p \leq 0.001$, Fig. 1I). The visual observations regarding modularity and clustering were quantified by computing afferent network measures (Fig. 1J – L). The ideal modularity Q differed significantly ($p \leq 0.001$, paired t-tests) from the respective randomized groups of matrices for both [^{18}F]FDG correlations (0.46 ± 0.02 for subject matrices and 0.22 ± 0.02 for randomized matrices) and FC (0.47 ± 0.05 for subject matrices and 0.25 ± 0.02 for randomized matrices). Similarly, clustering was significantly higher ($p \leq 0.001$, paired t-tests) for [^{18}F]FDG connectivity from the respective randomized groups (0.27 ± 0.09 for subject matrices and 0.14 ± 0.05 for randomized matrices), as well as for FC (0.27 ± 0.09 for subject matrices and 0.11 ± 0.04 for randomized matrices). Finally, the small-world properties of the outputs were computed using the small-world coefficient. For [^{18}F]FDG connectivity, a mean value of 1.42 ± 0.39 was found. For FC, the mean small-world coefficient was 1.73 ± 0.34. Both datasets were significantly higher than 1 ($p \leq 0.001$, one-sample *t*-test). On the individual level, one subject exhibited small-world coefficients lower than 1 for both [^{18}F]FDG connectivity and FC, and three other subjects had small-world coefficients lower than 1 for [^{18}F]FDG-PET.

3.2. Network-level connectivity analysis shows similar components for both readouts

Fig. 2 shows the analysis of a DMN-like network obtained for both modalities. The correlation matrices of [^{18}F]FDG connectivity and FC and the respective edges obtained from applying a 20% sparsity threshold are depicted, and Pearson's r correlation between both outputs is revealed. For ICA, the two similar components associated with the DMN are illustrated.

The correlation matrices obtained from pairwise analysis of dynamic [^{18}F]FDG tracer delivery fluctuations and FC of regions associated with the DMN revealed two clusters for both outputs (Fig. 2A). The first cluster included regions belonging to the anterior DMN, centred around the Cg. Other regions in this cluster were the mPFC, OFC and M1. The second cluster comprised posterior cortical regions, with lateral areas such as the PaC, S1 and V1, while the RS featured as a medial cortical region. The depiction of the common edges between both outputs yielded the observation that many edges were situated within the two respective clusters and fewer edges were situated between them. However, this observation was less pronounced for the [^{18}F]FDG-PET readout. A Pearson's r correlation coefficient of 0.55 ($p \leq 0.001$) between [^{18}F]FDG connectivity and FC within the DMN-like network was higher than that at the whole-brain level (Fig. 2B). Two components derived from the ICA of the two datasets were located around the posterior area of the DMN (Fig. 2C). The two cortical regions with the highest contributions to these components were the widely reported DMN hubs: the RS (11% in PET and 21% in fMRI) and Cg (3% in PET and 5% in fMRI). Other cortical regions contributed less than two percent of the signal in either component. However, large implications were observed from more posterior regions, such as the midbrain (32% in PET and 16% in fMRI) and the cerebellum (14% in PET and 57% in fMRI). Furthermore, CA1 (28%) and Th (11%) contributed to the signal in the PET-derived component.

Fig. 3 focuses on the connectivity within the basal ganglia network. The mean connectivity matrices for [^{18}F]FDG and BOLD-fMRI are depicted, along with the edges derived from applying a 20% whole-brain sparsity threshold. To assess similar information for both outputs, the common edges are shown and Pearson's r is calculated for the unthresh-

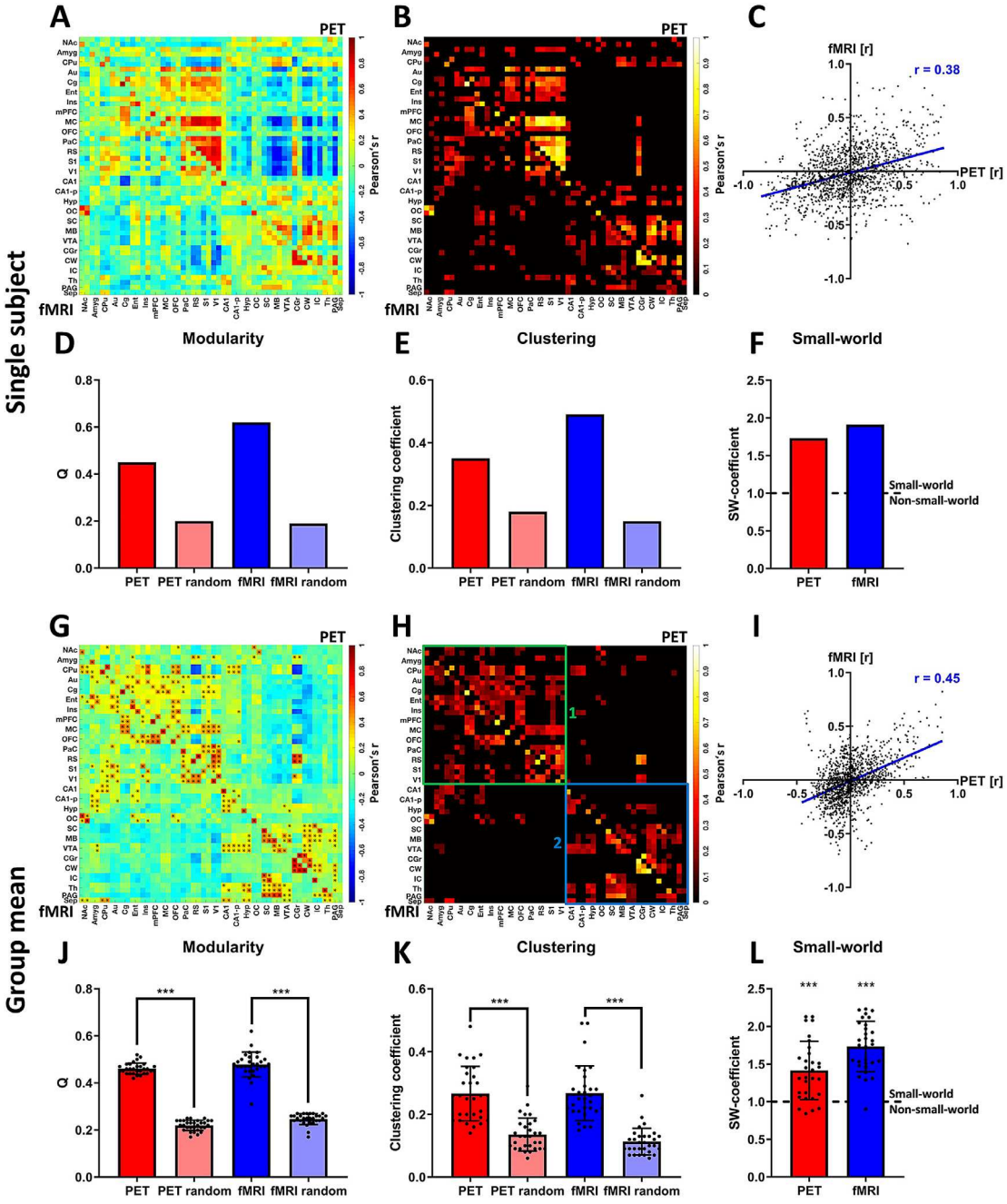

Fig. 1. Assessment of whole-brain [^{18}F]FDG correlations and FC. Panels (A)-(F) depict an exemplary analysis at the single-subject level: (A) PET/fMRI correlation matrix indicating [^{18}F]FDG-PET-derived correlations (upper half of the matrix above the diagonal) and fMRI-derived FC (lower half of the matrix below the diagonal). (B) Thresholded PET/fMRI correlation matrix (20% sparsity) indicating similar areas of [^{18}F]FDG connectivity and BOLD FC. (C) Scatter plot of all [^{18}F]FDG correlations and FC values to assess the correlation of both outputs on the whole-brain level. (D) Ideal modularities of [^{18}F]FDG connectivity and FC compared to the ideal modularity of respective randomized networks with the same average degrees. (E) Clustering coefficients of [^{18}F]FDG correlation matrices and FC compared to the clustering coefficients of respective randomized matrices with the same average degrees. (F) Small-world coefficients of [^{18}F]FDG connectivity and FC. The dotted line indicates the threshold (SW ≥ 1) for which networks are considered to have small-world properties. Panels (G)-(L) depict the analysis at the group-mean level: (G) Mean correlation matrix revealing similar patterns between [^{18}F]FDG correlations (above diagonal) and FC (below diagonal). * indicate significant correlations ($p \leq 0.05$, corrected for multiple comparisons using Bonferroni-Holm). (H) Mean positive correlation matrix thresholded to a sparsity of 20% to define similar clusters between [^{18}F]FDG correlations and FC. (1) Cluster indicating common [^{18}F]FDG connectivity and FC in the cortex and in the anterior subcortical regions. (2) Cluster indicating common subcortical, midbrain and cerebellar [^{18}F]FDG connectivity and FC. (I) Scatter plot of [^{18}F]FDG connectivity and FC along with Pearson's r coefficient to assess the correlation of both outputs. (J) Mean ideal modularity of [^{18}F]FDG correlations and FC of every subject compared to respective randomized networks with the same average degree (paired-t-tests). (K) Mean clustering coefficients of [^{18}F]FDG connectivity and FC of every subject compared to the respective randomized networks with the same average degree (paired-t-tests). (L) Small-world coefficients of [^{18}F]FDG connectivity and FC of every subject showing small-world properties for the majority of subjects for both outputs. Both group means were significantly higher than 1 ($p \leq 0.001$, one-sample t-tests). (*** represents a confidence interval of $p \leq 0.001$; dotted line in (L) indicates threshold for which networks are considered to have a small-world organization (SW-coefficient ≥ 1) or not to exhibit such organization (SW-coefficient < 1), while *** represents a confidence of $p \leq 0.001$ for the respective dataset being significantly higher than 1). FC = fMRI-derived functional connectivity, SW = small-world. For a list of abbreviations of all regions, please refer to *Supplementary Table 1. (For interpretation of the references to colour in this figure legend, the reader is referred to the web version of this article.)*

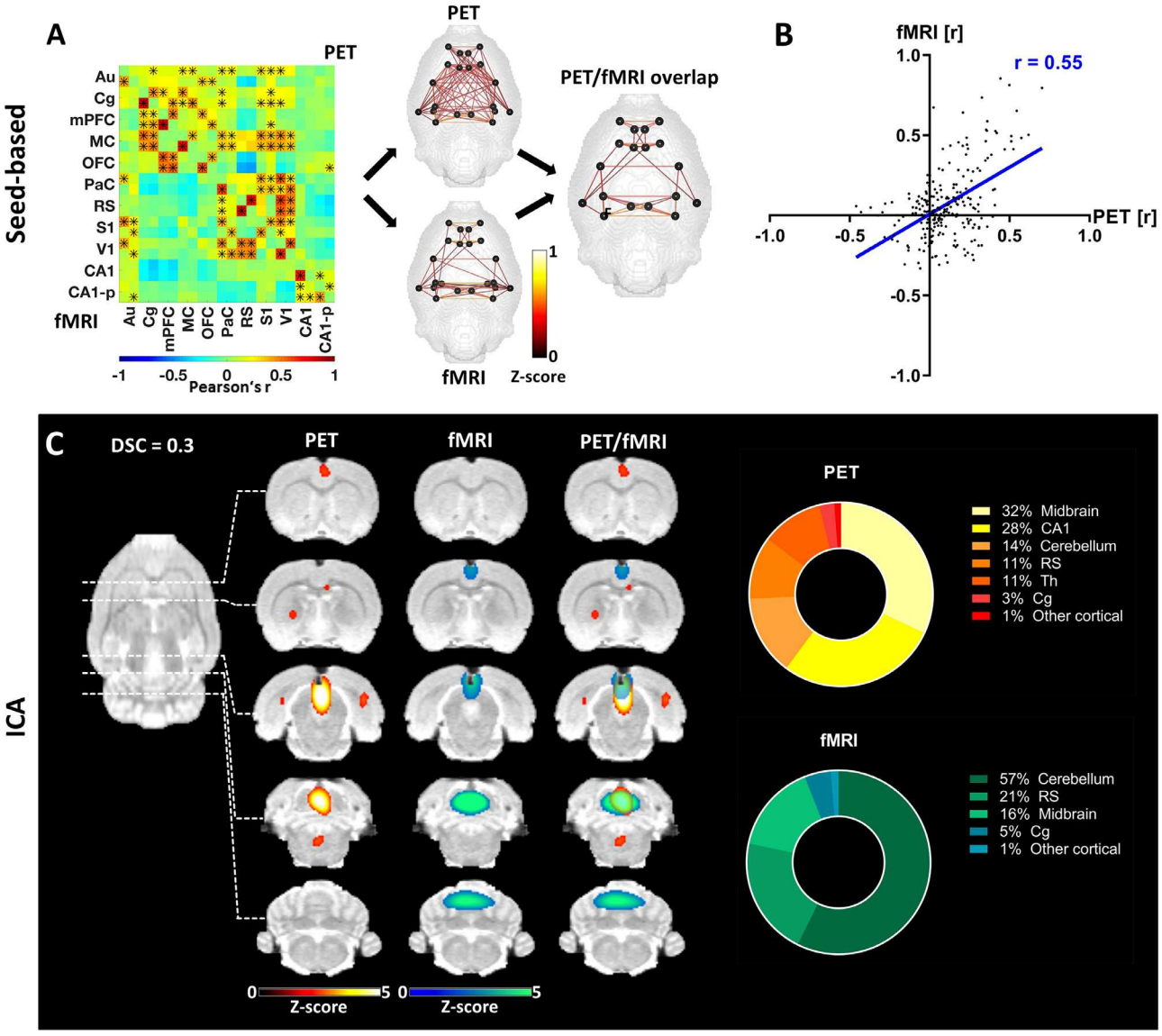

Fig. 2. Pairwise correlation analysis and ICA-derived connectivity of the DMN-like network. (A) Mean connectivity matrix of the DMN for [^{18}F]FDG-PET and BOLD-fMRI. The positive edges derived from a whole-brain sparsity threshold of 20% are depicted along with the common edges for both methods. * indicate significant correlations ($p \leq 0.05$, corrected for multiple comparison using Bonferroni-Holm). (B) Correlation of [^{18}F]FDG connectivity and FC within the DMN assessed using Pearson's r. (C) ICA-derived components of [^{18}F]FDG connectivity and FC comprising regions associated with the posterior DMN along with their overlap ($z \geq 1.96$) and the respective contributions of different regions to the ICA-derived components. The results are reported at group-mean level ($n = 30$).). FC = fMRI-derived functional connectivity, ICA = independent component analysis, DSC = Dice-Sörensen coefficient. For a list of abbreviations of all regions, please refer to *Supplementary Table 1*.

olded outputs. Second, two components exhibiting a significant spatial distribution along the striatum are presented along with the quantification of the contributions of different regions to the respective components.

The mean connectivity matrices of the basal ganglia network revealed more widely distributed connectivity patterns for FC than for [^{18}F]FDG correlations (Fig. 3A). The similarities of both outputs included pronounced connectivity between the CPu, Ins, CA1 and CA1-p. The quantification of similarity between both outputs using Pearson's r had a value of 0.3 ($p \leq 0.001$, Fig. 3B). Similar to the pairwise correlation approach, the ICA-derived components indicated an overlap in the anterior subcortical regions, especially in the striatum (Fig. 3C). The quantification of regional contributions confirmed that the CPu contributes extensively to the signal in both components (43% in PET and 60% in fMRI). Additionally, the second-highest contribution to both components was provided by the Th (17% for PET and 11% for fMRI). Other areas, such as the NAc, Ins and CA1, contributed to the signal in both components, while the Amyg and Hyp only featured in the fMRI output, and the MB exclusively featured in the PET-derived output.

Fig. 4 illustrates the connectivity in the cerebellar-midbrain network. First, the FC and [^{18}F]FDG connectivity derived using the pairwise correlation approach are shown, and the respective outputs compared. Second, two components derived from both PET and fMRI are presented and the regional contributions to the signal of each component are quantified voxel-wise.

The connectivity in the cerebellar and midbrain areas of the brain revealed increased spatial distribution for [^{18}F]FDG correlations (Fig. 4A). While both [^{18}F]FDG correlations and FC could be found within the cerebellum (CG and CW) and the midbrain areas (MB, SC, IC, VTA), in contrast to [^{18}F]FDG connectivity, no FC was detected between the midbrain regions and cerebellar regions. Nonetheless, a relatively high correlation of 0.65 ($p \leq 0.001$) between the two unthresholded out-

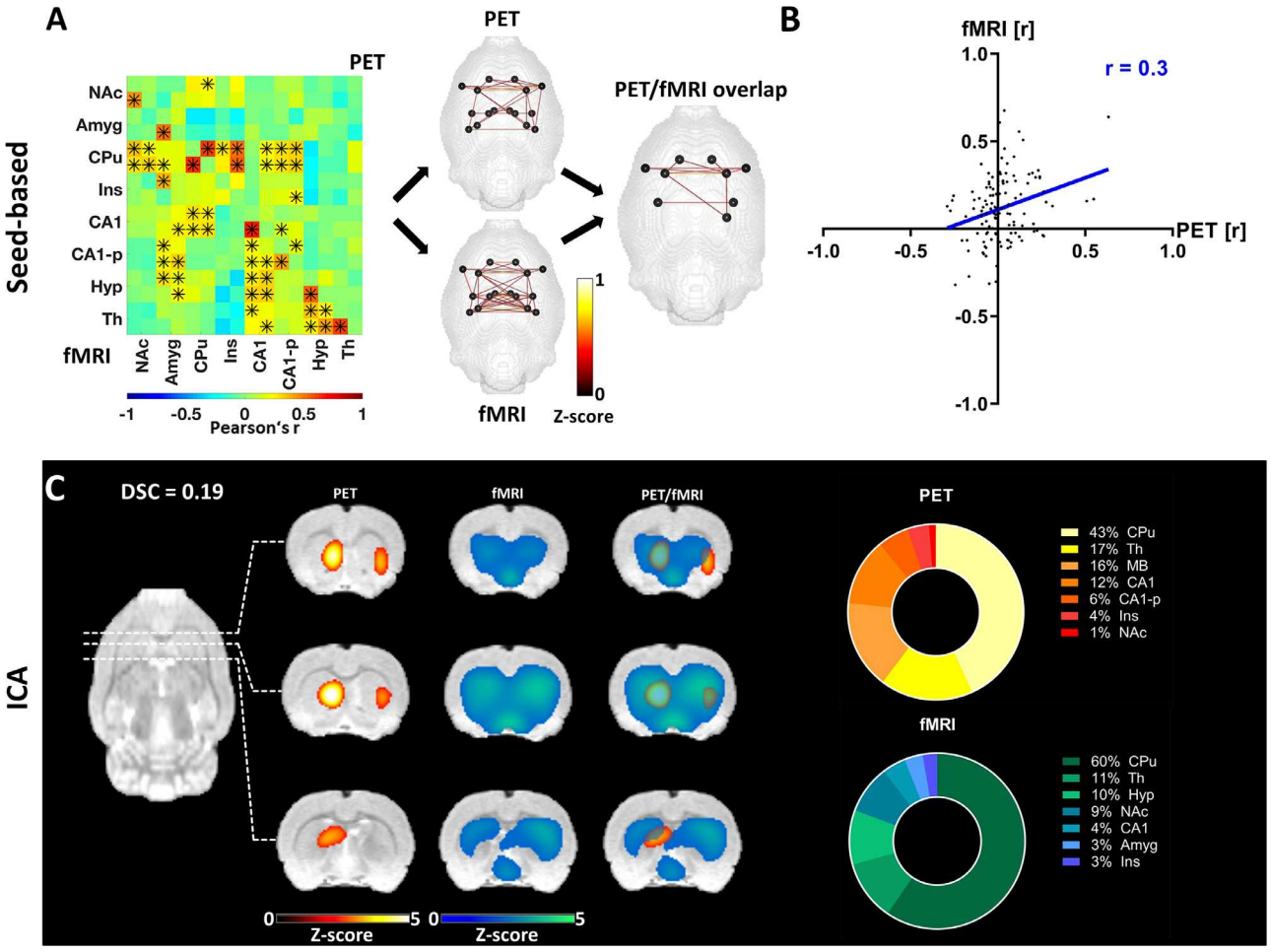

Fig. 3. Pairwise correlation analysis and ICA-derived connectivity of the basal ganglia network. (A) Mean connectivity matrix of the basal ganglia network for [^{18}F]FDG and BOLD-fMRI. The positive edges derived from a whole-brain sparsity threshold of 20% are depicted along with the common edges for both methods. * indicate significant correlations ($p \leq 0.05$, corrected for multiple comparisons using Bonferroni-Holm). (B) Correlation of [^{18}F]FDG connectivity and FC within the basal ganglia assessed using Pearson's r. (C) ICA-derived components of [^{18}F]FDG connectivity and FC comprising regions associated with the basal ganglia network along with their overlap ($z \geq 1.96$) and the percentage contribution of different regions to the ICA-derived components. The results are reported at group-mean level ($n = 30$). FC = fMRI-derived functional connectivity, ICA = independent component analysis, DSC = Dice-Sörensen coefficient. For a list of abbreviations of all regions, please refer to *Supplementary Table 1*.

puts of [^{18}F]FDG-PET and BOLD-fMRI was quantified using Pearson's r (Fig. 4B). Two separate components for the two areas were assessed using ICA. The cerebellar components (Fig. 4C) showed significant overlap, both having high contributions from the CG (65% in PET and 65% in fMRI) and the CW (32% in PET and 35% in fMRI). A further pair of components (Fig. 4D) was derived from both the midbrain and cerebellar areas. While the cerebellum provided the largest proportion of signal for both PET and fMRI, the MB also contributed to both components (9% in PET and 3% in fMRI) along with the IC (9% in PET and 19% in fMRI) and the SC (3% in PET and 2% in fMRI).

3.3. Single-subject correlations between hemodynamic and [^{18}F]FDG-PET-derived RSNs

We calculated correlations between the single-subject readouts of the three reported RSNs. The values are presented in Fig. 5.

On whole-brain level, all subjects correlated significantly ($p \leq 0.05$) and all respective p-values survived multiple comparison correction using Bonferroni-Holm. The correlations ranged from 0.08 to 0.42 with a mean value of 0.22 ± 0.07. In the DMN, the correlations ranged from 0.08 to 0.42 with a mean value of 0.29 ± 0.10. 28 out of 30 subjects correlated significantly ($p \leq 0.05$, uncorrected) and 26 out of the 30 p-values survived multiple comparison correction. In the basal ganglia network, correlations between [^{18}F]FDG-PET and BOLD-fMRI connectivities on single-subject level were in the range of −0.1 and 0.49, the mean value being 0.11 ± 0.13. [^{18}F]FDG connectivity and BOLD-derived FC correlated significantly for 12 out of 30 subjects before multiple comparison correction and for 3 out of 30 subjects after Bonferroni-Holm correction was applied. Finally, in the cerebellar-midbrain network the subject-level correlations of [^{18}F]FDG connectivity and FC were in the range between 0.14 and 0.65 with an average of 0.35 ± 0.18. 24 out of 30 single-subject [^{18}F]FDG correlation readouts and respective BOLD-fMRI outputs correlated significantly ($p \leq 0.05$) before multiple comparison correction and 12 out of 30 survived Bonferroni-Holm correction.

3.4. Complementary networks can be found in fMRI and PET-derived connectivity outputs

Fig. 4 focuses on the components found exclusively in the fMRI-derived ICA. Here, four cortical components and one subcortical component are presented from the anterior to posterior areas of the brain. For a list of all 20 components found in the fMRI-derived ICA, see the *Supplementary Results*.

In the component comprising the anterior DMN, the Cg acted as a main hub, contributing 36% of the signal (Fig. 6A). Further anterior cor-

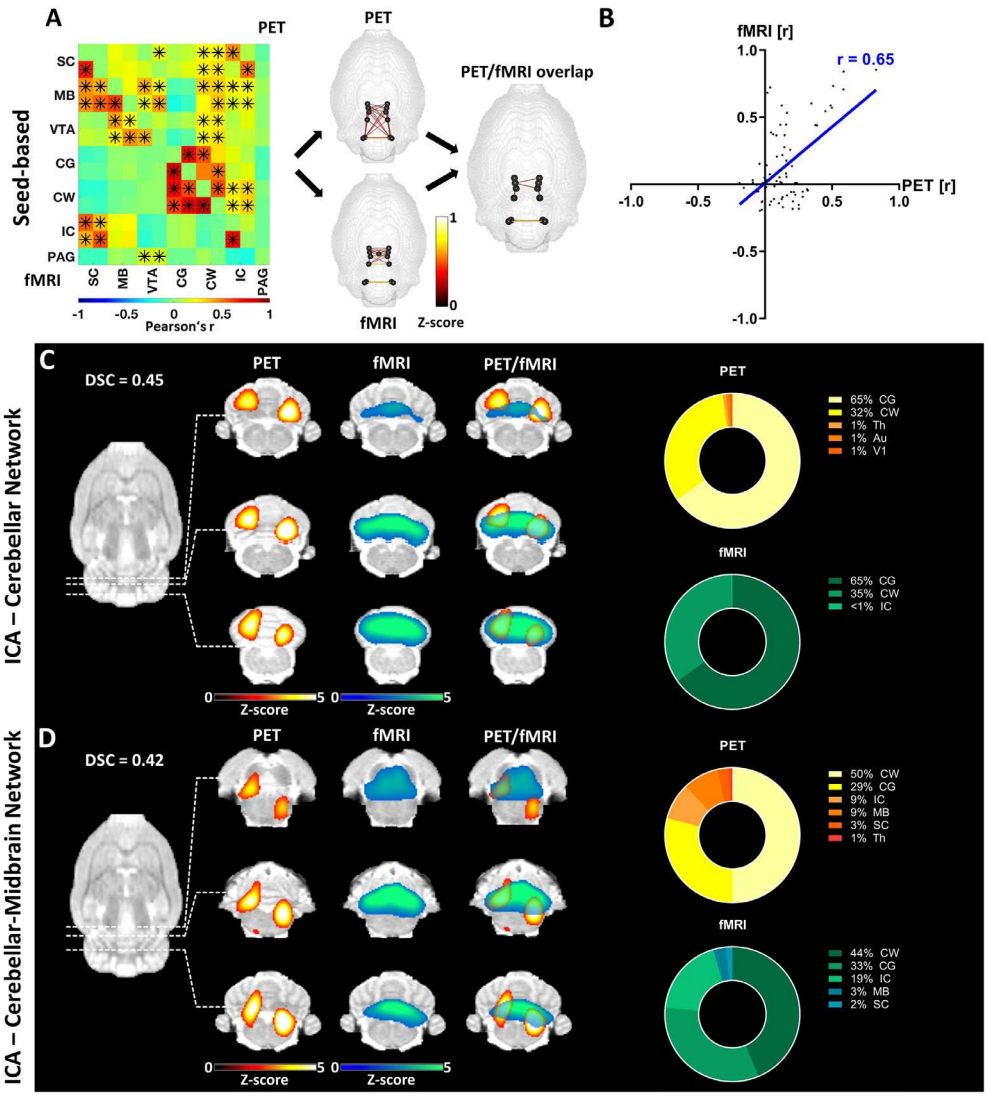

Fig. 4. Pairwise correlation analysis and ICA-derived connectivity of the cerebellar-midbrain network. (A) Mean connectivity matrix of the cerebellar-midbrain network for [^{18}F]FDG-PET and BOLD-fMRI. The positive edges derived from a whole-brain sparsity threshold of 20% are depicted along with the common edges for both methods. * indicate significant correlations ($p \leq 0.05$, corrected for multiple comparisons using Bonferroni-Holm). (B) Correlation of [^{18}F]FDG connectivity and FC within the cerebellar-midbrain network assessed using Pearson's r. (C) ICA-derived components [^{18}F]FDG-PET and BOLD-fMRI data ($z \geq 1.96$) comprising cerebellar regions along with their overlap and the contribution of different regions to the respective components. (D) ICA-derived components of [^{18}F]FDG-PET and BOLD-fMRI data ($z \geq 1.96$) comprising cerebellar and midbrain regions along with their overlap and the contribution of different regions to the respective components. The results are reported at group-mean level ($n = 30$). FC = fMRI-derived functional connectivity, ICA = independent component analysis, DSC = Dice-Sörensen coefficient. For a list of abbreviations of all regions, please refer to *Supplementary Table 1*.

tical areas with implications in this component were the mPFC (15%), M1 (14%) and OFC (10%). Subcortically, a significant signal could be found in the CPu (10%). Posteriorly, another main DMN hub, the RS, contributed 7% of the total signal, while 4% of the signal was derived from the S1 cortex.

Fifty-seven percent of a component representing the motor network (Fig. 6B) was found to be composed of M1, with further contributions from the Cg (24.%) and S1 (14%). The somatosensory network was derived to a proportion of 69% from S1 and 19% from M1 (Fig. 6C). The hippocampal network was mainly driven by CA1 (37%), while further signals could be found in cortical areas such as the S1, V1 and RS, as well as the Th (Fig. 6D). Finally, the visual network (Fig. 6E) was predominantly composed of V1 contributions (71%). Further contributions were provided by the RS (24%) and the Par (4%).

Three components found exclusively in the PET-derived ICA are depicted in Fig. 7. A list of all 20 components derived from the ICA applied to the PET data can be seen in the *Supplementary Results*.

The first component found exclusively in the PET-derived ICA (Fig. 7A) had the largest signal contributions from the Hyp (47%) and the RS (23%). Further signals could be detected in the OC (10%) and in anterior subcortical areas such as the NAc (6%) and the Amyg (2%). A smaller proportion of the signal was found posteriorly in the cerebellar and midbrain areas. A further component (Fig. 7B) was derived mainly from the Th (27%) and Hyp (22%). Smaller contributions were provided by other subcortical areas ranging from the anterior areas, including the CPu, NAc and Amyg, to the cerebellum. Finally, another spatially widely distributed subcortical component revealed the connectivity between the basal ganglia and the midbrain and the cerebellum (Fig. 7C). The majority of the signals stemmed from the CPu (39%), Th (15%), MB (15%) and CA1 (11%), with smaller implications from the CG, CA1-p, VTA, Ins and NAc.

4. Discussion

Resting-state FC studies have been derived primarily from MRI data due to the high spatial and temporal resolution and relative ease of access to MR systems. The analysis of BOLD-fMRI RSN has become more streamlined in recent years, providing reliable quantitative measures of brain function. However, fMRI has some disadvantages, relying on the convoluted BOLD signal as an indirect reflection of neural activity via hemodynamic changes (Buxton, 2012), as well as a high sensitivity to artefacts such as the spin-history artefact already occurring at millimetre-range movements (Yancey et al., 2011). Recent advances in PET scanner technology with an improved temporal resolution allow functional PET imaging using [^{18}F]FDG on the single-subject level (Villien et al., 2014). While [^{18}F]FDG-PET directly measures the glucose

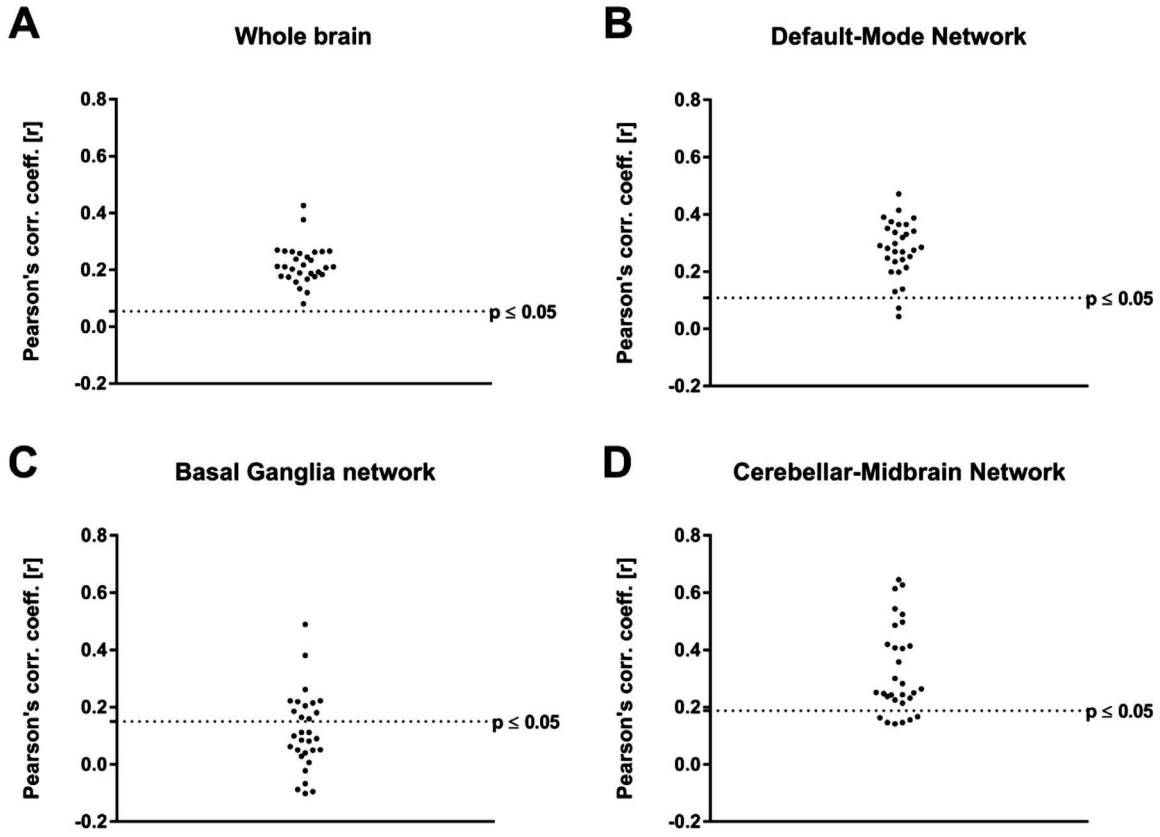

Fig. 5. Correlations between the [^{18}F]FDG and BOLD-fMRI readouts on single-subject level for every RSN. The subject-level correlations were tested for significance (A) at whole-brain level and in the (B) default-mode network, (C) basal ganglia network and (D) cerebellar-midbrain network with and without multiple comparison corrections. The dotted lines indicate significance without multiple comparison correction ($p \leq 0.05$).

consumption of cells, the BOLD signal is convoluted and weighted towards larger blood vessels (Wehrl et al., 2013). The recent advances in correlation analyses of [^{18}F]FDG-PET data (Amend et al., 2019; Wehrl et al., 2013) performed in the same way as fMRI-derived FC using pairwise correlations or ICA have provided the opportunity to gain functional information using PET and enhance the understanding on functional connectivity. In this context, the availability of small-animal hybrid PET/MR systems provides the opportunity to simultaneously study functional RSNs with both modalities. Preclinical studies exhibit several advantages, including high subject cohort homogeneity and improved control over the experimental and living conditions of the cohort. Here, we present for the first time a comparison of subject-wise derived RSNs through the simultaneous acquisition of dynamic [^{18}F]FDG-PET and fMRI data in rats.

In rats, fMRI-derived RSNs similar to those observed in humans have been reported by various groups (Becerra et al., 2011; Hutchison et al., 2010; Lu et al., 2012). Here, we report a DMN-like network, a basal ganglia network and a cerebellar-midbrain network observed using both BOLD-fMRI and [^{18}F]FDG-PET, highlighting the common substrate of the two outputs. However, these networks were characterized by differences in the extent of their connectivity patterns, emphasizing the complementarity of the two methods. This aspect is further supported by a number of RSNs exclusive to either of the two outputs, indicated by ICA components associated with the anterior DMN, the motor network, the sensory network, the hippocampal network and the visual network for the fMRI dataset and a network comprising the retrosplenial cortex and several subcortical regions, one driven mainly by the hypothalamus and thalamus and one across several subcortical regions for the [^{18}F]FDG-PET dataset.

4.1. Common RSNs for [^{18}F]FDG-PET and BOLD-fMRI reveal differences regarding spatial extents

The DMN is one of the most widely reported RSNs in humans (Raichle et al., 2001). In rats, the DMN has been reported as being composed of an anterior and a posterior sub-component (Lu et al., 2012). This observation is confirmed by the present study. For FC, the pairwise correlation approach indicated an anterior cluster around the cingulate cortex and a posterior one anchored by the retrosplenial cortex with sparser connectivity between the two groups of regions. [^{18}F]FDG correlations revealed a higher density of edges between the anterior and posterior parts of the DMN. ICA supported these findings: for fMRI, two separate anterior and posterior components associated with the DMN were observed. In contrast, only one component associated with the DMN was derived from the [^{18}F]FDG-PET ICA. This component exhibited higher overlap with the posterior fMRI-derived DMN component than with the anterior component. Intriguingly, both the PET-derived and the fMRI-derived components comprised extensive contributions from cerebellar and midbrain areas. This finding can be explained by the fact that the midbrain and the cerebellum both cover a larger volume compared to the retrosplenial and cingulate cortices (see *Supplementary Table 1*). Additionally, recent reports in the literature indicated involvements of these areas in the DMN. In a human study, Habas et al. (Habas et al., 2009) found cerebellar, thalamic and midbrain contributions to the DMN, as indicated by our data. Other reports appear to converge towards the hypothesis that the cerebellum may contribute extensively to the DMN (Castellazzi et al., 2018; Savini et al., 2019), although its role has not been fully resolved. Studies have indicated its potential involvement in the elaboration of the past and future together with the retrosplenial cortex (Addis et al., 2007). The absence of the

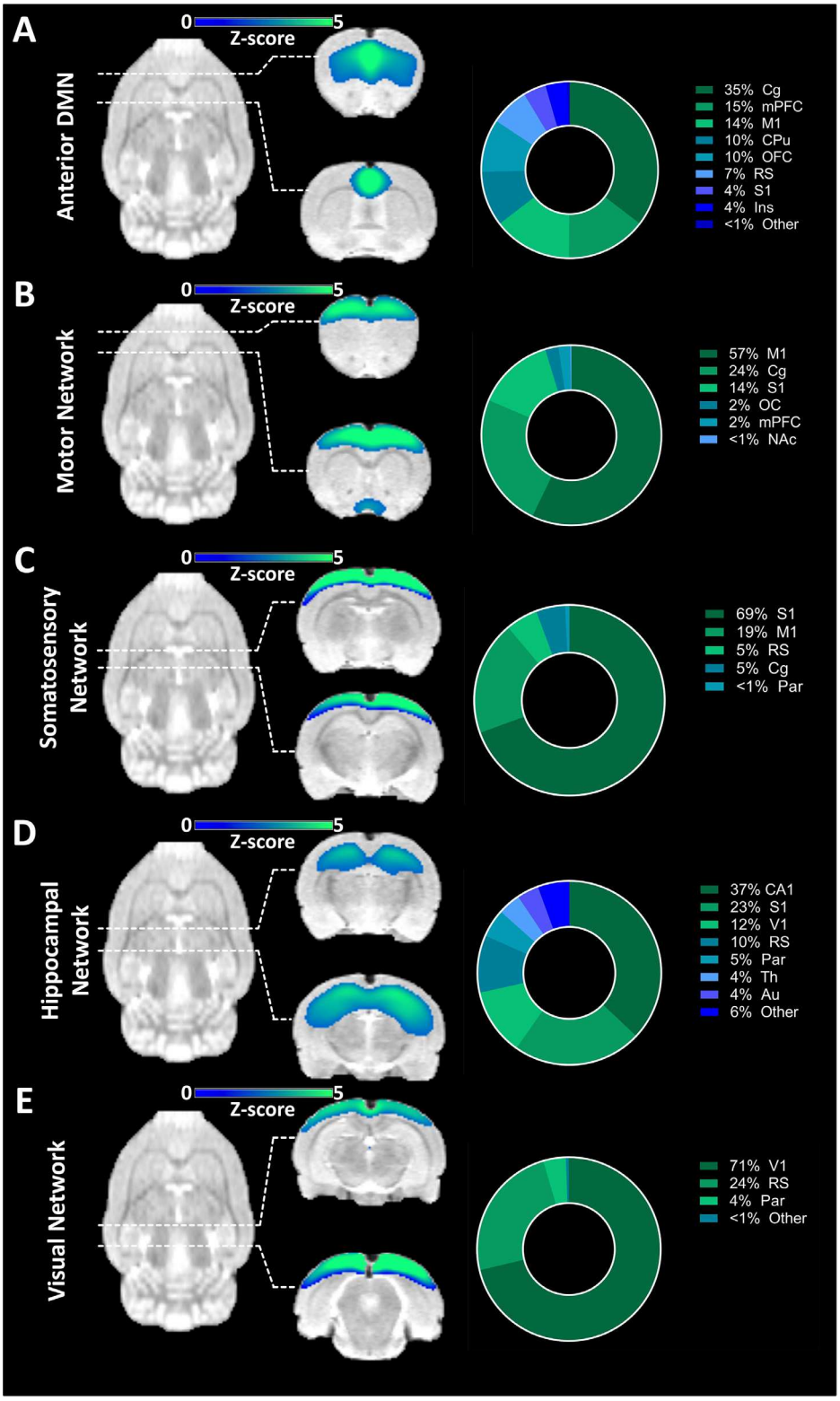

Fig. 6. Components found exclusively in fMRI-derived ICA. (A) Component comprising regions associated with the anterior DMN along with the regional quantification of the derived signal. (B) Component comprising the motor network along with the regional quantification of the derived signal. (C) Component comprising the somatosensory network along with the regional quantification of the derived signal. (D) Component comprising regions of the hippocampal network along with the regional quantification of the derived signal. (E) Component comprising the visual network along with the regional quantification of the derived signal. The results are reported at group-mean level (n = 30). ICA = independent component analysis, DMN = default-mode like network. For a list of abbreviations of all regions, please refer to *Supplementary Table 1*.

cerebellum from most reports could be a result of its exclusion due to a number of challenges it poses in fMRI, such as the risk of susceptibility artefacts (T2* effects) induced by nearby air-tissue interface in the ears (Batson et al., 2015; Becerra et al., 2011; Habas et al., 2009). In this respect, PET acquisitions are superior since they are not influenced by such artefacts. Nonetheless, both cerebellar and midbrain contributions to the DMN were also reported in rodents using fMRI (Becerra et al., 2011; Upadhyay et al., 2011). Our PET/fMRI data support the involvements of cerebellum and midbrain in the posterior DMN.

The second large-scale network featuring in the outputs of both modalities involved subcortical regions commonly termed the basal ganglia. The circuitry of this network is of particular interest since the basal ganglia have been shown to be chronologically amongst the first areas affected in several diseases, such as Parkinson's disease, Huntington´s

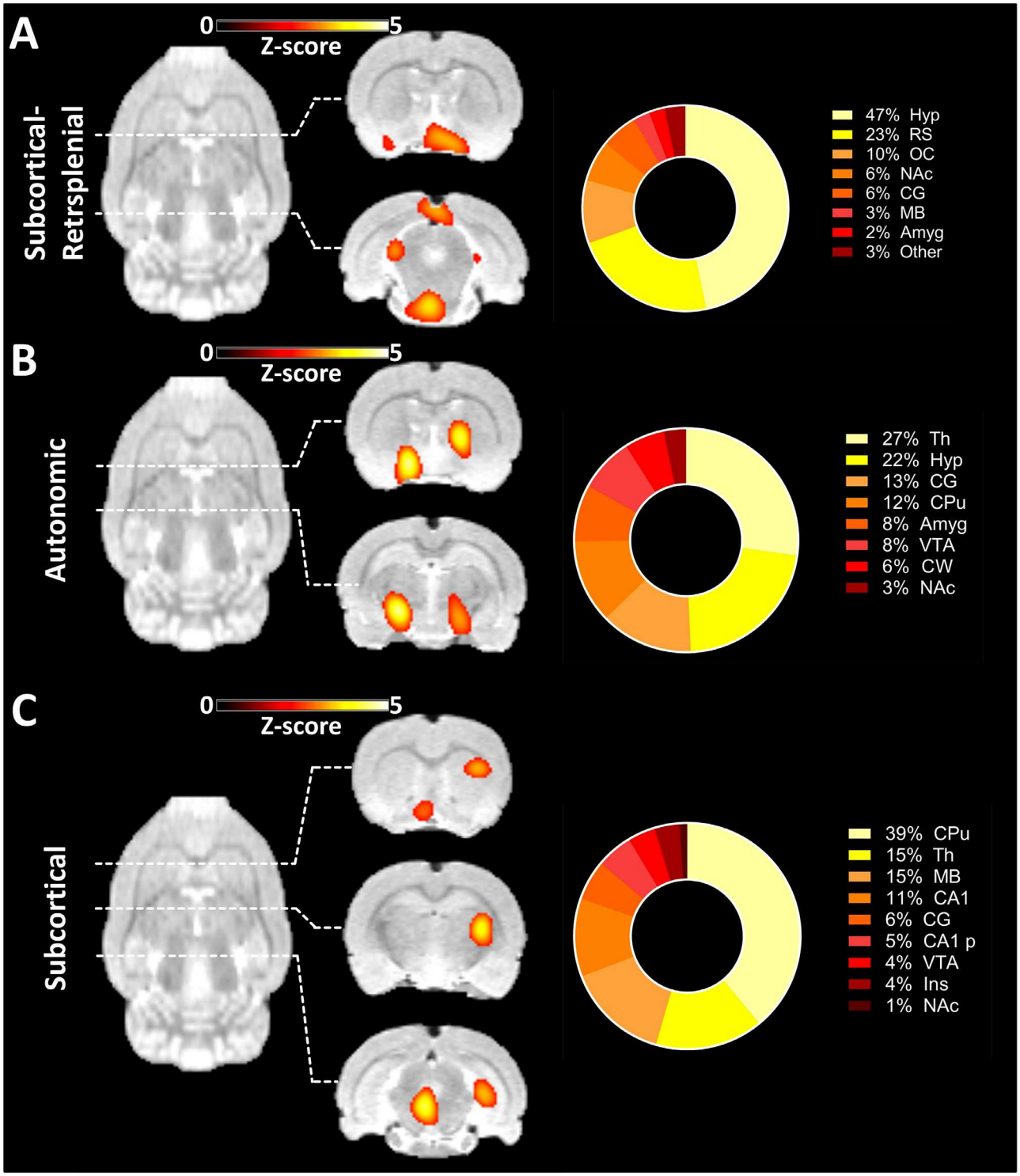

Fig. 7. Components found exclusively in [^{18}F]FDG-PET-derived ICA. (A) Component comprising the Hyp, RS, OC and other subcortical and posterior areas along with the regional quantification of the derived signal. (B) Component mainly composed of Th, Hyp and other subcortical areas along with the regional quantification of the derived signal. (C) Component comprising multiple subcortical areas along with the regional quantification of the derived signal. The results are reported at group-mean level (n = 30). ICA = independent component analysis. For a list of abbreviations of all regions, please refer to *Supplementary Table 1*.

disease or dystonia (DeLong and Wichmann, 2007). Reports of this network in rats provide contrasting information regarding the integration of separate regions into a single network. Becerra et al. reported two components involving the basal ganglia in awake rats (Becerra et al., 2011). Other groups have observed different components separately involving the striatum, hippocampus or thalamic areas with no apparent connection between them (Hutchison et al., 2010; Majeed et al., 2011). For fMRI we found similar ICA components including separate hippocampal and thalamic circuitry (see component 7 in *Supplementary Figure 3*). Using the pairwise correlation approach, a more pronounced connectivity between the different structures could be observed for FC. For [^{18}F]FDG, the pairwise correlation analysis showed decreased in-

tegration of the basal ganglia with pronounced connectivity predominantly in the anterior area around the striatum. This observation was enforced by the ICA applied to the [^{18}F]FDG-PET data. The highest overlap in regions associated with the basal ganglia network occurred between two components predominantly situated in the striatum.

The final network found to be similar for [^{18}F]FDG correlations and BOLD-fMRI FC involved cerebellar-midbrain circuitry. Interestingly, novel evidence suggests an integration of these structures into a coherent network with the basal ganglia network presented above (Bostan and Strick, 2018). The analysis of cerebellar-midbrain circuitry enabled similar observations applied to the DMN described above; while [^{18}F]FDG correlations suggested integration of midbrain and cerebellar circuitry, FC was pronounced within the cerebellum and the midbrain individually, but not between them. The performed ICA revealed one cerebellar component for both readouts and a second involving both cerebellum and midbrain. Interestingly, the cerebellar-midbrain component derived from [^{18}F]FDG-PET also suggests increased spatial integration due to the more distributed signal with stronger contributions from the midbrain and thalamus.

In addition to the group-mean calculations, we conducted subject-wise correlation analyses between [^{18}F]FDG and BOLD-fMRI readouts at whole-brain and RSN level, leading to two main conclusions. First, the subject [^{18}F]FDG-PET and BOLD-fMRI FC readouts correlated for all RSNs and on whole-brain level in the majority of subjects. Significance testing of the single-subject correlations indicated differing extents of coherence between [^{18}F]FDG correlations and FC depending on the RSN. Although the correlations between [^{18}F]FDG-PET outputs and FC for certain subjects were as high as for the group-mean data, on average they were lower compared to group-mean readouts. Especially in the basal ganglia network, less than half of the subjects exhibited significant correlations between [^{18}F]FDG-PET readouts and FC and merely three were significant following multiple comparison correction. These observations imply that there is a significant inter-subject variability in both [^{18}F]FDG correlations and FC which is likely not entirely consistent between subjects. In spite of the single-subject variability, at the employed group size of 30 subjects the [^{18}F]FDG-PET data and BOLD-fMRI FC converge to a higher correlation of the group-mean readouts. While inter-subject variability is a well-reported characteristic of resting-state fMRI (Chou et al., 2012) and appears to be similar for [^{18}F]FDG-PET, it will be of interest for future studies to investigate direct relationships between the subject-level variance of the two readouts and to decipher their physiological significance. If the subject-wise variance of [^{18}F]FDG correlations is able to partially explain that of FC, it may enhance the prospects of using connectivity as a tool for diagnosis or treatment monitoring in the future, especially in indications for which PET/MRI studies are more commonly performed, such as epilepsy (Shang et al., 2018).

4.2. Exclusive components derived from the BOLD-fMRI and [^{18}F]FDG-PET datasets respectively reveal connectivity segregation and integration

The independent components found to be exclusive to either fMRI or [^{18}F]FDG-PET appear to confirm the general trend suggested above. In general, the fMRI components can be described as being bilateral and having a limited anterior-posterior extent. Apart from the anterior DMN component, the other presented components were predominantly driven by a single brain area: the motor cortex, the sensory cortex, the hippocampus and the visual cortex. Such bilateral components were first described in rats by Hutchison et al. in 2010 (Hutchison et al., 2010).

Bilateral spatially limited components are observed much less frequently in the [^{18}F]FDG-PET-derived ICA output. The first exclusive component presented principally included the hypothalamus, olfactory cortex and retrosplenial cortex. The retrosplenial cortex is a cortical region of a much larger relative extent in rodents than in humans; hence, its function in rats may be of increased importance. Previous studies have shown the connections of the hypothalamus to frontal cortical regions and the hippocampus, suggesting its role in cognition and decision-making (Nelson et al., 2014). Additionally, the hypothalamus it has been shown to be involved in spatial and mnemonic functions (Maguire, 2001; Vann et al., 2009). Since smell, which is processed in the olfactory cortex, is one of the most dominant senses in rodents and because the hypothalamus is known to play a major role in homoeostatic behaviours (Toni et al., 2004), this network may play a role in adapting to the environment by collecting cues via the sense of smell along with decision-making and navigation using the retrosplenial cortex and appropriate homoeostatic regulation through the hypothalamus. The autonomic network shown in Fig. 7B has been described in earlier BOLD-fMRI studies in awake rats (Becerra et al., 2011; Liang et al., 2011). Though the observation of this circuitry in the [^{18}F]FDG-PET dataset may point towards the robustness of this method regarding anaesthesia, the interpretation of this network remains elusive. Finally, the spatially extensive component observed in Fig. 7C, comprised of basal ganglia, thalamus, midbrain and cerebellum, may represent a further hint towards an increased integration of these structures.

Our data strongly support the hypothesis that FC largely reflects interhemispheric connectivity between bilateral structures, while the [^{18}F]FDG correlation output reflects a more integrated model of brain connectivity, revealing more extensive modules of functionally connected brain areas. Since many neurological disorders, such as AD and PD, have been shown to affect the brain on a large scale involving several interconnected brain regions distal from the main pathology, the readout of [^{18}F]FDG-PET data will be a valuable tool to study brain connectivity changes in such diseases at early stages or to follow treatment responses.

4.3. Comparison of fMRI and [^{18}F]FDG-PET connectivity imaging

Several studies have aimed to compare FC to brain metabolism, metabolic connectivity or [^{18}F]FDG correlations (Aiello et al., 2015; Di et al., 2017; Passow et al., 2015b; Savio et al., 2017; Tomasi et al., 2017; Wehrl et al., 2013). Aiello et al. compared brain metabolism to fMRI measures such as FC, regional homogeneity (ReHo) or fractional amplitude of low frequency fluctuations (fALFF) in humans and indicated correlations between the readouts ranging from 0.47 to 0.55 using Spearman's ρ, which is in the same range as the correlation using Pearson's r presented in our study (Aiello et al., 2015). On whole-brain level, our reported Pearson's r correlation of 0.45 translates into a rank correlation of $\rho = 0.44$. Apart from the connectivity metric employed, the slightly lower values compared to those reported by Aiello might stem from the fact that, compared to the study by Aiello (Aiello et al., 2015), which only included the cortex, the present study was performed at whole-brain level. The overlaps between the networks we derived from BOLD-fMRI FC and [^{18}F]FDG correlations are also in line with the values reported previously for a seed-based approach by Biswal et al. in humans (Di et al., 2017). With respect to RSNs, one study compared networks derived from simultaneous [^{18}F]FDG-PET and fMRI acquisitions (Savio et al., 2017). Similarly to our data, the authors identified common components for fMRI and PET, as well as exclusive components for both outputs. Interestingly, the PET-exclusive components were also predominantly in subcortical brain areas (Savio et al., 2017), which is in line with our findings. However, none of the studies mentioned above derived [^{18}F]FDG correlations from dynamic [^{18}F]FDG-PET tracer delivery fluctuations. Two studies in humans have previously performed dynamic [^{18}F]FDG-PET correlation analyses (Passow et al., 2015b; Tomasi et al., 2017), however without acquiring the fMRI data simultaneously, making the comparison of the respective outputs difficult. Previously, we have shown an interplay between fMRI and dynamic [^{18}F]FDG-PET and the complementary information they provide in task-based and resting-state experiments (Wehrl et al., 2013). In the present study, we further support these findings with regard to RSNs.

As a general trend, both our study and the reports described above converge towards the conclusion that FC and [^{18}F]FDG correlation

readouts overlap partially while also offering significant complementary input. This is explained by the fact that while in essence, both methods are an indirect reflection of neural activity, the hemodynamic and [^{18}F]FDG tracer fluctuations they respectively measure occur inherently at different time-scales (Amend et al., 2019; Rischka et al., 2018; Tomasi et al., 2017; Wehrl et al., 2013). Simultaneous [^{18}F]FDG-PET/fMRI is therefore perfectly suited to delineate these two interconnected but distinct physiological readouts. BOLD-fMRI is able to capture hemodynamic changes using its second-range resolution and is complemented by [^{18}F]FDG-PET reflecting glucose consumption using minute-range time-windows. This temporal mismatch likely contributes to the complementarity reported using BOLD-fMRI and [^{18}F]FDG-PET in previous brain stimulation studies (Wehrl et al., 2013), as well as in the resting-state data reported here and elsewhere (Amend et al., 2019; Passow et al., 2015b; Tomasi et al., 2017).

Regarding the two types of analysis performed, several aspects need to be pointed out. First, while our ICA readout of the [^{18}F]FDG data generally mirrors the reports of previous studies in rats (Wehrl et al., 2013), many components indicate focal, unilateral signal. Using different numbers of components may contribute towards solving this issue; however, one of the main reasons for this observation is the relatively low signal-to-noise PET data have at voxel level. Therefore, voxel-wise approaches such as ICA or voxel-wise seed-based correlations are likely to be less suited for [^{18}F]FDG connectivity analysis compared to FC. Based on the reported data, we recommend the use of pair-wise correlation analysis including nodes of sufficient spatial extent to avoid particularly noisy signals.

4.4. Study limitations

There are several limitations to our study. First, fasting, a standard procedure for [^{18}F]FDG-PET scans, has been recently shown to impact fMRI-derived FC in mice (Tsurugizawa et al., 2019). Future studies are required to reveal the impact of fasting on the relationship between FC and [^{18}F]FDG correlations. Interestingly, the above-mentioned study reported an increase in retrosplenial FC being possibly associated with food-seeking. The [^{18}F]FDG-PET-exclusive component in our study comprising the retrosplenial cortex and hypothalamus may be related to this type of behaviour.

Additionally, the choice of isoflurane has been shown to influence rs-FC readouts (Paasonen et al., 2018; Williams et al., 2010). However, we kept isoflurane at a level previously indicated as feasible for FC acquisition in rodents (Hutchison et al., 2014) to minimize its effects. Importantly, previous studies evaluated interhemispheric FC as a measure of the effects of different anaesthesia regimes and dosages (Jonckers et al., 2014).The bilateral ICs, as well as the strong interhemispheric FC revealed by the pairwise correlation analysis for FC indicate isoflurane was at sufficiently low levels. Furthermore, isoflurane has been shown to impact [^{18}F]FDG uptake (Spangler-Bickell et al., 2016). For fMRI studies, a cocktail of isoflurane and medetomidine has been shown to have the most reduced impact on FC readout in rodents (Paasonen et al., 2018). Unfortunately, previous reports (Wehrl et al., 2013) have shown that the effects of medetomidine on [^{18}F]FDG metabolism are significantly more pronounced than those of isoflurane. Concerning the interpretation of our data, previous studies have reported a regionally differentiated impact of isoflurane on brain metabolism, cortical and thalamic [^{18}F]FDG uptake being most affected with more conserved metabolism in cerebellar and midbrain areas (Park et al., 2017; Spangler-Bickell et al., 2016). This may explain a certain bias of our [^{18}F]FDG readout towards the latter structures compared to FC, especially in the ICA analysis. Therefore, effects on the chosen anaesthesia cannot be excluded on the analysis performed in this study and the described network architecture is valid for this type of anaesthesia. Ultimately, whether and to which extent the choice of anaesthesia does influence the readout remains to be elucidated in future studies. On a general note, due to its inherent combination of two imaging modalities, finding an anaesthesia protocol suited for animal PET/fMRI will be one of the major future challenges of similarly designed studies. For an additional analysis and brief discussion on the [^{18}F]FDG uptake in the present study compared to previous reports in conscious and unconscious animals, please refer to *Supplementary Information*.

Furthermore, we discussed our findings in the context of previous studies performed in rodents but also in humans. While many RSNs have been shown to be reproducible and comparable amongst species, some differences cannot be excluded and should be kept in mind when directly comparing findings between species, in addition to the role played by the choice of anaesthesia.

Additionally, although potential benefits have been delineated (Li et al., 2019; Murphy and Fox, 2017), global normalization or global signal regression (GSR) is a topic of debate in rs-fMRI due to its decrease of sensitivity and induction of artificial negative correlations (Chuang et al., 2019). Due to the latter, we refrained from interpreting the negative correlations observed in our data. Nonetheless, global normalization is a standard method in [^{18}F]FDG-PET and previous studies investigating [^{18}F]FDG correlations using dynamic [^{18}F]FDG-PET reported global normalization as the method of choice (Amend et al., 2019; Passow et al., 2015b). Employing the same method for fMRI enabled an increased coherence between the analysis pipelines of the two datasets. Previous studies focused on rodent fMRI preprocessing and signal cleaning have shown that many approaches which are considered standard for human rs-fMRI cannot be easily translated to small animals (Chuang et al., 2019). Nonetheless, while further studies are clearly required to elucidate the effects of different preprocessing pipelines on both FC and [^{18}F]FDG correlations, to investigate the effect of global signal removal on the computation of FC we also employed an alternative approach recently described by Chuang et al. (Chuang et al., 2019) which did not involve global signal removal. Our comparison shows that global signal removal does not majorly affect our findings which could also be reproduced without applying this method (please refer to *Supplementary Results*).

Finally, as shown in our previous publication (Amend et al., 2019), one of the main drawbacks of inferring [^{18}F]FDG correlations using a bolus protocol is the inherent inability to achieve stable tracer kinetics. Since the data in the mentioned publication (Amend et al., 2019) indicated the importance of k1 for the readout, the analysis was performed over the course of the entire scan. Hence, it cannot be excluded that by choosing this approach the readout may be to a certain extent biased towards flow effects and when performing correlation analyses the resulting correlation coefficients may be higher compared to analyses performed over later periods of the scan. To this extent, infusion protocols may offer a more accurate subject-level reflection of the metabolic connectivity described on group level by previous studies (Horwitz et al., 1984; Ripp et al., 2020). Additionally, due to the potential bias of using the entire scans in bolus protocols towards tracer flow, results in pathological cohorts with inherent vasculature alterations should also be interpreted with caution when comparing them to data of healthy controls. However, major advantages of choosing the entire period of the scan include the straightforward implementation and the avoidance of user bias of choosing a specific scan period for the analysis. Although infusion protocols do enable a stable readout after achieving stable kinetics (Amend et al., 2019) and are fast becoming more widespread (Rischka et al., 2018; Villien et al., 2014), research on this topic is still at an incipient stage and infusion protocols are thus far still not widely established. Another drawback of infusion protocols is the period required to reach pseudo-equilibrium, an aspect particularly important for scans involving the use of anaesthesia. Therefore, at this stage bolus protocols represent a viable option which can be easily implemented for similarly designed studies both in a clinical and preclinical setting.

The main advantages of the performed study were the simultaneous PET/fMRI acquisitions and dynamic PET analysis. Our data reveal that simultaneously acquired PET data driven by their sub-pico-molar sensitivity (Price, 2001) complement resting-state fMRI network read-

outs. The use of simultaneous PET/fMRI data acquisition is essential to ensure a temporal coherence between the observations made on both physiological levels (Judenhofer et al., 2008; Wehrl et al., 2013). Dynamic PET is required for inferring subject-wise [^{18}F]FDG correlations from the time series of each subject, rather than on the group level from subject series of one single image per subject. Hence, dynamic PET acquisition is a prerequisite for potential future clinical applications.

5. Conclusion

Deriving [^{18}F]FDG correlations from dynamic [^{18}F]FDG-PET data provides important complementary information to BOLD-fMRI results regarding brain connectivity. Our data reveal a common substrate of both outputs with similar RSNs observed using the two methods. However, the added value of [^{18}F]FDG-PET was apparent both from the extent of the similar networks observed from both datasets and from the components exclusive to the [^{18}F]FDG-PET dataset. It is also important to note that [^{18}F]FDG reflects only one PET tracer amongst many; therefore, PET offers a multitude of possibilities to study different facets of brain metabolism and physiology. Our results indicate the potential of [^{18}F]FDG correlations to reflect a model of brain connectivity with enhanced integration of different brain areas by revealing several large-scale networks, including the cortical, subcortical, midbrain and cerebellar regions. These findings may be of interest for a basic understanding of brain functionality, as well as for studying and developing therapies for neurodegenerative and psychiatric diseases.

Funding

The research was funded by the German Ministry of Education and Research (BMBF, Grant No. 01GQ1415) to BJP and HFW, the Werner Siemens Foundation and the National Institute of Health (NIH R01 DA038895) to BBB.

Data availability

The original dataset will be made available on Mendeley.

Declaration of Competing Interest

The authors declare no conflict of interest.

Credit authorship contribution statement

Tudor M. Ionescu: Conceptualization, Methodology, Software, Validation, Investigation, Formal analysis, Data curation, Writing – original draft, Visualization. **Mario Amend:** Conceptualization, Investigation, Writing – review & editing, Supervision. **Rakibul Hafiz:** Methodology, Writing – review & editing. **Bharat B. Biswal:** Conceptualization, Methodology, Writing – review & editing, Funding acquisition. **Hans F. Wehrl:** Conceptualization, Methodology, Writing – review & editing, Funding acquisition. **Kristina Herfert:** Writing – review & editing. **Bernd J. Pichler:** Resources, Writing – review & editing, Supervision, Project administration, Funding acquisition.

Acknowledgements

We thank PD Dr. Gerald Reischl (Department of Preclinical Imaging and Radiopharmacy, Werner Siemens Imaging centre, Eberhard Karls University Tuebingen) for producing the [^{18}F]FDG tracer. Additionally, we acknowledge Dr. Julia Mannheim, Dr. Rebecca Rock, Ines Herbon and Stacy Huang (Department of Preclinical Imaging and Radiopharmacy, Werner Siemens Imaging centre, Eberhard Karls University Tuebingen) for their administrative and technical support. This study is also part of the PhD thesis of Tudor Ionescu.

Supplementary materials

Supplementary material associated with this article can be found, in the online version, at doi:10.1016/j.neuroimage.2021.118045.

References

Addis, D.R., Wong, A.T., Schacter, D.L., 2007. Remembering the past and imagining the future: common and distinct neural substrates during event construction and elaboration. Neuropsychologia 45, 1363–1377.
Aiello, M., Salvatore, E., Cachia, A., Pappata, S., Cavaliere, C., Prinster, A., Nicolai, E., Salvatore, M., Baron, J.C., Quarantelli, M., 2015. Relationship between simultaneously acquired resting-state regional cerebral glucose metabolism and functional MRI: a PET/MR hybrid scanner study. Neuroimage 113, 111–121.
Amend, M., Ionescu, T.M., Di, X., Pichler, B.J., Biswal, B.B., Wehrl, H.F., 2019. Functional resting-state brain connectivity is accompanied by dynamic correlations of application-dependent [(18)F]FDG PET-tracer fluctuations. Neuroimage 196, 161–172.
Badhwar, A., Tam, A., Dansereau, C., Orban, P., Hoffstaedter, F., Bellec, P., 2017. Resting-state network dysfunction in Alzheimer's disease: a systematic review and meta–analysis. Alzheimers Dement. (Amst.) 8, 73–85.
Barkhof, F., Haller, S., Rombouts, S.A., 2014. Resting-state functional MR imaging: a new window to the brain. Radiology 272, 29–49.
Batson, M.A., Petridou, N., Klomp, D.W.J., Frens, M.A., Neggers, S.F.W., 2015. Single Session Imaging of Cerebellum at 7 Tesla: obtaining Structure and Function of Multiple Motor Subsystems in Individual Subjects. PLoS ONE 10, e0134933.
Becerra, L., Pendse, G., Chang, P.C., Bishop, J., Borsook, D., 2011. Robust reproducible resting state networks in the awake rodent brain. PLoS ONE 6, e25701.
Biswal, B., Yetkin, F.Z., Haughton, V.M., Hyde, J.S., 1995. Functional connectivity in the motor cortex of resting human brain using echo-planar MRI. Magn. Reson. Med. 34, 537–541.
Bluhm, R.L., Miller, J., Lanius, R.A., Osuch, E.A., Boksman, K., Neufeld, R.W., Theberge, J., Schaefer, B., Williamson, P., 2007. Spontaneous low-frequency fluctuations in the BOLD signal in schizophrenic patients: anomalies in the default network. Schizophr. Bull. 33, 1004–1012.
Bostan, A.C., Strick, P.L., 2018. The basal ganglia and the cerebellum: nodes in an integrated network. Nat. Rev. Neurosci. 19, 338–350.
Bullmore, E., Sporns, O., 2009. Complex brain networks: graph theoretical analysis of structural and functional systems. Nat. Rev. Neurosci. 10, 186–198.
Buxton, R.B., 2012. Dynamic models of BOLD contrast. Neuroimage 62, 953–961.
Castellazzi, G., Bruno, S.D., Toosy, A.T., Casiraghi, L., Palesi, F., Savini, G., D'Angelo, E., Wheeler-Kingshott, C.A.M.G., 2018. Prominent changes in cerebro-cerebellar functional connectivity during continuous cognitive processing. Front. Cell. Neurosci. 12.
Chou, Y.-h., Panych, L.P., Dickey, C.C., Petrella, J.R., Chen, N.-k., 2012. Investigation of long-term reproducibility of intrinsic connectivity network mapping: a resting-state fMRI study. Am. J. Neuroradiol. 33, 833–838.
Chuang, K.H., Lee, H.L., Li, Z., Chang, W.T., Nasrallah, F.A., Yeow, L.Y., Singh, K., 2019. Evaluation of nuisance removal for functional MRI of rodent brain. Neuroimage 188, 694–709.
Cole, M.W., Pathak, S., Schneider, W., 2010. Identifying the brain's most globally connected regions. Neuroimage 49, 3132–3148.
Damoiseaux, J.S., Rombouts, S.A., Barkhof, F., Scheltens, P., Stam, C.J., Smith, S.M., Beckmann, C.F., 2006. Consistent resting-state networks across healthy subjects. Proc. Natl. Acad. Sci. U. S. A. 103, 13848–13853.
DeLong, M.R., Wichmann, T., 2007. Circuits and circuit disorders of the basal ganglia. Arch. Neurol. 64, 20–24.
Di, X., Biswal, B.B.Alzheimer's Disease Neuroimaging, I., 2012. Metabolic brain covariant networks as revealed by FDG-PET with reference to resting-state fMRI networks. Brain Connect 2, 275–283.
Di, X., Gohel, S., Thielcke, A., Wehrl, H.F., Biswal, B.B.Alzheimer's Disease Neuroimaging, I., 2017. Do all roads lead to Rome? A comparison of brain networks derived from inter-subject volumetric and metabolic covariance and moment-to-moment hemodynamic correlations in old individuals. Brain Struct Funct 222, 3833–3845.
Fox, M.D., Snyder, A.Z., Vincent, J.L., Corbetta, M., Van Essen, D.C., Raichle, M.E., 2005. The human brain is intrinsically organized into dynamic, anticorrelated functional networks. Proc. Natl. Acad. Sci. U. S. A. 102, 9673–9678.
Greicius, M.D., Krasnow, B., Reiss, A.L., Menon, V., 2003. Functional connectivity in the resting brain: a network analysis of the default mode hypothesis. Proc. Natl. Acad. Sci. U. S. A. 100, 253–258.
Greicius, M.D., Srivastava, G., Reiss, A.L., Menon, V., 2004. Default-mode network activity distinguishes Alzheimer's disease from healthy aging: evidence from functional MRI. Proc. Natl. Acad. Sci. U. S. A. 101, 4637–4642.
Habas, C., Kamdar, N., Nguyen, D., Prater, K., Beckmann, C.F., Menon, V., Greicius, M.D., 2009. Distinct cerebellar contributions to intrinsic connectivity networks. J. Neurosci. 29, 8586–8594.
Hahn, A., Gryglewski, G., Nics, L., Hienert, M., Rischka, L., Vraka, C., Sigurdardottir, H., Vanicek, T., James, G.M., Seiger, R., Kautzky, A., Silberbauer, L., Wadsak, W., Mitterhauser, M., Hacker, M., Kasper, S., Lanzenberger, R., 2016. Quantification of Task-Specific Glucose Metabolism with Constant Infusion of 18F-FDG. J. Nucl. Med. 57, 1933–1940.
Horwitz, B., Duara, R., Rapoport, S.I., 1984. Intercorrelations of glucose metabolic rates between brain regions: application to healthy males in a state of reduced sensory input. J. Cereb. Blood Flow Metab. 4, 484–499.

Humphries, M.D., Gurney, K., 2008. Network 'small-world-ness': a quantitative method for determining canonical network equivalence. PLoS ONE 3, e2051.
Hutchison, R.M., Hutchison, M., Manning, K.Y., Menon, R.S., Everling, S., 2014. Isoflurane induces dose-dependent alterations in the cortical connectivity profiles and dynamic properties of the brain's functional architecture. Hum. Brain Mapp. 35, 5754–5775.
Hutchison, R.M., Mirsattari, S.M., Jones, C.K., Gati, J.S., Leung, L.S., 2010. Functional networks in the anesthetized rat brain revealed by independent component analysis of resting-state FMRI. J. Neurophysiol. 103, 3398–3406.
Joel, D., Weiner, I., 1994. The organization of the basal ganglia-thalamocortical circuits: open interconnected rather than closed segregated. Neuroscience 63, 363–379.
Jonckers, E., Delgado y Palacios, R., Shah, D., Guglielmetti, C., Verhoye, M., Van der Linden, A., 2014. Different anesthesia regimes modulate the functional connectivity outcome in mice. Magn. Reson. Med. 72, 1103–1112.
Judenhofer, M.S., Wehrl, H.F., Newport, D.F., Catana, C., Siegel, S.B., Becker, M., Thielscher, A., Kneilling, M., Lichy, M.P., Eichner, M., Klingel, K., Reischl, G., Widmaier, S., Rocken, M., Nutt, R.E., Machulla, H.J., Uludag, K., Cherry, S.R., Claussen, C.D., Pichler, B.J., 2008. Simultaneous PET-MRI: a new approach for functional and morphological imaging. Nat. Med. 14, 459–465.
Lanzenberger, R., Kranz, G.S., Haeusler, D., Akimova, E., Savli, M., Hahn, A., Mitterhauser, M., Spindelegger, C., Philippe, C., Fink, M., Wadsak, W., Karanikas, G., Kasper, S., 2012. Prediction of SSRI treatment response in major depression based on serotonin transporter interplay between median raphe nucleus and projection areas. Neuroimage 63, 874–881.
Li, J., Kong, R., Liégeois, R., Orban, C., Tan, Y., Sun, N., Holmes, A.J., Sabuncu, M.R., Ge, T., Yeo, B.T.T., 2019. Global signal regression strengthens association between resting-state functional connectivity and behavior. Neuroimage 196, 126–141.
Liang, Z., King, J., Zhang, N., 2011. Uncovering intrinsic connectional architecture of functional networks in awake rat brain. J. Neurosci. 31, 3776–3783.
Lu, H., Zou, Q., Gu, H., Raichle, M.E., Stein, E.A., Yang, Y., 2012. Rat brains also have a default mode network. Proc. Natl. Acad. Sci. U. S. A. 109, 3979–3984.
Maguire, E.A., 2001. The retrosplenial contribution to human navigation: a review of lesion and neuroimaging findings. Scand. J. Psychol. 42, 225–238.
Majeed, W., Magnuson, M., Hasenkamp, W., Schwarb, H., Schumacher, E.H., Barsalou, L., Keilholz, S.D., 2011. Spatiotemporal dynamics of low frequency BOLD fluctuations in rats and humans. Neuroimage 54, 1140–1150.
Matthew Brett, J.-L.A., Valabregue, Romain, Poline, Jean-Baptiste, 2002. Region of interest analysis using an SPM toolbox. 8th Internation Conference on Functional Mapping of the Human Brain.
Murphy, K., Fox, M.D., 2017. Towards a consensus regarding global signal regression for resting state functional connectivity MRI. Neuroimage 154, 169–173.
Mwansisya, T.E., Hu, A., Li, Y., Chen, X., Wu, G., Huang, X., Lv, D., Li, Z., Liu, C., Xue, Z., Feng, J., Liu, Z., 2017. Task and resting-state fMRI studies in first-episode schizophrenia: a systematic review. Schizophr. Res. 189, 9–18.
Nelson, A.J., Hindley, E.L., Haddon, J.E., Vann, S.D., Aggleton, J.P., 2014. A novel role for the rat retrosplenial cortex in cognitive control. Learn. Mem. 21, 90–97.
Ogawa, S., Lee, T.M., Kay, A.R., Tank, D.W., 1990. Brain magnetic resonance imaging with contrast dependent on blood oxygenation. Proc. Natl. Acad. Sci. U. S. A. 87, 9868–9872.
Onnela, J.-P., Saramäki, J., Kertész, J., Kaski, K., 2005. Intensity and coherence of motifs in weighted complex networks. Phys. Rev. E 71, 065103.
Paasonen, J., Stenroos, P., Salo, R.A., Kiviniemi, V., Gröhn, O., 2018. Functional connectivity under six anesthesia protocols and the awake condition in rat brain. Neuroimage 172, 9–20.
Park, T.Y., Nishida, K.S., Wilson, C.M., Jaiswal, S., Scott, J., Hoy, A.R., Selwyn, R.G., Dardzinski, B.J., Choi, K.H., 2017. Effects of isoflurane anesthesia and intravenous morphine self-administration on regional glucose metabolism ([18F]FDG-PET) of male Sprague-Dawley rats. Eur. J. Neurosci. 45, 922–931.
Passow, S., Specht, K., Adamsen, T.C., Biermann, M., Brekke, N., Craven, A.R., Ersland, L., Gruner, R., Kleven-Madsen, N., Kvernenes, O.H., Schwarzlmuller, T., Olesen, R., Hugdahl, K., 2015a. A close link between metabolic activity and functional connectivity in the resting human brain. EJNMMI Phys 2, A78.
Passow, S., Specht, K., Adamsen, T.C., Biermann, M., Brekke, N., Craven, A.R., Ersland, L., Gruner, R., Kleven-Madsen, N., Kvernenes, O.H., Schwarzlmuller, T., Olesen, R.A., Hugdahl, K., 2015b. Default-mode network functional connectivity is closely related to metabolic activity. Hum. Brain Mapp. 36, 2027–2038.
Price, P., 2001. PET as a potential tool for imaging molecular mechanisms of oncology in man. Trends Mol. Med. 7, 442–446.
Raichle, M.E., MacLeod, A.M., Snyder, A.Z., Powers, W.J., Gusnard, D.A., Shulman, G.L., 2001. A default mode of brain function. Proc. Natl. Acad. Sci. U. S. A. 98, 676–682.
Reichardt, J., Bornholdt, S., 2006. Statistical mechanics of community detection. Phys. Rev. E 74, 016110.
Ripp, I., Stadhouders, T., Savio, A., Goldhardt, O., Cabello, J., Calhoun, V., Riedl, V., Hedderich, D., Diehl-Schmid, J., Grimmer, T., Yakushev, I., 2020. Integrity of neurocognitive networks in dementing disorders as measured with simultaneous PET/fMRI. J. Nucl. Med..
Rischka, L., Gryglewski, G., Pfaff, S., Vanicek, T., Hienert, M., Klobl, M., Hartenbach, M., Haug, A., Wadsak, W., Mitterhauser, M., Hacker, M., Kasper, S., Lanzenberger, R., Hahn, A., 2018. Reduced task durations in functional PET imaging with [(18)F]FDG approaching that of functional MRI. Neuroimage 181, 323–330.
Rubinov, M., Sporns, O., 2010. Complex network measures of brain connectivity: uses and interpretations. Neuroimage 52, 1059–1069.
Sanabria-Diaz, G., Martinez-Montes, E., Melie-Garcia, L.Alzheimer's Disease Neuroimaging, I., 2013. Glucose metabolism during resting state reveals abnormal brain networks organization in the Alzheimer's disease and mild cognitive impairment. PLoS ONE 8, e68860.
Savini, G., Pardini, M., Castellazzi, G., Lascialfari, A., Chard, D., D'Angelo, E., Gandini Wheeler-Kingshott, C.A.M., 2019. Default mode network structural integrity and cerebellar connectivity predict information processing speed deficit in multiple sclerosis. Front. Cell. Neurosci. 13.
Savio, A., Funger, S., Tahmasian, M., Rachakonda, S., Manoliu, A., Sorg, C., Grimmer, T., Calhoun, V., Drzezga, A., Riedl, V., Yakushev, I., 2017. Resting-state networks as simultaneously measured with functional MRI and PET. J. Nucl. Med. 58, 1314–1317.
Schiffer, W.K., Mirrione, M.M., Biegon, A., Alexoff, D.L., Patel, V., Dewey, S.L., 2006. Serial microPET measures of the metabolic reaction to a microdialysis probe implant. J. Neurosci. Methods 155, 272–284.
Seo, E.H., Lee, D.Y., Lee, J.-.M., Park, J.-.S., Sohn, B.K., Lee, D.S., Choe, Y.M., Woo, J.I., 2013a. Whole-brain functional networks in cognitively normal, mild cognitive impairment, and Alzheimer's disease. PLoS ONE 8, e53922.
Seo, E.H., Lee, D.Y., Lee, J.M., Park, J.S., Sohn, B.K., Lee, D.S., Choe, Y.M., Woo, J.I., 2013b. Whole-brain functional networks in cognitively normal, mild cognitive impairment, and Alzheimer's disease. PLoS ONE 8, e53922.
Shang, K., Wang, J., Fan, X., Cui, B., Ma, J., Yang, H., Zhou, Y., Zhao, G., Lu, J., 2018. Clinical Value of Hybrid TOF-PET/MR Imaging–Based Multiparametric Imaging in Localizing Seizure Focus in Patients with MRI-Negative Temporal Lobe Epilepsy. American Journal of Neuroradiology.
Spangler-Bickell, M.G., de Laat, B., Fulton, R., Bormans, G., Nuyts, J., 2016. The effect of isoflurane on 18F-FDG uptake in the rat brain: a fully conscious dynamic PET study using motion compensation. EJNMMI Res. 6, 86.
Sporns, O., 2010. Networks of the Brain. The MIT Press.
Sporns, O., Tononi, G., Kotter, R., 2005. The human connectome: a structural description of the human brain. PLoS Comput. Biol. 1, e42.
Tomasi, D.G., Shokri-Kojori, E., Wiers, C.E., Kim, S.W., Demiral, S.B., Cabrera, E.A., Lindgren, E., Miller, G., Wang, G.J., Volkow, N.D., 2017. Dynamic brain glucose metabolism identifies anti-correlated cortical-cerebellar networks at rest. J. Cereb. Blood Flow Metab. 37, 3659–3670.
Toni, R., Malaguti, A., Benfenati, F., Martini, L., 2004. The human hypothalamus: a morpho-functional perspective. J. Endocrinol. Invest. 27, 73–94.
Tsurugizawa, T., Djemai, B., Zalesky, A., 2019. The impact of fasting on resting state brain networks in mice. Sci. Rep. 9, 2976.
Upadhyay, J., Baker, S.J., Chandran, P., Miller, L., Lee, Y., Marek, G.J., Sakoglu, U., Chin, C.L., Luo, F., Fox, G.B., Day, M., 2011. Default-mode-like network activation in awake rodents. PLoS ONE 6, e27839.
Vann, S.D., Aggleton, J.P., Maguire, E.A., 2009. What does the retrosplenial cortex do? Nat. Rev. Neurosci. 10, 792–802.
Villien, M., Wey, H.-.Y., Mandeville, J.B., Catana, C., Polimeni, J.R., Sander, C.Y., Zürcher, N.R., Chonde, D.B., Fowler, J.S., Rosen, B.R., Hooker, J.M., 2014. Dynamic functional imaging of brain glucose utilization using fPET-FDG. Neuroimage 100, 192–199.
Wehrl, H.F., Hossain, M., Lankes, K., Liu, C.C., Bezrukov, I., Martirosian, P., Schick, F., Reischl, G., Pichler, B.J., 2013. Simultaneous PET-MRI reveals brain function in activated and resting state on metabolic, hemodynamic and multiple temporal scales. Nat. Med. 19, 1184–1189.
Williams, K.A., Magnuson, M., Majeed, W., LaConte, S.M., Peltier, S.J., Hu, X., Keilholz, S.D., 2010. Comparison of α-chloralose, medetomidine and isoflurane anesthesia for functional connectivity mapping in the rat. Magn. Reson. Imaging 28, 995–1003.
Xia, M., Wang, J., He, Y., 2013. BrainNet Viewer: a network visualization tool for human brain connectomics. PLoS ONE 8, e68910.
Yancey, S.E., Rotenberg, D.J., Tam, F., Chiew, M., Ranieri, S., Biswas, L., Anderson, K.J.T., Nicole Baker, S., Wright, G.A., Graham, S.J., 2011. Spin-history artifact during functional MRI: potential for adaptive correction. Med. Phys. 38, 4634–4646.
Zhang, N., Rane, P., Huang, W., Liang, Z., Kennedy, D., Frazier, J.A., King, J., 2010. Mapping resting-state brain networks in conscious animals. J. Neurosci. Methods 189, 186–196.

Supplementary Methods

Radiochemistry

A nuclear reaction using [^{18}O]water (Rotem, Leipzig, Germany) was employed to prepare [^{18}F]fluorine as [^{18}F]fluoride using the PETtrace cyclotron (GE Healthcare, Uppsala, Sweden).

The synthetization of the [^{18}F]FDG tracer was performed using mannose triflate (ABX, Radberg, Germany) in a TRACERlab MX_{FDG} synthesizer (GE Healthcare, Liège, Belgium) as described in previous protocols (Hamacher et al., 1986). After synthetization quality control was performed in accordance to GOP guidelines.

Paxinos brain atlas

The Paxinos brain atlas was used to parcelate the brains for ROI seed-based analysis into 25 bilateral regions, the periaqueaductal gray (PAG) and the septum (Sep), resulting in a total number of 52 brain regions. A list of all regions and their respective abbreviations is provided in Supplementary Table 3.

Supplementary Table 1: Brain regions included in the Paxinos rat brain atlas, including their respective volumes and abbreviations.

Brain region (ROI)	Hemisphere	ROI volume [mm^3]	Position on correlation matrix	Abbreviation
Nucleus Accumbens	left	7.944	1	NAc
	right		2	
Amygdala	left	21.120	3	Amyg
	right		4	
Caudate Putamen	left	43.552	5	CPu
	right		6	
Auditory Cortex	left	27.520	7	Au
	right		8	

Cingulate Cortex	left	14.480	9	Cg
	right		10	
Entorhinal Cortex	left	59.016	11	Ent
	right		12	
Insular Cortex	left	21.128	13	Ins
	right		14	
Medial Prefrontal Cortex	left	6.304	15	mPFC
	right		16	
Motor Cortex	left	32.608	17	M1
	right		18	
Orbitofrontal Cortex	left	18.936	19	OFC
	right		20	
Parietal Cortex	left	7.632	21	PaC
	right		22	
Retrosplenial Cortex	left	18.920	23	RS
	right		24	
Somatosensory Cortex	left	71.600	25	S1
	right		26	
Visual Cortex	left	36.136	27	V1
	right		28	
Anterodorsal Hippocampus	left	25.064	29	CA1
	right		30	
Posterior Hippocampus	left	9.784	31	CA1-p

	right		32	
Hypothalamus	left	18.352	33	Hyp
	right		34	
Olfactory Cortex	left	14.008	35	OC
	right		36	
Superior Colliculus	left	7.136	37	SC
	right		38	
Midbrain	left	11.448	39	MB
	right		40	
Ventral Tegmental Area	left	5.528	41	VTA
	right		42	
Cerebellum – grey matter	left	74.976	43	CG
	right		44	
Cerebellum – white mater	left	23.440	45	CW
	right		46	
Inferior Colliculus	left	5.744	47	IC
	right		48	
Thalamus	left	30.712	49	Th
	right		50	
Periaqueaductal Gray	-	9.904	51	PAG
Septum	-	9.36	52	Sep

Additionally to the whole-brain outputs three large-scale RSNs were selected for further analysis and comparison between [^{18}F]FDG correlations and FC. The DMN, basal ganglia

network and cerebellar-midbrain network comprised the regions listed in Supplementary Table 4.

Supplementary Table 2: Regions included in each of the RSN analyzed including DMN, basal ganglia network and cerebellar-midbrain network.

Default-mode network (DMN)	Basal ganglia network	Cerebellar-midbrain network
Au	NAc	SC
Cg	Amyg	MB
mPFC	CPu	VTA
MC	Ins	CG
OFC	CA1	CW
PaC	CA1-p	IC
RS	Hyp	PAG
S1	Th	
V1		
CA1		
CA1-p		

Seed-based fMRI and [^{18}F]FDG correlation analyses

To compute pair-wise correlation coefficients between the regions defined by the Paxinos rat brain atlas described above the respective regional time-series of the BOLD signal and [^{18}F]FDG activity were derived using the MarsBaR toolbox. Therefore, for each region a mean of the signals of all voxels comprising the respective regions was computed at each time-point:

$$Y_I = \frac{1}{N_I} \sum_{i \epsilon I} y_i \ , \qquad (1)$$

where I is the delineated brain ROI, Y_I its derived time-series, N_I is the number of voxels comprising ROI I and y_i is the time series of voxel i.

Pair-wise connectivity between the 52 different regions was derived by computing Pearson's r correlation coefficients between every pair of regions using an in-house written algorithm:

$$r = \frac{\sum_{i=1}^{n}(u_i - \bar{u})(v_i - \bar{v})}{\sqrt{\sum_{i=1}^{n}(u_i - \bar{u})^2}\sqrt{\sum_{i=1}^{n}(v_i - \bar{v})^2}} \ , \qquad (2)$$

Where r is Pearson's correlation coefficient, n is the number of samples, u_i and v_i are the single samples and $\bar{u}$ and $\bar{v}$ are the arithmetical sample means.

To enable group-level analysis mean correlation matrices were computed by averaging the computed correlation coefficients over all subjects. Therefore, the individual correlation coefficients were first transformed to Fischer's z-scores.

$$Z = \frac{1}{2}\ln\frac{(1+r)}{(1-r)} = \operatorname{arctanh}(r) \ , \qquad (3)$$

The thus derived Z-scores were then averaged over the 30 subjects. The obtained mean z-scores were retransformed to lie in the interval [−1, 1] and displayed as group-mean correlation matrices for both fMRI and [^{18}F]FDG-PET.

On whole-group level three network measures were computed to assess the network properties of the respective outputs.

Modularity is a measure assessing the ability of a network to be divided into groups by minimizing the between-group edges and maximizing the within-group edges. To calculate the modularity Q the modularity script of BCT was employed. The resolution gamma, a user input determining whether the detection of separate modules should yield smaller of larger modules, was kept to the default value of 1. A deterministic algorithm is employed to derive the optimal community structure. Subsequently the maximized modularity is computed (Reichardt and Bornholdt, 2006):

$$Q = \sum_s e_{ss} - (\sum_r e_{rs})^2 \quad , \qquad (4)$$

Where e_{ss} is the fraction of links within the community s, while e_{ss} is the fraction of links between the communities r and s.

The clustering coefficient of each node reflects the fraction of its neighbours that are also neighbours of each other (Onnela et al., 2005). On network level the mean clustering coefficient was computed by averaging the correlation coefficients of the different nodes:

$$\bar{C} = \frac{1}{n}\sum_{i=1}^{n} C_i \quad , \qquad (5)$$

Where $\bar{C}$ is the mean clustering coefficient, n is the number of nodes and C_i is the clustering coefficient of node i.

Finally, the small-world coefficient was computed for each individual network to assess whether the networks exhibited small-world organization. The small-world coefficient is computed based on the clustering coefficient described above and on the characteristic path length of the matrix:

$$\sigma = \frac{\frac{C}{C_r}}{\frac{L}{L_R}} \quad , \qquad (6)$$

Where σ is the small-world coefficient, C the mean clustering coefficient of the graph, C_r the mean clustering coefficient of a randomized graph with the same degree distribution, L the characteristic path length of the graph and L_R the characteristic path length of a randomized graph with the same degree distribution. Therefore, calculating the characteristic path length of each matrix is required. This measure represents the average shortest path length of the network, hence the lowest number of edges required for one node of the matrix to reach another. The characteristic path length is computed using the following formula:

$$L = \frac{1}{n(n-1)} * \sum_{u \neq v} d(n_u, n_v) \quad , \qquad (7)$$

Where L is the characteristic path length, n is the number of nodes in the network and $d(n_u, n_v)$ is the shortest path length between nodes n_u and n_v. To compute the characteristic path length weighted matrices must be converted into distance matrices. To this extent, the Floyd-Marshall algorithm was employed using the Brain Connectivity Toolbox:

$$d(n_u, n_v) = \frac{1}{w(n_u,n_v)} \quad , \tag{8}$$

Where $w(n_u, n_v)$ represents the connection weight of the edge between nodes n_u and n_v.

ICA algorithm and Dice-Sörensen coefficient

ICA was performed using the GIFT toolbox. A binary mask of the Paxinos rat brain atlas was used as a template to derive potential components from the volume contained in the atlas. Further parameters were kept to default values. For additional analysis, all components were transformed to Z-scores using the Z-shift utility in GIFT. The transformed maps of the independent components were then thresholded to Z-scores ≥ 1.96, corresponding to $p \leq 0.05$ (Di et al., 2012).

To determine the spatial overlap between the generated fMRI and [^{18}F]FDG-PET components the Dice-Sörensen coefficient (DSC) was computed pairwise between both datasets.

$$DSC = \frac{2|X \cap Y|}{|X|+|Y|} \quad , \tag{9}$$

Where $|X|$ is the number of voxels in component X, $|Y|$ is the number of voxels in component Y and $|X \cap Y|$ is the number of overlapping voxels between components X and Y.

Significance testing of [^{18}F]FDG correlations and FC

To validate the readout of the study, we compared the readouts of [^{18}F]FDG-PET data and FC including only edges tested for significance on group level ($p \leq 0.05$) using Bonferroni-Holm correction for multiple comparison. Specifically, since the study's main focus was placed upon positive correlations, we applied the Bonferroni-Holm correction method on the positive correlations for both [^{18}F]FDG-PET and BOLD-fMRI FC. To compare the readouts of [^{18}F]FDG-PET and FC Dice-Sörensen coefficients were then computed for the surviving edges at the whole-brain level, as well as for the default-mode, basal ganglia and cerebellar-midbrain network.

Impact of attenuation

To investigate the impact of attenuation on the [^{18}F]FDG-PET readout, we scanned an additional total of 6 male Lewis rats (269 ± 6.4 g) for 60 minutes in an Inveon microPET

(Siemens Healthineers) small animal PET scanner. For each animal, 13-minute transmission scans were acquired after the PET scans using a Co-57 point source for attenuation correction. All scan parameters, including anesthesia (1.3% isoflurane), temperature control of the animals and the amount (30.5 ± 2.8 MBq) and bolus delivery of the [^{18}F]FDG tracer injected matched the parameters used for the PET/fMRI scans. Additionally, we placed the same brain surface MRI coil onto the animals' heads to investigate its effect on the attenuation of the PET data and on the [^{18}F]FDG correlation analysis. We reconstructed all scans in 60 1-minute frames using OSEM 2D, as for the datasets acquired using our simultaneous PET/fMRI system. However, we reconstructed each scan twice, once with and once without applying attenuation (AC) to the reconstruction. Most preprocessing and analysis steps to derive [^{18}F]FDG correlations from the acquired scans were performed for both datasets identically to the procedure described in the main manuscript for the scans acquired using the PET/fMRI system. The only difference between the preprocessing of two datasets was that the scans acquired in the Inveon microPET system were only coregistered and not also spatially normalized to the Schiffer rat brain atlas, due to the lack of an MRI-derived anatomical reference.

Impact of global signal removal

To investigate whether the removal of the global signal from the fMRI data prior to FC calculation had a significant impact on the readout of the present study we employed an alternative method for signal cleaning not involving global signal removal described recently by Chuang et al. (Chuang et al., 2019). Briefly, the first 10 principal components (PCs) of the BOLD time series signal in each rat's extracerebral tissues were extracted using marsbar. Since the global brain BOLD signal fluctuations in do not correspond to any specific brain regions and therefore not likely of neural origin, they can be used as regressors for cleaning the signal of interest, similarly to white matter or cerebral spinal fluid signal in humans. Therefore, we have also added selected PCs of the BOLD signal from tissues outside the brain as described by Chang et al. (Chuang et al., 2019) to the six motion regressors to clean the BOLD signal for each rat. Finally, the BOLD timecourses cleaned using the described method were extracted from each region using marsbar and subject-wise and group-level FC matrices were computed identically to the description in the main text.

Recording of physiological parameters

An additional cohort of healthy male Lewis rats (n = 3) was employed to record physiological parameters under the same condition as the ones reported in the main manuscript. Briefly, anaesthesia was induced at 3% isoflurane and then reduced to 2% for 10 minutes to simulate the preparation steps prior to the scan. Afterwards, the animals were placed onto the dedicated small-animal bed and the isoflurane was further reduced to 1.3%. The temperature was maintained at 36.5° C using a rectal probe and a feedback-controlled system and physiological parameters were recorded by attaching a pulse oximeter (SA Instruments, Stony Brook, NY, USA) onto the hindpaw. Heart rates, respiration rates and peripheral blood oxygenation levels (SpO_2) were recorded over a period of 60 minutes and documented at 5-minute intervals.

Effect of anaesthesia on brain metabolism

Potential effects of the anaesthesia on [^{18}F]FDG uptakes in different regions of the brain were investigated by performing a comparison to literature data reporting [^{18}F]FDG uptakes in the rat brain both under isoflurane and in the awake condition (Spangler-Bickell et al., 2016). Specifically, the mentioned study indicated differing uptake distributions across the brain by computing whole-brain normalized values for the cortex, striatum, cerebellum, diencephalon, inferior colliculi and vestibular nuclei for anaesthetised and awake animals. The values were calculated over the period 38-75 minutes after bolus injection. Here, the analysis was replicated over the period 38-60 minutes, since only 60-minute long scans were performed for the regions mentioned above with the exception of the vestibular nuclei due to the unavailability of a respective ROI.

Supplementary Results and Discussion

Blood glucose levels

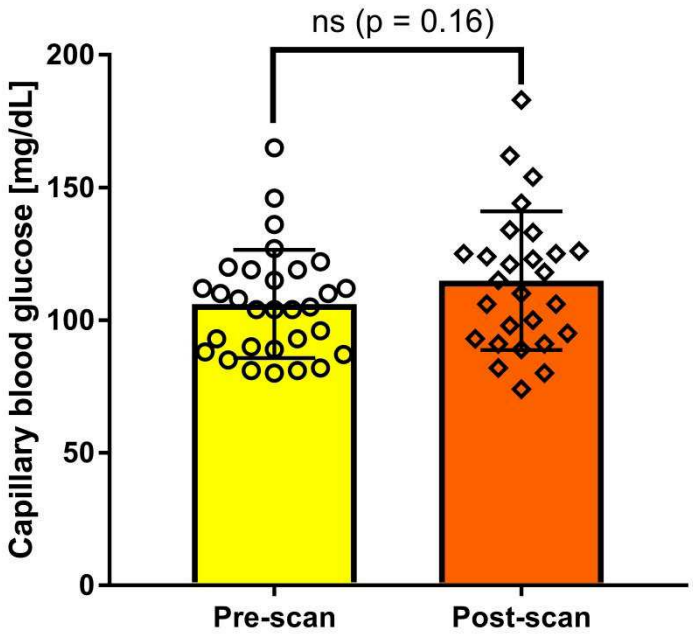

Supplementary Figure 1: Capillary blood glucose levels of the scanned rats before and after the scan (n=30). No significant difference could be found between the two measurements (ns stands for non-significant).

Seed-based connectivity

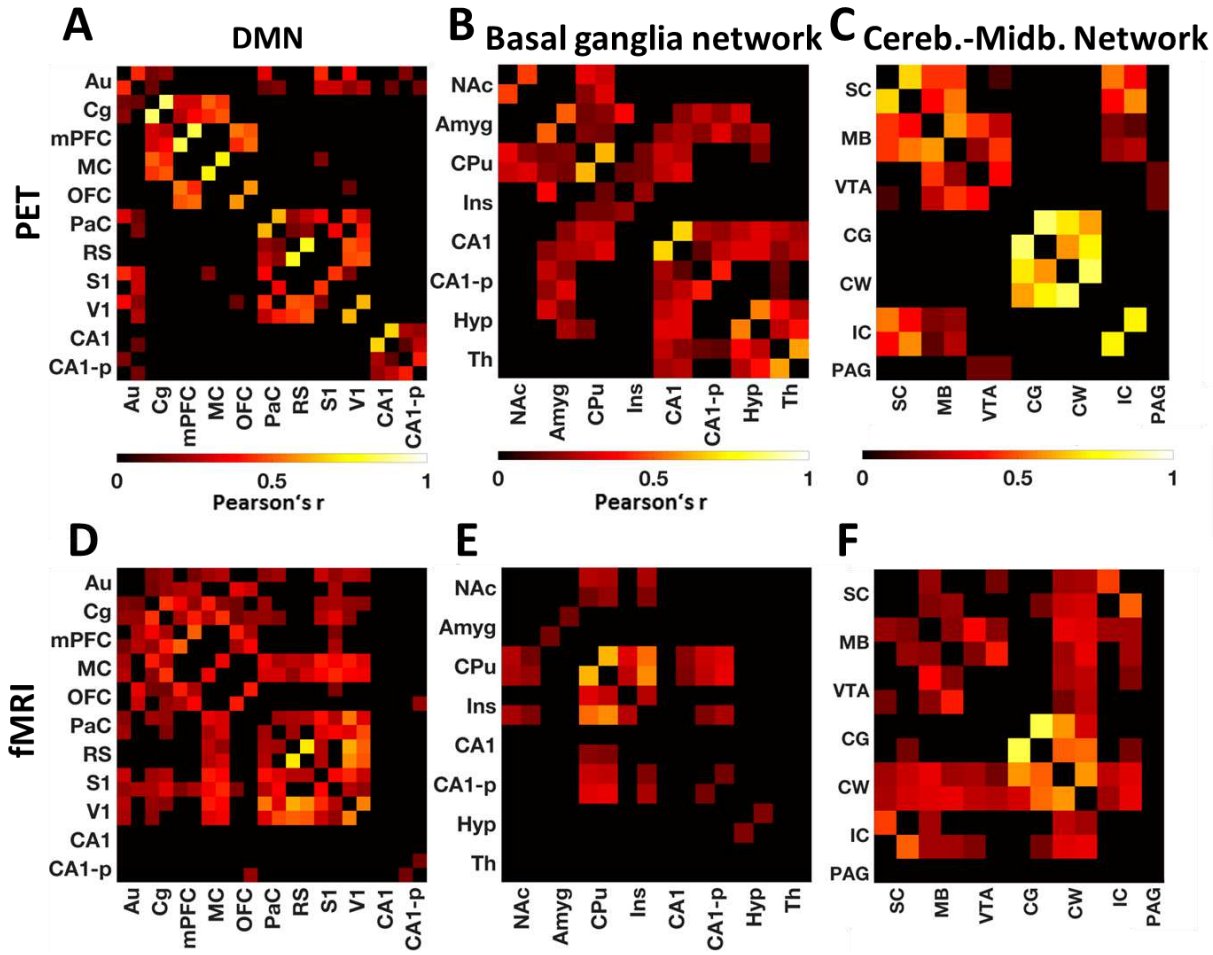

Supplementary Figure 2: FC and [^{18}F]FDG correlations for three RSNs. (A) PET-derived correlations in the DMN. **(B)** PET-derived correlations in the basal ganglia network. **(C)** PET-derived correlations in the cerebellar-midbrain network. **(D)** fMRI-derived FC in the DMN. **(E)** fMRI-derived FC in the basal ganglia network. **(F)** fMRI-derived FC in the cerebellar-midbrain network.

ICA

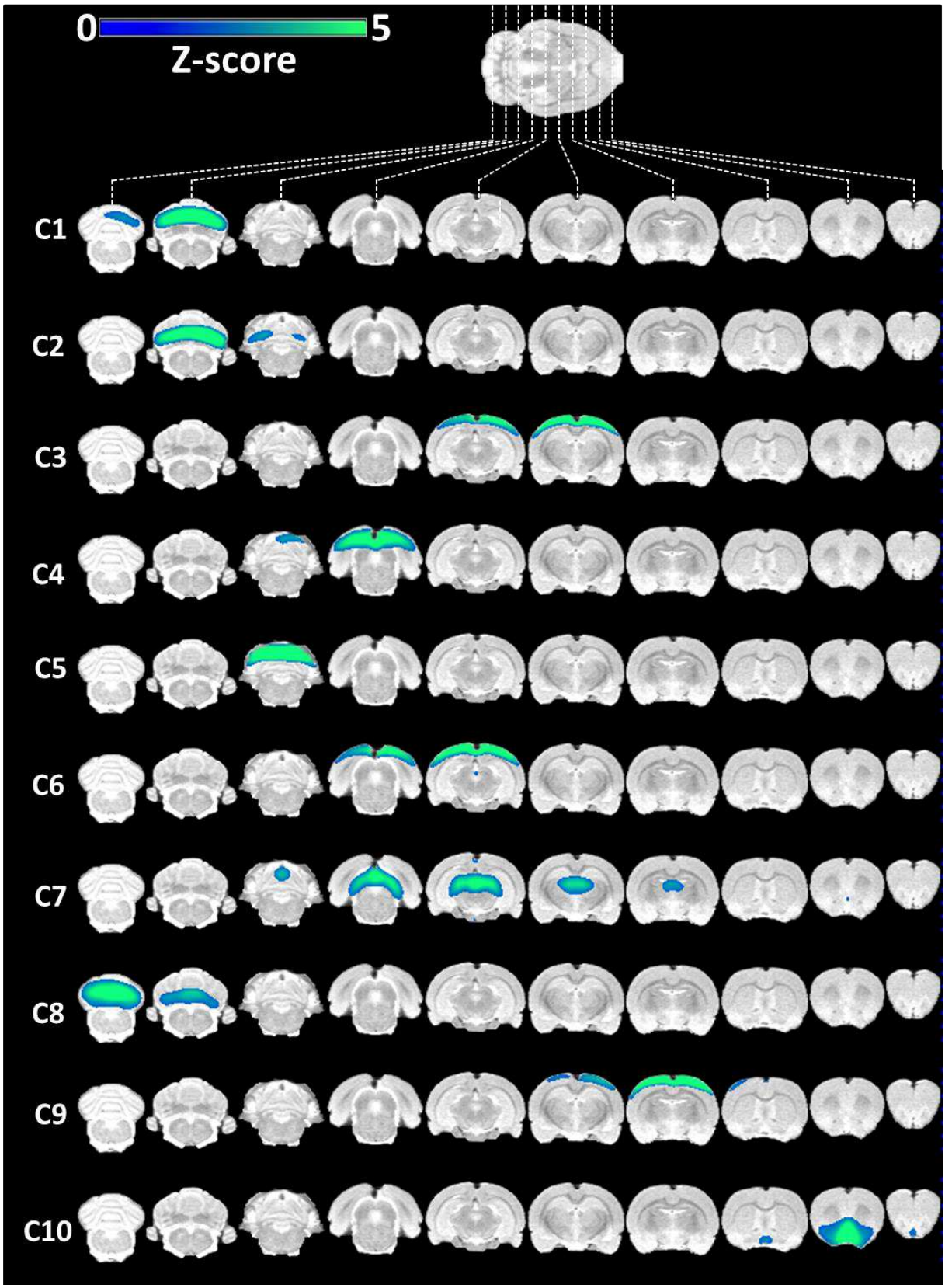

Supplementary Figure 3: Components 1-10 derived from the BOLD-fMRI dataset (thresholded at Z ≥ 1.96).

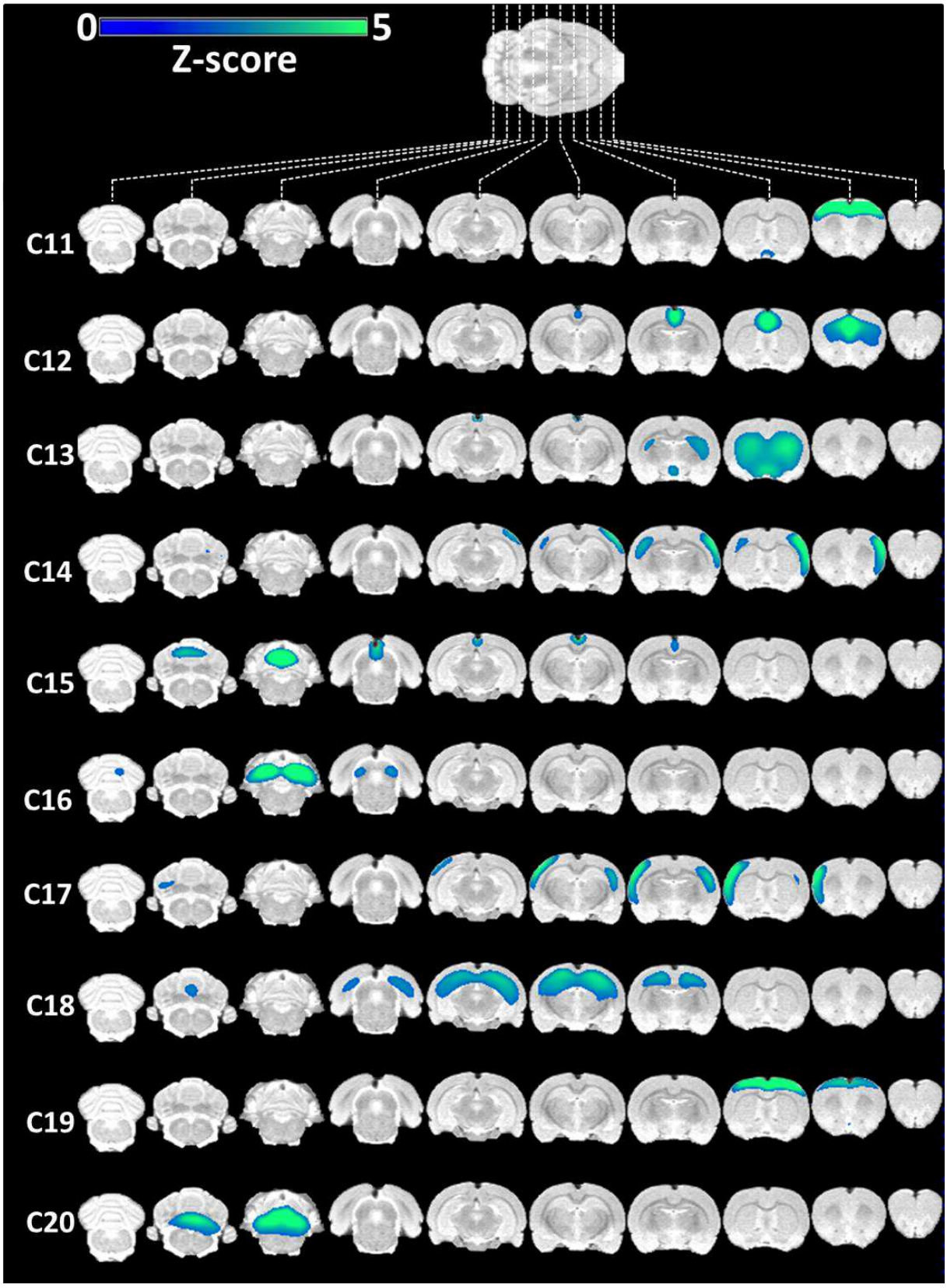

Supplementary Figure 4: Components 11-20 derived from the BOLD-fMRI dataset (thresholded at Z ≥ 1.96).

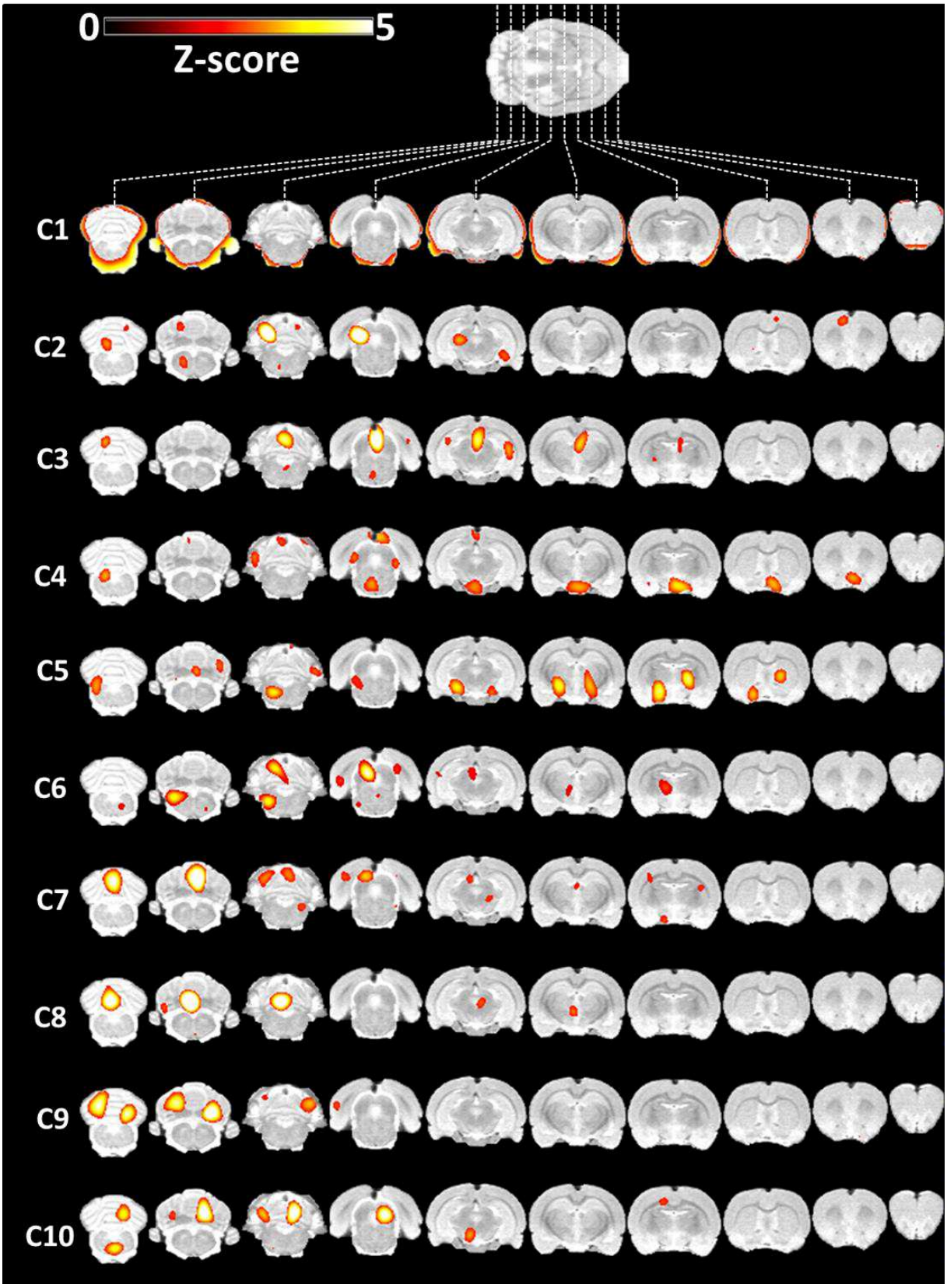

Supplementary Figure 5: Components 1-10 derived from the [^{18}F]FDG-PET dataset (thresholded at Z ≥ 1.96).

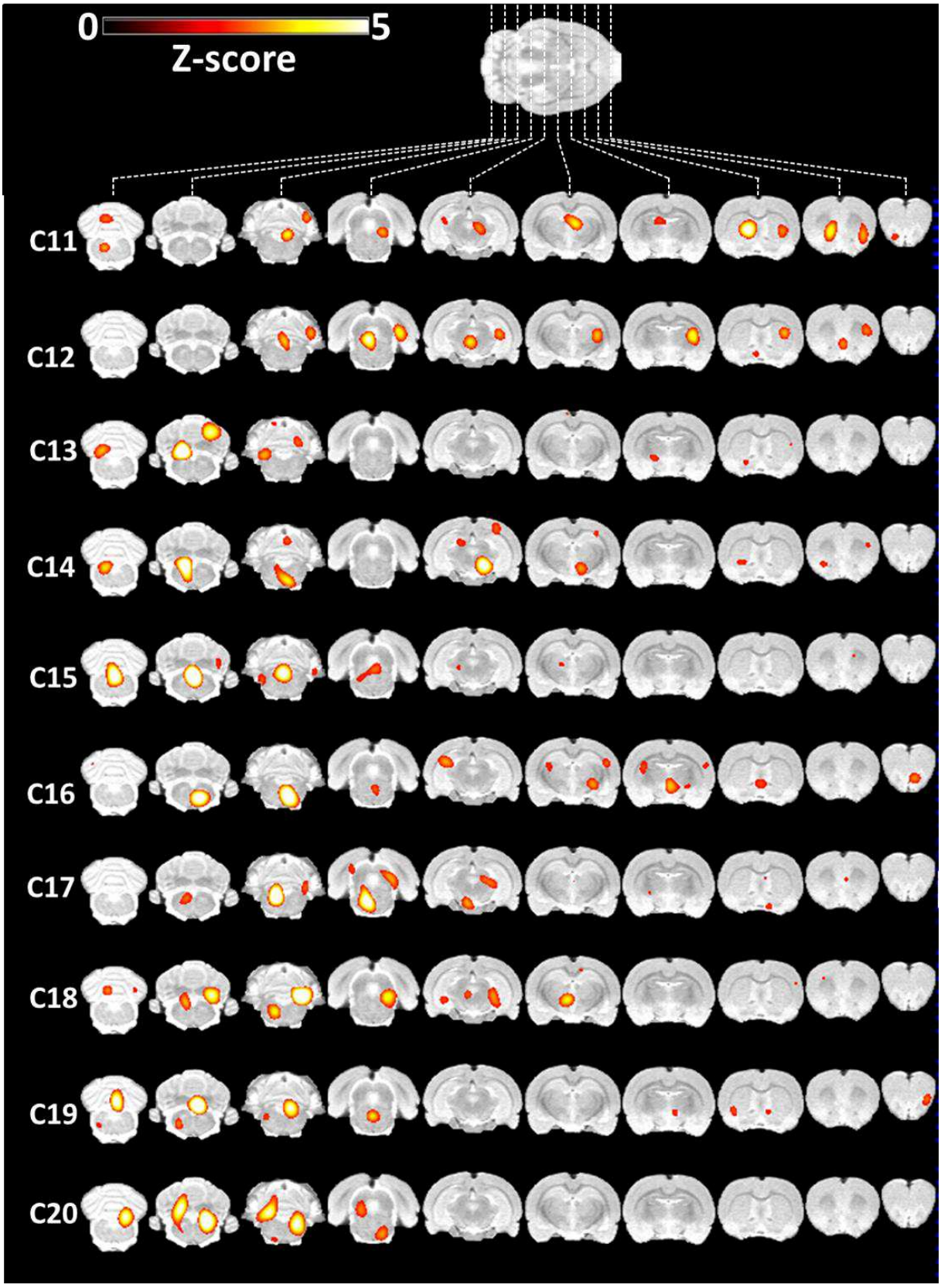

Supplementary Figure 6: Components 11-20 derived from the [^{18}F]FDG-PET dataset (thresholded at Z ≥ 1.96).

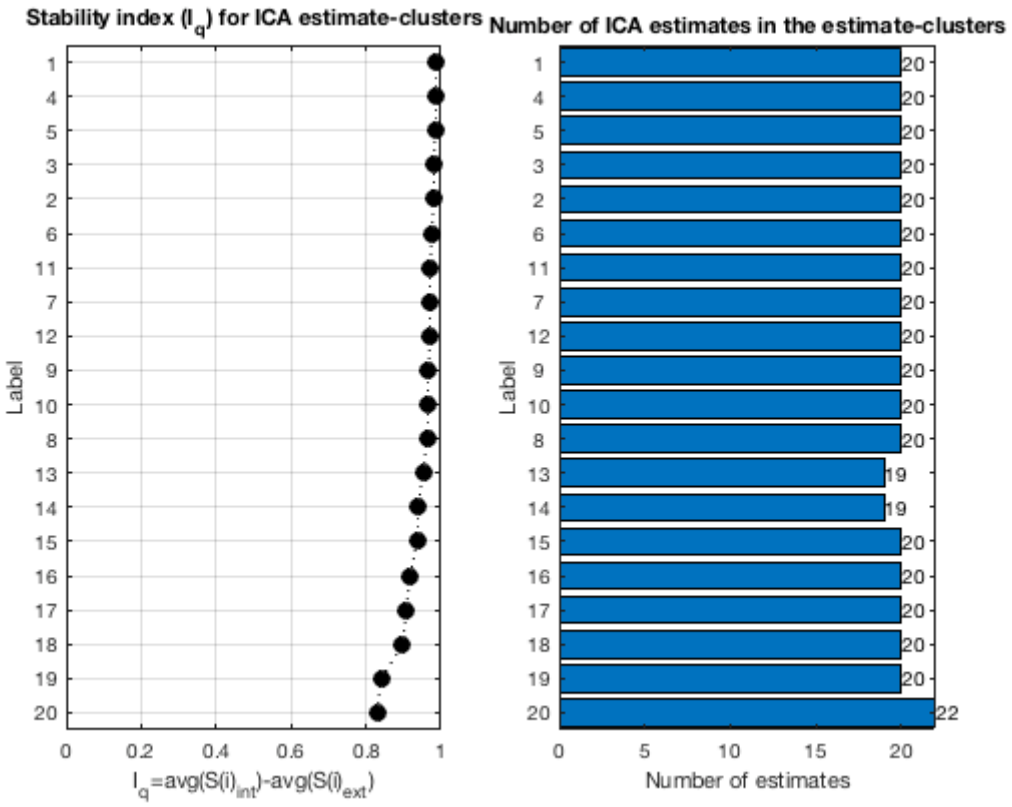

Supplementary Figure 7: ICASSO results for the stability of the [^{18}F]FDG-PET-derived independent components.

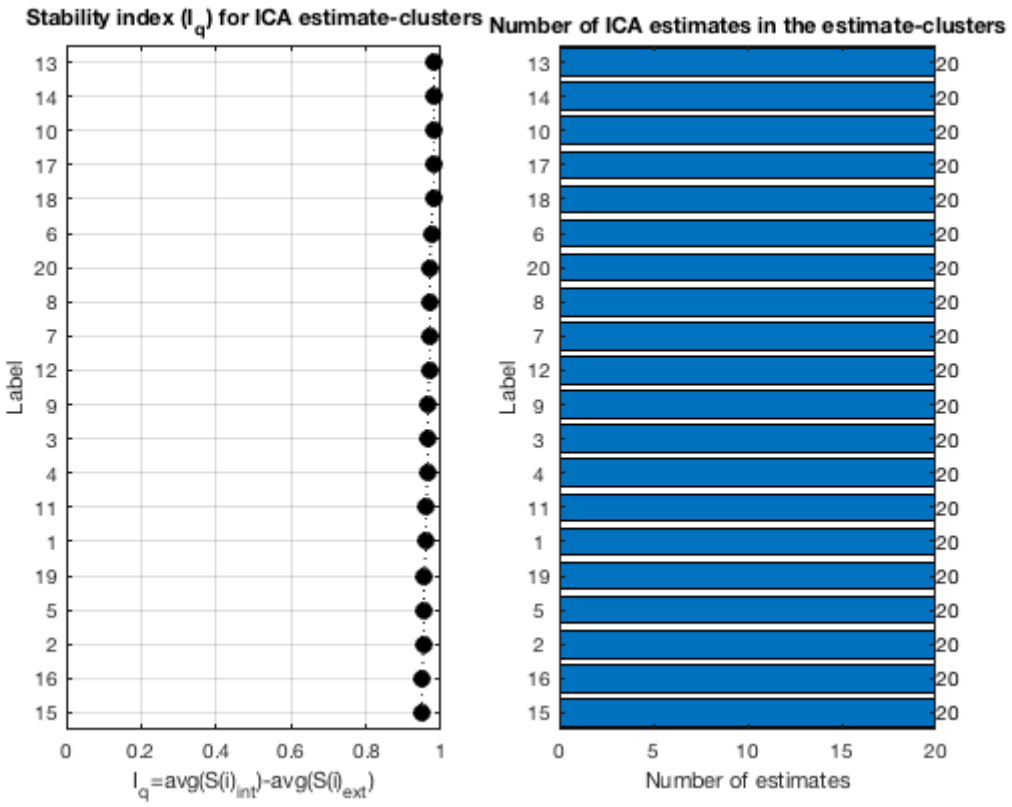

Supplementary Figure 8: ICASSO results for the stability of the BOLD-fMRI-derived independent components.

Significance testing of [^{18}F]FDG correlations and FC

Matrices containing only significant edges ($p \leq 0.05$, Bonferroni-Holm correction) are depicted in Supplementary Figure 9 on whole brain and network level.

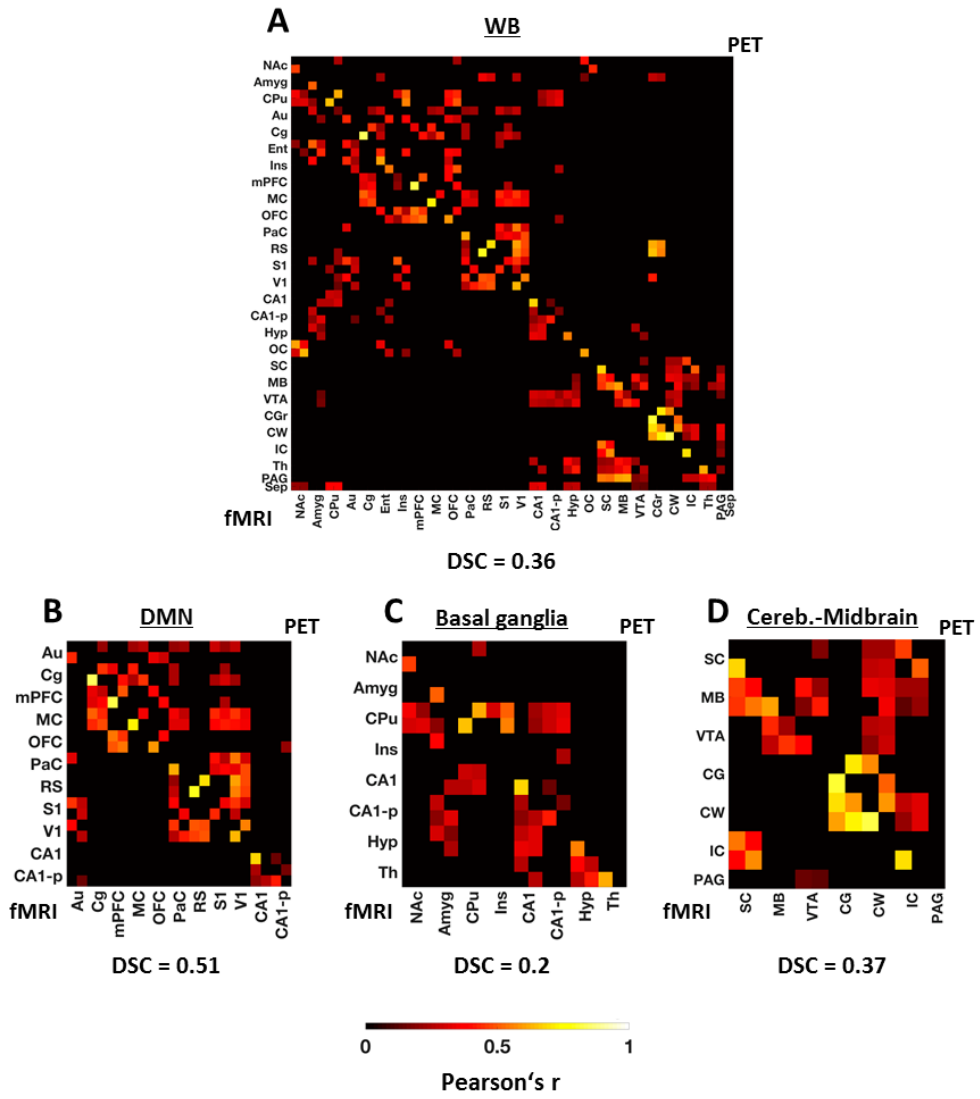

Supplementary Figure 9: Second-level t-tested group-mean [^{18}F]FDG correlations and FC on whole-brain and for the default-mode, basal ganglia and cerebellar-midbrain network. (A) Group-mean fMRI and [^{18}F]FDG PET-derived whole-brain correlation matrices. Each edge was tested for significance ($p \leq 0.05$, Bonferroni-Holm correction). **(B)** Group-mean fMRI and [^{18}F]FDG PET-derived DMN correlation matrices. Each edge was tested for significance ($p \leq 0.05$, Bonferroni-Holm correction). **(C)** Group-mean fMRI and [^{18}F]FDG PET-derived basal ganglia network correlation matrices. Each edge was tested for significance ($p \leq 0.05$, Bonferroni-Holm correction). **(D)** Group-mean fMRI and [^{18}F]FDG PET-derived cerebellar-midbrain network correlation matrices. Each edge was tested for significance ($p \leq 0.05$, Bonferroni-Holm correction). Abbreviations: WB = whole brain; fMRI = functional magnetic resonance imaging; PET = positron emission tomography; DSC = Dice-Sörensen coefficient; DMN = default-mode network; Cereb-Midbrain = Cerebellar-Midbrain network. For a list of abbrevations of the regions please refer to **Supplementary Table 3**.

Out of the 557 single positive FC edges and 584 available positive [^{18}F]FDG correlations 194 FC edges and 146 [^{18}F]FDG correlations survived significance testing and correction for multiple comparisons using the Bonferroni-Holm method at a $p \leq 0.05$. The Dice-Sörensen

coefficient for the surviving edges was 0.36. The areas of overlap were largely comparable to the overlap between the two readouts at the 20% sparsity threshold reported in the main manuscript. Specifically, for the DMN, a DSC of 0.51 was computed between the Bonferroni-Holm-corrected significant edges with the most extensive overlap occurring within the posterior and anterior clusters of the DMN. For the basal ganglia network, the DSC of 0.2 is comparable with the DSC computed for the overlap of the ICA components. The majority of common edges involved the CPu, confirming the observation enabled by both the ICA basal ganglia component and the 20% sparsity-thresholded matrices. Finally, cerebellar-midbrain network's DSC was 0.37 with overlaps occurring for connections between midbrain regions on one hand and within the cerebellum on the other hand. Edges between midbrain areas and cerebellar areas survived for [^{18}F]FDG-PET but not for FC, in line with the findings of the 20% sparsity readouts and of the ICA.

Impact of attenuation correction

Since we are currently developing an attenuation correction algorithm for PET/fMRI, no attenuation correction was included in the reconstruction of the PET data in our study. However, we postulated that due to the small dimensions of the rat brain compared to the human brain, corroborated with the nature of the analysis investigating temporal pairwise correlations of regional [^{18}F]FDG uptakes, the lack of attenuation correction would have a negligible impact on the readout of our study. To test this hypothesis, we scanned a total of 6 rats in a dedicated small-animal PET scanner and performed pairwise [^{18}F]FDG correlation analysis with and without the inclusion of AC for the reconstruction of the PET data.

In Supplementary Figure 10A the two mean correlation matrices derived with and without attenuation correction are depicted. The difference between the outputs was quantified by subtracting all values computed without AC from those calculated with the inclusion of AC (Supplementary Figure 10B).

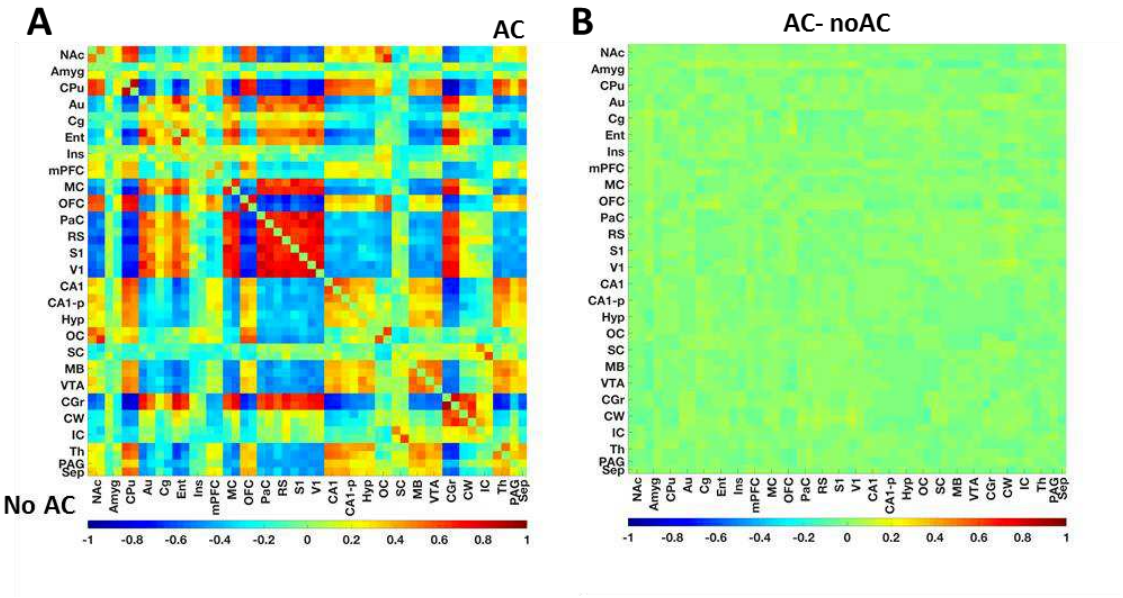

Supplementary Figure 10: Impact of attenuation correction on [^{18}F]FDG correlation readout. (A) Whole-brain pair-wise mean [^{18}F]FDG correlation matrices evaluated for the same dataset reconstructed with (values above diagonal) and without (values below diagonal) attenuation correction. **(B)** Difference between the two readouts computed by subtraction of the two outputs. (n = 6)

The average difference between the two readouts was r = 0.0001, while the maximum difference between two correlation coefficients was r = 0.1. No pairwise correlation was significantly different between the readouts with and without attenuation correction ($p \leq 0.05$, Bonferroni-Holm corrected).

Impact of global signal removal

To investigate the impact of the performed global signal removal on the output and the findings of the study, we repeated the analysis using a different preprocessing pipeline for the fMRI dataset that did not involve global signal removal. The FC computed without global signal removal using the nuisance regression method described by Chuang et al. (Chuang et al., 2019) and its overlap with [^{18}F]FDG correlations in comparison to the overlap between FC and [^{18}F]FDG correlations including global signal removal are presented in Supplementary Figure 11.

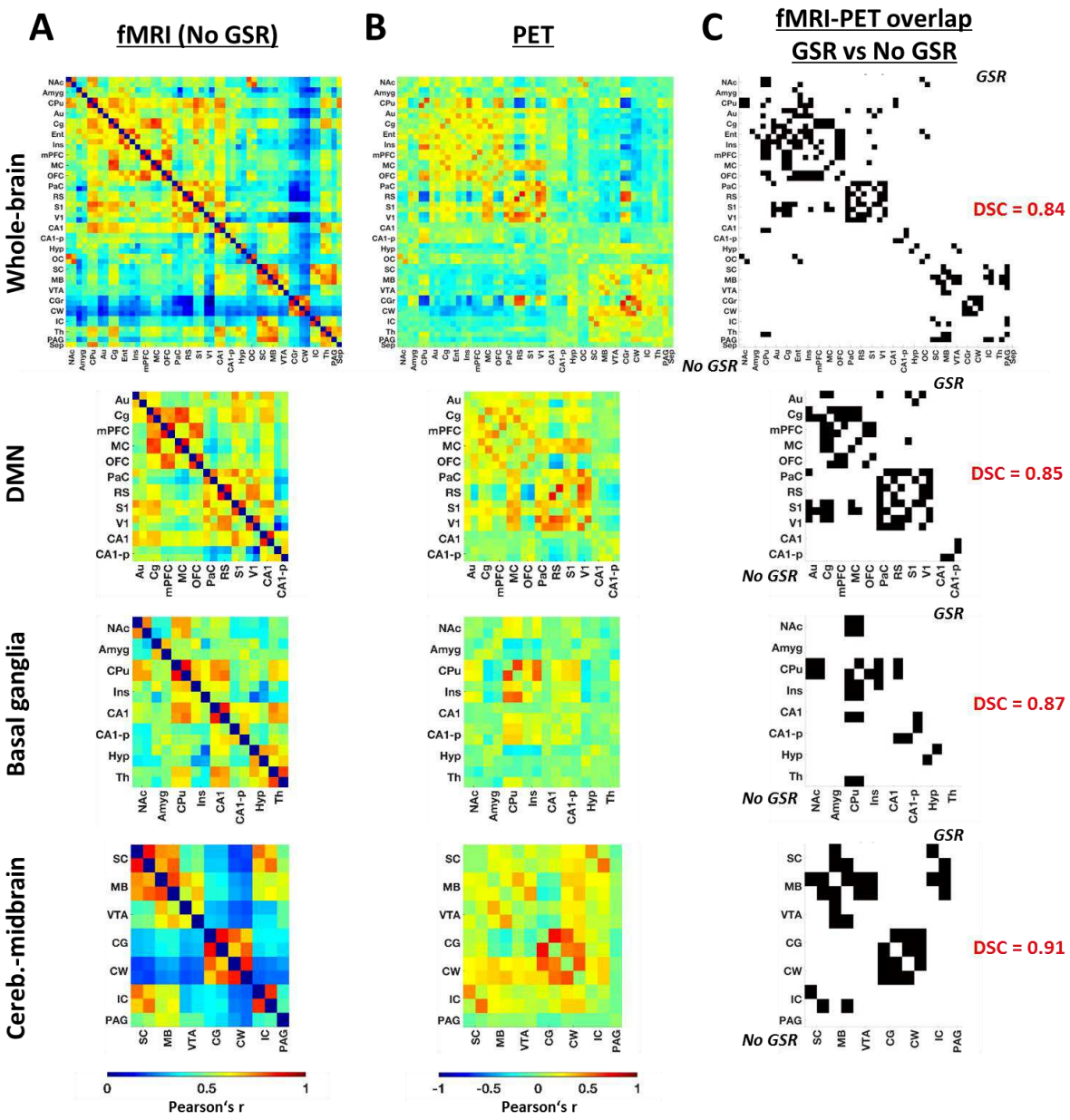

Supplementary Figure 11: Comparison of overlap between fMRI and [^{18}F]FDG correlations with and without global signal removal. (A) Functional connectivity matrices obtained from the fMRI data without using global signal removal on whole-brain level and for the default-mode, basal ganglia and cerebellar-midbrain networks. **(B)** [^{18}F]FDG correlation matrices on whole-brain level and for the default-mode, basal ganglia and cerebellar-midbrain networks. **(C)** Comparison of overlaps at whole-brain and network level between FC and [^{18}F]FDG correlations at a 20% sparsity threshold without global signal removal (halves of the matrices under diagonals) and with global signal removal (halves of matrices above diagonals). Overlapping [^{18}F]FDG connectivity – BOLD-fMRI FC edges are indicated in black. Dice-Sörensen coefficients were computed to indicate the extent to which the overlaps between [^{18}F]FDG correlations and FC match for the two preprocessing approaches. Abbreviations: FC = fMRI-derived functional connectivity; GSR = global signal removal, DMN = defalt-mode network. For a list of abbreviations of the different regions please refer to **Supplementary Table 3**.

We found very similar FC patterns computed without the removal of global signal (Supplementary Figure 11A) compared to the FC acquired using global signal removal (Figure 1). To quantify whether the overlap with the [^{18}F]FDG-PET readout (Supplementary Figure 11B) drastically changes when the global signal is not removed we applied the same 20% sparsity threshold as for the GSR data. The overlap patterns between FC and [^{18}F]FDG-PET connectivity were very similar between the two procedures on whole-brain level and for each of the three investigated networks (Supplementary Figure 11C). We quantified the similarity of the overlaps using DSC and obtained high values of 0.84 on whole-brain level, 0.85 in the DMN, 0.87 in the basal ganglia network and 0.91 in the cerebellar-midbrain network. Conclusively, we showed that removing the global signal from the fMRI data only had a minor impact on the readout obtained in this study.

Recording of physiological parameters

The results of the physiological recordings in an additional cohort under the same experimental conditions are presented in Supplementary Figure 12.

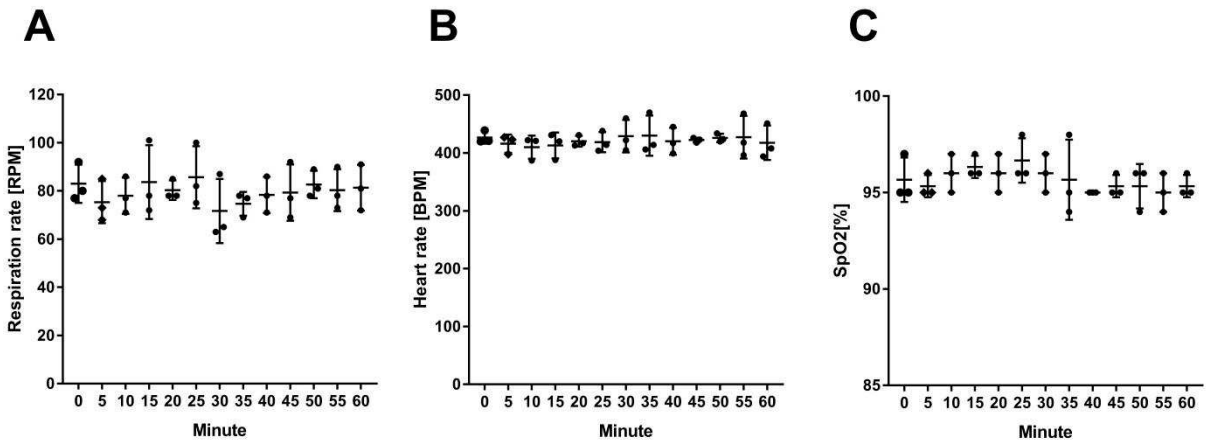

Supplementary Figure 12: Recording of physiological parameters using pulse oximetry in an additional cohort (n = 3): (A) Respiration rates, **(B)** Heart rates, **(C)** SpO_2 levels.

Respiration rates remained largely constant, the mean values recorded at all time-points ranging between 70 and 90 respirations per minute (rpm) with an average of 79.6 ± 8.7 rpm over all animals and time-points. Major outliers were sparse, including a single value above 100 rpm (101 rpm) for one animal and no value beneath 60 rpm. Similarly, heart rates remained largely constant between animals and over the 60 minutes of the scans, averaging 421.3 ± 19.2 respirations per minute (rpm). Moreover, the average values recorded over all time-points remained within a narrow margin between 410 and 430 rpm. Slightly lower

values were recorded for one animal, with heart rates lower than 400 rpm at six time-points; however, not lower than 388 rpm. A further animal had slightly increased heart rates between 460 and 470 bpm at three time-points. Finally, peripheral SpO_2 values were constant as well and remained at normal physiological levels over the courses of the scans. The average SpO_2 level over all animals and timepoints was 95.7 ± 1%. At all timepoints, SpO_2 remained on average above the 95% level. Between animals, oxygenation levels were also comparable for most time-points, only being reduced to 94% for one animal at one time-point and for a further animal at two time-points.

Taken together, our results indicate stable physiology was maintained over the course of the scans and between animals, replicating previous findings at low isoflurane levels (1.15-1.25%) in spontaneously breathing rats (Sicard and Duong, 2005), indicating normoxia (97%) at 21% O_2.

Effect of anaesthesia on brain metabolism

The time-activity curves and a comparison between whole-brain normalized [^{18}F]FDG uptake values and similar data reported previously (Spangler-Bickell et al., 2016) for specific regions is presented in Supplementary Figure 13.

A

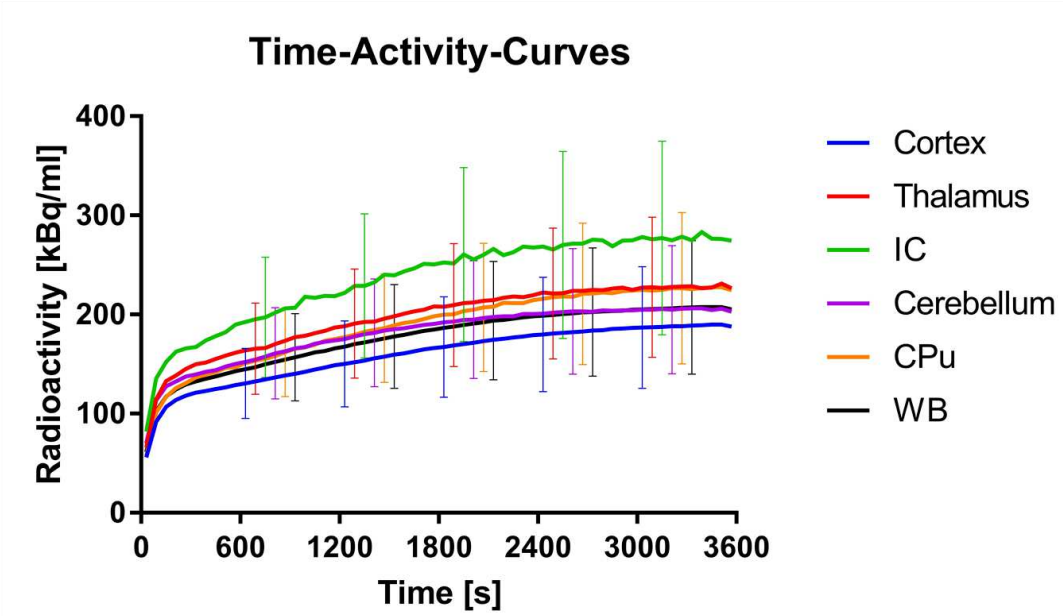

B

Region	Normalized to WB (frame 38-60)	Spangler-Bickell EJNMMI-Res. 2016 unconscious (frame 38-75)	Spangler-Bickell EJNMMI-Res. 2016 conscious (frame 38-75)
Cortex	0.91	0.90	1.06
Thalamus	1.10	1.10	1.22
Inf. Colliculi	1.33	1.20	1.26
Cerebellum	1.00	1.05	1.00
Caudate Putamen	1.08	1.12	1.15

Supplementary Figure 13: Effect of isoflurane anaesthesia on [^{18}F]FDG uptake. (A) Average time activity curves for the cortex, thalamus, inferior colliculi, cerebellum, caudate putamen and whole-brain including standard deviations at different experimental time-points. **(B)** Average whole-brain normalized uptake values for the regions in (A) compared to literature values for rats anesthetized with isoflurane and in awake condition computed between minute 38 and the respective ends of the scans (n = 30). Abbreviations: TACs = time-activity curves, IC = inferior colliculi, CPu = caudate putamen, WB = whole brain.

The most prominent difference in [^{18}F]FDG uptake reported by Spangler-Bickell et al. was found for the cortex. Specifically, cortical uptake was found to be lower than the whole-brain average for unconscious animals (0.9) and higher for conscious animals (1.06). The average cortical uptake value of 0.91 in the present cohort was in line with the data reported for unconscious animals by Spangler-Bickell et al. The other regional uptake values were also comparable with the data of Spangler-Bickell, however differences between the conscious and unconscious states were lower in other areas compared to the cortex. The normalized uptake

in the thalamus was however similar to the cortex in line with the value indicated by Spangler-Bickell et al. in unconscious animals (1.10 for both studies) and lower compared to conscious rats (1.22). Similar data regarding the decrease in thalamic and cortical [^{18}F]FDG uptake was reported by Park et al. (Park et al., 2017).

Taken together, the [^{18}F]FDG uptake in the present study is in line with the uptake patterns associated with the unconscious state in previous reports (Park et al., 2017; Spangler-Bickell et al., 2016). While the differences reported between the conscious and unconscious states regarding [^{18}F]FDG uptake may also influence the [^{18}F]FDG correlation analysis, the exact implications on the resting-state architecture described here cannot be elucidated based on the present data. Nonetheless, although awake animal studies are becoming more widespread and are undoubtedly of interest for certain experimental questions, anesthesia will remain a prerequisite for different types of studies, such as pharmacological or stimulus-evoked fMRI. Therefore, the [^{18}F]FDG correlation architecture described here is of major interest for future preclinical research. Potential differences to the awake state or under different anesthesia conditions remain to be elucidated by future studies.

2.2 Striatal and Prefrontal D2R and SERT Distributions Contrastingly Correlate with Default-Mode Connectivity

The article included in this chapter was published in (Ionescu et al., 2021a):

NeuroImage, Volume 243, 2021, 118501, ISSN 1053-8119
https://doi.org/10.1016/j.neuroimage.2021.118501.
"Striatal and prefrontal D2R and SERT distributions contrastingly correlate with default-mode connectivity"
Tudor M. Ionescu, Mario Amend, Rakibul Hafiz, Bharat B. Biswal, Andreas Maurer, Bernd J. Pichler, Hans F. Wehrl, Kristina Herfert

NeuroImage 243 (2021) 118501

Contents lists available at ScienceDirect

NeuroImage

journal homepage: www.elsevier.com/locate/neuroimage

Striatal and prefrontal D2R and SERT distributions contrastingly correlate with default-mode connectivity

Tudor M. Ionescu[a], Mario Amend[a], Rakibul Hafiz[b], Bharat B. Biswal[b], Andreas Maurer[a], Bernd J. Pichler[a], Hans F. Wehrl[a,1], Kristina Herfert[a,1,*]

[a] Werner Siemens Imaging Center, Department of Preclinical Imaging and Radiopharmacy, Eberhard Karls University Tuebingen, Tuebingen, Germany
[b] Department of Biomedical Engineering, New Jersey Institute of Technology, University Heights, Newark, NJ, USA

ARTICLE INFO

Keywords:
Resting-state functional connectivity
Monoamines
D2 receptor
Serotonin transporter
Simultaneous PET/fMRI

ABSTRACT

Although brain research has taken important strides in recent decades, the interaction and coupling of its different physiological levels is still not elucidated. Specifically, the molecular substrates of resting-state functional connectivity (rs-FC) remain poorly understood. The aim of this study was elucidating interactions between dopamine D2 receptors (D2R) and serotonin transporter (SERT) availabilities in the striatum (CPu) and medial prefrontal cortex (mPFC), two of the main dopaminergic and serotonergic projection areas, and the default-mode network. Additionally, we delineated its interaction with two other prominent resting-state networks (RSNs), the salience network (SN) and the sensorimotor network (SMN).

To this extent, we performed simultaneous PET/fMRI scans in a total of 59 healthy rats using [^{11}C]raclopride and [^{11}C]DASB, two tracers used to image quantify D2R and SERT respectively. Edge, node and network-level rs-FC metrics were calculated for each subject and potential correlations with binding potentials (BP_{ND}) in the CPu and mPFC were evaluated.

We found widespread negative associations between CPu D2R availability and all the RSNs investigated, consistent with the postulated role of the indirect basal ganglia pathway. Correlations between D2Rs in the mPFC were weaker and largely restricted to DMN connectivity. Strikingly, medial prefrontal SERT correlated both positively with anterior DMN rs-FC and negatively with rs-FC between and within the SN, SMN and the posterior DMN, underlining the complex role of serotonergic neurotransmission in this region.

Here we show direct relationships between rs-FC and molecular properties of the brain as assessed by simultaneous PET/fMRI in healthy rodents. The findings in the present study contribute to the basic understanding of rs-FC by revealing associations between inter-subject variances of rs-FC and receptor and transporter availabilities. Additionally, since current therapeutic strategies typically target neurotransmitter systems with the aim of normalizing brain function, delineating associations between molecular and network-level brain properties is essential and may enhance the understanding of neuropathologies and support future drug development.

1. Introduction

Resting-state functional connectivity (rs-FC) derived from functional magnetic resonance imaging (fMRI) studies has emerged as a promising biomarker to assess brain function and dysfunction over the last two decades (Biswal et al., 1995). While rs-FC has already been proven to be a valuable tool for the basic understanding of brain pathology (Badhwar et al., 2017), there are still many unresolved aspects regarding its emergence and modulation. One important, still not elucidated question is the modulatory role of neurotransmitters and receptors on rs-FC. In most studies, pharmacological MRI (ph-MRI) has been used to investigate the impact of neurotransmitters on rs-FC (Kelly et al., 2009; Cole et al., 2013). However, its output reflects the active pharmacological manipulation of the entire brain rather than the effects of intrinsic regional dependencies between neurotransmitter signaling and rs-FC. To this extent, PET/fMRI studies are a powerful approach to investigate brain network modulation by different neurotransmitter systems (Roffman et al., 2016; McCutcheon et al., 2019; Vidal et al., 2018; Hahn et al., 2012; Nagano-Saito et al., 2017). However, only a few studies have employed simultaneous PET/fMRI, a prerequisite for an accurate temporal and spatial cross-correlation (Roffman et al., 2016; Vidal et al., 2018).

* Corresponding author.
E-mail address: kristina.herfert@med.uni-tuebingen.de (K. Herfert).
[1] These authors are contribute equally to this work

https://doi.org/10.1016/j.neuroimage.2021.118501.
Received 12 May 2021; Received in revised form 23 July 2021; Accepted 20 August 2021
Available online 22 August 2021.

Here, we present a simultaneous PET/fMRI study in rats to delineate the relations between regional D2 receptor (D2R) and serotonin transporter (SERT) availabilities studied with PET and resting-state networks (RSNs) acquired by fMRI. Recently, Conio et al. revealed opposing roles of dopamine (DA) and serotonin (5-HT) on three human RSNs: the default-mode network (DMN), postulated to be involved in functions such as self-reference, memory formation and imagination (Andrews-Hanna, 2012), the sensorimotor network (SMN), regulating sensory processing (Göttlich et al., 2013) and the salience network (SN), playing important roles in salience attribution and reward and being assumed to mediate the interplay between the DMN and task-positive networks such as the SMN (Seeley, 2019; Seeley et al., 2007).

In the study by Conio et al., the authors investigated the effects of monoaminergic synthesis in the raphé nuclei and substantia nigra on the mentioned RSNs (Conio et al., 2019). Here, we selected the same three RSNs for investigation in our study, focusing on the DMN, due to its prominent role in different pathologies (Badhwar et al., 2017, Göttlich et al., 2013, Yan et al., 2019). However, in contrast to the paper by Conio et al., we aimed to elucidate the correlations of D2R and SERT distributions in the caudate putamen (CPu) and medial prefrontal cortex (mPFC), two of the most prominent dopaminergic and serotonergic projection areas. Our preclinical data acquired using uniform cohorts regarding age, strain, gender, nutrition, and living conditions are likely to reflect correlations driven by intrinsic differences between individual subjects. We chose to focus on DA and 5-HT due to their modulatory role in several important brain functions, including motor control, motivation, mood, and emotion and thus their involvement in different neurodegenerative and psychiatric diseases such as Parkinson's disease (PD) and major depressive disorder (MDD) (Conio et al., 2019; Bhagwagar et al., 2018; Roussakis et al., 2016). Insight into the intrinsic correlations of D2R and SERT with rs-FC may improve therapy and drug development for such pathologies.

2. Materials and methods

2.1. Animals

Male Lewis rats (n = 59) provided by Charles River Laboratories (Sulzfeld, Germany) were divided into two cohorts for [^{11}C]raclopride (365 ± 49 g, n = 29) and [^{11}C]DASB (354 ± 37 g, n = 30, see *Supplementary Fig. 1* for the rat weights). These weights corresponded to ages of approximately 15 weeks. The rats were kept on a 12-h day-night cycle at a room temperature of 22 °C and 40–60% humidity and received standard chow food and water *ad-libitum*. All experiments were conducted according to the German federal regulations regarding use and care of experimental animals and were approved by the local authorities (Regierungspräsidium Tübingen).

Initially, a total of 50 rats were scanned using [^{11}C]DASB and 37 rats were scanned using [^{11}C]raclopride. 20 scans of the [^{11}C]DASB cohort and 8 scans of the [^{11}C]raclopride cohort had to be excluded. For the [^{11}C]DASB cohort, 14 animals had to be excluded due to technical issues (e.g. motion, tracer production, terminated tracer infusion), 4 rats due to paravenous catheters and 2 rats died during or before the scan. For the [^{11}C]raclopride cohort, 6 rats had to be excluded due to technical difficulties and 2 rats due to paravenous catheters.

2.2. Radiotracer synthesis

For a detailed account of radiotracer synthesis, please refer to *Supplementary Methods*.

The radioactive tracers had molar activities of 83 ± 29 GBq/μmol for [^{11}C]raclopride and 57 ± 37 GBq/μmol for [^{11}C]DASB at the start of the PET acquisition (*Supplementary Fig. 1B and C*).

2.3. Simultaneous PET/MRI experiments

Anesthesia was induced in knock-out boxes by delivering 3% isoflurane in regular air until reflex tests indicated sufficient sedation. For the following preparation steps the concentration of isoflurane was reduced to 2%. The weights of the animals were measured and a catheter was placed into a tail vein using a 30G needle for tracer administration. Subsequently, the rats were transferred onto a dedicated feedback temperature-controlled rat bed (Medres, Cologne, Germany). A rectal probe was positioned to monitor and maintain a stable body temperature at 36.5°C and a breathing pad was used to observe respiration rates. Finally, the animals were introduced into the PET/MRI scanner and the isoflurane concentration was reduced to 1.3 % during the scan.

The scans were acquired using a small-animal 7 T ClinScan scanner (Bruker BioSpin MRI, Bruker, Ettlingen, Germany) with a linearly polarized RF coil (Bruker) of 72 cm in diameter for transmission and a four channel rat brain coil (Bruker) for reception. Localizer scans were first acquired to accurately position the rat brains into the center of the PET/MRI field of view. Subsequently, local field homogeneity was optimized by measuring local magnetic field maps. Anatomical reference scans were then performed using T2-weighted MRI sequences (TR: 1800 ms, TE: 67.11 ms, FOV: 40 x 32 x 32 mm^3, image size: 160 x 128 x 128 px, Rare factor: 28, averages: 1). Finally, T2*-weighted gradient echo EPI sequences (TE: 18 ms, TR: 2500 ms, 0.25 mm isotropic resolution, FoV 25 x 23 mm^2, image size: 92 x 85 x 20 px, slice thickness: 0.8 mm, 20 slices) were acquired for functional MR imaging.

A small-animal PET insert developed in cooperation with Bruker (Bruker Biospin, Ettlingen Germany) was used for [^{11}C]DASB and [^{11}C]raclopride acquisitions. This insert is the second generation of a PET insert developed in-house described previously (Judenhofer et al., 2008). Both generations of PET inserts have similar technical specifications. The radioactive tracers were applied via a bolus plus constant infusion protocol with a K_{bol} of 38.7 min using an initial bolus of 341 ± 65.2 MBq for [^{11}C]raclopride and 152 ± 44 MBq for [^{11}C]DASB in a volume of 0.48 ml over 20 s, followed by a constant infusion of 15 μl/min until the end of the scan. PET/fMRI acquisition was started simultaneously with the tracer injection and was performed over a period of 80 min. The PET data were saved as list-mode files and reconstructed using an ordered-subsets expectation maximization 2D (OSEM-2D) algorithm written in-house.

2.4. Data preprocessing

Preprocessing was performed using Statistical Parametric Mapping 12 (SPM 12, Wellcome Trust Centre for Neuroimaging, University College London, London, United Kingdom) and Analysis of Functional NeuroImages (AFNI, National Institute of Mental Health (NIMH), Bethesda, Maryland, USA) as reported previously (Amend et al., 2019). In addition, we added a nuisance removal based on a method reported elsewhere (Chuang et al., 2019). First, all fMRI scans were realigned using SPM and the three translation and three rotation motion parameters were stored. Additionally, mean images were created for all scans and used to create binary masks using AFNI. Additional binary brain masks were created for the T2-weighted anatomical MRI reference scans and the reconstructed PET scans. The masks were applied for brain extraction from all mentioned datasets. For fMRI, images containing extracerebral tissue were also created for later use. The skull-stripped PET and fMRI scans were then coregistered to their respective anatomical references. Afterwards, the anatomical reference scans were used to calculate spatial normalization parameters to the Schiffer rat brain atlas and the obtained normalization parameters were applied to the fMRI and PET datasets. Coregistration and normalization were visually evaluated for each subject and every modality. Then, nuisance removal was performed for the fMRI scans. To this extent, a multiple linear regression model was applied containing the six motion parameters stored after initial realignment, as well as the first 10 principal components of

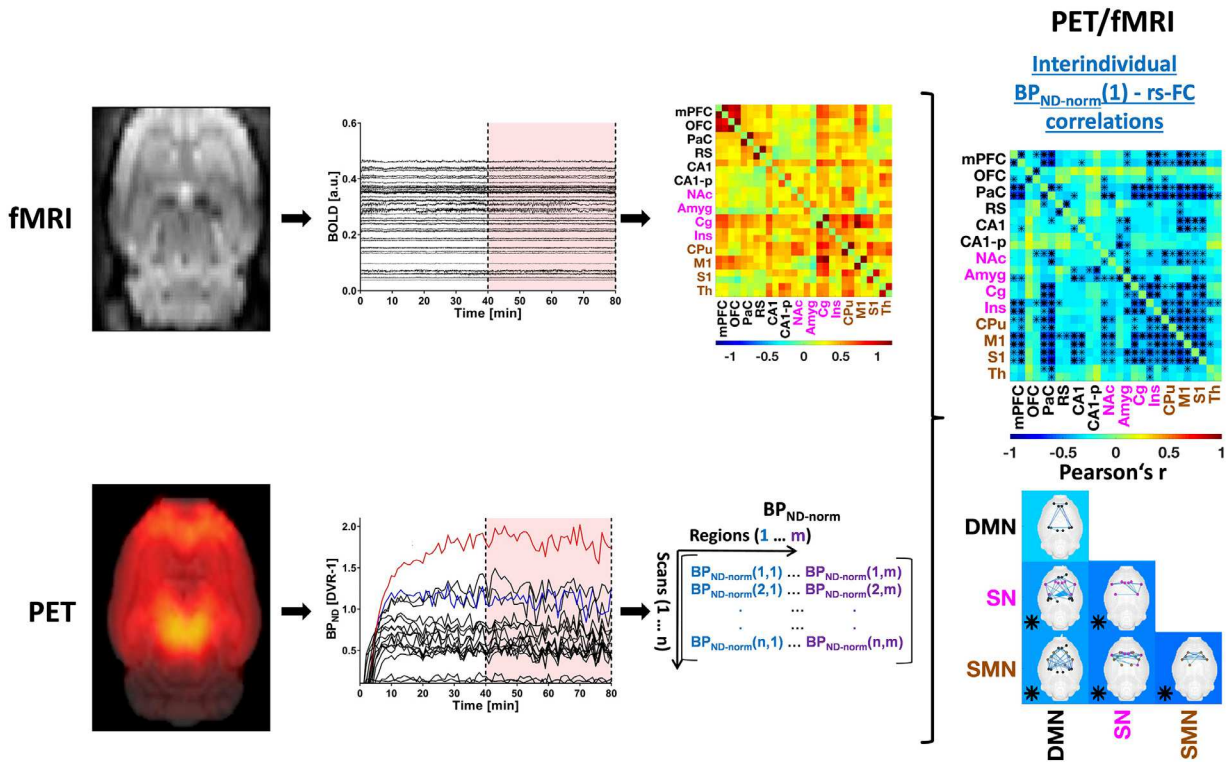

Fig. 1. PET/fMRI data analysis following preprocessing. fMRI: regional BOLD time-courses were extracted from each scan and subject and rs-FC matrices were computed. PET: regional DVR-1 values were extracted from 40 to 80 min after tracer injection for each scan and subsequently normalized to whole brain values. PET-fMRI: For every region the correlations of its subject-wise $BP_{ND\text{-}norm}$ values and every subject-wise rs-FC edge were calculated, resulting in inter-individual correlation matrices per region between respective PET tracer binding and rs-FC.

the signal extracted from the images containing extra-cerebral tissues, as described by Chuang et al. (2019). Finally, a 1.5 x 1.5 x 1.5 mm^3 full-width-half-maximum Gaussian kernel was applied to all fMRI and PET datasets for spatial smoothing (Wehrl et al., 2013).

2.5. Data analysis

In the following, an overview of the analysis of the preprocessed data is provided. A graphical description of the analysis pipeline used is shown in Fig. 1.

2.6. Functional MRI data analysis

Rs-FC was calculated using a seed-based approach in the interval from 40 to 80 min after scan start to ensure tracer equilibrium for PET (please refer to PET data analysis section). To this extent, 28 regions comprising the DMN, SN and SMN were selected from the Schiffer rat brain atlas (a list of the regions is provided in *Supplementary Table 1*). The SPM toolbox Marseille Boîte À Région d'Intérêt (MarsBaR) was employed to extract fMRI time-courses from all regions (Matthew Brett et al., 2002). These were then used to calculate pairwise Pearson's r correlation coefficients for each dataset, generating correlation matrices containing 28 x 28 elements. Self-correlations were set to zero. The computed Pearson's r coefficients then underwent Fischer's transformation into z values for further analysis.

Several rs-FC metrics were computed to quantify the properties of the analyzed networks. In addition to edge-wise rs-FC, regional node strengths were calculated as the sum of all correlations of one node to the regions belonging to the same network. Inter-network node strengths were defined as the sum of the correlations of one node to the regions of another network. On a network level, within-network strengths were defined as the sum of all edges comprising a network. Between-network strengths were calculated as the sum of all correlations between two sets of regions belonging to two networks (Rubinov and Sporns, 2010).

For a detailed report of these steps please refer to *Supplementary Methods*.

2.7. PET data analysis

Static PET scans were reconstructed from 40 to 80 min after the start of the PET data acquisition to ensure tracer equilibrium between target and reference region. To enhance signal-to-noise ratios and due to the negligible differences in tracer uptake between left and right hemispheres, each bilateral region of the Schiffer rat brain atlas was merged to one volume of interest (VOI). Following preprocessing, tracer uptake values of the 27 generated VOIs were calculated for each dataset. Binding potentials (BP_{ND}) values were computed from the DVR-1 (Eq. (1)) using the whole cerebellum as a reference region for [^{11}C]raclopride and the cerebellar grey matter as a reference region for [^{11}C]DASB (Turkheimer et al., 2012; Walker et al., 2016).

$$BP_{ND} = \frac{V_T - V_{ND}}{V_{ND}} = \frac{V_T}{V_{ND}} - 1 = DVR - 1,$$

where:

- BP_{ND} is the binding potential
- V_T is the total volume of distribution
- V_{ND} is the volume of distribution in a reference tissue
- DVR is the distribution volume ratio

For the generation of BP_{ND} maps, the above equation was applied for each voxel, where V_{ND} was defined as the mean uptake of all voxels included in the reference region, while V_T was the uptake of each respective voxel, resulting in single BP_{ND} value for each voxel in every subject.

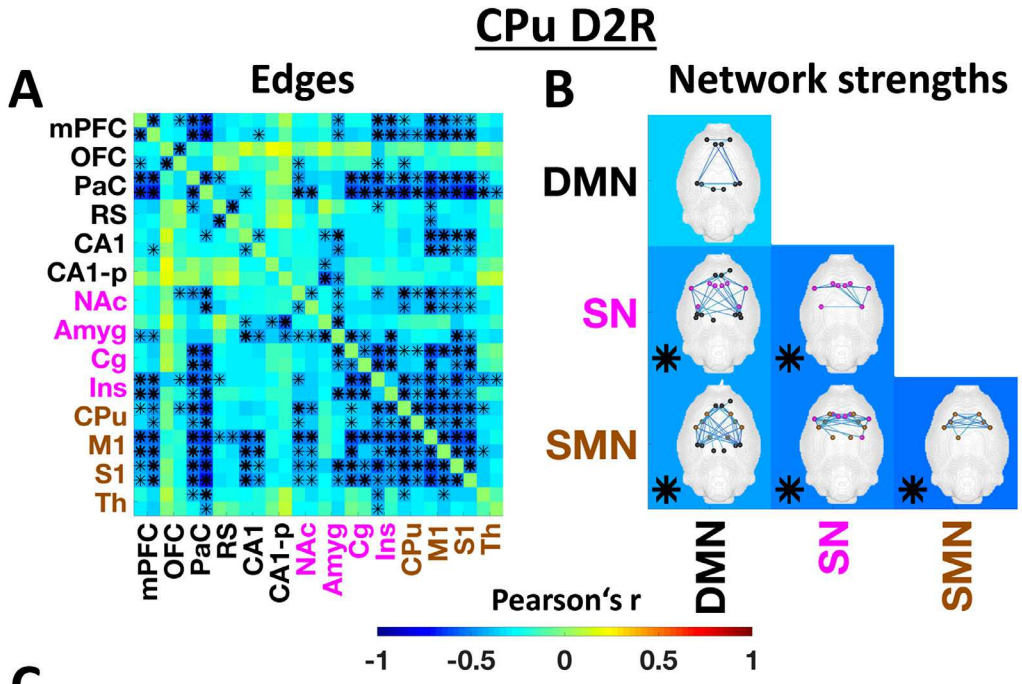

C

Node strengths

	mPFC	OFC	PaC	RS	CA1	CA1-p	NAc	Amyg	Cg	Ins	CPu	M1	S1	Th
DMN	-0.48*	-0.24	-0.50*	-0.24	-0.33	-0.09	-0.36	-0.42*	-0.36	-0.48*	-0.43*	-0.51*	-0.50*	-0.25
SN	-0.41*	-0.17	-0.60*	-0.30	-0.40*	-0.33	-0.42*	-0.46*	-0.52*	-0.53*	-0.45*	-0.55*	-0.58*	-0.28
SMN	-0.48*	-0.17	-0.63*	-0.32	-0.42*	-0.22	-0.44*	-0.31	-0.45*	-0.53*	-0.52*	-0.57*	-0.58*	-0.33

Fig. 2. Correlations between D2R availability in the CPu and rs-FC. (A) The correlation matrix indicates all correlations between CPu [^{11}C]raclopride $BP_{ND\text{-}norm}$ and pairwise rs-FC values between regions comprising the DMN, SN and SMN. DMN regions are depicted in black, SN regions in magenta and SMN regions in brown color. * indicates statistically significant correlations ($p < 0.05$, bold asterisks indicate correlations surviving FDR correction). (B) Matrix indicating correlations between CPu [^{11}C]raclopride $BP_{ND\text{-}norm}$ and within-network or between-network connectivity strengths for the DMN, SN and SMN. * indicates statistically significant correlations ($p < 0.05$, bold asterisks indicate correlations surviving FDR correction). The brain maps depict the within-network or between-network edges significantly correlating with CPu $BP_{ND\text{-}norm}$ values. (C) Table indicating the correlations (Pearson's r) of CPu [^{11}C]raclopride $BP_{ND\text{-}norm}$ and the rs-FC strengths of each analyzed region (averaged between left and right hemisphere) to the DMN, SN and SMN. Significant correlations are highlighted by the underlying color (DMN – black, SN – magenta, SMN - brown) and asterisks. Correlations surviving FDR correction are underlined. Abbreviations: D2R = D2 receptor, $BP_{ND\text{-}norm}$ = normalized binding potential, rs-FC = resting-state functional connectivity, CPu = caudate putamen, DMN = default-mode network, SN = salience network, SMN = sensorimotor network. For a list of abbreviations of all regions please refer to *Supplementary Table 1*.

Using the subject BP_{ND} maps group-level BP_{ND} maps were calculated for both cohorts. For correlation analyses, VOI-based BP_{ND} values were calculated, V_T representing the mean uptake of all voxels comprised by the respective VOI. Previous similar studies reported adjusting BP_{ND} values for mean global signal to control for global effects (Roffman et al., 2016). The mentioned study indicated the high inter-individual correlations between BP_{ND} values of different regions. Here, we reproduced the finding by calculating the correlations between regional BP_{ND} values and confirmed this observation (please refer to *Supplementary Information*). Thus, since our aim was to elucidate the correlations of rs-FC with the distributions of either D2R or SERT binding between different regions, in our study individual BP_{ND} values also underwent a global normalization for each dataset to discard such effects, generating normalized BP_{ND} values ($BP_{ND\text{-}norm}$), as described in the study mentioned above (Roffman et al., 2016).

2.8. PET/fMRI data analysis

To investigate the influence of [^{11}C]raclopride and [^{11}C]DASB in the CPu and mPFC on rs-FC, we evaluated the relationships between their $BP_{ND\text{-}norm}$ values and rs-FC measures described above. Inter-individual correlations between regional $BP_{ND\text{-}norm}$ values and rs-FC metrics were calculated using Pearson's r. This procedure was performed between each regional $BP_{ND\text{-}norm}$ and every rs-FC metric described above to determine potential correlations between edges, regional node strengths, inter-regional node strengths, within-network strengths and between-network strengths and regional D2R or SERT densities. Additionally, the computed correlations between $BP_{ND\text{-}norm}$ and each rs-FC metric were tested for statistical significance and a false discovery rate (FDR) correction was performed for a threshold of 0.05 using the Benjamini-Hochberg procedure separately for each metric and tracer employed.

The BrainNetViewer toolbox was used for the visualization of correlating edges (Xia et al., 2013).

3. Results

The results indicate inter-subject correlations between rs-FC and [^{11}C]raclopride and [^{11}C]DASB $BP_{ND\text{-}norm}$ values in the CPu and mPFC. The significances depicted were calculated at $p < 0.05$ (both uncorrected and FDR-corrected using Benjamini-Hochberg, please refer to corresponding figure legends). For more detailed information, correlations with significances of $p < 0.01$ and $p < 0.001$ are indicated in the *Supplementary Information* for all presented matrices.

3.1. D2 receptor availability in CPu correlates with widespread reduced rs-FC

Due to the importance of dopamine in the CPu in modulating brain function, we aimed to elucidate the intrinsic correlation of D2R availability in this region to the rs-FC of the DMN, SN and SMN (Fig. 2).

D2R availability in the CPu was negatively correlated with rs-FC between all three analyzed networks, as depicted in Fig. 2. On edge level (Fig. 2A), most significant correlations involved the mPFC (23 anti-correlated edges) and PaC (35 anti-correlated edges) in the DMN, Cg (21 anti-correlated edges) and Ins (29 anti-correlated edges) in the SN and the CPu (27 anti-correlated edges), M1 (36 anti-correlated edges) and S1 (36 anti-correlated edges) in the SMN.

SN and SMN within-network strengths (Fig. 2B) were anti-correlated to the D2R availability in the CPu (r = -0.52 ($p < 0.05$, FDR-corrected) for SN and r = -0.53 ($p < 0.05$, FDR-corrected) for SMN). Similarly, the between-network connectivity was anti-correlated for each pair of networks (r = -0.45 ($p < 0.05$, FDR-corrected) between DMN and SN, r = -0.46 ($p < 0.05$, FDR-corrected) between DMN and SMN; r = -0.51 ($p < 0.05$, FDR-corrected) between SN and SMN).

The correlations calculated for within-network and between-network node strengths and CPu D2R availabilities also included significant values for nodes belonging to all three networks (Fig. 2C). The connectivity strengths of six regions, including mPFC, PaC, Ins, CPu, M1 and S1 to all three networks were significantly anti-correlated to D2R binding the striatum ($p < 0.05$, FDR-corrected). The strongest negative correlations were observed for the SMN, ranging up to r = -0.63 for the rs-FC of PaC, a total of nine regions being negatively correlated with the SMN at a significance threshold of $p < 0.05$ including FDR correction (r = -0.48 for mPFC, r= -0.42 for CA1, r = -0.44 for NAc, r = -0.45 for Cg, r = -0.53 for Ins, r = -0.52 for CPu, r = -0.57 for M1, r = -0.58 for S1). The node strengths of the same regions to the SN, with the exception of the Amyg, also correlated negatively with CPu [^{11}C]raclopride binding at $p < 0.05$ with FDR correction, the correlation coefficients ranging up to r = -0.60 for PaC and r = -0.58 for S1. The node strengths of seven regions to the DMN anti-correlated significantly ($p < 0.05$, FDR correction) with CPu D2R density (ranging from r = -0.42 for Amyg to r = -0.51 for M1).

3.2. Medial prefrontal D2R correlates negatively with rs-FC of regions involved in cognitive control

We investigated the relationships between medial prefrontal D2R availability and rs-FC due to the reported role of dopamine in cognitive control mediated by this brain region (Fig. 3).

Compared to the widespread relationships between D2R binding in the CPu and rs-FC, the correlations observed between medial prefrontal [^{11}C]raclopride $BP_{ND\text{-}norm}$ values and the rs-FC of the three analyzed RSNs were sparse and to a large extent involved the DMN (Fig. 3). Specifically, 45 of the 52 edges significantly anti-correlated to D2R availability involved at least one region belonging to the DMN (Fig. 3A). The strongest correlations occurred for the edges between mPFC and MC (up to r = -0.53, $p < 0.05$, FDR-corrected).

On network level (Fig. 3B), the medial prefrontal D2R availability was significantly anti-correlated with the within-network DMN rs-FC strength (r = -0.40, $p < 0.05$), as well as the rs-FC between DMN and SMN (r = -0.40, $p < 0.05$). Connectivity strengths within and between SN and SMN did not correlate significantly with medial prefrontal D2R binding.

The within-network strengths of three posterior DMN regions were negatively correlated with D2R binding in the mPFC (Fig. 3C), including RS (r = - 0.38, $p < 0.05$), CA1 (r = -0.41, $p < 0.05$) and CA1-p (r = -0.38, $p < 0.05$). In addition, anti-correlated connectivity to the DMN was detected in the CPu (r = -0.37, $p < 0.05$), as well as in the S1 (r = -0.37, $p < 0.05$) and Th (r = -0.40, $p < 0.05$), all regions being part of the SMN. In contrast, only the rs-FC of CA1-p (r = -0.41, $p < 0.05$) to the SN, as well as the rs-FC of mPFC (r = -0.41, $p < 0.05$) and CA1 (r = -0.43, $p < 0.05$) correlated negatively with medial prefrontal D2R availability.

3.3. SERT availability in the CPu negatively correlates with SN connectivity

Correlations between rs-FC and [^{11}C]DASB binding in the CPu are presented in Fig. 4.

Correlations of SERT availability in the CPu with rs-FC were subtle and mainly restricted to SN connectivity. Specifically, negative correlations were found between SERT availability and 7 out of 28 edges in the SN. Five edges of the NAc and Ins respectively to other SN regions were significantly anti-correlated with SERT binding in the CPu ($p \leq 0.05$, Fig. 4A). Additionally, NAc and Ins edges to regions outside the SN including CPu, S1 and and RS correlated negatively with SERT availability in the CPu. Finally, 3 out of 4 edges between the CPu itself and S1 correlated negatively with SERT availability. The sparse edge-wise correlations did not however translate to correlations with either within or between-network rs-FC (Fig. 4B). Nonetheless, the integration of NAc and Ins within the SN correlated negatively with SERT availability in the CPu ($p < 0.05$, Fig. 4C). Interestingly, multiple edges involving DMN rs-FC correlated positively, though not significantly with SERT density in the striatum, in contrast to the negative correlations observed between striatal SERT availability and salience rs-FC and to a lesser extent SMN rs-FC.

3.4. Prefrontal SERT specifically correlates with anterior DMN rs-FC

Expressing the highest [^{11}C]DASB binding of the entire cortex, we evaluated the mPFC to elucidate whether its SERT availability correlates with the rs-FC of the DMN, SN and SMN (Fig. 5).

The correlations of the investigated edges with medial prefrontal SERT availability were heterogeneous (Fig. 5A). Specifically, the short-range rs-FC within the anterior DMN comprised of mPFC and OFC correlated positively with [^{11}C]DASB binding, reaching up to r = 0.45 ($p < 0.05$) between left and right mPFC. In contrast, long-range rs-FC of the OFC was anti-correlated to mPFC SERT within the DMN to PaC and RS (r = -0.49, $p < 0.01$ between right OFC and right RS) as well as to the SMN regions CPu (r = -0.43, $p < 0.05$ between left OFC and CPu), M1 and S1 (r = -0.5, $p < 0.01$ between right OFC and right S1). Further negative correlations were found for edges between RS and regions belonging to the SN, such as NAc (r = -0.45, $p < 0.05$ for right RS – left NAc), Amyg (r = -0.41, $p < 0.05$ for right RS – left Amyg), or Ins (r = -0.5, $p < 0.01$ for right RS – right Ins). Finally, several edges involving both SN and SMN nodes were significantly reduced at higher medial prefrontal SERT availabilities. Most prominently, 16 edges of the Ins to regions including RS, Amyg, Cg, CPu, M1 and S1 were anti-correlated. Additionally, mPFC [^{11}C]DASB binding was negatively correlated with 14 S1 edges to regions such as OFC, Amyg, Cg, Ins, CPu and M1.

On a network level the rs-FC between SN and SMN was reduced significantly (r = -0.36, $p < 0.05$) by increasing SERT availability in the mPFC (Fig. 5B). The rs-FC between and within the other RSNs was not

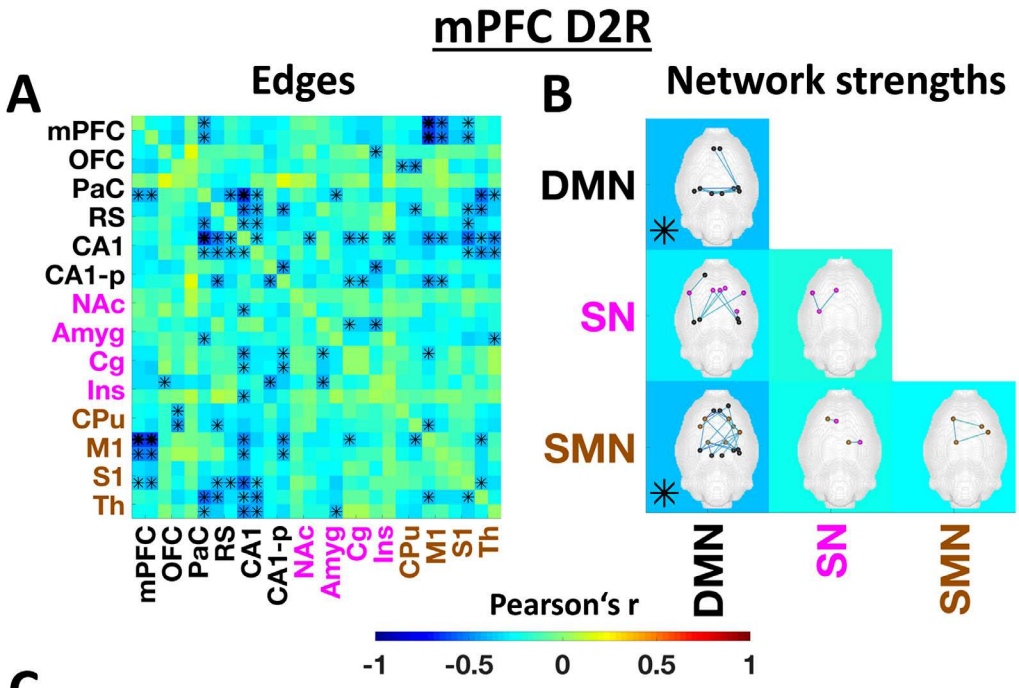

C

Node strengths

	mPFC	OFC	PaC	RS	CA1	CA1-p	NAc	Amyg	Cg	Ins	CPu	M1	S1	Th
DMN	**-0.37***	-0.26	-0.29*	**-0.38***	**-0.41***	-0.38*	-0.22	-0.27	-0.30	-0.30	**-0.37***	-0.34	**-0.37***	**-0.40***
SN	-0.25	-0.17	-0.19	-0.18	-0.31	**-0.41***	-0.13	-0.26	-0.22	-0.14	-0.18	-0.26	-0.22	-0.19
SMN	**-0.41***	-0.18	-0.19	-0.34	**-0.43***	-0.33	-0.14	-0.30	-0.16	-0.14	-0.27	-0.24	-0.19	-0.31

Fig. 3. Correlations between D2R availability in the mPFC and rs-FC. (A) The correlation matrix indicates all correlations between mPFC [^{11}C]raclopride $BP_{ND\text{-}norm}$ and pairwise rs-FC values between regions comprising the DMN, SN and SMN. DMN regions are depicted in black, SN regions in magenta and SMN regions in brown color. * indicates statistically significant correlations ($p < 0.05$, bold asterisks indicate correlations surviving FDR correction). (B) Matrix indicating correlations between mPFC [^{11}C]raclopride $BP_{ND\text{-}norm}$ and within-network or between-network connectivity strengths for the DMN, SN and SMN. * indicates statistically significant correlations ($p < 0.05$, bold asterisks indicate correlations surviving FDR correction). The brain maps depict the within-network or between-network edges significantly correlating with mPFC $BP_{ND\text{-}norm}$ values. (C) Table indicating the correlations (Pearson's r) of mPFC [^{11}C]raclopride $BP_{ND\text{-}norm}$ and the rs-FC strengths of each analyzed region (averaged between left and right hemisphere) to the DMN, SN and SMN. Significant correlations are highlighted by the underlying color (DMN – black, SN – magenta, SMN - brown) and asterisks. Correlations surviving FDR correction are underlined. Abbreviations: D2R = D2 receptor, $BP_{ND\text{-}norm}$ = normalized binding potential, rs-FC = resting-state functional connectivity, mPFC = medial prefrontal cortex, DMN = default-mode network, SN = salience network, SMN = sensorimotor network. For a list of abbreviations of all regions please refer to *Supplementary Table 1*.

significantly associated to SERT levels in this region. Finally, Fig. 5C indicates significant correlations between region-wise rs-FC to the three RSNs and medial prefrontal SERT availability. The Ins was the only region with significantly anti-correlated rs-FC to the DMN ($r = -0.37$, $p < 0.05$) and the only node with significantly anti-correlated rs-FC to all three RSNs ($r = 0.38$, $p < 0.05$ to the SN and $r = 0.5$, $p < 0.01$ to the SMN) with medial prefrontal SERT availability. Five regions, including RS, Cg, M1 and S1 in addition to Ins had significantly lower rs-FC strength to the SN, while OFC ($r = -0.44$, $p < 0.05$), M1 and S1 (both $r = -0.38$, $p < 0.05$) were significantly less connected to the SMN at increasing [^{11}C]DASB bindings in the mPFC.

We further elucidated the way prefrontal SERT binding shifts the rs-FC balance towards the anterior DMN, by calculating the correlation of medial prefrontal [^{11}C]DASB binding with the difference of the average rs-FC within the anterior DMN and the average rs-FC between the anterior DMN and the posterior DMN, SN and SMN (please refer to *Supplementary Information*). This analysis yielded a highly significant correlation value of $r = 0.63$ ($p = 0.0003$), emphasizing the shift in processing balance by the corroborated positive correlation of the anterior DMN within-network rs-FC with the negative correlation of the anterior DMN between-network rs-FC with medial prefrontal SERT binding.

4. Discussion

Elucidating the link between molecular variations of brain receptors and transporters and macroscale metrics such as rs-FC will primarily enhance our understanding about drug mechanisms of action and several brain pathologies. Here we show that D2R and SERT availabilities correlate with rs-FC in a regionally specific manner in the healthy rat brain (see Fig. 6 for a summary of the findings).

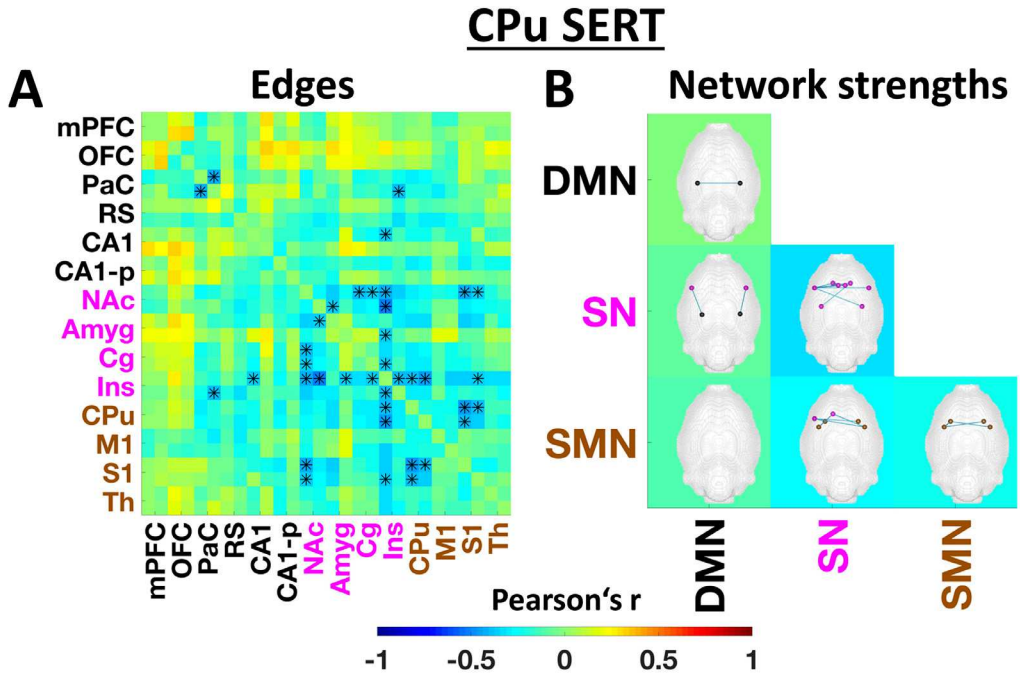

C

Node strengths

	mPFC	OFC	PaC	RS	CA1	CA1-p	NAc	Amyg	Cg	Ins	CPu	M1	S1	Th
DMN	0.04	0.05	-0.10	-0.05	0.07	0.00	-0.17	0.07	-0.03	-0.15	-0.14	-0.19	-0.04	0.00
SN	0.04	0.17	-0.21	-0.16	-0.10	-0.20	-0.40*	-0.20	-0.24	-0.40*	-0.34	-0.14	-0.32	-0.18
SMN	-0.01	0.07	-0.12	-0.15	-0.12	-0.17	-0.29	-0.12	-0.20	-0.35	-0.33	-0.17	-0.24	-0.15

Fig. 4. Correlations between SERT availabilities in the CPu and rs-FC. (A) The correlation matrix indicates all correlations between CPu [^{11}C]DASB $BP_{ND\text{-}norm}$ values and pairwise rs-FC values between regions comprising the DMN, SN and SMN. DMN regions are depicted in black, SN regions in magenta and SMN regions in brown color. * indicates statistically significant correlations ($p < 0.05$, uncorrected). (B) Matrix indicating correlations between CPu [^{11}C]DASB $BP_{ND\text{-}norm}$ and within-network or between-network connectivity strengths for the DMN, SN and SMN. * indicates statistically significant correlations ($p < 0.05$, uncorrected). The brain maps depict the within-network or between-network edges significantly correlating with CPu [^{11}C]DASB $BP_{ND\text{-}norm}$ values. (C) Table indicating the correlations of CPu [^{11}C]DASB $BP_{ND\text{-}norm}$ and the rs-FC strengths of each analyzed region (averaged between left and right hemisphere) to the DMN, SN and SMN. Significant correlations are highlighted by the underlying color (DMN – black, SN – magenta, SMN - brown) and asterisks ($p < 0.05$. Abbreviations: SERT = serotonin transporter, $BP_{ND\text{-}norm}$ = normalized binding potential, rs-FC = resting-state functional connectivity, CPu = caudate putamen, mPFC = medial prefrontal cortex, DMN = default-mode network, SN = salience network, SMN = sensorimotor network. For a list of abbreviations of all regions please refer to *Supplementary Table 1*.

4.1. D2 receptor density in the CPu is negatively correlated with rs-FC across all RSNs

DA and the mesolimbic system in particular, expressing the highest density of dopaminergic receptors, are of paramount importance for numerous neurological disorders for which rs-FC can serve as a biomarker (Cole et al., 2013). The D2Rs investigated in the present study using [^{11}C]raclopride drive the indirect striatal pathway, a circuit involved in the inhibition of motor activity via the ventrolateral nucleus of the thalamus postulated to be heavily involved in PD (Smith et al., 1998; Bartels and Leenders, 2009). The largest negative correlation with D2R availability in the caudate putamen observed in our study occurred in the SMN, in line with the increased activity of the indirect pathway mediated by higher D2R densities. However, our data also suggests anti-correlation with DMN and SN rs-FC. Regions comprising these networks may be mediated along different pathways by striatal D2Rs, as shown previously (Kellendonk et al., 2006). Specifically, striatal D2R overexpression in mice has been shown to modulate ventral tegmental activity (Krabbe et al., 2015). One of the effects of this modulation is the impairment of functional connectivity between VTA and mPFC, resulting in abnormal prefrontal processing and affecting working memory (Duvarci et al., 2018). Intriguingly, the connectivity between the medial prefrontal cortex and other areas correlated strongly to D2R availability in the caudate putamen in our study, in line with the reports discussed above.

Two studies acquiring PET and fMRI in the same cohort have previously investigated the interaction of dopamine receptors and rs-FC. First, using [^{11}C]NNC112, a ligand binding to the dopamine D1 receptor, Roffman et al. (2016) have shown negatively correlated striatal D1R availability with the rs-FC between left and right mPFC. This is in contrast to the lack of correlation between [^{11}C]raclopride binding and the rs-FC between left and right mPFC shown here, underlining the differ-

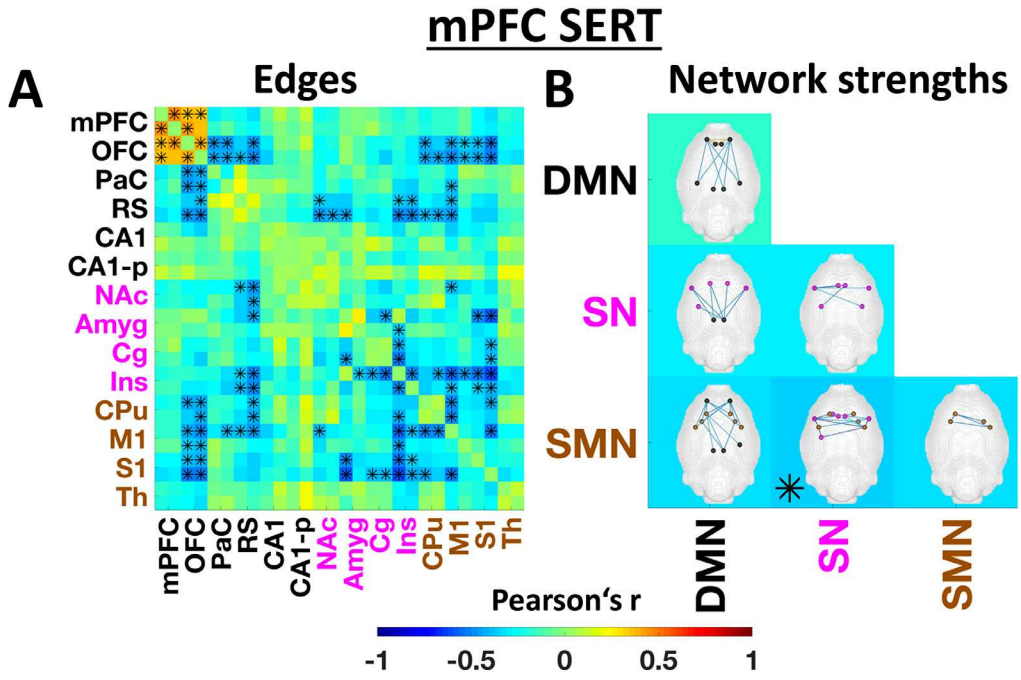

C

Node strengths

	mPFC	OFC	PaC	RS	CA1	CA1-p	NAc	Amyg	Cg	Ins	CPu	M1	S1	Th
DMN	-0.03	-0.21	-0.20	-0.24	-0.09	-0.09	-0.26	-0.16	-0.21	-0.37*	-0.33	-0.33	-0.35	-0.15
SN	-0.14	-0.24	-0.24	-0.44*	-0.12	-0.08	-0.19	-0.18	-0.37*	-0.38*	-0.25	-0.39*	-0.52*	-0.12
SMN	-0.23	-0.44*	-0.13	-0.34	-0.18	-0.03	-0.18	-0.26	-0.28	-0.50*	-0.27	-0.38*	-0.38*	-0.16

Fig. 5. Correlations between SERT availabilities in the mPFC and rs-FC. (A) The correlation matrix indicates all correlations between mPFC [^{11}C]DASB $BP_{ND\text{-}norm}$ values and pairwise rs-FC values between regions comprising the DMN, SN and SMN. DMN regions are depicted in black, SN regions in magenta and SMN regions in brown color. * indicates statistically significant correlations ($p < 0.05$, uncorrected). (B) Matrix indicating correlations between mPFC [^{11}C]DASB $BP_{ND\text{-}norm}$ and within-network or between-network connectivity strengths for the DMN, SN and SMN. * indicates statistically significant correlations ($p < 0.05$, uncorrected). The brain maps depict the within-network or between-network edges significantly correlating with mPFC [^{11}C]DASB $BP_{ND\text{-}norm}$ values. (C) Table indicating the correlations of mPFC [^{11}C]DASB $BP_{ND\text{-}norm}$ and the rs-FC strengths of each analyzed region (averaged between left and right hemisphere) to the DMN, SN and SMN. Significant correlations are highlighted by the underlying color (DMN – black, SN – magenta, SMN - brown) and asterisks ($p < 0.05$, uncorrected). Abbreviations: SERT = serotonin transporter, $BP_{ND\text{-}norm}$ = normalized binding potential, rs-FC = resting-state functional connectivity, CPu = caudate putamen, mPFC = medial prefrontal cortex, DMN = default-mode network, SN = salience network, SMN = sensorimotor network. For a list of abbreviations of all regions please refer to *Supplementary Table 1*.

ent functions of D1 and D2 receptors. Another study showed that DA release capacity to D2/3 receptors in the striatum was negatively correlated to the salience network connectivity (McCutcheon et al., 2019), which is in line with our findings, indicating the translatability of this study design among species. Interestingly, in the above-mentioned study DA synthesis capacity correlated with salience rs-FC. The authors corroborated their findings to the hypothesis that DA synthesis reflects a general dopaminergic tone that would be necessary for the attribution of salience. At the same time, DA release would indicate spontaneous stimulus-independent firing mediating aberrant attributions of salience. Our data thus support the mentioned hypothesis.

4.2. Medial prefrontal D2R availability is associated with reduced DMN connectivity

Several reports have suggested an essential role of DA in the prefrontal cortex, an associative cortical area involved in the top-down control of several cognitive mechanisms (Celada et al., 2013). The balance between D1 and D2 receptors available in this region has been linked to normal brain function and is postulated to play a critical role in psychiatric diseases such as schizophrenia (Avery and Krichmar, 2015). It is assumed that D1 and D2 receptors play complementary roles in functions such as associative learning, with D2R promoting cognitive flexibility. Thus, increased prefrontal D2R availability destabilizes network states promoting flexible behavior (Puig et al., 2014; Durstewitz et al., 2000; Kahnt et al., 2015). This hypothesis is supported by our current findings, indicating negatively correlated rs-FC, especially in the DMN.

4.3. Striatal SERT subtly impacts salience network circuitry

While serotonergic innervation in the striatum by the raphé nuclei has been demonstrated (Azmitia and Segal, 1978), the role of serotonin in the striatum remains largely elusive. The endogenous levels

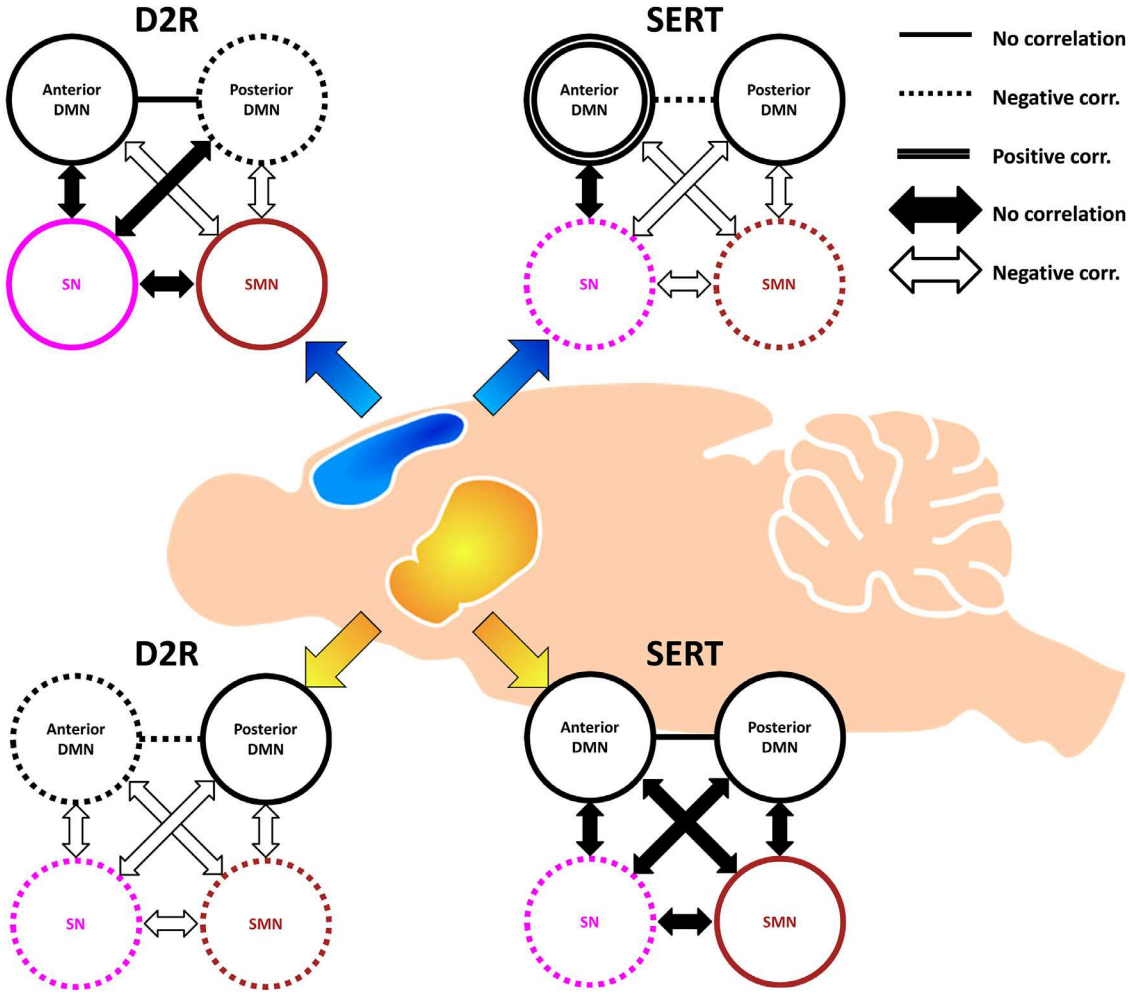

Fig. 6. Qualitative summary of the findings. In the mPFC (blue) D2Rs are negatively correlated with posterior DMN rs-FC and the rs-FC between DMN and SMN. SERT availability in the mPFC is negatively correlated with rs-FC between anterior and posterior DMN, yet positively correlated with anterior DMN rs-FC. The rs-FC between SN and SMN is also anti-correlated with medial prefrontal SERT density. In the CPu (yellow) D2R was negatively correlated with rs-FC within and between all networks except for the largely unaffected posterior DMN, while SERT availability correlated negatively with SN rs-FC and did not correlate to rs-FC in other networks. Interrupted lines indicate negatively correlated within-network rs-FC, empty arrows indicate negatively correlated between-network rs-FC. Single continuous lines and full arrows indicate no correlation of within and between-network rs-FC. Double lines indicate positive correlation of within-network rs-FC. Abbreviations: D2R = D2 receptor, SERT = serotonin transporter, DMN = default-mode network, SN = salience network, SMN = sensorimotor network, corr = correlation.

of serotonin determined in the striatum at resting state (0.5 – 2 nM) appear insufficient to directly impact dopaminergic activity in this region (Navailles and De Deurwaerdère, 2011), which may explain the relatively sparse correlations observed here between SERT density and rs-FC.

The hypothesis indicating a subtle, yet physiologically significant role of serotonin in the striatum is supported by macroscale findings, including those generated by rs-FC studies. Specifically, FC between the raphé nuclei and the striatum has been reported to be negatively correlated with connectivity of the salience network with subcortical regions in schizophrenia (Han et al., 2020). The significant effects observed in the present study mirror the findings by Han et al. (2020), being largely confined to salience connectivity. Potential pathological roles of such correlations include the postulated aberrant salience attribution in schizophrenia, as well as the reported deficient motivation (Han et al., 2020), a hypothesis supported by the significantly anti-correlated rs-FC strength of the nucleus accumbens within the salience network found in our study. Intriguingly, similar findings of negatively correlated salience rs-FC with D2 availability in the striatum have been reported (Sorg et al., 2013), which is also confirmed by the findings in the present study. Therefore, our data indicate that striatal D2R and SERT densities have similar effects on the salience network in particular, both being anti-correlated with its rs-FC. However, two aspects must be underlined. First, our data indicate that striatal D2R correlations with rs-FC are stronger than those of SERT and also involve the two other investigated networks. Secondly, potential direct interactions between SERT and D2R in the striatum could not be elucidated using the present study design. Due to the similar effects of D2R and SERT underlined above, future studies assessing both parameters along with rs-FC in the same cohort are of interest to elucidate potential three-way interactions.

4.4. Medial prefrontal SERT density has opposing effects on anterior and posterior default-mode connectivity

Our data indicate that SERT availability in the mPFC has a heterogeneous impact on rs-FC, localized positive correlations in the anterior DMN being corroborated with more widespread negative correlations in the SN and SMN.

The associations observed in the present study could provide important insights for MDD and related disorders, which are associated with disrupted serotonergic neurotransmission. In MDD, cortical 5-HT levels are believed to be decreased, one of the possible causes being an increased expression of SERT (Parsey et al., 2006; Willeit et al., 2008; Newberg et al., 2012). Due to the rostro-caudal gradient in serotonergic innervation it is widely postulated that 5-HT in the prefrontal cortex may play an essential role in rs-FC modulation and thereby in numerous psychiatric diseases including MDD (Celada et al., 2013; Lanzenberger et al., 2012). In MDD, most rs-FC research has focused on the DMN, a network associated with a state of enhanced rumination. Taken together, past studies indicate increased rs-FC in frontal areas corroborated with decreases in the posterior default-mode hubs (Yan et al., 2019). In line with these findings, we demonstrate correlated local rs-FC within the prefrontal cortex with medial prefrontal SERT availability and concurrent with negatively correlated rs-FC in the posterior DMN, as well as in the SMN and SN. A localized prefrontal rs-FC increase with its concurrent dissociation from most other areas of the brain may indicate an enhanced state of rumination corroborated with a loss of top-down control and regulation (Lemogne et al., 2012; An et al., 2017; Savitz and Drevets, 2009; Savitz and Drevets, 2009; Lui et al., 2011). Another interesting aspect of our data is the negative correlation between insular cortex connectivity and all RSNs, in particular the task-positive SMN, with prefrontal SERT densities. Being the main hub of the salience network, this finding may suggest that disturbed regulation of DMN-SMN balance, one of the main functions of the SN (Conio et al., 2019; Manoliu et al., 2014), is at least in part associated with prefrontal serotonergic function.

Our findings also complement recent work on bipolar disorder. This psychiatric disorder is characterized by two contrasting phases – a depressive and a manic phases (Magioncalda et al., 2015). First, several publications have shown these two phases are also accompanied by opposing changes in RSNs – namely, a tilt toward the DMN in the depressive phase and toward the SMN in the manic phase (Martino et al., 2016; Russo et al., 2020). The contrasting role of the two networks in bipolar disorder has been underlined through various metrics (Martino et al., 2016; Zhang et al., 2019). Further investigation showed the central role of medial prefrontal connectivity, its regional homogeneity being decreased in the manic phase (Russo et al., 2020). Finally, recent advances have shown the central role of dopamine and serotonin in bipolar disorder, the latter postulated to promote the depressive phase by enhancing DMN rs-FC (Martino and Magioncalda, 2021; Magioncalda and Martino, 2021).

Using sequential [^{11}C]WAY-100635 PET/fMRI Hahn et al. investigated the modulations of the DMN by regional 5-HT$_{1A}$ receptor availabilities (Hahn et al., 2012). The authors found reduced DMN rs-FC at increased 5-HT$_{1A}$ receptor binding in the dorsal medial prefrontal cortex, in line with our results using [^{11}C]DASB. However, when comparing the study by Hahn et al. with the present study, it should be kept in mind that Hahn et al. investigated correlations between rs-FC and a particular 5-HT receptor subtype. Investigating a single 5-HT receptor subtype provides one possible modulation of the rs-FC elicited by 5-HT (Celada et al., 2013), while imaging SERT availability as done in our study may represent a more general reflection of regional serotonergic tone. The two approaches should be seen as complementary and future studies investigating the influence of both SERT and different 5-HT receptors on rs-FC will further enhance our understanding of the serotonergic system.

4.5. Serotonergic and dopaminergic correlations with rs-FC

Our work investigates transporter and receptor correlations with rs-FC and, importantly, does not directly investigate the respective neurotransmitter concentrations. PET studies using [^{11}C]raclopride have been shown to provide an indirect measure of (extra)synaptic dopamine availability (Park and Park, 2000; Patel et al., 2008), a higher D2R availability possibly reflecting a lower synaptic dopamine content, which may impact rs-FC in downstream pathways. However, in a steady-state condition, the measured binding is a complex interplay between neurotransmitter concentration and receptor density, making it difficult to interpret the present data in terms of neurotransmitter concentrations. Regarding [^{11}C]DASB, previous studies have indicated its potential negative correlation with endogenous serotonin levels, however only as a result of strong pharmacological interventions (Yamamoto et al., 2007; Lundquist et al., 2007). Other factors such as transporter internalization may also play an important role in terms of tracer binding (Paterson et al., 2010). Importantly, as for [^{11}C]raclopride, the studies mentioned above only report correlations between tracer binding and the respective neurotransmitter after pharmacological challenges, inferences at steady-state cannot be made at present. The recent study by Conio et al. indicated specific, mainly opposite roles of the two neurotransmitters in the modulation of DMN, SN, and SMN (Conio et al., 2019). However, the authors primarily focused on the correlation between rs-FC and neurotransmitter synthesis at the raphé nuclei and substantia nigra. Our study complements the proposed model by showing that the availabilities of receptors in projection areas also play essential roles in the way the respective neurotransmitters modulate rs-FC. Future studies will be required to further investigate the mechanisms underlying the observed correlations both in terms of neurotransmitter concentrations and receptor or transporter availabilities. Importantly, as opposed to neurotransmitters such as the mainly excitatory glutamate or the mainly inhibitory GABA, DA and 5-HT modulate brain function heterogeneously (Ciranna, 2006). The heterogeneity of the modulatory effects may stem from the various DA and 5-HT receptor subtypes interacting with glutamate and GABA in differing manners and their different distributions across the brain (Ciranna, 2006). Additionally, several studies have suggested a relationship between DA and 5-HT in disease, reward and addiction (Hjorth et al., 2019; Fischer and Ullsperger, 2017). Anatomically, it has been shown that the raphé nuclei send serotonergic projections to the ventral tegmental area (Fischer and Ullsperger, 2017; Wang et al., 2019), both in turn receiving top-down afferents from the prefrontal cortex (Challis and Berton, 2015; Harte and O'Connor, 2004; Vazquez-Borsetti et al., 2009). In our study, additional analysis analyses showed medial prefrontal SERT availability correlated positively with the short-path rs-FC between VTA and MB (*Supplementary Fig. 12*). This finding hints towards the role of serotonergic prefrontal top-down modulation on the relationship between the raphé nuclei and the VTA and conversely may represent one of the ways of interaction between serotonergic and dopaminergic neurotransmission. Such complex loops mediated by several regions and neurotransmitters may be further elucidated by PET/fMRI studies employing several tracers in the same cohort.

4.6. Limitations and general remarks

Performing the present study on animals had both limitations and advantages. In contrast to human studies, our data were acquired under anesthesia and only included male subjects. However, through the high cohort homogeneities, factors of no interest affecting the readout, such as nutrition, age or lifestyle could be excluded. In terms of analysis, our results can be affected by several factors, such as the inclusion or exclusion of certain regions from respective networks. Furthermore, other metrics characterizing the BOLD signal, such as its variation (SD-BOLD) can further elucidate the aspects discussed in this work. Finally, due to the relatively low cohort sizes compared to human studies, some of the correlations presented did not survive multiple comparison corrections and must be therefore interpreted with caution. On the biological side, our readout only sheds light on a small portion of possible interactions between dopaminergic, and serotonergic neurotransmission and rs-FC, studies involving other receptors and transporters being of interest in the future. A more detailed discussion on all these aspects, including a number of additional analysis analyses performed can be found in the *Supplementary Information*.

5. Conclusion

The present study shows that the regional availabilities of D2R and SERT have specific fingerprints on RSNs. The simultaneously acquired PET/fMRI data in rats enable the investigation of the modulatory role of neurotransmitter systems on rs-FC at baseline levels. Further studies exploring the correlations of other neurotransmitter systems such as norepinephrine with rs-FC will be of great value to elucidate their respective influence on brain function. Future similarly designed studies may improve the general understanding of brain function on multiple levels, as well as the development of novel drug therapies for several psychiatric diseases.

Funding

- Bundesministerium für Bildung und Forschung (BMBF, Grant No. 01GQ1415) to BJP and HFW
- Werner Siemens Foundation to BJP
- National Institute of Health (NIH, Grant No. R01 DA038895) to BBB

Data availability

The original dataset will be made available.

Declaration of Competing Interest

The authors declare no conflict of interest.

Credit authorship contribution statement

Tudor M. Ionescu: Conceptualization, Methodology, Software, Validation, Formal analysis, Investigation, Data curation, Writing – original draft, Visualization. **Mario Amend:** Investigation, Writing – review & editing. **Rakibul Hafiz:** Methodology, Software, Writing – review & editing. **Bharat B. Biswal:** Conceptualization, Writing – review & editing, Supervision, Project administration, Funding acquisition. **Andreas Maurer:** Writing – review & editing. **Bernd J. Pichler:** Resources, Writing – review & editing, Supervision, Project administration, Funding acquisition. **Hans F. Wehrl:** Conceptualization, Methodology, Writing – review & editing, Supervision, Project administration, Funding acquisition. **Kristina Herfert:** Writing – review & editing, Visualization, Supervision, Project administration.

Acknowledgments

We thank Dr. Julia Mannheim, Dr. Rebecca Rock, Dr. Neele Hübner, Dr. Andreas Dieterich, Ines Herbon, Stacy Huang, Funda Cay, Linda Schramm and Sandro Aidone (Werner Siemens Imaging Center, Department of Preclinical Imaging, University of Tuebingen) for their technical and adminstrative support. We thank the Radiopharmacy department (Werner Siemens Imaging Center, University of Tuebingen) for the tracer production. This study is also part of the PhD thesis of Tudor Ionescu.

Supplementary materials

Supplementary material associated with this article can be found, in the online version, at doi:10.1016/j.neuroimage.2021.118501.

References

Amend, M., Ionescu, T.M., Di, X., Pichler, B.J., Biswal, B.B., Wehrl, HF., 2019. Functional resting-state brain connectivity is accompanied by dynamic correlations of application-dependent [(18)F]FDG PET-tracer fluctuations. Neuroimage 196, 161–172. doi:10.1016/j.neuroimage.2019.04.034, Epub 2019/04/15PubMed PMID: 30981858.

An, J., Wang, L., Li, K., Zeng, Y., Su, Y., Jin, Z., et al., 2017. Differential effects of antidepressant treatment on long-range and short-range functional connectivity strength in patients with major depressive disorder. Sci. Rep. 7 (1). doi:10.1038/s41598-017-10575-9, 10214-PubMed PMID: 28860564.

Andrews-Hanna, JR., 2012. The brain's default network and its adaptive role in internal mentation. Neuroscientist 18 (3), 251–270. doi:10.1177/1073858411403316, Epub 06/15PubMed PMID: 21677128.

Avery, M.C., Krichmar, JL., 2015. Improper activation of D1 and D2 receptors leads to excess noise in prefrontal cortex. Front Comput. Neurosci. 9, 31. doi:10.3389/fncom.2015.00031, PubMed PMID: 25814948.

Azmitia, E.C., Segal, M., 1978. An autoradiographic analysis of the differential ascending projections of the dorsal and median raphe nuclei in the rat. J. Comparat. Neurol. 179 (3), 641–667. doi:10.1002/cne.901790311, Epub 1978/06/01PubMed PMID: 565370.

Badhwar, A., Tam, A., Dansereau, C., Orban, P., Hoffstaedter, F., Bellec, P., 2017. Resting-state network dysfunction in Alzheimer's disease: A systematic review and meta-analysis. Alzheimers Dement (Amst) 8, 73–85. doi:10.1016/j.dadm.2017.03.007, PubMed PMID: 28560308.

Bartels, A.L., Leenders, KL., 2009. Parkinson's disease: the syndrome, the pathogenesis and pathophysiology. Cortex 45 (8), 915–921. doi:10.1016/j.cortex.2008.11.010.

Bhagwagar, Z., Whale, R., Cowen, PJ., 2018. State and trait abnormalities in serotonin function in major depression. Br. J. Psychiatry 180 (1), 24–28. doi:10.1192/bjp.180.1.24, Epub 01/02.

Biswal, B., Yetkin, F.Z., Haughton, V.M., Hyde, JS., 1995. Functional connectivity in the motor cortex of resting human brain using echo-planar MRI. Magn. Reson. Med. 34 (4), 537–541. doi:10.1002/mrm.1910340409, PubMed PMID: 8524021.

Celada, P., Puig, M.V., Artigas, F., 2013. Serotonin modulation of cortical neurons and networks. Front Integr. Neurosci. 7, 25. doi:10.3389/fnint.2013.00025, PubMed PMID: 23626526.

Challis, C., Berton, O., 2015. Top-down control of serotonin systems by the prefrontal cortex: a path toward restored socioemotional function in depression. ACS Chem. Neurosci. 6 (7), 1040–1054. doi:10.1021/acschemneuro.5b00007, Epub 03/17PubMed PMID: 25706226.

Chuang, K.H., Lee, H.L., Li, Z., Chang, W.T., Nasrallah, F.A., Yeow, L.Y., et al., 2019. Evaluation of nuisance removal for functional MRI of rodent brain. Neuroimage 188, 694–709. doi:10.1016/j.neuroimage.2018.12.048, PubMed PMID: 30593905.

Ciranna, L., 2006. Serotonin as a modulator of glutamate- and GABA-mediated neurotransmission: implications in physiological functions and in pathology. Curr. Neuropharmacol. 4 (2), 101–114. doi:10.2174/157015906776359540, PubMed PMID: 18615128.

Cole, D.M., Beckmann, C.F., Oei, N.Y., Both, S., van Gerven, J.M., Rombouts, SA., 2013. Differential and distributed effects of dopamine neuromodulations on resting-state network connectivity. Neuroimage 78, 59–67. doi:10.1016/j.neuroimage.2013.04.034, PubMed PMID: 23603346.

Cole, D.M., Oei, N.Y., Soeter, R.P., Both, S., van Gerven, J.M., Rombouts, S.A., et al., 2013. Dopamine-dependent architecture of cortico-subcortical network connectivity. Cereb Cortex 23 (7), 1509–1516. doi:10.1093/cercor/bhs136, PubMed PMID: 22645252.

Conio, B., Martino, M., Magioncalda, P., Escelsior, A., Inglese, M., Amore, M., et al., 2019. Opposite effects of dopamine and serotonin on resting-state networks: review and implications for psychiatric disorders. Mol. Psychiatry doi:10.1038/s41380-019-0406-4, PubMed PMID: 30953003.

Durstewitz, D., Seamans, J.K., Sejnowski, TJ., 2000. Dopamine-mediated stabilization of delay-period activity in a network model of prefrontal cortex. J. Neurophysiol. 83 (3), 1733–1750. doi:10.1152/jn.2000.83.3.1733, Epub 2000/03/11PubMed PMID: 10712493.

Duvarci, S., Simpson, E.H., Schneider, G., Kandel, E.R., Roeper, J., Sigurdsson, T., 2018. Impaired recruitment of dopamine neurons during working memory in mice with striatal D2 receptor overexpression. Nature Commun. 9 (1), 2822. doi:10.1038/s41467-018-05214-4.

Fischer, A.G., Ullsperger, M., 2017. An update on the role of serotonin and its interplay with dopamine for reward. Front. Human Neurosci. 11 (484). doi:10.3389/fnhum.2017.00484.

Göttlich, M., Münte, T.F., Heldmann, M., Kasten, M., Hagenah, J., Krämer, UM., 2013. Altered resting state brain networks in Parkinson's disease. PloS one 8 (10). doi:10.1371/journal.pone.0077336, e77336-ePubMed PMID: 24204812.

Han, S., Cui, Q., Guo, X., Fan, Y.-S., Guo, J., Zong, X., et al., 2020. Disconnectivity between the raphe nucleus and subcortical dopamine-related regions contributes altered salience network in schizophrenia. Schizophrenia Res. 216, 382–388. doi:10.1016/j.schres.2019.11.006.

Hahn, A., Wadsak, W., Windischberger, C., Baldinger, P., Höflich, A.S., Losak, J., et al., 2012. Differential modulation of the default mode network via serotonin-1A receptors. Proc. Natl. Acad. Sci. USA. 109 (7), 2619–2624. doi:10.1073/pnas.1117104109, Epub 01/30PubMed PMID: 22308408.

Harte, M., O'Connor, W.T., 2004. Evidence for a differential medial prefrontal dopamine D1 and D2 receptor regulation of local and ventral tegmental glutamate and GABA release: A dual probe microdialysis study in the awake rat. Brain Res. 1017 (1), 120–129. doi:10.1016/j.brainres.2004.05.027.

Hjorth, O.R., Frick, A., Gingnell, M., Hoppe, J.M., Faria, V., Hultberg, S., et al., 2019. Expression and co-expression of serotonin and dopamine transporters in social anxiety disorder: a multitracer positron emission tomography study. Molecular Psychiatry doi:10.1038/s41380-019-0618-7.

Judenhofer, M.S., Wehrl, H.F., Newport, D.F., Catana, C., Siegel, S.B., Becker, M., et al., 2008. Simultaneous PET-MRI: a new approach for functional and morphological imaging. Nat Med. 14 (4), 459–465. doi:10.1038/nm1700, PubMed PMID: 18376410.

Kahnt, T., Weber, S.C., Haker, H., Robbins, T.W., Tobler, PN., 2015. Dopamine D2-receptor

blockade enhances decoding of prefrontal signals in humans. J. Neurosci. 35 (9), 4104–4111. doi:10.1523/jneurosci.4182-14.2015.
Kellendonk, C., Simpson, E.H., Polan, H.J., Malleret, G., Vronskaya, S., Winiger, V., et al., 2006. Transient and selective overexpression of dopamine D2 receptors in the striatum causes persistent abnormalities in prefrontal cortex functioning. Neuron 49 (4), 603–615. doi:10.1016/j.neuron.2006.01.023.
Kelly, C., de Zubicaray, G., Di Martino, A., Copland, D.A., Reiss, P.T., Klein, D.F., et al., 2009. L-dopa modulates functional connectivity in striatal cognitive and motor networks: a double-blind placebo-controlled study. J. Neurosci. 29 (22), 7364–7378. doi:10.1523/JNEUROSCI.0810-09.2009, PubMed PMID: 19494158; PubMed Central PMCID: PMCPMC2928147.
Krabbe, S., Duda, J., Schiemann, J., Poetschke, C., Schneider, G., Kandel, E.R., et al., 2015. Increased dopamine D2 receptor activity in the striatum alters the firing pattern of dopamine neurons in the ventral tegmental area. Proc. Natl. Acad. Sci. 112 (12), E1498–EE506. doi:10.1073/pnas.1500450112.
Lanzenberger, R., Kranz, G.S., Haeusler, D., Akimova, E., Savli, M., Hahn, A., et al., 2012. Prediction of SSRI treatment response in major depression based on serotonin transporter interplay between median raphe nucleus and projection areas. Neuroimage 63 (2), 874–881. doi:10.1016/j.neuroimage.2012.07.023, Epub 2012/07/26PubMed PMID: 22828162.
Lemogne, C., Delaveau, P., Freton, M., Guionnet, S., Fossati, P., 2012. Medial prefrontal cortex and the self in major depression. J. Affect. Disorders 136 (1-2), e1–e11. doi:10.1016/j.jad.2010.11.034, Epub 2010/12/28PubMed PMID: 21185083.
Lui, Su, Wu, Q., Qiu, L., Yang, X., Kuang, W., Chan, RC.K., et al., 2011. Resting-state functional connectivity in treatment-resistant depression. Am. J. Psychiatry 168 (6), 642–648. doi:10.1176/appi.ajp.2010.10101419, PubMed PMID: 21362744.
Lundquist, P., Roman, M., Syvänen, S., Hartvig, P., Blomquist, G., Hammarlund-Udenaes, M., et al., 2007. Effect on [11C]DASB binding after tranylcypromine-induced increase in serotonin concentration: Positron emission tomography studies in monkeys and rats. Synapse 61 (6), 440–449. doi:10.1002/syn.20382.
Magioncalda, P., Martino, M., 2021. A unified model of the pathophysiology of bipolar disorder. Molecul. Psychiatry doi:10.1038/s41380-021-01091-4.
Magioncalda, P., Martino, M., Conio, B., Escelsior, A., Piaggio, N., Presta, A., et al., 2015. Functional connectivity and neuronal variability of resting state activity in bipolar disorder–reduction and decoupling in anterior cortical midline structures. Hum Brain Mapp 36 (2), 666–682. doi:10.1002/hbm.22655, Epub 2014/10/14PubMed PMID: 25307723; PubMed Central PMCID: PMCPMC6869107.
Manoliu, A., Meng, C., Brandl, F., Doll, A., Tahmasian, M., Scherr, M., et al., 2014. Insular dysfunction within the salience network is associated with severity of symptoms and aberrant inter-network connectivity in major depressive disorder. Frontiers Human Neurosci. 7 (930). doi:10.3389/fnhum.2013.00930.
Matthew Brett, J.-.L.A., Valabregue, R., Poline, J.-.B., 2002. Region of interest analysis using an SPM toolbox. In: Proceedings of the 8th International Conference on Functional Mapping of the Human Brain. Sendai JapanJune 2-6.
McCutcheon, R.A., Nour, M.M., Dahoun, T., Jauhar, S., Pepper, F., Expert, P., et al., 2019. Mesolimbic dopamine function is related to salience network connectivity: an integrative positron emission tomography and magnetic resonance study. Biol. Psychiatry 85 (5), 368–378. doi:10.1016/j.biopsych.2018.09.010, PubMed PMID: 30389131; PubMed Central PMCID: PMCPMC6360933.
Martino, M., Magioncalda, P., Huang, Z., Conio, B., Piaggio, N., Duncan, N.W., et al., 2016. Contrasting variability patterns in the default mode and sensorimotor networks balance in bipolar depression and mania. Proc. Natl. Acad. Sci. 113 (17), 4824–4829. doi:10.1073/pnas.1517558113.
Martino, M., Magioncalda, P., 2021. Tracing the psychopathology of bipolar disorder to the functional architecture of intrinsic brain activity and its neurotransmitter modulation: a three-dimensional model. Molecular. Psychiatry doi:10.1038/s41380-020-00982-2.
Nagano-Saito, A., Lissemore, J.I., Gravel, P., Leyton, M., Carbonell, F., Benkelfat, C., 2017. Posterior dopamine D2/3 receptors and brain network functional connectivity. Synapse 71 (11). doi:10.1002/syn.21993.
Navailles, S., De Deurwaerdère, P., 2011. Presynaptic control of serotonin on striatal dopamine function. Psychopharmacol. 213 (2), 213–242. doi:10.1007/s00213-010-2029-y.
Newberg, A.B., Amsterdam, J.D., Wintering, N., Shults, J., 2012. Low brain serotonin transporter binding in major depressive disorder. Psychiatry Res. 202 (2), 161–167. doi:10.1016/j.pscychresns.2011.12.015, Epub 06/12PubMed PMID: 22698760.
Park, M.-.H., Park, E-H., 2000. Synaptic concentration of dopamine in rat striatal slices in relationship to [3H]raclopride binding to the dopamine D2 receptor. Arch. Pharmacal. Res. 23 (4), 360–366. doi:10.1007/BF02975448.
Parsey, R.V., Hastings, R.S., Oquendo, M.A., Huang, Y.Y., Simpson, N., Arcement, J., et al., 2006. Lower serotonin transporter binding potential in the human brain during major depressive episodes. Am. J. Psychiatry 163 (1), 52–58. doi:10.1176/appi.ajp.163.1.52, PubMed PMID: 16390889.
Patel, V.D., Lee, D.E., Alexoff, D.L., Dewey, S.L., Schiffer, WK., 2008. Imaging dopamine release with positron emission tomography (PET) and (11)C-raclopride in freely moving animals. Neuroimage 41 (3), 1051–1066. doi:10.1016/j.neuroimage.2008.02.065, Epub 2008/04/30PubMed PMID: 18442926.
Paterson, L.M., Tyacke, R.J., Nutt, D.J., Knudsen, GM., 2010. Measuring endogenous 5-HT release by emission tomography: promises and pitfalls. J. Cerebral Blood Flow Metabol. 30 (10), 1682–1706. doi:10.1038/jcbfm.2010.104.
Puig, M.V., Antzoulatos, E.G., Miller, EK., 2014. Prefrontal dopamine in associative learning and memory. Neuroscience 282, 217–229. doi:10.1016/j.neuroscience.2014.09.026, Epub 09/18PubMed PMID: 25241063.
Roffman, J.L., Tanner, A.S., Eryilmaz, H., Rodriguez-Thompson, A., Silverstein, N.J., Ho, N.F., et al., 2016. Dopamine D1 signaling organizes network dynamics underlying working memory. Sci. Adv. 2 (6), e1501672. doi:10.1126/sciadv.1501672, PubMed PMID: 27386561; PubMed Central PMCID: PMCPMC4928887.
Roussakis, A.-.A., Politis, M., Towey, D., Piccini, P., 2016. Serotonin-to-dopamine transporter ratios in Parkinson disease relevance for dyskinesias. Neurology 86 (12), 1152–1158. doi:10.1212/wnl.0000000000002494.
Rubinov, M., Sporns, O., 2010. Complex network measures of brain connectivity: uses and interpretations. Neuroimage 52 (3), 1059–1069. doi:10.1016/j.neuroimage.2009.10.003, PubMed PMID: 19819337.
Russo, D., Martino, M., Magioncalda, P., Inglese, M., Amore, M., Northoff, G., 2020. Opposing changes in the functional architecture of large-scale networks in bipolar mania and depression. Schizophrenia Bulletin 46 (4), 971–980. doi:10.1093/schbul/sbaa004.
Savitz, J.B., Drevets, WC., 2009. Imaging phenotypes of major depressive disorder: genetic correlates. Neuroscience 164 (1), 300–330. doi:10.1016/j.neuroscience.2009.03.082.
Savitz, J., Drevets, WC., 2009. Bipolar and major depressive disorder: neuroimaging the developmental-degenerative divide. Neurosci. Biobehav. Rev. 33 (5), 699–771. doi:10.1016/j.neubiorev.2009.01.004.
Seeley, WW., 2019. The salience network: a neural system for perceiving and responding to homeostatic demands. J. Neurosci. 39 (50), 9878–9882. doi:10.1523/jneurosci.1138-17.2019.
Seeley, W.W., Menon, V., Schatzberg, A.F., Keller, J., Glover, G.H., Kenna, H., et al., 2007. Dissociable intrinsic connectivity networks for salience processing and executive control. J. Neurosci. 27 (9), 2349–2356. doi:10.1523/jneurosci.5587-06.2007, Epub 2007/03/03PubMed PMID: 17329432; PubMed Central PMCID: PMCPMC2680293.
Smith, Y., Bevan, M.D., Shink, E., Bolam, JP., 1998. Microcircuitry of the direct and indirect pathways of the basal ganglia. Neuroscience 86 (2), 353–387. doi:10.1016/s0306-4522(98)00004-9, Epub 1999/01/09PubMed PMID: 9881853.
Sorg, C., Manoliu, A., Neufang, S., Myers, N., Peters, H., Schwerthöffer, D., et al., 2013. Increased intrinsic brain activity in the striatum reflects symptom dimensions in schizophrenia. Schizophrenia Bull. 39 (2), 387–395. doi:10.1093/schbul/sbr184.
Turkheimer, F.E., Selvaraj, S., Hinz, R., Murthy, V., Bhagwagar, Z., Grasby, P., et al., 2012. Quantification of ligand PET studies using a reference region with a displaceable fraction: application to occupancy studies with [(11)C]-DASB as an example. J. Cerebral Blood Flow Metabol. Offic. J. Int. Soc. Cerebral Blood Flow Metabol. 32 (1), 70–80. doi:10.1038/jcbfm.2011.108, Epub 08/03PubMed PMID: 21811290.
Vazquez-Borsetti, P., Cortes, R., Artigas, F., 2009. Pyramidal neurons in rat prefrontal cortex projecting to ventral tegmental area and dorsal raphe nucleus express 5-HT2A receptors. Cereb. Cortex 19 (7), 1678–1686. doi:10.1093/cercor/bhn204, Epub 2008/11/26PubMed PMID: 19029064; PubMed Central PMCID: PMCPMC2693622.
Vidal, B., Fieux, S., Redouté, J., Villien, M., Bonnefoi, F., Le Bars, D., et al., 2018. *In vivo* biased agonism at 5-HT(1A) receptors: characterisation by simultaneous PET/MR imaging. Neuropsychopharmacology 43 (11), 2310–2319. doi:10.1038/s41386-018-0145-2, Epub 07/06PubMed PMID: 30030540.
Walker, M., Ehrlichmann, W., Stahlschmidt, A., Pichler, B.J., Fischer, K., 2016. *In vivo* evaluation of 11C-DASB for quantitative SERT Imaging in rats and mice. J. Nucl. Med. 57 (1), 115–121. doi:10.2967/jnumed.115.163683, Epub 2015/10/31PubMed PMID: 26514178.
Wang, H.-.L., Zhang, S., Qi, J., Wang, H., Cachope, R., Mejias-Aponte, C.A., et al., 2019. Dorsal raphe dual serotonin-glutamate neurons drive reward by establishing excitatory synapses on VTA mesoaccumbens dopamine neurons. Cell Rep. 26 (5). doi:10.1016/j.celrep.2019.01.014, 1128-42.e7PubMed PMID: 30699344.
Wehrl, H.F., Hossain, M., Lankes, K., Liu, C.C., Bezrukov, I., Martirosian, P., et al., 2013. Simultaneous PET-MRI reveals brain function in activated and resting state on metabolic, hemodynamic and multiple temporal scales. Nat. Med. 19 (9), 1184–1189. doi:10.1038/nm.3290, PubMed PMID: 23975025.
Willeit, M., Sitte, H.H., Thierry, N., Michalek, K., Praschak-Rieder, N., Zill, P., et al., 2008. Enhanced serotonin transporter function during depression in seasonal affective disorder. Neuropsychopharmacology 33 (7), 1503–1513. doi:10.1038/sj.npp.1301560, PubMed PMID: 17882235.
Xia, M., Wang, J., He, Y., 2013. BrainNet Viewer: A Network Visualization Tool for Human Brain Connectomics. PLoS One 8, e68910.
Yamamoto, S., Onoe, H., Tsukada, H., Watanabe, Y., 2007. Effects of increased endogenous serotonin on the in vivo binding of [11C]DASB to serotonin transporters in conscious monkey brain. Synapse 61 (9), 724–731. doi:10.1002/syn.20422.
Yan, C.-.G., Chen, X., Li, L., Castellanos, F.X., Bai, T.-.J., Bo, Q.-.J., et al., 2019. Reduced default mode network functional connectivity in patients with recurrent major depressive disorder. Proc. Natl. Acad. Sci. USA 116 (18), 9078–9083. doi:10.1073/pnas.1900390116, Epub 04/12PubMed PMID: 30979801.
Zhang, J., Magioncalda, P., Huang, Z., Tan, Z., Hu, X., Hu, Z., et al., 2019. Altered global signal topography and its different regional localization in motor cortex and hippocampus in mania and depression. Schizophr. Bull 45 (4), 902–910. doi:10.1093/schbul/sby138, Epub 2018/10/05PubMed PMID: 30285255; PubMed Central PMCID: PMCPMC6581125.

Supplementary Methods

Schiffer rat brain atlas

The division in different brain regions was performed based on the Schiffer rat brain atlas provided in the PMOD software (PMOD Technologies LLC, Zurich, Switzerland). A total of 14 regions were selected. In Supplementary Table 3 a list of the regions, their volumes and abbreviations is provided.

Supplementary Table 3: Regions selected for analysis from the Schiffer brain atlas, along with their volumes and abbreviations.

Brain region (ROI)	ROI volume [mm^3]	Abbreviation
Nucleus Accumbens	7.944	NAc
Amygdala	21.120	Amyg
Caudate Putamen	43.552	CPu
Cingulate Cortex	14.480	Cg
Insular Cortex	21.128	Ins
Medial Prefrontal Cortex	6.304	mPFC
Motor Cortex	32.608	MC
Orbitofrontal Cortex	18.936	OFC
Parietal Cortex	7.632	PaC
Retrosplenial Cortex	18.920	RS
Somatosensory Cortex	71.600	S1
Anterodorsal Hippocampus	25.064	CA1
Posterior Hippocampus	9.784	CA1-p
Thalamus	30.712	Th

Supplementary Table 4 lists the regions comprising each of the analyzed resting-state networks.

Supplementary Table 4: Regions comprising every analyzed resting-state network.

Default-mode network (DMN)	Salience network	Sensory-motor network
mPFC	NAc	CPu
OFC	Amyg	M1
PaC	Cg	S1
RS	Ins	Th
CA1		
CA1-p		

Radiotracer synthesis

[^{11}C]Raclopride synthesis was performed as described by Langer et al. (Langer et al., 1999) with the optimized HPLC conditions of van Laeken et al. (Van Laeken et al., 2013). After dilution with water, the isolated fraction was trapped on a conditioned Strata-X cartridge (Phenomenex, Aschaffenburg, Germany), eluted with 0.5 ml ethanol and diluted with 5 ml phosphate-buffered saline.

[^{11}C]DASB was synthesized similar to the procedure reported by Wilson et al. (Wilson et al., 2000). Briefly, [^{11}C]MeI was trapped in a solution of 2 mg precursor in 500 µl DMSO. After heating to 100 °C for 2 min the reaction was diluted with 1.5 ml HPLC eluent (3 mM Na_2HPO_4 containing 64 % MeCN) and purified on a Luna C18(2) column (250 mm x 10 mm, Phenomenex). The isolated peak was diluted with 70 ml water containing 20 mg sodium ascorbate, loaded onto a conditioned Strata-X cartridge (Phenomenex), eluted with 0.5 ml ethanol and diluted with 5 ml phosphate-buffered saline.

The radioactive tracers had molar activities of 82 ± 28 GBq/µmol for [^{11}C]raclopride and 50 ± 16 GBq/µmol for [^{11}C]DASB at the start of the PET acquisition (Supplementary Figure 2B and C).

Seed-based resting-state functional connectivity analysis

To derive rs-FC between the selected regions the regional time-series of the preprocessed fMRI scans were extracted using the MarsBaR toolbox. Every regional BOLD time-course was computed as the mean of all the time-courses of the voxels comprising the respective region:

$$Y_I = \frac{1}{N_I} \sum_{i \epsilon I} y_i \ , \qquad (1)$$

where I is the delineated brain ROI, Y_I its derived time-series, N_I is the number of voxels comprising ROI I and y_i is the time series of voxel i.

Pearson's r correlation coefficients were calculated between each the extracted signals from each pair of regions to determine seed-based rs-FC employing an algorithm written in-house:

$$r = \frac{\sum_{i=1}^{n}(u_i - \bar{u})(v_i - \bar{v})}{\sqrt{\sum_{i=1}^{n}(u_i - \bar{u})^2}\sqrt{\sum_{i=1}^{n}(v_i - \bar{v})^2}} \ , \qquad (2)$$

where r is Pearson's correlation coefficient, n is the number of samples, u_i and v_i are the single samples and $\bar{u}$ and $\bar{v}$ are the arithmetical sample means.

Since the cerebellum was excluded from fMRI analysis, as it was used as reference region for the determination of BP_{nd} values, the approach yielded individual 48 x 48 correlation matrices. The 48 self-correlations were set to zero; thus, each individual scan included 2256 pair-wise correlation coefficients.

For group-level analyses, the calculated correlation coefficients were first transformed into Fischer's z-scores:

$$Z = \frac{1}{2}\ln\frac{(1+r)}{(1-r)} = \operatorname{arctanh}(r) \ , \qquad (3)$$

Each z-score was averaged over the two cohorts respectively.

Calculation of anterior DMN connectivity balance

To investigate the rs-FC of the DMN in further detail in association with medial prefrontal SERT availabilities the the average connectivity between the anterior DMN, comprised of

mPFC and OFC, and the posterior DMN, comprised of RS, Par, CA1 and CA1-p, was subtracted from the average connectivity within the anterior DMN, computed as a mean of all edges between mPFC and OFC. A larger difference implies that the within-network connectivity of the anterior DMN is more pronounced in relationship to its between-network connectivity to the posterior DMN. We performed correlations between the obtained data and medial prefrontal [^{11}C]DASB bindings to evaluate the association between this metric and SERT in this region.

Supplementary Results

The bodyweights of the scanned animals and the radioactivity of the injected tracers are depicted in Supplementary Figure 14.

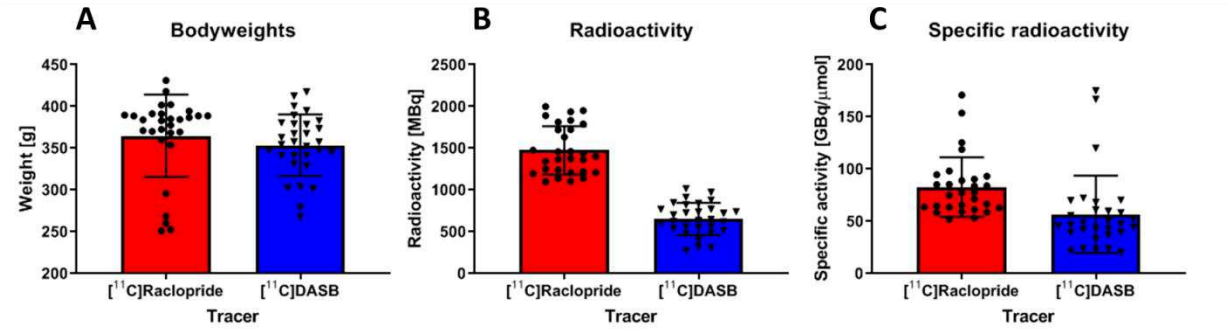

Supplementary Figure 14: (A) Bodyweights of the used rats, (B) radioactivity and (C) specific radioactivity values of injected tracers (n = 29 for [^{11}C]raclopride and n = 30 for [^{11}C]DASB).

The distributions of the injected tracers, as well as the three RSNs investigated are presented in Supplementary Figure 15.

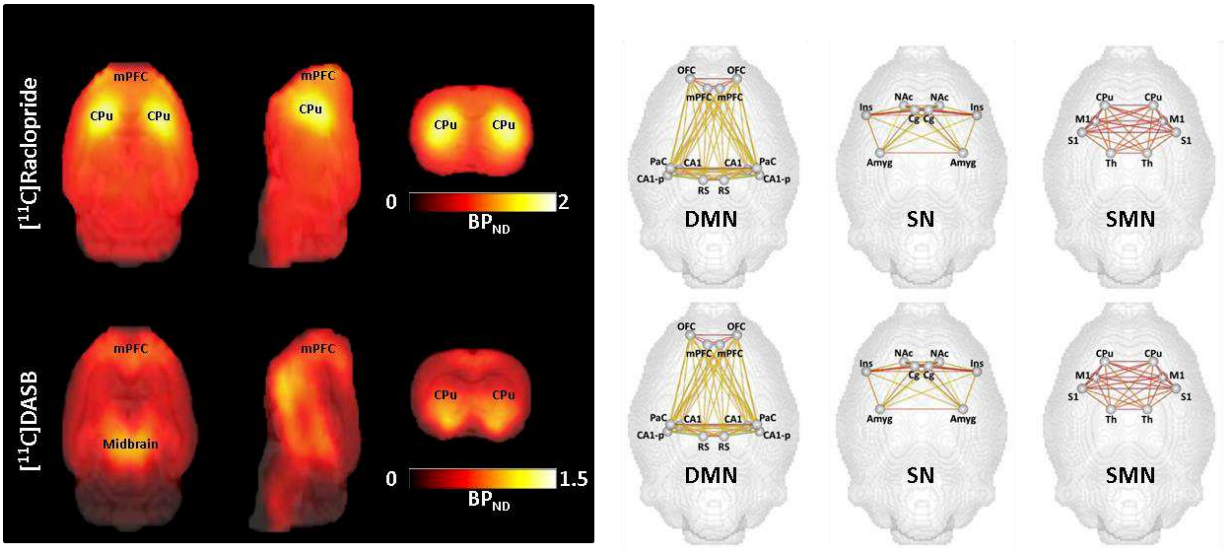

Supplementary Figure 15: PET and fMRI analyses. (A) Group-mean [^{11}C]raclopride and [^{11}C]DASB BP_{ND} maps. **(B)** Resting-state networks extracted from the mean rs-FC analysis performed for the [^{11}C]raclopride (upper row) and [^{11}C]DASB (lower row) cohorts. Connectivity patterns are presented for the default-mode network, salience network and sensory-motor network. Abbreviations: DMN = default-mode network; SN = salience network; SMN = sensorimotor network. Please refer to *Supplementary Table 2* for a list of regions comprising each network.

The variance between regional BP_{ND} values was observed to be mainly driven by global variance between subjects, confirming previous findings in a similar context (Roffman et al., 2016). The scatter plots between the average WB BP_{ND} values for each subject and the corresponding BP_{ND} values of the CPu and mPFC are shown in Supplementary Figure 16. Since our aim was to delineate differences between regions across subjects, rather than global differences, we normalized the BP_{ND} values to exclude unexplained global effects similarly to the method indicated by Roffman et al. (Roffman et al., 2016) for the type of analysis performed.

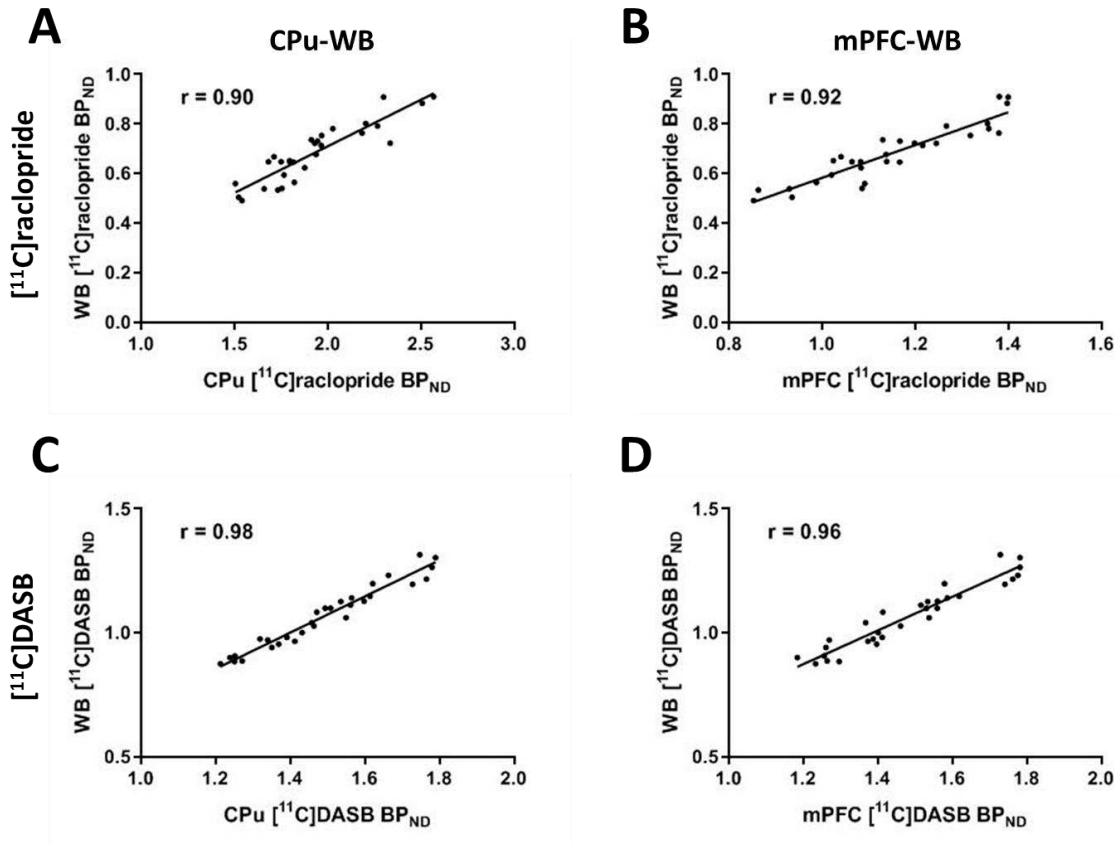

Supplementary Figure 16: Scatter plots indicating correlations of global BP_{ND} variance with CPu and mPFC variance in [^{11}C]raclopride and [^{11}C]DASB. [^{11}C]raclopride: **(A)** CPu – WB, **(B)** mPFC-WB; [^{11}C]DASB: **(C)** CPu – WB, **(D)** mPFC – WB. Abbreviations: CPu = caudate putamen, WB = whole brain, mPFC = medial prefrontal cortex..

The scatter plots corresponding to the correlations between all networks presented in the main manuscript are depicted in Supplementary Figure 17 - Supplementary Figure 20.

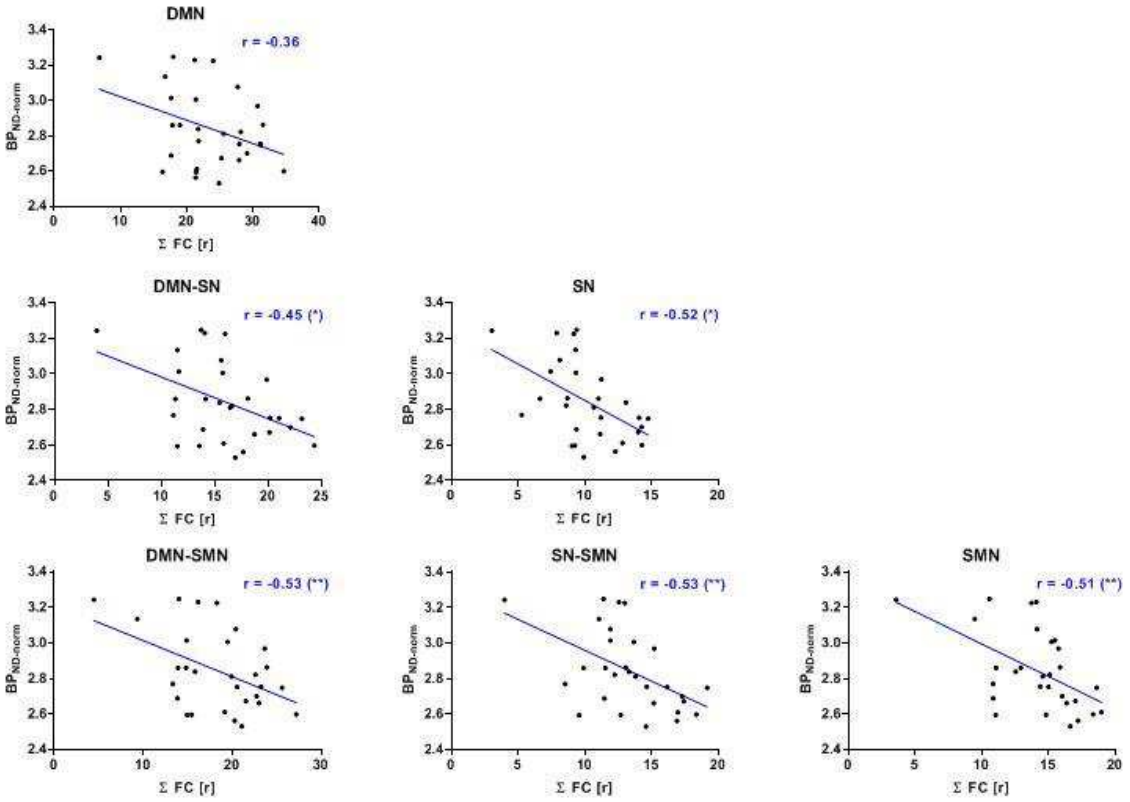

Supplementary Figure 17: Scatter plots depicting the correlations between CPu [^{11}C]raclopride $BP_{ND\text{-}norm}$ values and within and between-network rs-FC. Abbreviations: DMN = default-mode network, SN = salience network, SMN = sensorimotor network.

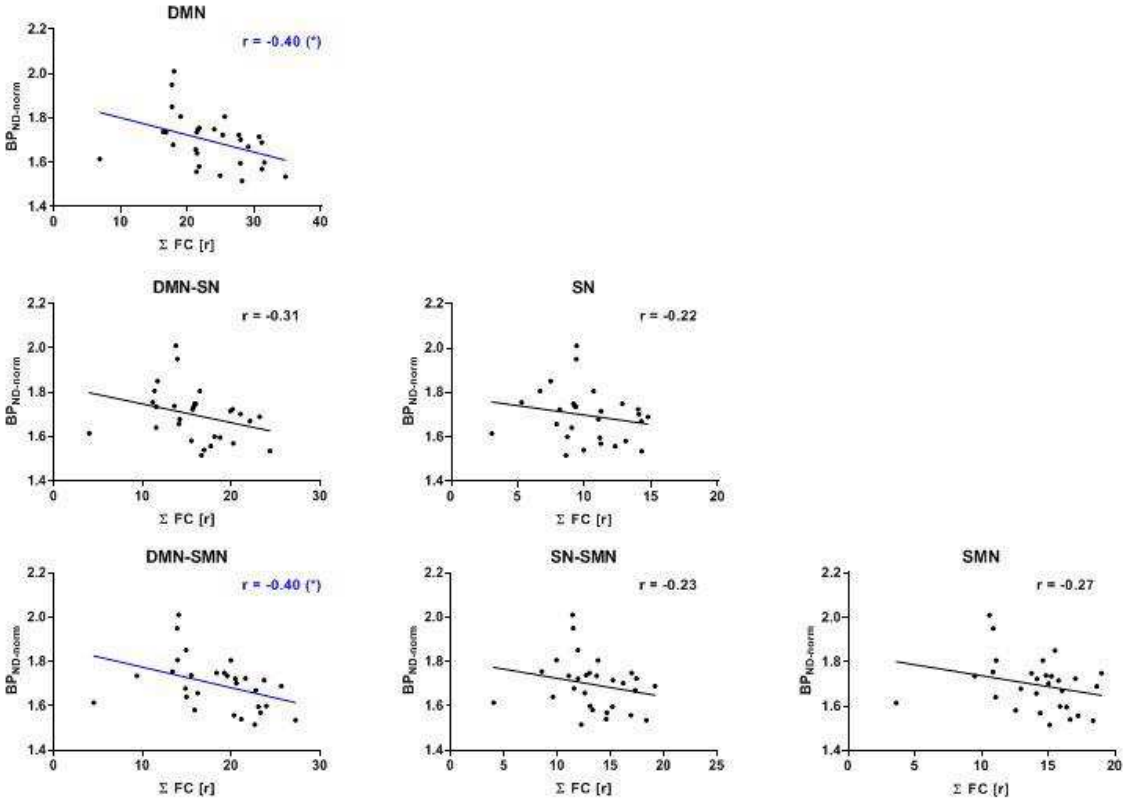

Supplementary Figure 18: Scatter plots depicting the correlations between mPFC [^{11}C]raclopride $BP_{ND\text{-}norm}$ values and within and between-network rs-FC. Abbreviations: DMN = default-mode network, SN = salience network, SMN = sensorimotor network.

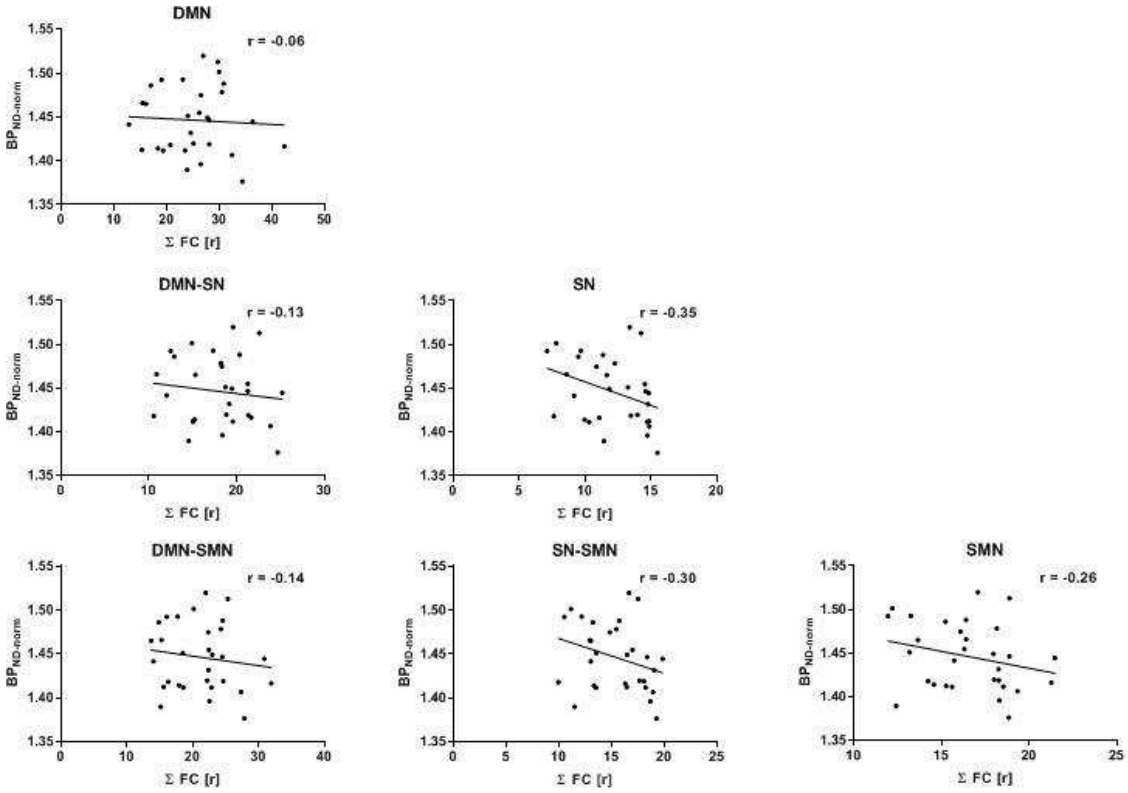

Supplementary Figure 19: Scatter plots depicting the correlations between CPu [^{11}C]DASB $BP_{ND\text{-}norm}$ values and within and between-network rs-FC. Abbreviations: DMN = default-mode network, SN = salience network, SMN = sensorimotor network.

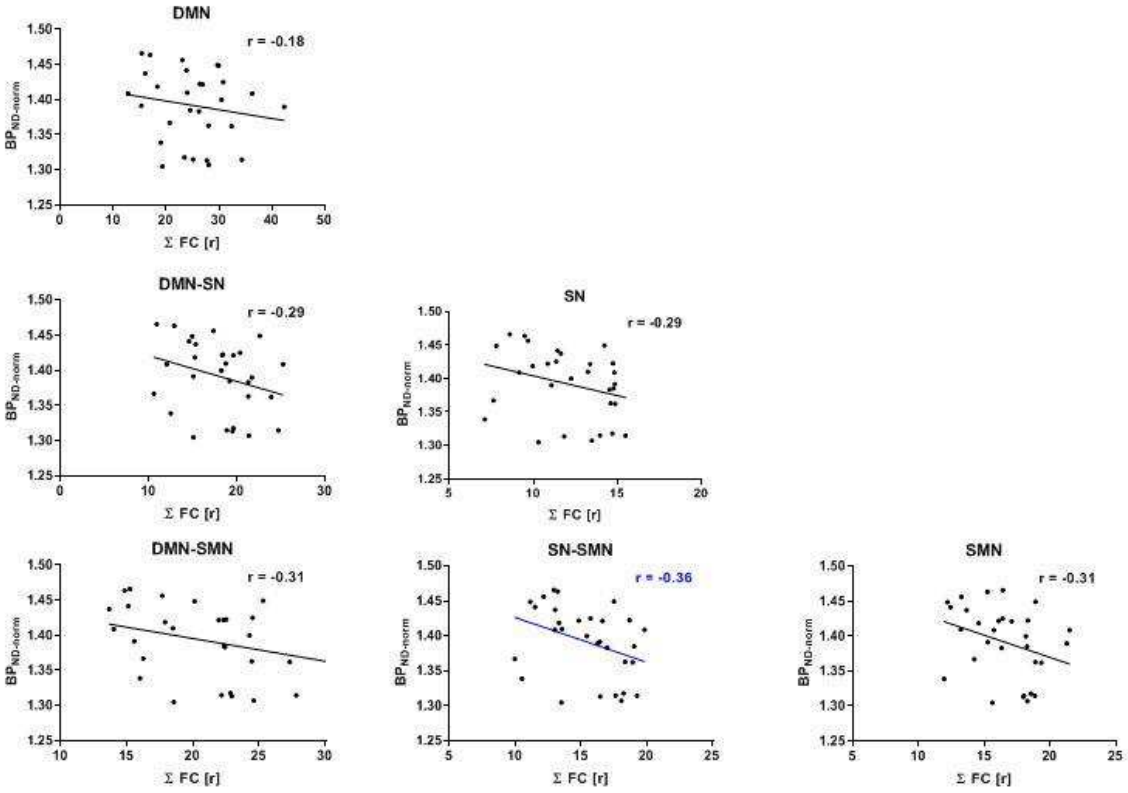

Supplementary Figure 20: Scatter plots depicting the correlations between mPFC [^{11}C]DASB $BP_{ND\text{-}norm}$ values and within and between-network rs-FC. Abbreviations: DMN = default-mode network, SN = salience network, SMN = sensorimotor network.

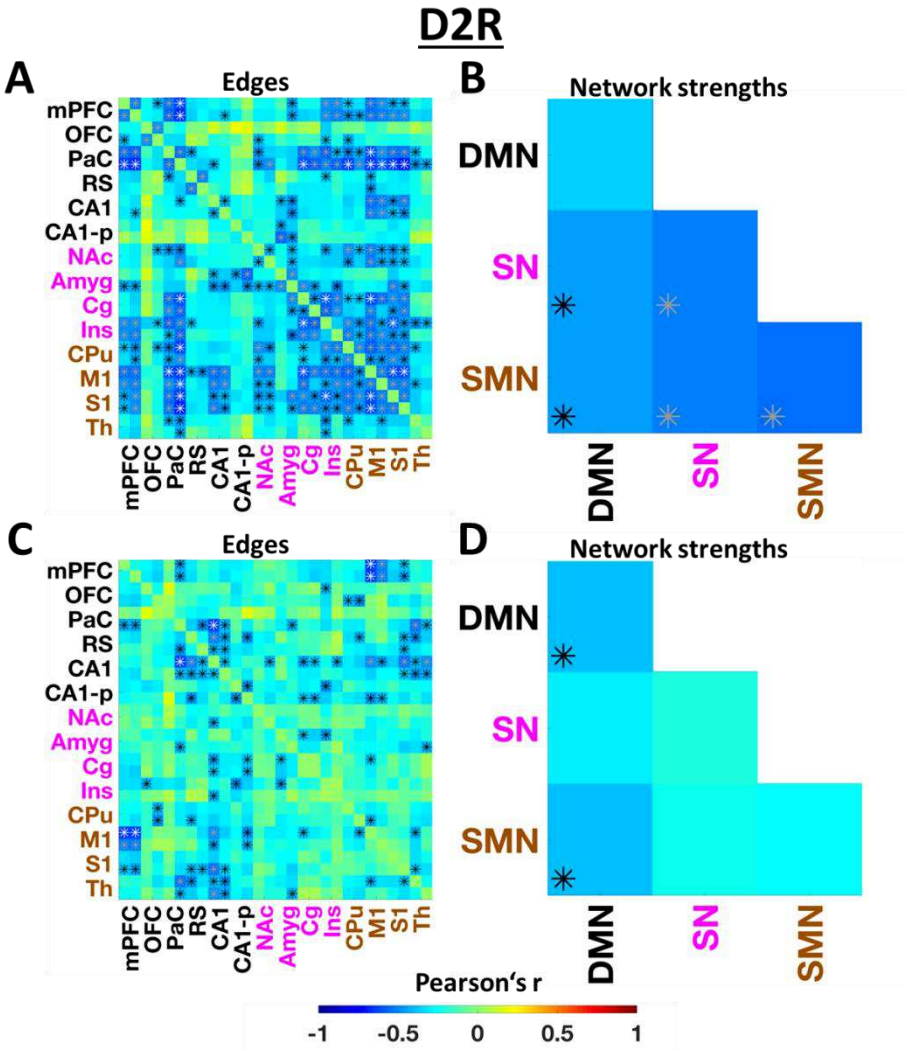

Supplementary Figure 21: Significant correlations for CPu (A and B) and mPFC (C and D) [^{11}C]raclopride bindings and rs-FC shown at uncorrected thresholds of $p < 0.05$ (black asterisks), $p < 0.01$ (grey asterisks) and $p < 0.001$ (white asterisks).

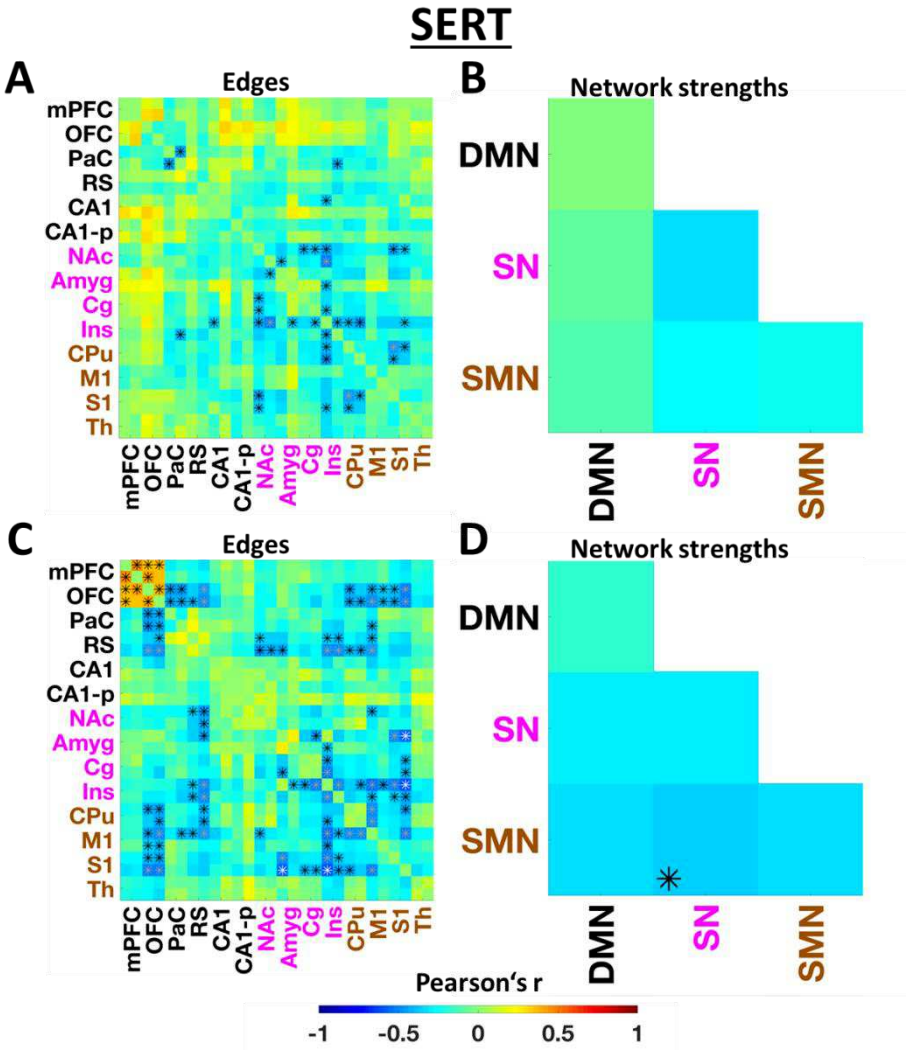

Supplementary Figure 22: Significant correlations for CPu (A and B) and mPFC (C and D) [^{11}C]DASB bindings and rs-FC shown at uncorrected thresholds of p < 0.05 (black asterisks), p < 0.01 (grey asterisks) and p < 0.001 (white asterisks).

We performed an additional analysis to further emphasize the effect according to which mPFC SERT binding positively correlates with rs-FC within the anterior DMN in contrast to rs-FC between the anterior DMN and posterior DMN, SN and SMN, shifting the balance to anterior DMN processing (Supplementary Figure 23).

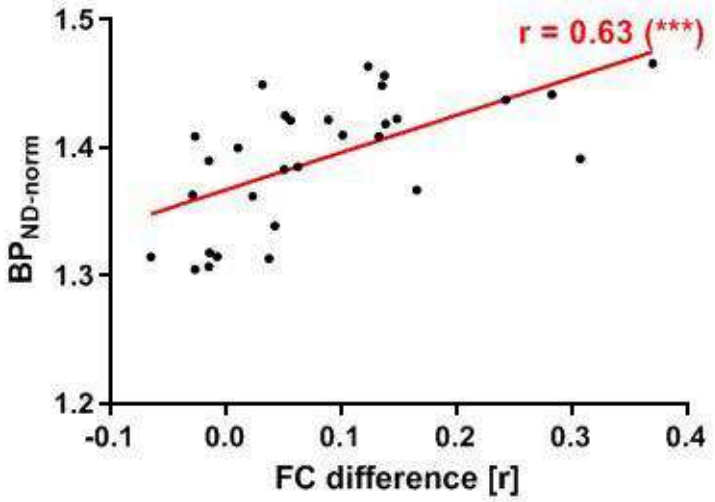

Supplementary Figure 23: Correlation between [^{11}C]DASB binding in the mPFC and the difference of the average connectivity within the anterior DMN, comprising all edges between mPFC and OFC, and the rs-FC between the anterior DMN and the posterior DMN, SN and SMN was highly significant (r = 0.63, p = 0.0003).

One potential caveat of our readout is the current lack of consensus regarding certain regions comprising different resting-state networks. Here, for the DMN we based our analysis on previous studies on the rat default-mode network (Hsu et al., 2016b; Lu et al., 2012), indicating the orbitofrontal, prelimbic, retrosplenial, cingulate, posterior parietal, visual and auditory cortices, as well as the hippocampus as part of the DMN. However, with the aim to increase the translatability to the human DMN structure of our readout, we did not include the auditory and visual cortices, since most human studies regard these regions as being part of separate networks (Rosazza and Minati, 2011). Additionally, we included the cingulate cortex into the salience network, previous literature regarding it as a central hub of this network (Seeley, 2019; Uddin et al., 2019). While being less characterized as definite part of the DMN compared to the medial prefrontal and retrosplenial cortices, the orbitofrontal cortex and hippocampus are still regularly regarded as part of the DMN (Rosazza and Minati, 2011; Uddin et al., 2019), hence we also included them as part of this network in our study. However, the inclusion or exclusion of certain regions can have effects on the presented data, as indicate exemplarily in Supplementary Figure 24.

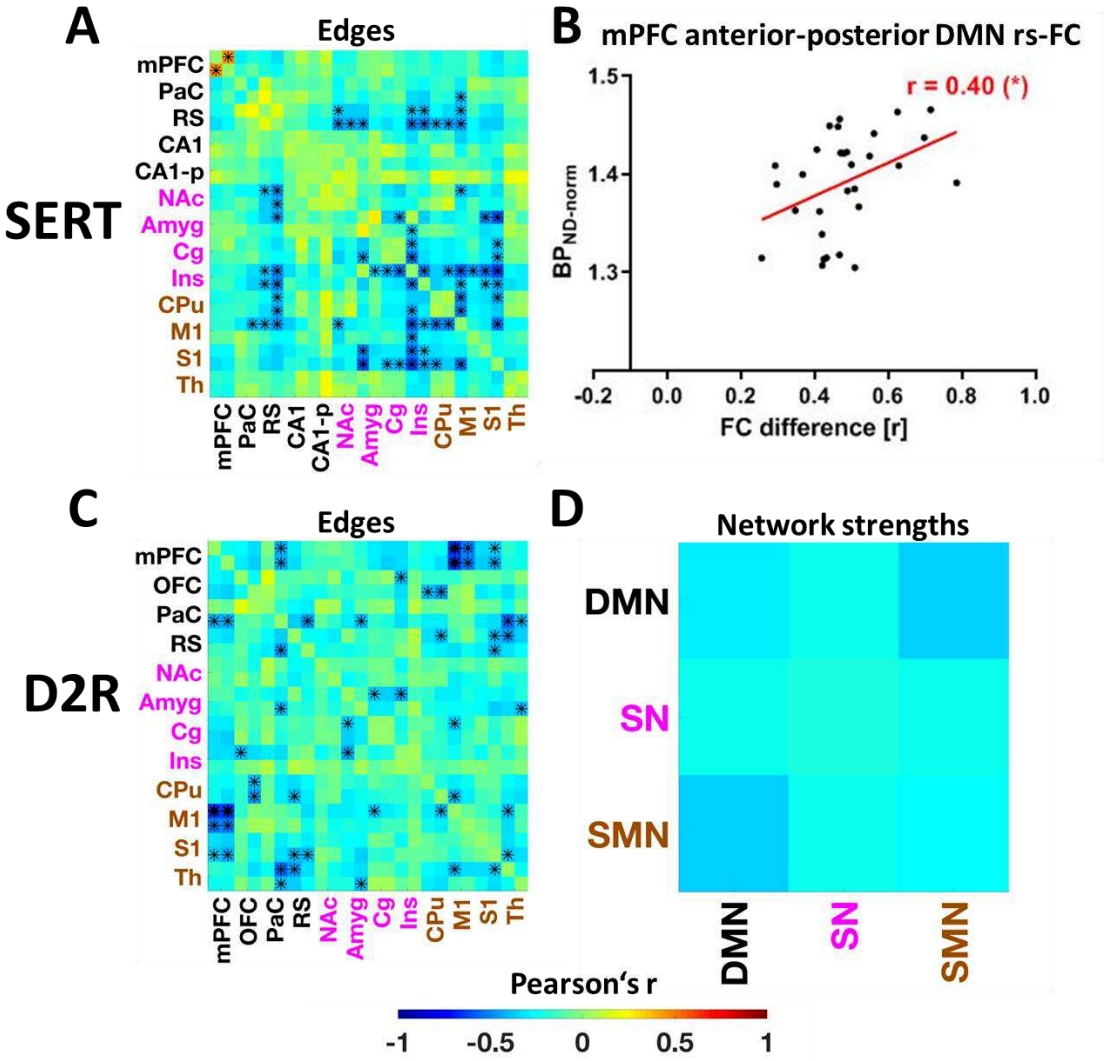

Supplementary Figure 24: Exemplary effects of exclusion or inclusion of regions from networks on readout. (A) Exclusion of the OFC from the DMN decreases **(B)** correlation of the medial prefrontal SERT availability to the difference between the connectivity of the mPFC to the anterior and posterior DMN, yet it still remains significant (r = 0.40). **(C)** Exclusion of the CA1 and CA1-p regions strongly reduces **(D)** the correlation of D2R availability in the mPFC to DMN within-network connectivity and to its connectivity with the SMN, indicating the role of the hippocampus in the observed readout.

Additionally to the presented data, we performed analyses on the rs-FC between the three networks and midbrain areas where dopaminergic and serotonergic tracts originate, defined in the Schiffer atlas by the ventral tegmental area (VTA) and midbrain (MB). Intriguingly, positive correlations were found between medial prefrontal SERT availability and MB-VTA rs-FC, similar to the positive correlations observed with anterior DMN rs-FC. However, the data must be interpreted with caution, since the MB area comprises both the dopaminergic substantia nigra and part of the serotonergic raphé nuclei. The results of this analysis are presented in Supplementary Figure 25.

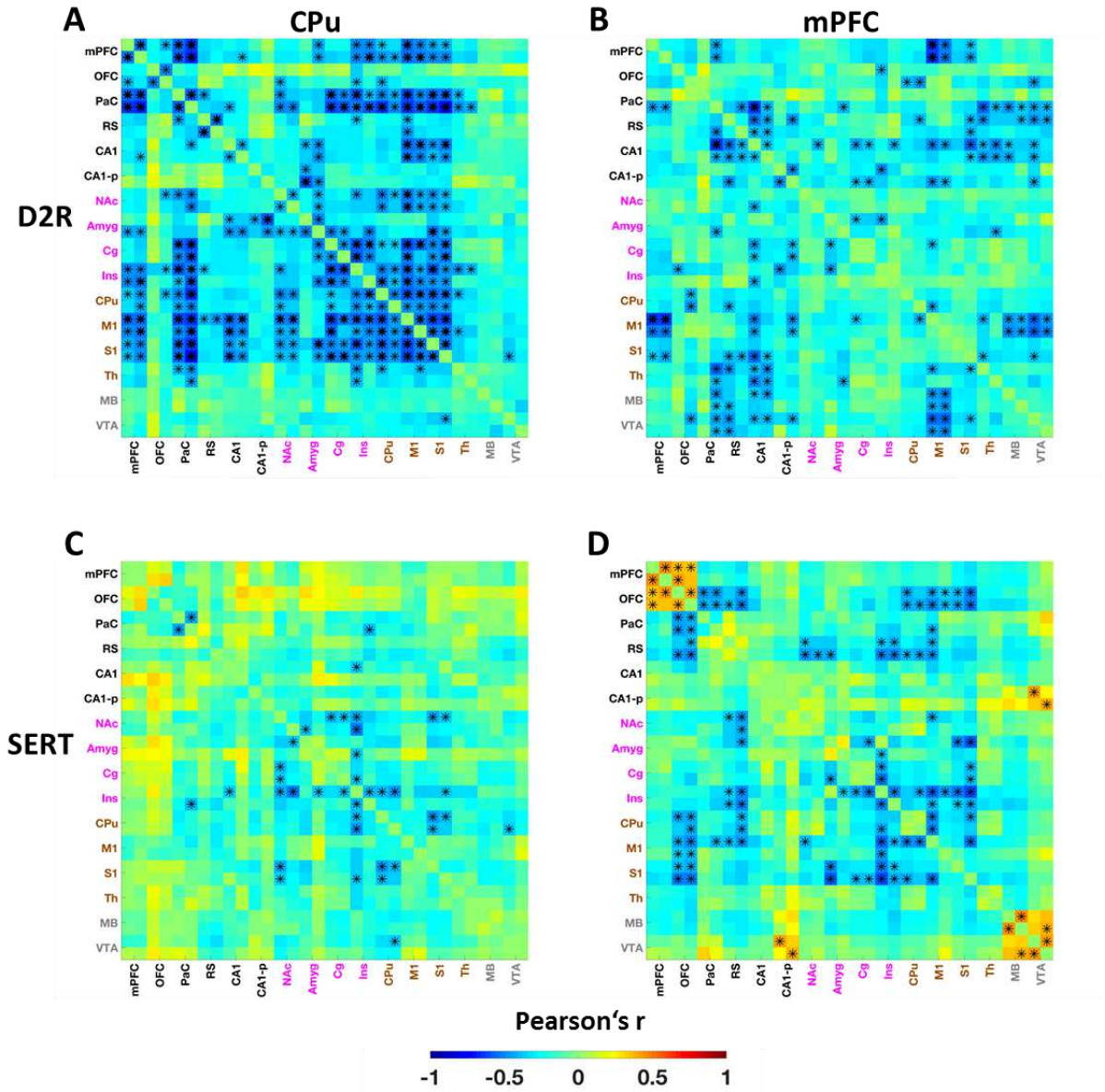

Supplementary Figure 25: Analysis including the midbrain (MB) and ventral tegmental area (VTA) in addition to the DMN, SN and SMN. (A) Correlations with CPu D2R bindings, **(B)** Correlations with mPFC D2R bindings, **(C)** Correlations with CPu SERT bindings, **(D)** Correlations with mPFC SERT bindings.

We performed additional analyses on the correlation between [^{11}C]raclopride and [^{11}C]DASB striatal and medial prefrontal bindings and the temporal variability of the BOLD signal (SD-BOLD) in the three investigated networks. SD-BOLD, similarly to the fractional amplitude of low frequency fluctuations (fALFF), has been suggested to be a measure of intrinsic brain activity in a specific area or region (Conio et al., 2019).

Supplementary Table 5: Correlations (Pearson's r) between (A) [^{11}C]raclopride and (B) [^{11}C]DASB bindings in the CPu and mPFC and SD-BOLD in the DMN, SN and SMN.

Correlations with network-level SD-BOLD

A [^{11}C]Raclopride

Network	CPu	mPFC
DMN	-0.39	-0.35
SN	-0.44	-0.14
SMN	-0.44	-0.23

B [^{11}C]DASB

Network	CPu	mPFC
DMN	-0.11	0.23
SN	-0.23	-0.04
SMN	-0.35	-0.03

Our readout indicates negative correlations between striatal D2Rs and all networks ($p < 0.05$), in line with the correlations observed with rs-FC. Intriguingly, a positive, although lower correlation was also observed between medial prefrontal SERT and the SD-BOLD in the DMN, also in good accordance with the positive correlations reported with the anterior DMN rs-FC.

Limitations and general remarks

While the anesthesia was kept at levels recommended previously (Hutchison et al., 2014) and shown to enable stable physiological readouts (Ionescu et al., 2021b), some confounding effects cannot be excluded for either of the fMRI (Hutchison et al., 2014), [^{11}C]raclopride (McCormick et al., 2011) or [^{11}C]DASB readouts (Whittington and Virag, 2006). However, performing such experiments in small laboratory animals opens up the great opportunity to study such interactions under very controlled conditions and maximized cohort uniformity. Factors such as nutrition, lifestyle, age or gender known to impact D2R and SERT availabilities in a regionally specific manner (Daws and Gould, 2011; Olsen, 2011) can be excluded when interpreting the observed correlations, thereby enabling an inherently

complementary readout to human studies. Hence, our study only included male rats. The hormonal changes occurring during the female menstrual cycle have been shown to affect not only resting-state functional connectivity (Arélin et al., 2015; Hidalgo-Lopez et al., 2020), but also monoaminergic expression, including serotonin (Wihlbäck et al., 2004) and dopamine (Hidalgo-Lopez and Pletzer, 2017). Importantly, animal studies have shown direct correlations between the menstrual cycle and D2 receptor availabilities (Czoty et al., 2009) using PET.

Furthermore, some of the correlations presented in our study are moderate and did not survive FDR correction. Two factors may represent possible causes for this issue. First, compared to large clinical studies, the sizes of our cohorts are relatively limited. Second, D2R and SERT densities are not the sole modulators of rs-FC, other neurotransmitters and receptor types probably having as of yet undiscovered associations with rs-FC. Therefore, our study sheds light on a part of the picture of interactions between neurotransmitter systems and rs-FC; similarly designed studies are still required to thoroughly elucidate this aspect. Importantly, PET/fMRI offers the possibility to generate multi-level data on this very complex matter. In future, a PET/fMRI database, similar to already existing fMRI databases, may be of interest for potential large cohort meta-analyses to this extent. Since most psychiatric medications aim to normalize brain function by interacting with certain receptors or transporters, applying novel analysis methods, as well as machine learning approaches to this type of data can help understand the link between molecular changes and functional changes in the brain, enable the accurate prediction of drug therapies and improve development of treatment strategies for psychiatric disorders.

2.3 Neurovascular Uncoupling: Multimodal Imaging Delineates the Acute Effects of MDMA

The article included in this chapter is currently available ahead of print in The Journal of Nuclear Medicine (Ionescu et al., 2022):

Journal of Nuclear Medicine, Sep 2022, jnumed.122.264391
DOI: 10.2967/jnumed.122.264391
"Neurovascular Uncoupling: Multimodal Imaging Delineates the Acute Effects of 3,4-Methylenedioxymethamphetamine"
Tudor M. Ionescu, Mario Amend, Tadashi Watabe, Jun Hatazawa, Andreas Maurer, Gerald Reischl, Bernd J. Pichler, Hans F. Wehrl, Kristina Herfert

Neurovascular Uncoupling: Multimodal Imaging Delineates the Acute Effects of 3,4-Methylenedioxymethamphetamine

MDMA Induces Neurovascular Uncoupling

Tudor M. Ionescu [1], Mario Amend [1], Tadashi Watabe [1,2], Jun Hatazawa [2], Andreas Maurer[1], Gerald Reischl[1,3], Bernd J. Pichler [1,3], Hans F. Wehrl [1]*, Kristina Herfert [1]*

* contributed equally

[1] Werner Siemens Imaging Center, Department of Preclinical Imaging and Radiopharmacy, Eberhard Karls University Tuebingen, Germany

[2] Department of Nuclear Medicine and Tracer Kinetics, Osaka University, Japan

[3] Cluster of Excellence iFIT (EXC 2180) "Image Guided and Functionally Instructed Tumor Therapies", University of Tübingen, Germany

Corresponding author: Kristina Herfert (kristina.herfert@med.uni-tuebingen.de)

Address: Roentgenweg 13, 72076 Tuebingen, Germany, Tel: +4970712987680

Keywords: Methylenedioxymethamphetamine, Neurovascular Coupling, PET/fMRI, Hemodynamics, Metabolism, Serotonin

Abstract

Background: Psychedelic compounds such as methylenedioxymethamphetamine (methylenedioxymethamphetamine) have attracted increasing interest in recent years due to their therapeutic potential in psychiatric disorders. To understand the acute effects of psychedelic drugs *in vivo*, blood-oxygenation-level-dependent functional magnetic resonance imaging (BOLD-fMRI) has been widely used in recent years. In particular, fMRI studies have suggested that methylenedioxymethamphetamine leads to inhibition of brain activity, challenging previous hypotheses indicating mainly excitatory effects based, among others, on increased metabolism shown by ^{18}F-fluorodeoxyglucose functional positron emission tomography (^{18}F-FDG-fPET). However, interpretation of hemodynamic changes induced by psychedelics is difficult due to their potent vascular effects.

Methods: We aimed to delineate the acute effects of methylenedioxymethamphetamine using simultaneous PET/fMRI in rats. For this purpose, hemodynamic changes measured by BOLD-fMRI were related to alterations in glucose utilization and serotonin transporter (SERT) occupancy using ^{18}F-FDG-fPET/fMRI and ^{11}C-DASB-PET/fMRI.

Results: We show that methylenedioxymethamphetamine induces localized increases in glucose metabolism in limbic projection areas involved in emotional processing. The increased glucose metabolism was accompanied by global cerebral and extracerebral hemodynamic decreases. We further demonstrate a strong correlation between SERT occupancies and regional BOLD reductions after acute methylenedioxymethamphetamine.

Discussion: Our data indicate that hemodynamic decreases after acute methylenedioxymethamphetamine are of non-neuronal nature and initiated peripherally. Within the brain, methylenedioxymethamphetamine induces neuronal activation in limbic projection areas, while increased serotonin levels induced by SERT blockage cause neurovascular uncoupling through direct vascular effects. Correct understanding of the *in vivo* mechanism of methylenedioxymethamphetamine not only supports ongoing research but also warrants a reassessment of previous studies on neuronal effects of psychedelics relying on neurovascular coupling and recommends ^{18}F-FDG-fPET as a potentially more robust measure for pharmacological research.

Introduction

Psychedelic drugs, including lysergic acid diethylamide, psilocybin, and methylenedioxymethamphetamine (methylenedioxymethamphetamine), have recently gained increasing attention due to their potential benefits for treating psychiatric disorders (Andersen et al., 2021). Methylenedioxymethamphetamine-assisted psychotherapy is currently in a phase three clinical trial to treat severe post-traumatic stress disorder (PTSD) with encouraging initial results (Mitchell et al., 2021). Research in this area is also increasingly associated with the development of imaging techniques as quantitative biomarkers in addition to behavioral parameters (Andersen et al., 2021). To investigate the mechanisms of psychedelic drugs in vivo, magnetic resonance imaging (MRI) methods inferring neuronal activity through neurovascular coupling, such as blood oxygenation level-dependent functional MRI (BOLD-fMRI) and arterial spin labeling, have been widely used (Carhart-Harris et al., 2012; Carhart-Harris et al., 2015; Dipasquale et al., 2019). Interestingly, research performed over the last decade using the aforementioned methods has shown that psychedelic compounds such as methylenedioxymethamphetamine (Carhart-Harris et al., 2015) and psilocybin (Carhart-Harris et al., 2012) inhibit brain activity, contradicting previous studies that indicated mainly excitatory effects (Quate et al., 2004; Soto-Montenegro et al., 2007; Vollenweider et al., 1997; Wilkerson and London, 1989).

However, the use of hemodynamic methods may be insufficient to understand the effects of psychedelics on neuronal activity. First, psychedelic drugs elicit their effects by strongly affecting one or more neurotransmitter systems (Gough et al., 1991). Thus, it is crucial to evaluate hemodynamic changes in relation to neurotransmitter alterations. Second, in addition to neuronal effects, increased of neurotransmitters such as serotonin elicited by psychedelic compounds can have potent vascular effects (Cohen et al., 1996; Kim et al., 2018; Van Nueten et al., 1985). This aspect is particularly critical for methods based on neurovascular coupling, such as BOLD-fMRI and arterial spin labeling. The emergence of hybrid positron emission tomography (PET)/MRI allows simultaneous assessment of brain function at multiple physiological levels. The combination of PET with pharmacological MRI (phMRI) can offer important complementary insight on drug mechanisms (Hansen et al., 2017; Sander et al., 2013). Furthermore, recent developments in the administration of 2-^{18}F-fluoro-2-deoxyglucose (^{18}F-FDG) PET via constant infusion (Villien et al., 2014) have paved the way towards functional PET (fPET). FPET enables the imaging of changes in glucose metabolism at a resolution of minutes (Rischka et al., 2018), providing a more robust indirect measure of

neuronal activity compared to fMRI, being largely immune to vascular changes (Villien et al., 2014).

We aimed to exploit the potential of multimodal imaging to characterize the acute effects of methylenedioxymethamphetamine using PET/fMRI. First, we performed ^{18}F-FDG fPET/fMRI scans to simultaneously determine hemodynamic and metabolic changes elicited by methylenedioxymethamphetamine and thereby elucidate potential inhibitory or excitatory actions of this compound. In a second cohort, we used ^{11}C-3-amino-4-(2-dimethylaminomethylphenylsulfanyl)-benzonitrile (^{11}C-DASB) to investigate relationships between hemodynamic alterations and changes in serotonin transporter (SERT) availability, one of methylenedioxymethamphetamine's main targets (Morefield et al., 2011).

Material and Methods

Animals

Male Lewis rats (n = 29) were obtained from Charles River Laboratories (Sulzfeld, Germany) and divided into two groups: ^{18}F-FDG fPET/fMRI scans were performed in 17 animals (361 ± 19 g), while ^{11}C-DASB PET/fMRI were performed in 11 animals (365 ± 19 g). Nine fMRI datasets were excluded from the study due to motion during acquisition. One ^{11}C-DASB PET and two ^{18}F-FDG fPET datasets were excluded from the analysis because of paravenous tracer injections. The animals were kept at a room temperature of 22 °C and 40-60% humidity under a 12-hour light-dark cycle. The rats were fed with standard diet and received tap water ad libitum. Animals were fasted for six hours before the start of the experiments. All experiments were performed in accordance with the German Federal Regulations on the Use and Care of Laboratory Animals and approved by the Tuebingen regional council. Two additional cohorts scanned under the same ^{18}F-FDG fPET/fMRI and ^{11}C-DASB PET/fMRI protocols, but exposed to phosphate-buffered saline (PBS) instead of methylenedioxymethamphetamine, are presented in the Supplementary Information (Amend et al., 2019; Brodde, 1982; Carhart-Harris et al., 2012; Carhart-Harris et al., 2015; Cohen et al., 1996; Dipasquale et al., 2019; Disselhorst et al., 2022; Ferrington et al., 2006; Gough et al., 1991; Hamacher et al., 1986; Hodkinson et al., 2012; Hutchison et al., 2014; Ionescu et al., 2021b; López-González et al., 2020; Martínez-Maestro et al., 2019; Passie et al., 2002; Quate et al., 2004; Sander et al., 2013; Schaller et al., 2013; Schiffer et al., 2006; Solbach et al., 2004; Spangler-Bickell et al., 2016; Villien et al., 2014; Walker et al., 2016; Wehrl et al., 2013; Wilson et al., 2000).

Simultaneous PET/fMRI Experiments

The animals were scanned under 1.3% isoflurane and constant monitoring of breating rates and temperatures (Supplementary Figure 26) using a 7T small-animal MRI scanner (ClinScan, Bruker, Ettlingen, Germany). T2-weighted anatomical reference scans and fMRI scans (TR: 2000ms, TE: 18ms) were performed using a linearly polarlized RF coil for transmission and a four-channel surface rat brain coil for reception. The PET scans were acquired simultaneously using an in-house developed insert and reconstructed into 100 frames of 1 minute using an ordered-subsets-expectation-maximization-2D (OSEM-2D) algorithm. The methylenedioxymethamphetamine challenges (3.2 mg/kg) were applied 40 minutes after starting the scans. For additional details on the experimental procedure, please refer to Supplementary Methods.

Data Analysis

Statistical Parametric Mapping 12 (SPM 12, Wellcome Trust Centre for Neuroimaging, University College London, London, United Kingdom) via Matlab (The MathWorks, Natick, MA, USA) and Analysis of Functional NeuroImages (AFNI, National Institute of Mental Health, Bethesda, Maryland, USA) were used for data preprocessing as previously reported (Amend, 2019). An extensive description of all preprocessing and analysis steps can be found in the Supplementary Information. Average time courses were extracted from all datasets after preprocessing using the MarsBaR toolbox (Matthew Brett, June 2-6, 2002) and regions of interest (Supplementary Table 6) defined by the Schiffer atlas (Schiffer et al., 2006). For a complete list of the regions, please refer to the legend of Figure 11, for additional details to Supplementary Information. Additionally, extra-cerebral BOLD-fMRI signals were extracted using binary masks generated using AFNI. The general linear model (GLM) available in SPM was applied to determine voxels with significantly altered fMRI and PET signals after methylenedioxymethamphetamine exposure. For all datasets, the baseline was defined as the period between 30 and 40 minutes after scan start, after tracer equilibrium had been reached between the high target and reference regions. The ^{18}F-FDG fPET data were normalized using the cerebellar uptake. For ^{11}C-DASB PET the cerebellar gray matter was chosen as reference region. For all methods, the signal at baseline was compared to six 10-minute blocks between the challenge (40 minutes after scan start) and the end of the scan (100 minutes after scan start). Group-level t-maps were generated for all cohorts, methods and time-periods. All t-maps were subjected to voxel-wise signal quantification to determine the regional contributions of brain regions selected. The average t-scores of all voxels comprising each

region were calculated for each period and modality to compare the respective spatial patterns of methylenedioxymethamphetamine effects on hemodynamics, glucose metabolism, and SERT occupancy.

Results

Metabolic Increases Accompany Hemodynamic Reductions

First, we investigated the relationship between hemodynamic and metabolic changes following acute methylenedioxymethamphetamine using simultaneous ^{18}F-FDG fPET/fMRI (Figure 10, Figure 11, Supplementary Figure 27).

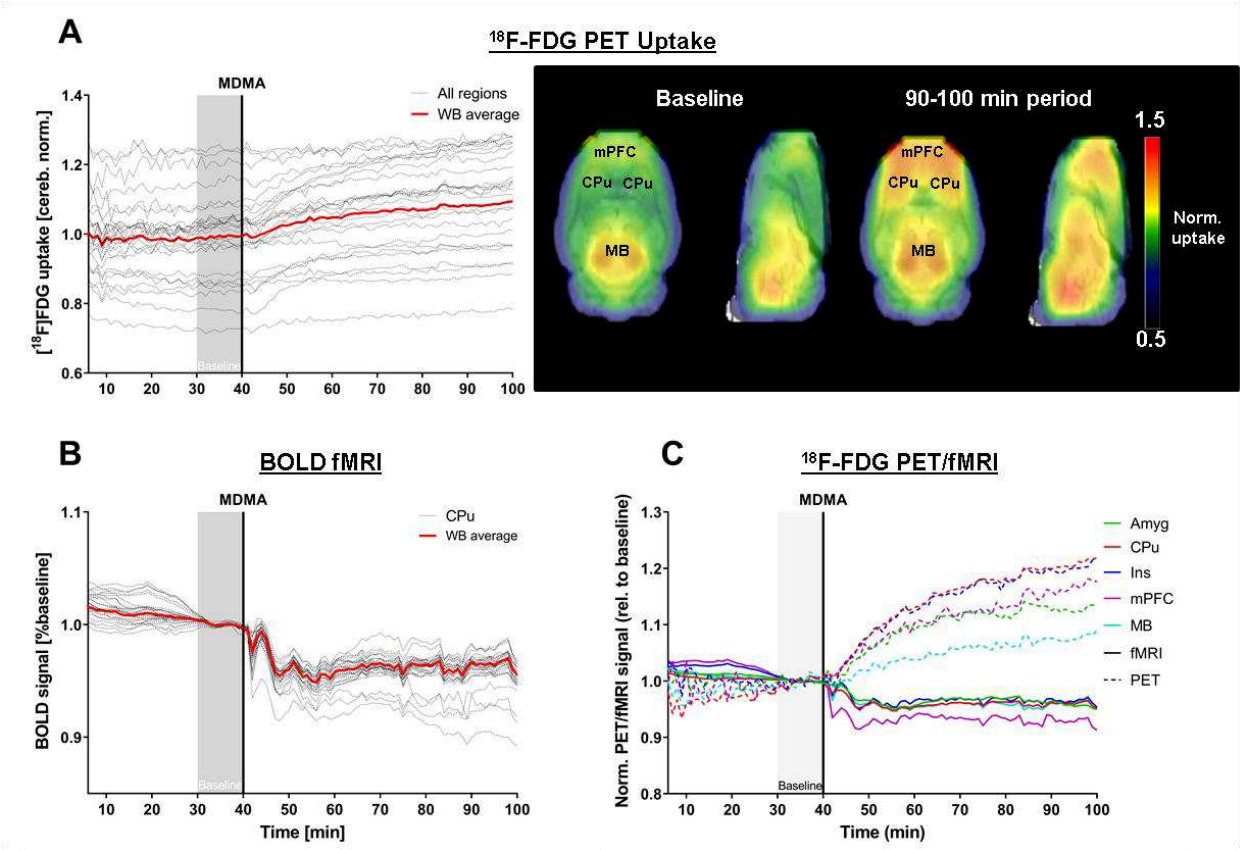

Figure 10: Region-wise evaluation of ^{18}F-FDG fPET and BOLD-fMRI signal changes. (A) TACs for all regions and whole-brain average. Voxel-wise normalized uptake maps indicate ^{18}F-FDG uptake at baseline and at the 90-100 minutes time-period. (B) Regional BOLD-fMRI signals normalized to respective baselines periods. (C) Both signals were normalized to the baseline period over the last ten minutes before methylenedioxymethamphetamine administration for a common frame of reference.

The normalized ^{18}F-FDG fPET TACs of all regions and the average whole-brain TAC and voxel-wise uptake maps (Figure 10A) indicated an increase in metabolism in the midbrain, anterior subcortical and frontal cortical areas, whereas more minor or no changes occurred in posterior cortical regions. Notably, we found a simultaneous decrease in hemodynamics, as

indicated by BOLD-fMRI (Figure 10B). The whole-brain-averaged BOLD-fMRI signal was reduced by 4.5% fifteen minutes after the challenge. Importantly, the data revealed that the decreases were of global nature and occurred in all regions investigated. A temporal comparison of the ^{18}F-FDG fPET and BOLD signal changes relative to baseline is shown in Figure 10C. The highest metabolic increases occurred in frontal areas, including the CPu (22%), Ins (21%), mPFC (18%), and Amyg (13.5%). Temporally, increases in all regions (>1%) were observed within 5 minutes of challenge.

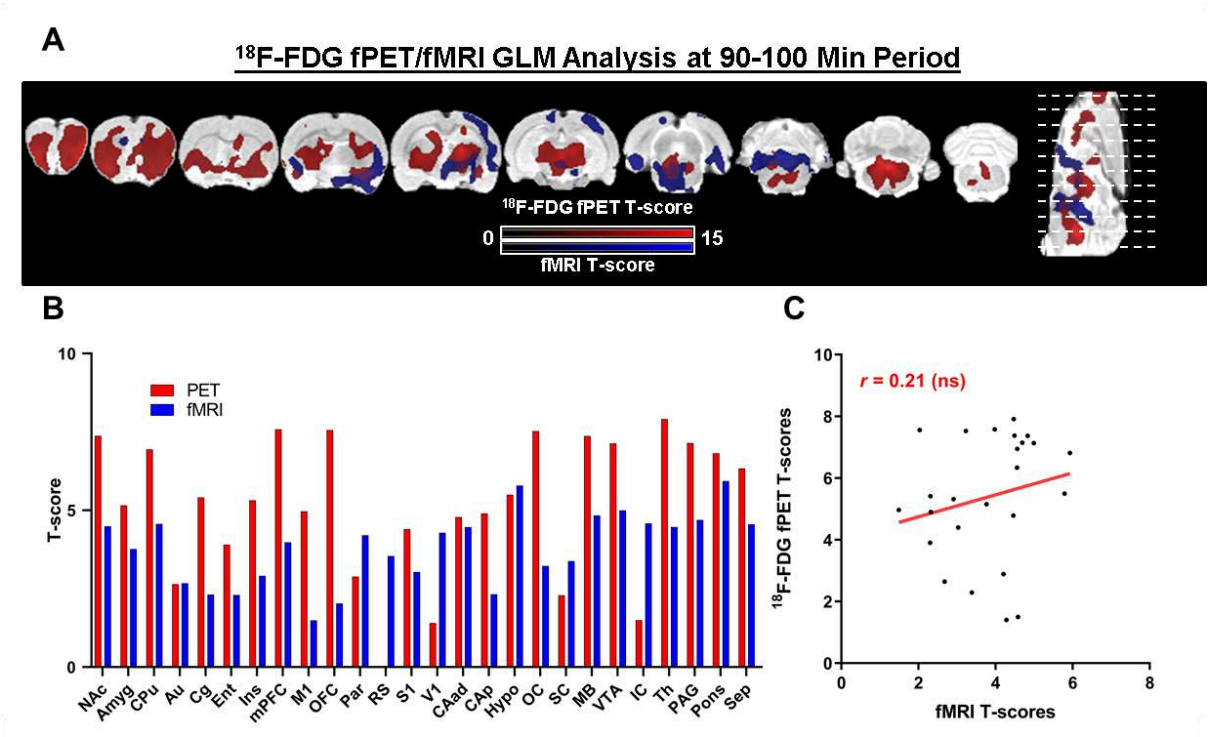

Figure 11: GLM analysis of ^{18}F-FDG-fPET/fMRI cohort. (A) Voxel-wise analysis of both signals in the 90-100 minute block ($p<0.05$ FWE-corrected at voxel level for PET, $p<0.001$ at voxel level with $p<0.05$ FWE cluster-level correction for fMRI, n=15 for fPET, n=9 for fMRI). (B) The bar diagram indicates average t-scores for each region and modality. (C) The average regional t-scores are plotted in a scatter diagram to evaluate the spatial correlation of both readouts. NAc: nucleus accumbens, Amyg: Amygdala, CPu: caudate putamen, Au: auditory cortex, Cg: cingulate cortex, Ent: entorhinal cortex, Ins: insular cortex, mPFC: medial prefrontal cortex, M1: motor cortex, OFC: orbitofrontal cortex, Par: parietal cortex, RS: retrosplenial cortex, S1: somatosensory cortex, V1: visual cortex, CAad: anterodorsal hippocampus, CAp: posterior hippocampus, Hypo: hypothalamus, OC: olfactory cortex, SC: superior colliculus, MB: midbrain, VTA: ventral tegmental area, IC: inferior colliculus, Th: thalamus, PAG: periacquaeductal gray, Sep: septum.

The voxel-wise GLM analyses presented in Figure 11 revealed metabolic increases across several subcortical areas and in frontal cortical areas in the period between 90-100 minute period. The mPFC and OFC (t=7.6 for both), along with MB (t=7.4), Th (t=7.9) and NAc (t=7.4) exhibited the most significant ^{18}F-FDG increases. The most significant BOLD-fMRI

decreases occurred in posterior areas such as the MB (t=4.8), VTA (t=5.0), Hypo (t=5.8), and Pons (t=5.9). The t-scores of metabolic increases and hemodynamic decreases did not correlate significantly (r=0.21).

SERT Occupancy Changes Induced by Methylenedioxymethamphetamine Correlate with BOLD Decreases

To further elucidate the molecular underpinnings of the observed hemodynamic decreases, we evaluated BOLD-fMRI changes concurrently with alterations in SERT availability using ^{11}C-DASB PET/fMRI in a second cohort (Figure 12, Figure 13, Supplementary Figure 28).

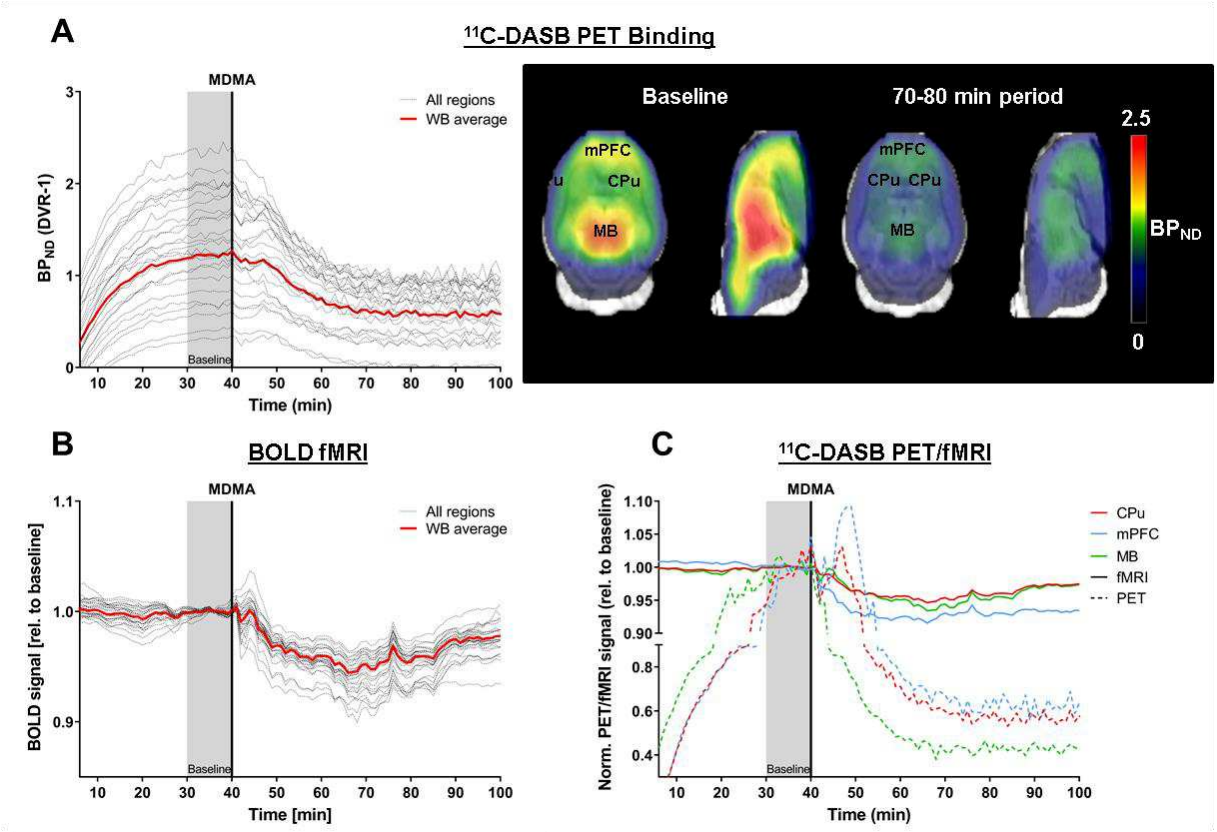

Figure 12: Region-wise evaluation of [^{11}C]DASB PET and BOLD-fMRI signal changes. (A) Dynamic BP_{ND} for all regions and whole-brain average. Voxel-wise maps indicate [^{11}C]DASB binding at baseline, as well as 70-80 minutes after scan start. (B) Regional BOLD fMRI signals normalized to respective baselines. (C) Temporal comparison of PET and BOLD signal changes (normalized to the baseline) in CPu, mPFC, and MB.

The ^{11}C-DASB BP_{ND} reached equilibrium 30 minutes after injection (Figure 12A). After the challenge, binding in all regions decreased either immediately (1-2 minutes after the challenge) in areas with high binding values (BP_{ND} > 1.8) or with a delay of approximately 10 minutes in regions with lower ^{11}C-DASB binding values. At 30 minutes post-challenge, the bindings remained stable until the end of the scan period. Similarly to the ^{18}F-FDG

fPET/fMRI cohort, all regional BOLD signals decreased within 6 minutes after the challenge (Figure 12B). Temporally, regions with higher baseline SERT availability showed a faster response than regions with lower baseline SERT availability (Figure 12C). For example, ^{11}C-DASB binding in the MB (BP_{ND}=2.1), decreased immediately after challenge. In contrast, ^{11}C-DASB binding in the CPu (BP_{ND}=1.6) and mPFC (BP_{ND}=1.6) remained stable or increased shortly. After approximately 10 minutes, ^{11}C-DASB binding decreased in all regions until it reached equilibrium at 30-40 minutes after the challenge (39% decrease for mPFC, 44% decrease for CPu). BOLD decreases occurred homogeneously, peaking 30 minutes post-challenge (~8.5% in mPFC, ~5.5% in CPu, and ~6.5% in MB).

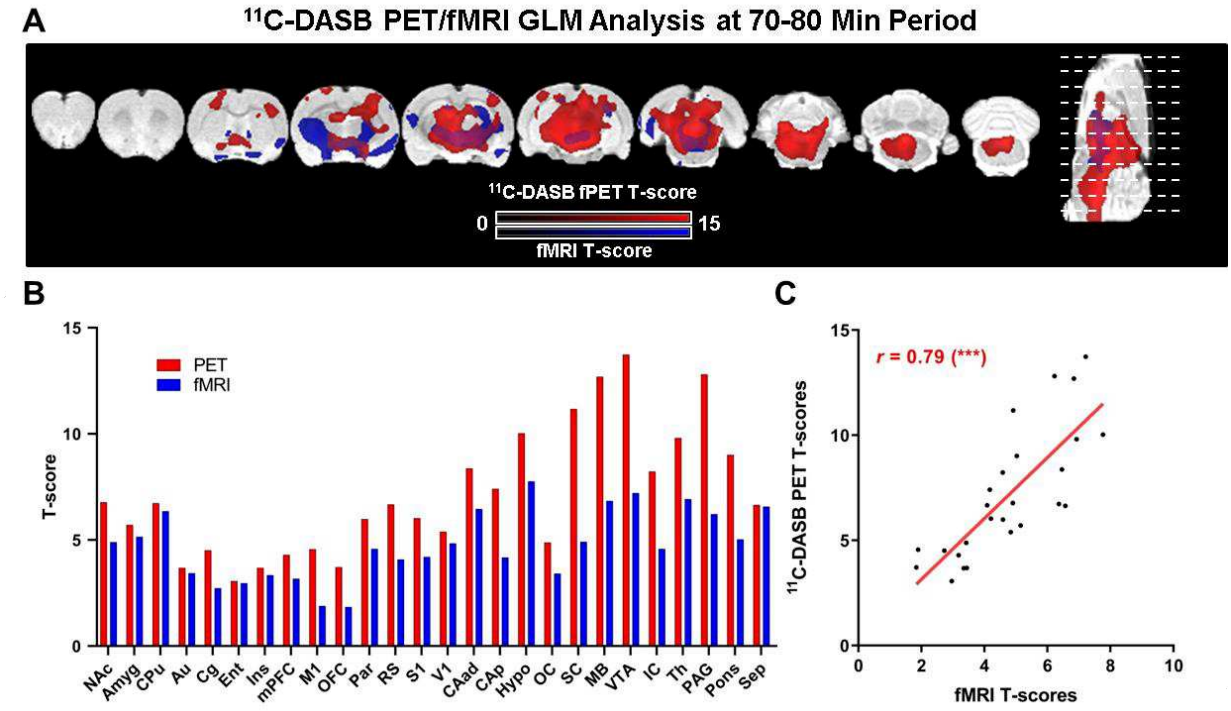

Figure 13: GLM analysis of ^{11}C-DASB-PET/fMRI cohort. (A) Voxel-wise analysis of both signals in the 70-80-minute block. The voxelwise maps are presented at ($p<0.05$, voxel-level FWE-correction for PET and $p<0.001$ at voxel level with $p<0.05$ FWE cluster-level correction for fMRI, n=11). (B) The bar diagrams indicates average t-scores for each region and modality. (C) The regional t-scores are plotted in a scatter diagram to evaluate spatial correlation of both readouts (***$p<0.001$).

Figure 13 shows the voxel-wise decreases at 70-80 minutes after scan start. Regional averages showed the strongest decreases in the VTA (t=13.7), PAG (t=12.8) and MB (t=12.7) for ^{11}C-DASB and in the Hypo (t = 7.8), VTA (t=7.2) and Th (t=6.9) for BOLD-fMRI. Remarkably, regional t-scores of both readouts correlated strongly (r=0.79, $p<0.001$).

Hemodynamic reductions also occur in non-neuronal tissues

The limited spatial extent of hemodynamic changes compared with the metabolic and SERT occupancy alterations may be due to the smaller magnitudes of the BOLD decreases. To further clarify this aspect, we merged the fMRI scans from both cohorts (Figure 14). We also extracted the BOLD signals from extracerebral areas to investigate whether the BOLD decreases are specific to neuronal tissue.

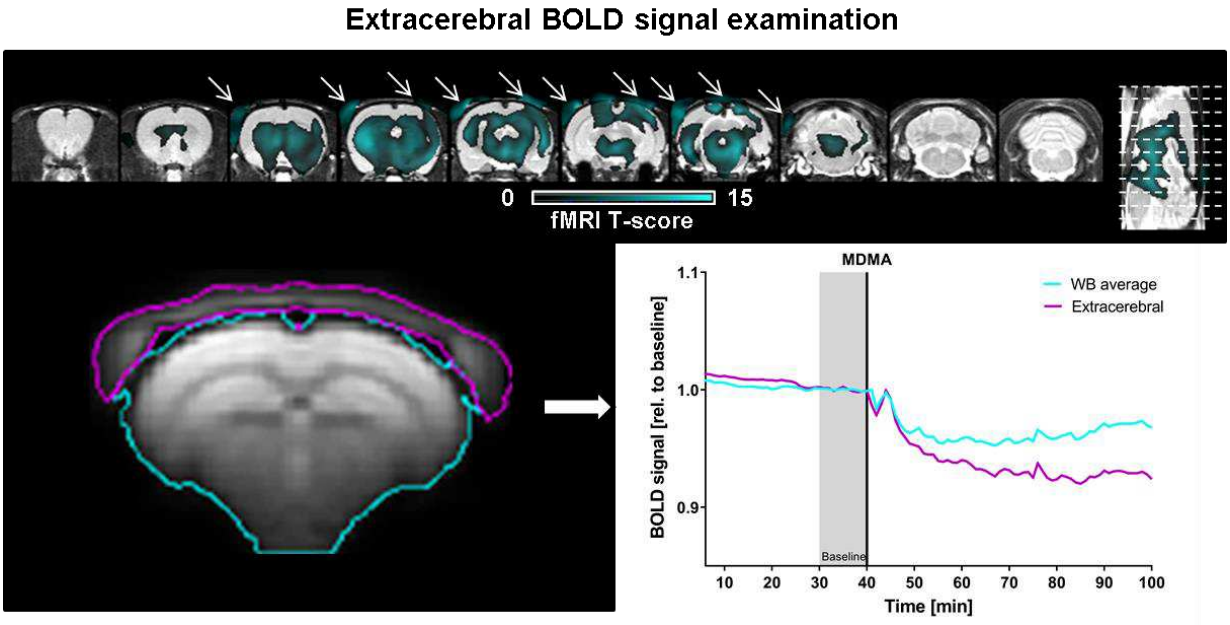

Figure 14: GLM analysis of BOLD decreases after merging BOLD-fMRI datasets acquired in both cohorts (n=20). Data are shown at $p < 0.05$, FWE-corrected at the voxel level. Arrows indicate extracerebral decreases. Average BOLD signals were extracted from the extracerebellar regions and plotted along with the whole-brain signal.

After merging the cohorts, the BOLD-fMRI decreases were widespread and, intriguingly, also occurred in non-neuronal areas (Figure 14). The average extracerebral BOLD signal decreased coherently with the cerebral BOLD signal, both reaching maximum reductions 27 minutes after the challenge (cerebral BOLD: 4.8%, extracerebral BOLD: 7.4%).

Additional Analyses

For analyses of the PBS cohort and a comparison with the readouts shown after methylenedioxymethamphetamine application, please refer to Supplementary Figure 29 and Supplementary Figure 30. Furthermore, we extracted GLM alterations induced by MDMA for both ^{11}C-DASB and ^{18}F-FDG cohorts in each subject to demonstrate the feasibility of subject-level PET inferences using our approach (Supplementary Figure 31, Supplementary Figure

32). Additionally, we reproduced the metabolic changes using whole-brain normalization and validated the choice of the cerebellum for normalization (Supplementary Figure 33). Moreover, we examined the robustness of our correlation between hemodynamic and SERT decreases by using beta-values and subject-level GLM readouts (Supplementary Figure 34). Finally, we compared the temporal characteristics of the observed hemodynamic, metabolic and SERT availability changes (Supplementary Figure 35).

Discussion

Our data indicate that increased neuronal activity after methylenedioxymethamphetamine is accompanied by neurovascular uncoupling, possibly mediated through the vascular effects of serotonin following SERT blockage.

Simultaneous Uncoupling Between Metabolism and Hemodynamics

Studies measuring glucose utilization have shown mixed results, yet mainly increased metabolism following psychedelic challenges (Ferrington et al., 2006; Quate et al., 2004; Soto-Montenegro et al., 2007; Vollenweider et al., 1997), suggesting neuronal activation. However, more recent work with arterial spin labeling challenged this hypothesis and argued that brain activity is solely decreased under methylenedioxymethamphetamine (Carhart-Harris et al., 2015). Our study confirms that this finding also holds true in rodents. The authors of the study above speculated that methylenedioxymethamphetamine exerts inhibitory effects directly through 5-HT1A receptors (Andrade, 2011; Carhart-Harris et al., 2015) Comparable reductions under acute psilocybin reported by the same group were attributed to the inhibitory effects of 5-HT2A receptors (Carhart-Harris et al., 2012). On a side note, the hemodynamic decreases for methylenedioxymethamphetamine and psilocybin in humans were predominantly located in the right hemisphere (Carhart-Harris et al., 2012; Carhart-Harris et al., 2015), similarly to our study, thereby supporting the translatability of our readout. Notably, the authors argued that possible discrepancies with previous work indicating increased metabolism using ^{18}F-FDG PET (Vollenweider et al., 1997) might be due to its inferior temporal resolution (Carhart-Harris et al., 2012). Therefore, the authors claimed that the reported increases may represent a rebound in glucose metabolism after the acute inhibition captured by fMRI (Carhart-Harris et al., 2012). We agree that earlier ^{18}F-FDG PET or ex vivo studies (Ferrington et al., 2006; Quate et al., 2004; Soto-Montenegro et al., 2007; Vollenweider et al., 1997) measuring cerebral glucose utilization lacked temporal specificity due to methodological limitations, limiting their interpretability in terms of acute effects. An

additional confound is that the the studies compared different, relatively small cohorts having received either placebo or methylenedioxymethamphetamine. The present work overcomes all these limitations. The constant infusion protocols used for both tracers enabed the delineation of pharmacological effects (a) immediately after the challenge at 1-minute intervals, (b) simultaneously with hemodynamic alterations and (c) within the same subjects. Therefore, we demonstrate that the uncoupling between flow and metabolism previously shown (Cohen et al., 1996; Ferrington et al., 2006; Quate et al., 2004) does occur simultaneously within the same subjects.

Origin of Peripheral and Cerebral Hemodynamic Decreases

We show that non-neuronal effects dominate hemodynamic changes induced by methylenedioxymethamphetamine. In particular, our data shed light on two separate phenomena. First, the temporal coherence between hemodynamic reductions in cerebral and extracerebral areas suggests that vascular effects occur at the periphery. The 5-HT_{2A}, which is postulated, along with the 5-HT_{1B} receptor, to mediate vasoconstrictive effects (Gamoh et al., 2013; Ullmer et al., 1995), is one of the main targets of methylenedioxymethamphetamine (Dipasquale et al., 2019; Roseman et al., 2014). However, because methylenedioxymethamphetamine has a much stronger affinity to the 5-HT_{2A} receptor than to the 5-HT_{1B} receptor (Dipasquale et al., 2019), direct agonist action of methylenedioxymethamphetamine at the 5-HT_{2A} in peripheral blood vessels likely drives our results (Ullmer et al., 1995). Previous work has demonstrated the role of 5-HT_{2A} in vasoconstriction of the carotid artery, the main vessel providing blood supply to the brain (Buchborn et al., 2020; Yakovlev et al., 2014). In addition to peripheral effects, the cerebral hemodynamic decreases are also likely of serotonergic nature. Previous work has indicated that serotonin impacts brain hemodynamics (Kim et al., 2018; Van Nueten et al., 1985) and that direct manipulation of the raphé nuclei constricts cerebral microvasculature (Cohen et al., 1996). In contrast to the peripheral hemodynamic reductions, which can be attributed solely to the direct effects of methylenedioxymethamphetamine, the decreases in the brain may additionally be triggered by increased synaptic serotonin levels following SERT blockage. This finding is supported by the high correlation between SERT blockage and hemodynamic decreases in BOLD-fMRI, suggesting that increased levels of endogenous serotonin may modulate cerebral hemodynamics. The exact involvements of different receptors need to be investigated futurely, for instance by combining psychedelic challenges with respective antagonists. Our results warrant a reevaluation of previous data (Carhart-Harris et al., 2012;

Carhart-Harris et al., 2015) and generally calls for caution when interpreting findings relying on neurovascular coupling under pharmacological challenges (Carhart-Harris et al., 2015; Dipasquale et al., 2019; Roseman et al., 2014).

Anatomy and Physiology of Increased Metabolism

We demonstrate that methylenedioxymethamphetamine increases the metabolisms of different regions, likely due to neuronal activation, fPET having been shown to reliably map onto neuronal activity while being independent of hemodynamic changes (Villien et al., 2014). Interestingly, the metabolic increases were more weighted toward serotonergic projection areas than the reductions in SERT availability. First, this finding is in line with the hypothesis that most of the glucose is consumed postsynaptically (Attwell and Laughlin, 2001). Second, the areas showing increased metabolism are consistent at a functional level with the majority of previously reported behavioral effects of methylenedioxymethamphetamine. The signals observed in the nucleus accumbens, amygdala, and insula allign well with salience changes known from imaging and behavioral studies (Carhart-Harris et al., 2015; Seeley et al., 2007). In particular, the nucleus accumbens is involved in responses to numerous drugs (Olsen, 2011). The amygdala, insula, and orbitofrontal cortex are strongly involved in emotional processes (Phan et al., 2002). Activity in the olfactory cortex and olfactory bulb could indicate increased food-seeking or sexual arousal (Pfaus et al., 2009; Sumnall et al., 2006). Enhanced metabolic activity in sensory cortices is in concordance with heightened sensations elicited by methylenedioxymethamphetamine (Sumnall et al., 2006). Furthermore, the aforementioned 5-HT_{2A} receptor exhibits a strong anterior-posterior gradient in the cortex, being strongly expressed in frontal areas cortex (Andrade and Weber, 2010), overlapping with the activations shown using fPET and has been shown to be responsible for serotonergic activation in projection areas such as the prefrontal cortex (Puig and Gulledge, 2011).

Other factors may play a role in the findings and there are also certain limitations which need to be taken into consideration when contemplating our data. Please refer to Supplementary Information for a thorough discussion on these aspects.

Conclusion

The present study shows the potential of multimodal imaging in drug research. We demonstrate the acute neurovascular uncoupling methylenedioxymethamphetamine,

characterized by increased neuronal activity in monoaminergic projection areas and accompanied by vascular depression of serotonergic nature. Our results provide important insight into the mechanism of action of methylenedioxymethamphetamine and pave the way for the application of ^{18}F-FDG-fPET and hybrid fPET/fMRI in drug research.

Funding

The research was funded by the Eberhard Karls University Tübingen, Faculty of Medicine (fortüne 2209-0-0 and 2409-0-0) to HFW, the Carl Zeiss Foundation to KH, the Werner Siemens Foundation to BJP and the international exchange grant of the Osaka medical research foundation for intractable diseases to TW.

Acknowledgements

We acknowledge Julia Mannheim, Rebecca Rock, Neele Hübner, Andreas Dieterich, Ines Herbon, Stacy Huang, Sandro Aidone, Linda Schramm and the Radiopharmacy Department for their administrative and technical support. The graphical abstract was generated using BioRender. This work is also part of the Ph.D. thesis of Tudor M Ionescu.

Declaration of Competing Interests

The authors declare no conflict of interest.

Key points

Question: Despite the surge in interest in methylenedioxymethamphetamine for psychiatric diseases, its acute mechanisms are still elusive due to methodological caveats of previous imaging studies.

Pertinent findings: Global decreases in BOLD-fMRI are of vascular, rather than neuronal nature and strongly correlate with SERT occupancy measured simultaneously using ^{11}C-DASB. In contrast, ^{18}F-FDG-fPET indicates simultaneous increases in limbic glucose consumption, potentially mapping onto neuronal activation.

Implications for patient care: The study underlines the caveats of BOLD-fMRI and other hemodynamic methods when strong vascular effects are present and recommends the use of ^{18}F-FDG-fPET as an alternative for tracking neuronal activity *in vivo* following pharmacological challenges in drug research.

Supplementary Methods

Experimental Design

Animals were placed in knock-out boxes, and anesthesia was induced with 3% isoflurane in regular air. Reflex tests were performed to determine sufficient sedation. For subsequent preparation procedures, the isoflurane concentration was reduced to 2%. After the weight of the animals was determined, a catheter with a 30-G needle was positioned in a tail vein to administer the radioactive tracer. Another catheter was placed into the other tail vein for methylenedioxymethamphetamine administration. Animals were then placed on a dedicated temperature-controlled small animal bed (Medres, Cologne, Germany). The temperature was monitored and maintained at 36.5°C with a rectal probe, and respiratory rates were monitored using a breathing pad. Rats were then placed in the scanner, and the isoflurane concentration was decreased to 1.3% throughout the scan.

Scans were performed using a 7-T small-animal MRI scanner (ClinScan, Bruker Biospin, Ettlingen, Germany) using a 72-mm-diameter linearly polarized RF coil (Bruker) for transmission and a four-channel rat brain coil (Bruker) for reception. First, localizer scans were performed to position the brains in the center of the field of view. Local magnetic field maps were then generated to optimize local field homogeneity. Subsequently, T2-weighted MRI sequences (TR: 1800 ms, TE: 67.11 ms, FOV: 40 x 32 x 32 mm3, image size: 160 x 128 x 128 px, Rare factor: 28, averages: 1) were performed to obtain anatomical references. Finally, fMRI imaging was performed using T2*-weighted gradient-echo EPI sequences (TR: 2000ms, TE: 18ms, 0.25 mm isotropic resolution, FoV 25 x 23 mm2, image size: 92 x 85 x 20 px, slice thickness: 0.8 mm, 20 slices). PET scans were acquired using a PET insert developed in collaboration with Bruker (Disselhorst et al., 2022). PET and fMRI acquisitions were started simultaneously 30 seconds before tracer injection and performed over 100 minutes after tracer injection. PET data were saved as list-mode files for later reconstruction into dynamic scans of 100 1-minute frames using an ordered-subsets expectation maximization 2D (OSEM-2D) algorithm.

A pharmacological methylenedioxymethamphetamine challenge of 3.2 mg/kg was administered 40 minutes after tracer injection over 30 seconds.

Schiffer rat brain atlas

The rat brains were subdivided into several brain regions according to the Schiffer rat brain atlas. A total of 54 regions were selected. A list of regions, their volumes and abbreviations can be found in Supplementary Table 6.

Supplementary Table 6: List of regions selected according to the Schiffer rat brain atlas.

Brain region (ROI)	**Hemisphere**	**ROI volume [mm^3]**	**Abbreviation**
Nucleus Accumbens	left	7.9	NAc
	right		
Amygdala	left	21.1	Amyg
	right		
Caudate Putamen	left	43.5	CPu
	right		
Auditory Cortex	left	27.5	Au
	right		
Cingulate Cortex	left	14.5	Cg
	right		
Entorhinal Cortex	left	59.0	Ent
	right		
Insular Cortex	left	21.1	Ins
	right		
Medial Prefrontal Cortex	left	6.3	mPFC
	right		
Motor Cortex	left	32.6	M1
	right		
Orbitofrontal Cortex	left	18.9	OFC
	right		
Parietal Cortex	left	7.6	PaC
	right		
Retrosplenial Cortex	left	18.9	RS
	right		
Somatosensory Cortex	left	71.6	S1

	right		
Visual Cortex	left	36.1	V1
	right		
Anterodorsal Hippocampus	left	25.1	CA1
	right		
Posterior Hippocampus	left	9.8	CA1-p
	right		
Hypothalamus	left	18.4	Hyp
	right		
Olfactory Cortex	left	14.0	OC
	right		
Superior Colliculus	left	7.1	SC
	right		
Midbrain	left	11.4	MB
	right		
Ventral Tegmental Area	left	5.5	VTA
	right		
Cerebellum – grey matter	left	75.0	CG
	right		
Cerebellum – white mater	left	23.4	CW
	right		
Inferior Colliculus	left	5.7	IC
	right		
Thalamus	left	30.7	Th
	right		
Periaqueaductal Gray	-	9.9	PAG
Septum	-	9.4	Sep

Radiotracer synthesis

^{11}C-DASB synthesis was performed in a modified procedure (Solbach et al., 2004) compared to the report by Wilson et al. (Wilson et al., 2000). In brief, a solution of 2 mg of precursor in 500 µL DMSO was used to trap ^{11}C-methyliodide. After the reaction was heated to 100 °C for 2 min, dilution was performed with 1.5 mL of HPLC eluent (3 mM Na_2HPO_4 with 64 %

acetonitrile). Purification was performed on a Luna C18 column (250 mm x 10 mm, Phenomenex, Torrance, CA, USA). The isolated peak was diluted afterwards using 70 mL water with 20 mg sodium ascorbate, then loaded onto a conditioned Strata-X cartridge (Phenomenex), eluted with 0.5 mL of ethanol and diluted with 5 mL of phosphate-buffered saline.

^{11}C-DASB injected activities were 175 ± 66 MBq/mL and molar activities were 86 ± 25 GBq/µmoL at the time of injection, resulting in an average dose of 364 MBq per animal. ^{11}C-DASB was applied using a bolus plus constant infusion protocol with an initial bolus of 0.58 mL over the first 20 seconds and a constant infusion of 15 µL/min (total volume: 2.08 mL) over the remainder of the scan (k_{bol} = 37.8 min).

The ^{18}O(p,n)^{18}F nuclear reaction using ^{18}O-water (Rotem, Leipzig, Germany) was employed to prepare ^{18}F-fluorine as ^{18}F-using the PETtrace cyclotron (GE Healthcare, Uppsala, Sweden). ^{18}F-FDG was synthesized in a TRACERlab MX_{FDG} synthesizer (GE Healthcare, Liège, Belgium) using mannose triflate (ABX, Radeberg, Germany), as described previously (Hamacher et al., 1986). Quality control after synthesis was executed in accordance to GMP guidelines. For ^{18}F-FDG, a constant infusion protocol was applied, the tracer (150 MBq/mL pre-scan dose) being infused at a rate of 8 µL/min over 100 minutes (800 µL total volume), resulting in total doses of 120 MBq per animal (Amend et al., 2019).

Temperature monitoring

The temperature was documented in 10-minute intervals for both the methylenedioxymethamphetamine cohort in a subset of 12 scans and for the PBS cohort (Supplementary Figure 26). No major changes of temperature induced by the methylenedioxymethamphetamine challenge were observed.

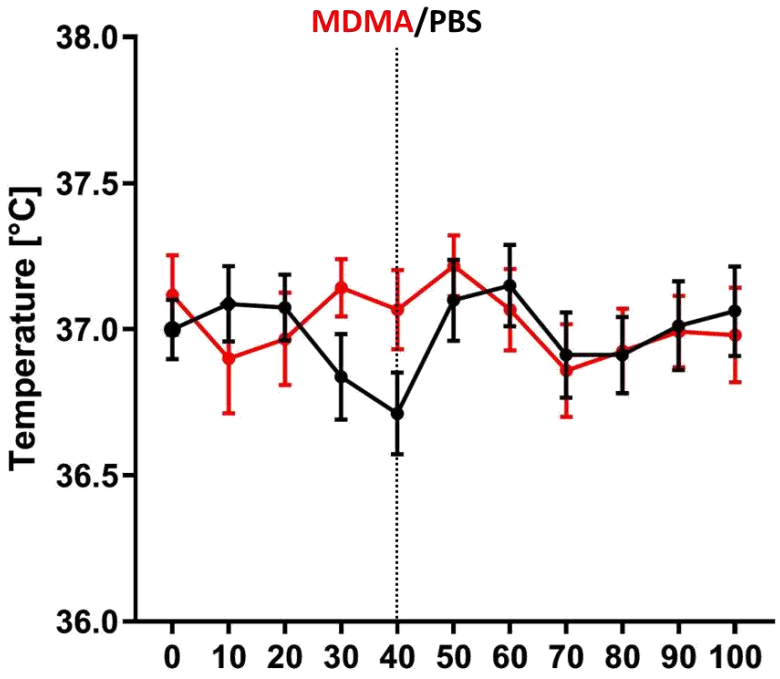

Supplementary Figure 26: Temperatures over the course of the scan for methylenedioxymethamphetamine (n = 12, red) and PBS (n = 8, black). The data are presented as mean ± SEM.

Preprocessing

All fMRI and dynamic PET datasets were first realigned using SPM. Average images were generated for each fMRI and PET dataset . Using these average images and the T2-weighted anatomical references binary masks were created for extracting the brain from each fMRI, PET and anatomical scan. Subsequently, the skull-stripped fMRI and PET datasets were coregistered to the respective skull-stripped anatomical reference scans using SPM. Afterwards, the anatomical references scans were used to calculate spatial normalization parameters to the Schiffer rat brain atlas (Schiffer et al., 2006) which were then used to spatially normalize the fMRI and PET datasets. Finally, all fMRI and PET datasets underwent spatial smoothing using a 1.5 x 1.5 x 1.5 mm^3 Gaussian kernel, corresponding to the spatial resolution of the PET datasets.

^{11}C-DASB BP_{ND} values were calculated using the following formula:

$BP_{ND} = \frac{C_T - C_R}{C_R} = \frac{C_T}{C_R} - 1 = DVR - 1$, where

- BP_{ND} is the non-displaceable binding potential

- C_T is the concentration of the tracer in the tissue of interest
- C_R is the concentration of the tracer in the reference region
- DVR is the distribution volume ratio

General Linear Model Analysis

The cerebellar gray matter was used as a reference region as previously recommended for rats (Walker et al., 2016). For ^{18}F-FDG fPET the cerebellum was used as a reference region, since it has been shown to outperform whole-brain normalization, which bears several caveats (López-González et al., 2020). To further investigate the appropriateness of our reference region for the ^{18}F-FDG normalization, we investigated the slopes of the average raw TACs of the cerebellum and the striatum, a region exhibiting strongly increased metabolism after the challenge. Similar analytical approaches assessing uptake slopes for ^{18}F-FDG fPET have been reported previously (Villien et al., 2014).

For PET data analysis, mean images of the dynamic 1-minute frames were generated over seven measurement periods: between 30 and 40 minutes following tracer injection as baseline, and for each of the subsequent 10-minute periods after methylenedioxymethamphetamine exposure (40-50 minutes, 50-60 minutes, 60-70 minutes, 70-80 minutes, 80- 90 minutes and 90-100 minutes after scan start). Paired t-maps were then calculated between the baseline and each block after methylenedioxymethamphetamine for ^{18}F-FDG using voxel-wise normalized uptake maps and for ^{11}C-DASB using voxel-wise DVR-1 maps.

For fMRI, a first-level analysis was applied to the individual scans using the pseudo block approach reported for phMRI (Hodkinson et al., 2012). To allow a direct comparison with the PET readout, the same six 10-minute blocks between methylenedioxymethamphetamine challenge and the end of the scans (40-50 minutes, 50-60 minutes, 60-70 minutes, 70-80 minutes, 80-90 minutes, and 90-100 minutes after scan start) were compared with the baseline 10- minute block before methylenedioxymethamphetamine injection. After estimating the GLM parameters, statistical parametric maps were generated by interrogating the data using contrast vectors between each block after methylenedioxymethamphetamine and baseline. The generated maps were then used to delineate group-level effects through a second-level analysis. Initially, binary masks were used to perform the analyses only within the brain. The binary masks were removed for later analysis of extracerebral hemodynamic alterations.

In addition to the voxel-wise analysis generated from static PET images presented in the main manuscript, an analysis was performed using the dynamic datasets. The analysis was

performed similarly to the fMRI dataset by generating first-level contrasts between the baseline (30-40 minutes after scan start) and the 10-minute periods after methylenedioxymethamphetamine administration. The first-level contrasts were then used to produce group-level contrasts in a second-level analysis. Additionally, we also calculated subject-level correlations for ^{11}C-DASB and BOLD-fMRI effects exerted by methylenedioxymethamphetamine.

Furthermore, to investigate the impact of employing different metrics on the correlations between hemodynamic and SERT availability decreases, we used the beta values provided for ^{11}C-DASB-PET and BOLD-fMRI to calculate the correlations.

PBS Cohort

To generate control datasets, simultaneous PET/fMRI scans were acquired using the same protocols using both ^{11}C-DASB (n = 4) and ^{18}F-FDG (n = 4). One dataset from each cohort was excluded due to technical issues. The preprocessing and analysis of the remaining scans (n=3 per group) was performed identically to the methylenedioxymethamphetamine cohort.

Supplementary Results

Voxel-wise PET Maps

Voxel-wise PET maps for ^{11}C-DASB indicating BP_{ND} values and for normalized ^{18}F-FDG uptake were generated for the baseline (30-40 minutes after scan start) and for each 10-minute period after methylenedioxymethamphetamine administration. The respective ^{18}F-FDG PET uptake maps can be seen in Supplementary Figure 27. The respective ^{11}C-DASB PET BP_{ND} maps are shown in Supplementary Figure 28. The figures illustrate increase in ^{18}F-FDG uptake and the gradual decrease in ^{11}C-DASB binding elicited by the acute methylenedioxymethamphetamine challenge.

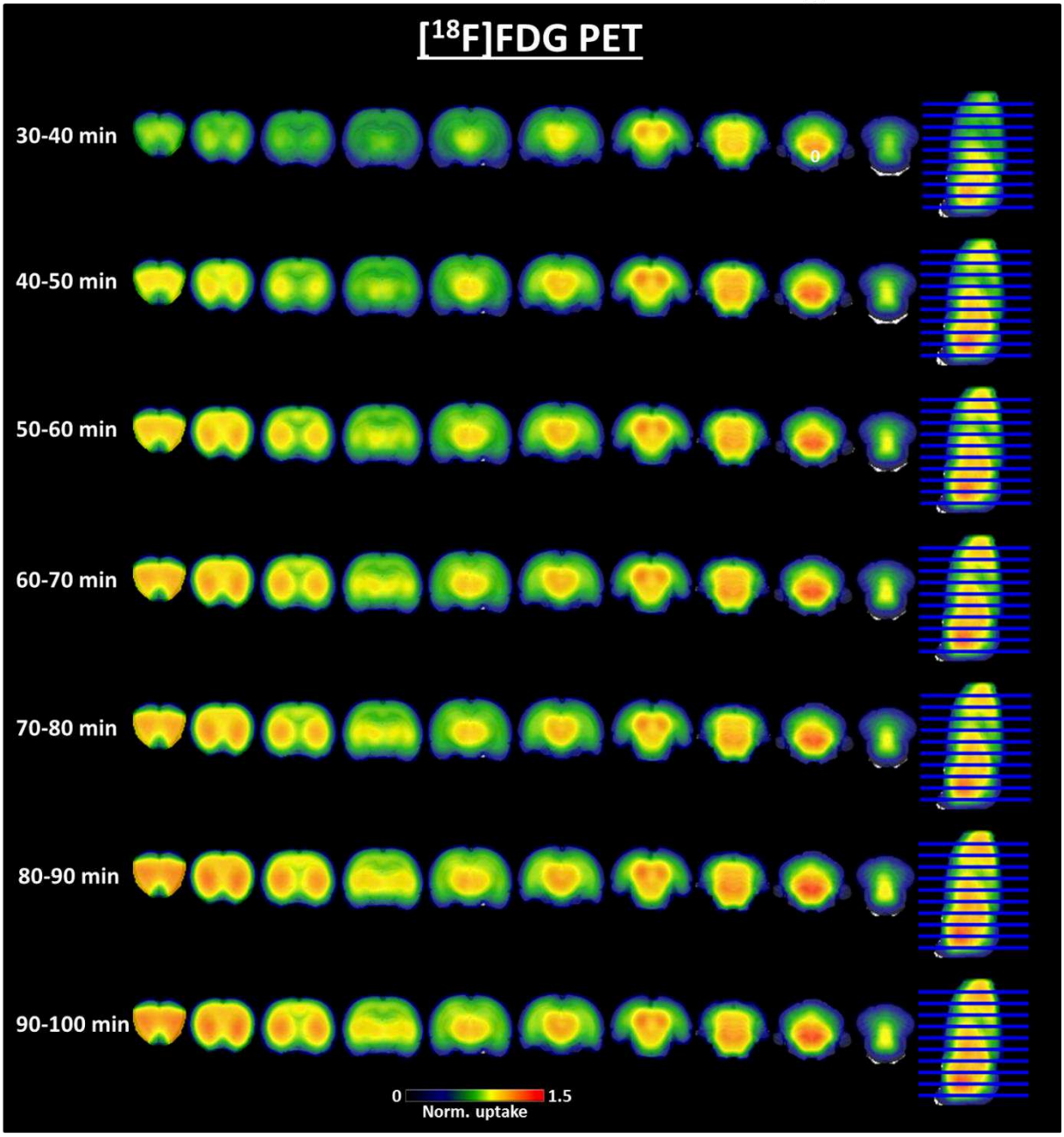

Supplementary Figure 27: Group-average normalized ^{18}F-FDGuptake maps for each analyzed time period. The uptake maps were calculated voxel-wise by normalizing the value of each voxel through the average uptake in the cerebellum. The maps indicate the gradual increase in glucose metabolism after the methylenedioxymethamphetamine challenge, particularly in anterior cortical and subcortical areas.

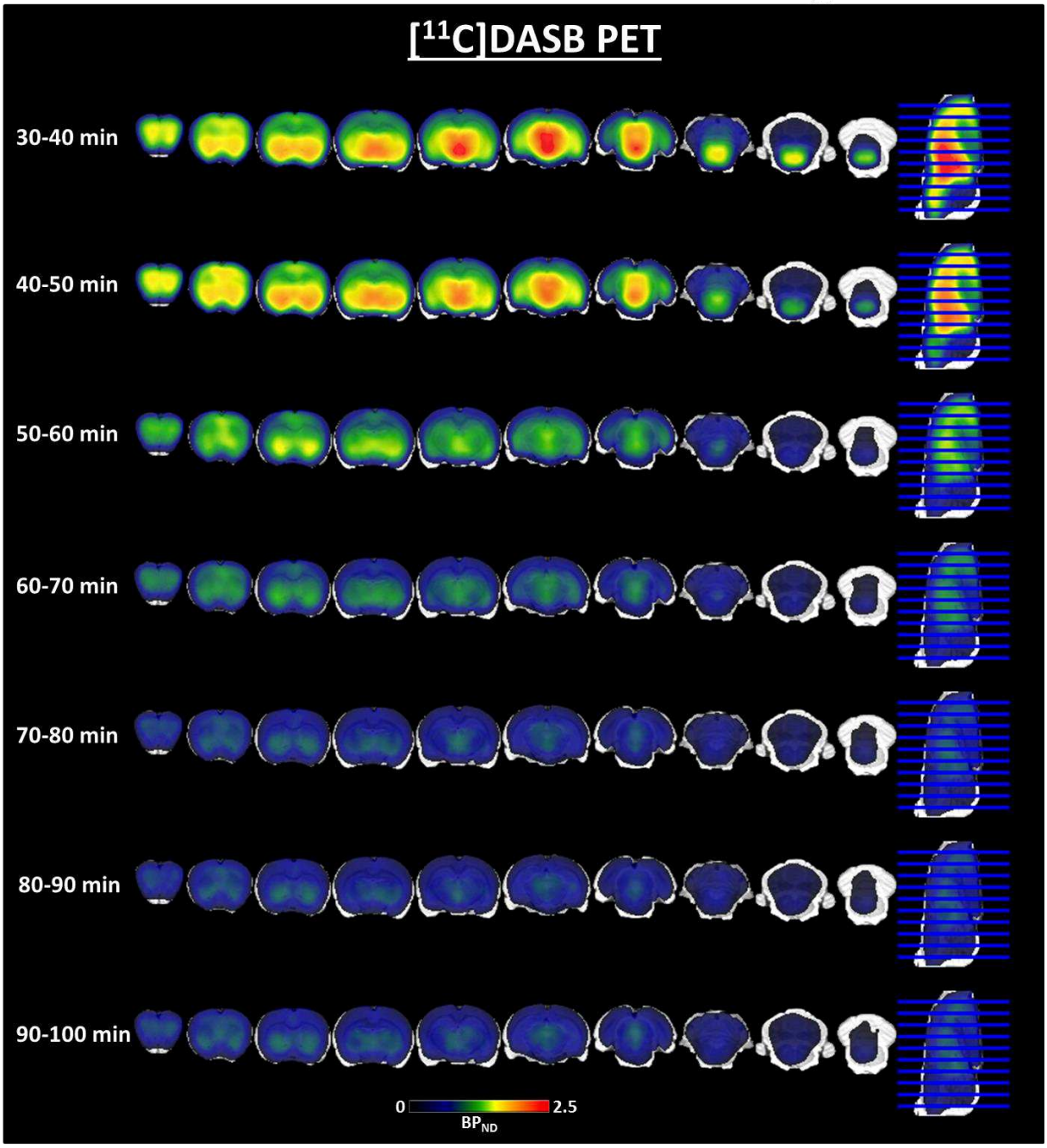

Supplementary Figure 28: Group-average ^{11}C-DASB binding maps for each analyzed time period. Voxel-wise BP_{ND} values were calculated as DVR-1 using the cerebellar gray matter as a reference region. The images indicate the decreased SERT availability after acute methylenedioxymethamphetamine injection.

PBS Cohort

For group-level analysis, we merged the fMRI datasets acquired with ^{11}C-DASB and ^{18}F-FDG, therefore a total of 6 scans were used.

Supplementary Figure 29 indicates average BOLD time-courses extracted from cerebral and extracerebral areas and plotted for comparison to the respective time-courses extracted from

the methylenedioxymethamphetamine cohort. Additionally, two-sample t-tests were performed comparing the alterations of the BOLD signal to baseline between both cohorts. Significantly higher decreases were observed for the methylenedioxymethamphetamine cohort across the areas indicated in the main manuscript.

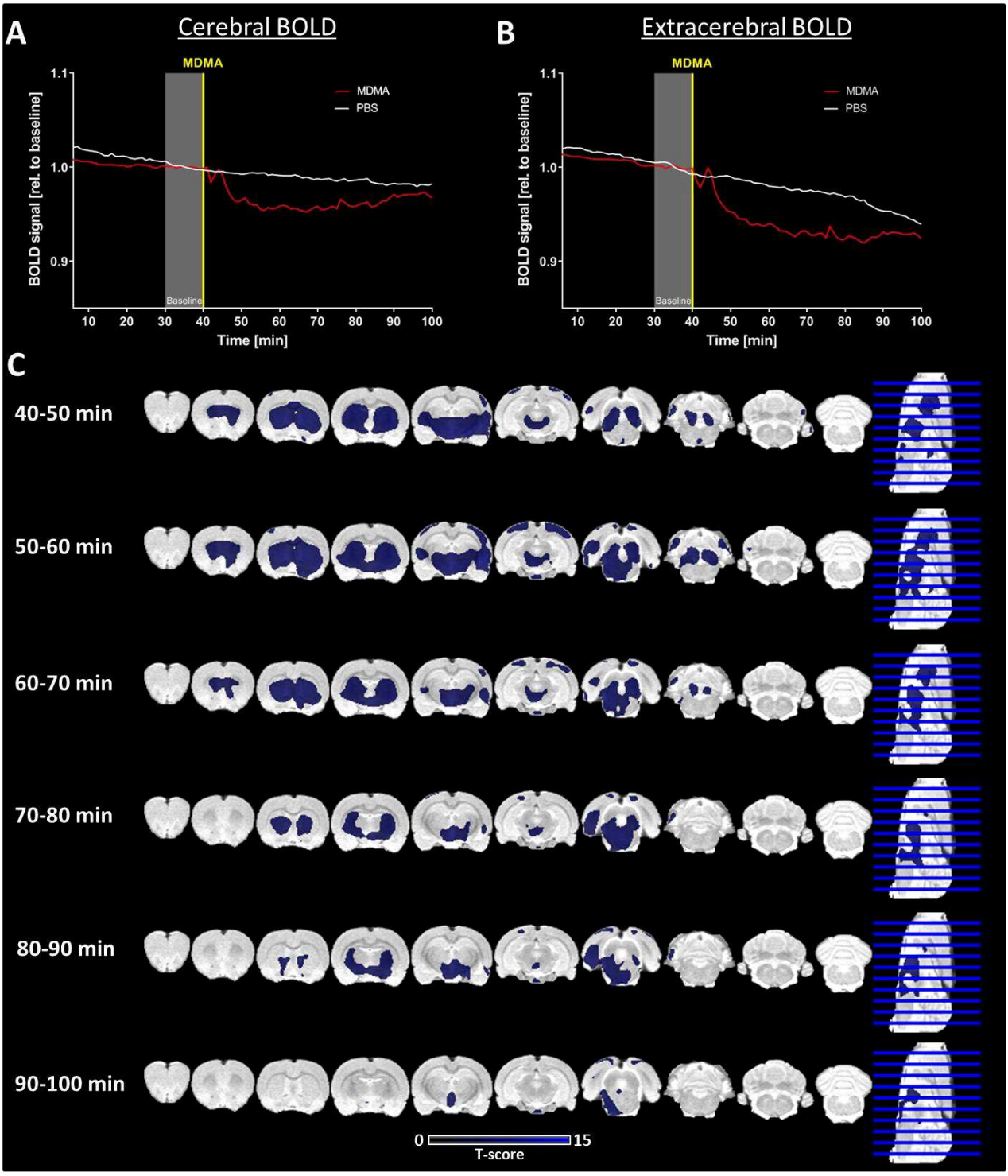

Supplementary Figure 29: Comparison between BOLD-fMRI signal changes in methylenedioxymethamphetamine and PBS cohorts. (A) Group-average whole-brain BOLD signal over the courses of the scans normalized to baseline from minute 30 to 40. (B) Group-average extracerebral BOLD signal

over the courses of the scans normalized to baseline from minute 30 to 40. (C) Voxel-wise two-sample t-tests between changes to baseline (30-40 minutes after scan start) at each subsequent time-period for methylenedioxymethamphetamine and PBS cohorts (Methylenedioxymethamphetamine > PBS, $p < 0.001$ (voxel-level), $p < 0.05$ FWE cluster-level correction).

Linear temporal decreases, potentially driven by longitudinal effects of the used anesthesia, were observed in both cohorts (Supplementary Figure 29A and B). In contrast to the strong decreases induced by methylenedioxymethamphetamine, however, no alterations were observed after the PBS challenge, as confirmed by the between-sample voxel-wise analysis (Supplementary Figure 29C).

Group-average regional ^{18}F-FDG normalized uptake and ^{11}C-DASB BP_{ND} values were generated for the PBS cohorts. Neither readout indicated alterations induced by the PBS injection (Supplementary Figure 30).

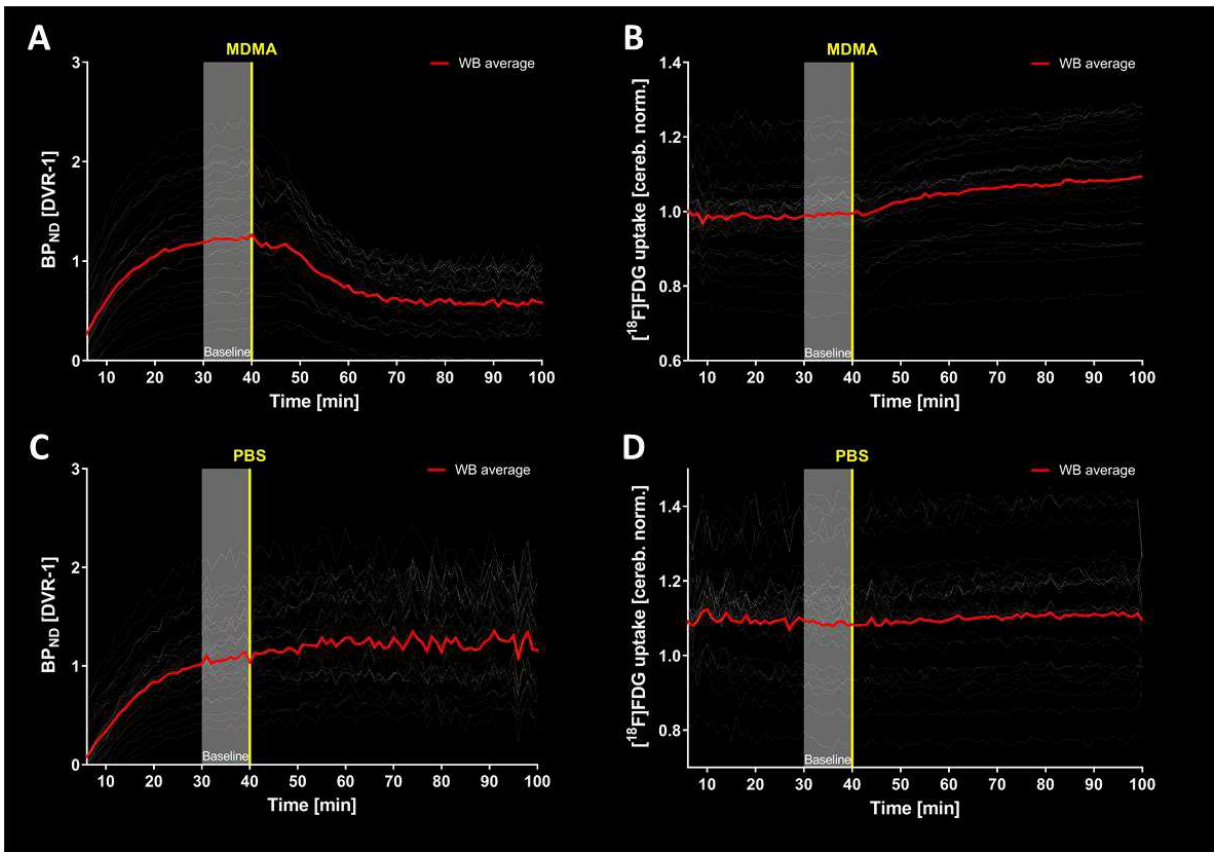

Supplementary Figure 30: Comparison between methylenedioxymethamphetamine and PBS effects on ^{11}C-DASB binding and ^{18}F-FDG uptake. (A) Group-average ^{11}C-DASB binding potentials for all regions and whole brain in methylenedioxymethamphetamine cohort. (B) Group-average ^{18}F-FDG uptakes for all regions and whole brain in methylenedioxymethamphetamine cohort. (C) Group-average ^{11}C-DASB binding potentials for all regions and whole brain in PBS cohort. (D) Group-average ^{18}F-FDG uptakes for all regions and whole brain in PBS cohort. Sample sizes: ^{11}C-DASB methylenedioxymethamphetamine: n = 11; ^{18}F-FDG methylenedioxymethamphetamine: n = 15; ^{11}C-DASB PBS: n = 3; ^{18}F-FDG PBS: n = 3.

Subject-level GLM PET analysis

Three single-subject first-level GLM analysis results and the second-level group-average results are shown in Supplementary Figure 31 and Supplementary Figure 32, respectively, indicating decreases in ^{11}C-DASB binding potentials and ^{18}F-FDG uptakes 50-60 minutes following methylenedioxymethamphetamine administration compared to baseline.

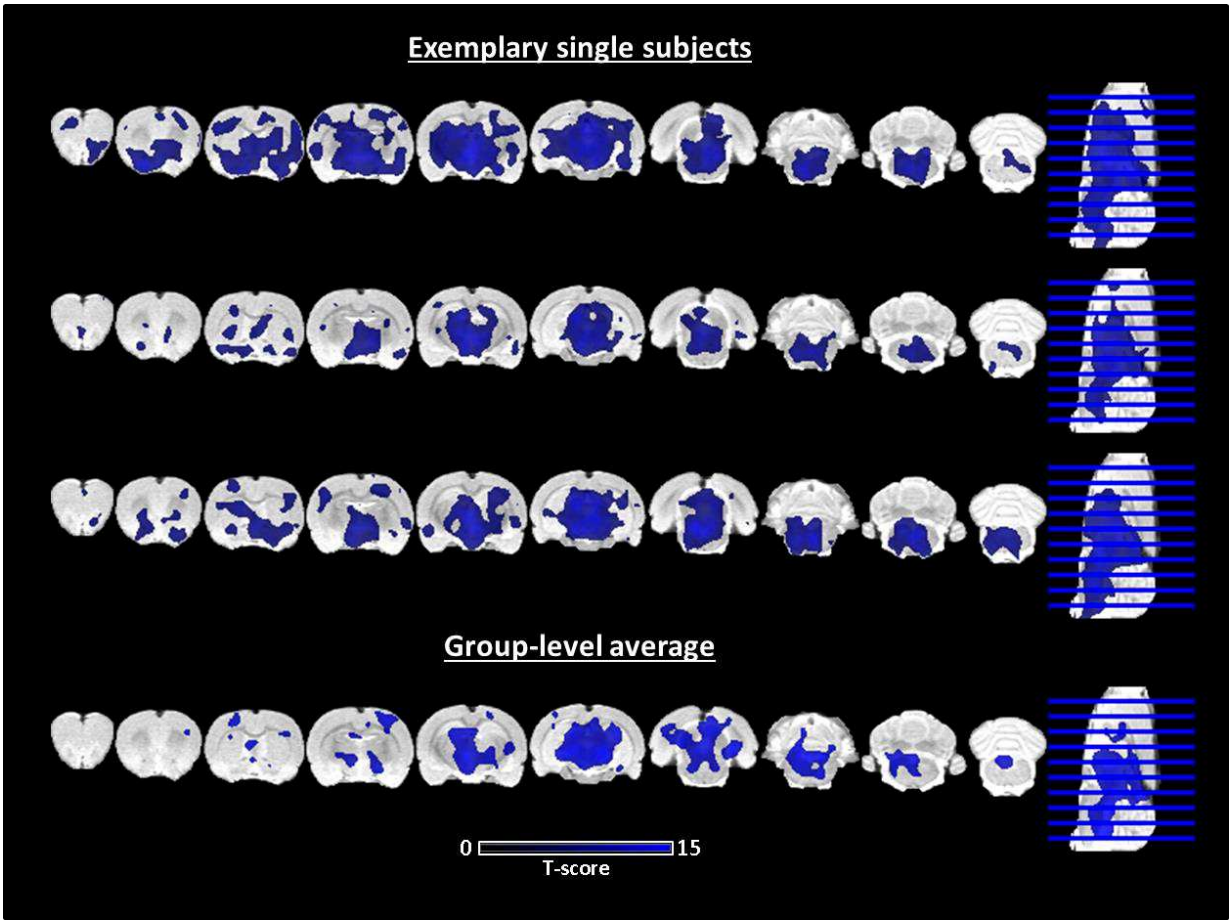

Supplementary Figure 31: First-level analysis of ^{11}C-DASB PET datasets indicating decreased binding potentials in three exemplary subjects and in the generated group-average readout in the period 50-60 minutes after the methylenedioxymethamphetamine challenge compared to baseline ($p < 0.05$, FWE corrected).

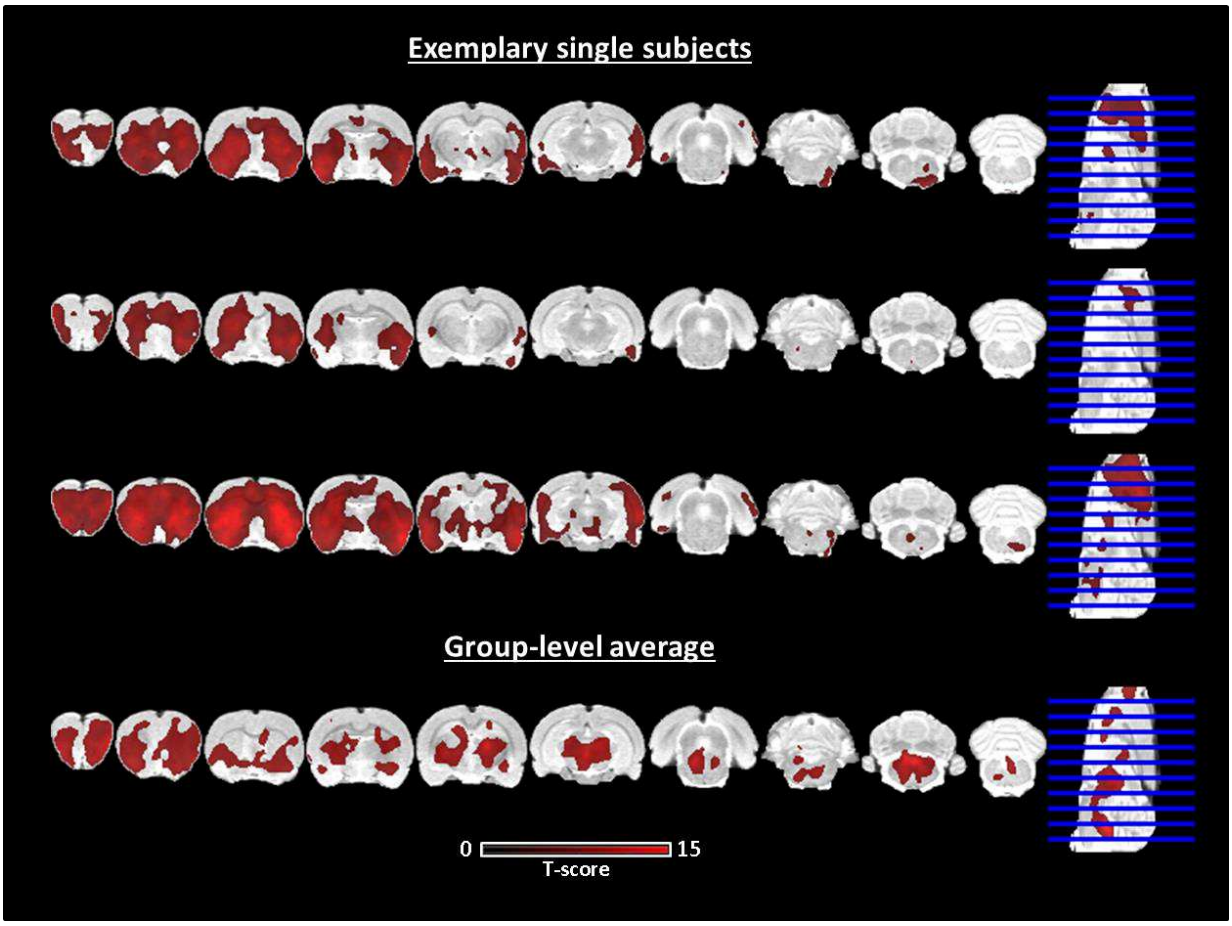

Supplementary Figure 32: First-level analysis of ^{18}F-FDG PET datasets indicating increased uptakes in three exemplary subjects and in the generated group-average readout in the period 50-60 minutes after the methylenedioxymethamphetamine challenge compared to baseline ($p < 0.05$, FWE corrected).

Cerebellar Normalization

To investigate the validity of the cerebellum as pseudo-reference region for ^{18}F-FDG normalization, we took two approaches. First, we performed an additional anaylsis using whole-brain normalization. Secondly, we fitted the the TACs in the baseline period, defined as the final 10 minutes before the challenge, in the striatum and cerebellum to investigate changes in[^{18}F-FDG after the pharmacological challenge (Supplementary Figure 33).

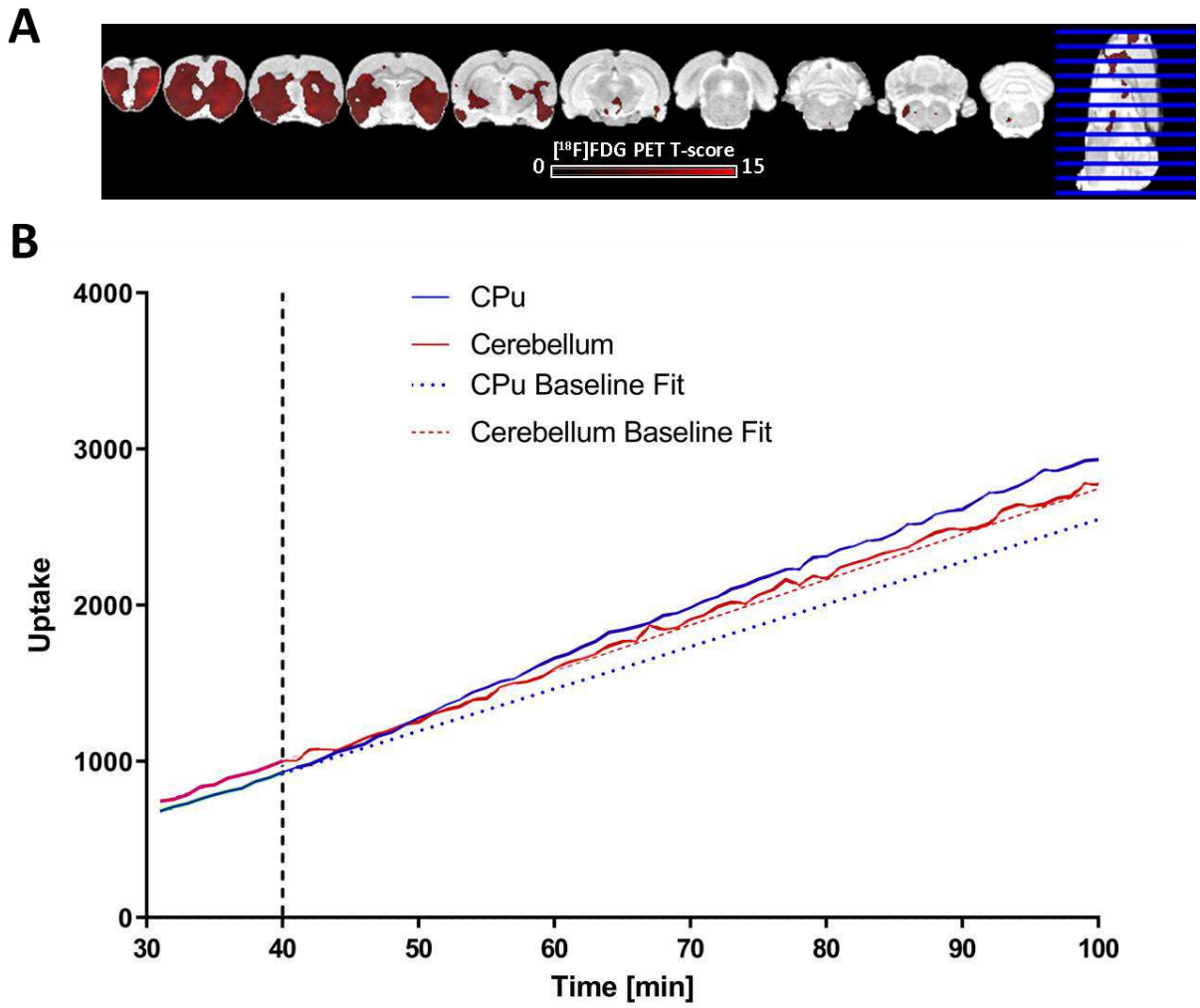

Supplementary Figure 33: Evaluation of cerebellar normalization for ^{18}F-FDG-fPET. (A) Using global normalization, increases can be seen in the same frontal areas using cerebellar normalization, however of lower magnitude ($p < 0.001$, $p < 0.05$ cluster-level FWE correction). (B) Average ^{18}F-FDG TACs in the cerebellum and caudate putamen. The respective dotted lines indicate the linear fit computed over the 10 minutes prior to the challenge. To compare the fits with the respective uptakes following the challenge, their slopes are projected to the end of the scans.

Similar patterns of metabolic increases were observed when employing whole-brain normalization, yet the magnitudes were lower compared to the cerebellar normalization approach (Supplementary Figure 33A). The linear regressions in Supplementary Figure 33B provided very accurate fits for both cerebellar ($R^2 = 0.9986$) and striatal ($R^2 = 0.9988$) TACs. However, whereas postchallenge cerebellar uptake remained in fairly good agreement with the fit calculated from the baseline, striatal ^{18}F-FDG uptake increased immediately after the challenge. This was quantified by comparing the respective regression slopes before and after challenge. There was little difference for the cerebellum, with the post-challenge slope being

4% higher than the prechallenge slope. In contrast, the slope in the striatum increased by 25% after challenge compared with the slope of the pre-challenge fit.

Evaluation of Correlation Robustness between BOLD-fMRI and ^{11}C-DASB PET changes

To further investigate if the correlation between the alterations observed in hemodynamic and SERT occupancy following methylenedioxymethamphetamine exposure remains valid when applying different analytical approaches, we performed a number of additional analyses (Supplementary Figure 34).

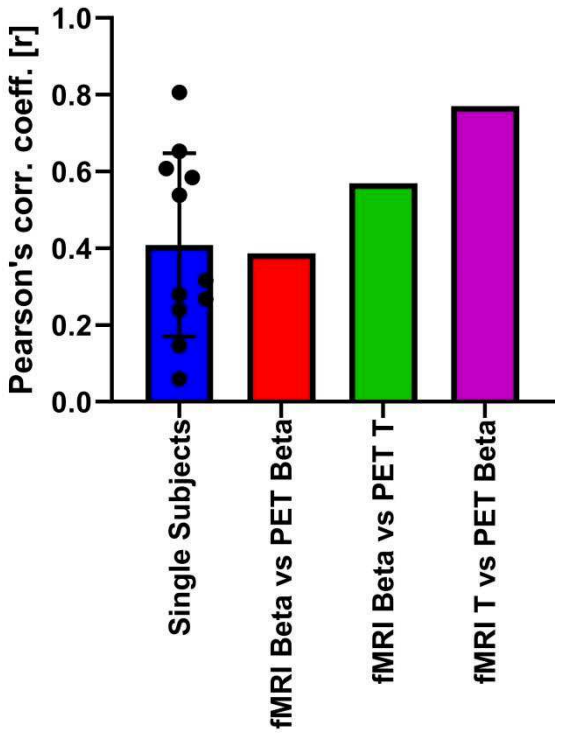

Supplementary Figure 34: BOLD-fMRI – ^{11}C-DASB-PET correlations using different metrics: single-subject correlations (blue), fMRI beta values vs PET beta values (red), fMRI beta values vs PET t-scores (green) and fMRI t-scores vs PET beta values.

At single-subject level, although for all subjects the two readouts correlated significantly, we observed a relatively high variability between them, the r values ranging from 0.05 to 0.8. On average, the single-subject correlation between hemodynamic and SERT availability decreases was 0.41 ($p < 0.05$). For group-level analysis, when employing beta values for both readouts instead of the t-scores used in the main manuscript, the correlation decreased to $r = 0.39$, but remained significant ($p < 0.05$). Going further the data showed that the difference between t-score and beta-value correlations was driven by fMRI beta values, since replacing

the PET t-scores with beta values while retaining the fMRI t-scores did not strongly affect the readout ($r = 0.77$, $p < 0.001$). On the other side, retaining PET t scores and changing the fMRI metric to beta values also reduced the correlation to 0.57 ($p < 0.01$).

Temporal characterization of the observed changes

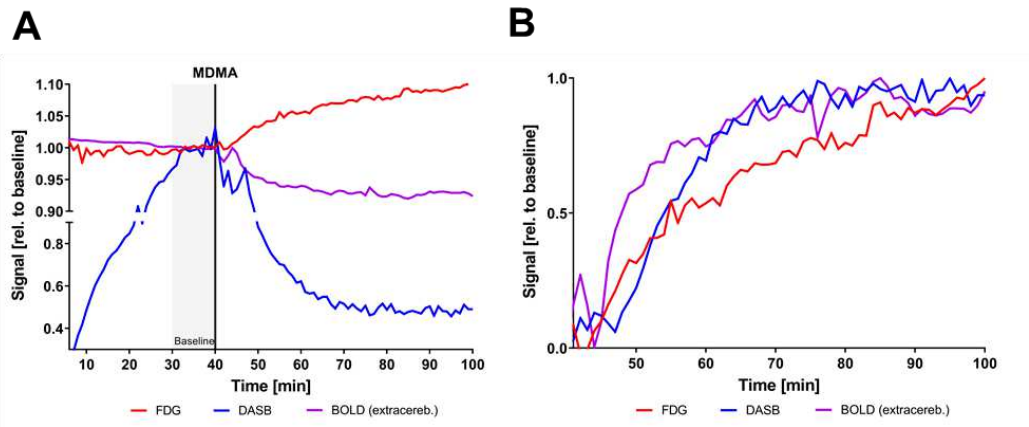

Supplementary Figure 35: Temporal alterations of the three signals (A) in relation to their respective baselines, (B) relative to their respective maximum changes (0=no change, 1=maximum change)..

The temporal characteristics of hemodynamic and SERT availability decreases were highly comparable, both reaching 90% of their maximum changes 30 minutes after the challenge (Figure 6). In contrast to the other two datasets, [^{18}F]FDG increased linearly, reaching 90% of the maximum change only 45 minutes after the challenge, with the whole-brain average [^{18}F]FDG TAC continuing to increase until the end of the scan. This finding suggests that metabolic increase may persist longer than one hour after the MDMA challenge included in the scans.

Supplementary Discussion

The power of multimodal imaging

We show the ability of multimodal imaging to elucidate *in vivo* effects of drugs due to the complementary readout provided by PET, which is much less reliant on hemodynamic parameters (Villien et al., 2014). While BOLD-fMRI can be a very useful method and exhibits various advantages to PET in terms of spatial or temporal resolution, in addition to not requiring the administration of radioactive substances, its convoluted substrate can make its mapping onto neuronal activity challenging, as demonstrated by our study. Adding PET to the equation can be advantageous, as also shown by previous work. Different activation and functional connectivity patterns have been reported using simultaneous ^{18}F-FDG fPET and

fMRI (Ionescu et al., 2021b; Wehrl et al., 2013). Additionally, PET/fMRI imaging has yielded strong complementary insight in previous pharmacological studies (Sander et al., 2013).

The present study demonstrates that advanced imaging technology can offer tremendous insight in understanding the mechanism of drugs compared to unimodal scans. Future research employing similar study protocols in either clinical or preclinical pathological cohorts would be of significant interest to elucidate how the acute effects of drugs such methylenedioxymethamphetamine revealed by PET in addition to fMRI correlate with therapeutic outcomes. Importantly, we show that our study design employing constant tracer infusion can enable the reliable mapping of effects in single subjects. This is a major improvement to the pure group-average readout obtainable when applying the tracer as a single bolus, since it enables clinical translatability. When investigating the relation between hemodynamic and SERT availability changes single-subject level on average we observed significant correlations. However, it remains interesting to see if future studies may elucidate whether the variability seen on single-subject level is physiologically significant or just of methodological nature.

The additional effects of methylenedioxymethamphetamine to those discussed by us need to be briefly stated. First, methylenedioxymethamphetamine and endogenous serotonin bind to other receptors highly expressed in the brain, such as the 5-HT_1 receptor family (Dipasquale et al., 2019). Also, the neuronal activations indicated by fPET and hemodynamic changes mapped using fMRI could be caused by the effects of methylenedioxymethamphetamine on other neurotransmitters (Gough et al., 1991). For example, dopamine, similarly to serotonin, has been shown to cause vasoconstriction when released at high concentrations (Brodde, 1982). However, the strong correlation between SERT occupancy and hemodynamic changes implies that serotonin affects brain microcirculation more strongly compared to other neurotransmitters, in line with previous hypotheses (Cohen et al., 1996; Ferrington et al., 2006; Quate et al., 2004). Interestingly, although both methylenedioxymethamphetamine and psilocybin have potent serotonergic actions, psilocybin has a very low affinity to the SERT, unlike methylenedioxymethamphetamine (Passie et al., 2002). Thus, it is interesting that both drugs induce similar spatial patterns of hemodynamic decreases (Carhart-Harris et al., 2012; Carhart-Harris et al., 2015). Since of all serotonergic receptors, psilocybin has the highest affinity to the 5-HT_{2A} receptor (Passie et al., 2002), which has been shown to induce vasoconstriction peripherally, it is reasonable to assume that this is similar in the brain. To accurately elucidate the substrates of hemodynamic and metabolic changes, distributions of all drug targets are required. PET/MRI imaging offers the opportunity to elucidate the effects

of psychedelic drugs by combining data on transporters and receptors with hemodynamics measured by BOLD-fMRI. Recent work has demonstrated how insight into different receptor distributions can be used to better understand changes in BOLD-fMRI data (Dipasquale et al., 2019). Such analytical approaches are of interest to gain a deeper understanding of drug mechanisms.

Study limitations

The present study was performed on anesthetized animals. Preclinical studies offer many advantages compared to human studies, such as high cohort homogeneity regarding age, strain, and gender. However, the effects of the used anesthesia must be considered especially when compared to similar human awake studies. Generally, interactions between the drug and the used anesthesia cannot be excluded. Studies comparing the readout of the methylenedioxymethamphetamine challenge under awake conditions and different anesthesia protocols are therefore necessary in the future. Nonetheless, we kept the anesthesia at levels indicated previously for fMRI scans under isoflurane in terms of physiology and readout (Hutchison et al., 2014). Additionally, the fact that the anatomical patterns of the BOLD decreases was in concordance with previous data acquired in awake humans supports the translatability of our findings (Carhart-Harris et al., 2015). Furthermore, not only BOLD can be affected by the isoflurane anesthesia, but also metabolism and consequently the ^{18}F-FDG readout. Earlier studies have shown that under isoflurane the ^{18}F-FDG distribution is significantly altered. For instance, while in awake animals the cortical uptake is above the whole-brain average, under isoflurane it decreases below the average of the brain (Spangler-Bickell et al., 2016). Since already at rest such alterations are evident, it is natural to infer that they would also translate when looking at either pharmacological or non-pharmacological stimulations, but it is difficult to speculate precisely in which manner. Anesthesia is a more general confound in small-animal studies and significant work still needs to be performed to have a better sense of the confounds generated compared to the awake condition.

While previous evidence suggests the higher robustness of fPET compared to fMRI to hemodynamic changes (Villien et al., 2014), their effects on the ^{18}F-FDG uptakes after the challenge cannot be excluded entirely. However, our data investigating the TAC slopes pre- and post challenge provide evidence that fPET remained largely unaffected to such effects since for the cerebellar uptake after the challenge remained stable compared to the substantial increase shown for the striatum. The data emphasize that the cerebellum is a valid reference region for our study and suggest that potential hemodynamic effects were largely negligible.

In conclusion, the use of fPET for inferring neuronal activity, although very promising, is still at a very early stage. Therefore, a number of aspects remain to be clarified both methodologically and in terms of the physiological basis and relationship to BOLD changes. While increased glucose consumption is regularly associated with positive BOLD responses, there is some evidence of increased glucose consumption measured by functional magnetic resoncance spectroscopy during deactivation in a checkerboard stimulation paradigm (Martínez-Maestro et al., 2019) or decreased glucose consumption during stimulation (Schaller et al., 2013). Such occurances show, that similarly to BOLD changes, metabolic increases do not necessarily map onto neuronal activation or vice-versa and further work is needed to further clarify these aspects.

Furthermore, our BOLD-fMRI scans did not cover the entire brain, therefore information from parts of the cerebellum was not captured. In addition, the use of a surface coil likely resulted in a poorer quality BOLD signal in deeper brain stuctures compared to the cortex. Studies covering all brain areas with volume coils may be more sensitive to the effects of this drug on hemodynamic level. This aspect may to a certain extent explain the difference in correlations when using beta values instead of t-scores.

3. Discussion

Whether at rest or under stimulation, the function of the brain involves several simultaneous, inter-connected processes taking place at different spatial, temporal and physiological scales. For most pathologies, examining only one aspect of brain function has proven to be insufficient to develop working therapies. The present work shows the value of employing simultaneous PET/fMRI for elucidating complementary aspects of the two modalities to study brain function *in vivo*.

3.1 BOLD-fMRI and [^{18}F]FDG PET: Similar but not Identical

First, this thesis highlights the complementarity of the presumably very comparable readouts of dynamic [^{18}F]FDG PET and BOLD-fMRI in two different cases: resting-state functional connectivity and brain activation after a pharmacological challenge using MDMA (Ionescu et al., 2021b; Ionescu et al., 2022).

3.1.1 [^{18}F]FDG PET for Resting-state Functional Connectivity

RsFC computed using BOLD-fMRI has been proposed as a potential biomarker for brain function in recent decades (Ripp et al., 2020). The increased interest in the analysis of brain [^{18}F]FDG PET data has also led to new research in the field of metabolic functional networks, derived from [^{18}F]FDG uptakes. The readout of different studies needs to be differentiated depending on the type of methodology employed. To this extent, metabolic connectivity computed over static [^{18}F]FDG PET scans of different subjects is here referred to as static PET-derived rsFC (sPET-rsFC). If the correlations were calculated within the same subject, analogously to fMRI, the readout is referred to as bolus dynamic PET-derived rsFC (bdPET-rsFC) in case the tracer was applied as a bolus. If the tracer was applied as an infusion, the readout is referred to as infusion dynamic PET-derived rsFC (idPET-rsFC).

In the first publication comprising this thesis (Ionescu et al., 2021b), bdPET-rsFC and BOLD-derived rsFC (BOLD-rsFC) were computed and compared using different approaches. On whole-brain level, the data showed that the correlations computed from [^{18}F]FDG PET data are neither completely different from BOLD-rsFC, nor do they overlap to a very high extent (Ionescu et al., 2021b). The whole-brain level comparison between the two readouts obtained using the seed-based approach indicated moderate correlation and overlap. Interestingly however, both outputs were shown to exhibit comparable graph theory properties. The partial overlap observed on whole-brain level could also be detected on network level, where three common networks for both modalities were identified together with a number of modality-

exclusive RSNs. Seed-based analysis and ICA were both employed, since previous work has indicated the dependence on the analytical approach when comparing PET-rsFC and BOLD-rsFC (Ionescu et al., 2021b). For sPET-rsFC, Wu et al. demonstrated good overlap with BOLD-rsFC using seed-based analysis (Wu et al., 2009). In contrast, in a later study ICA has indicated much lower overlap between both readouts (Di et al., 2012). Specifically, a number of classic RSNs such as the DMN could not be identified using ICA from the static [^{18}F]FDG PET data. In addition, the connectivity between the different components was generally lower compared to the BOLD-derived components. The same group performed direct comparisons between the two methods in more recent work (Di et al., 2017). They indicated only moderate correlation ($\rho = 0.31$) and overlaps between BOLD-rsFC and sPET-rsFC. Interestingly, the authors indicated that the sPET-rsFC readout was more similar to both BOLD-rsFC and to intersubject gray matter volume (GMV) correlations, than GMV and BOLD-rsFC to each other. They suggested that the readout obtained from sPET-rsFC is at an intermediate position between GMV and BOLD-rsFC data (Di et al., 2017). This complements the conclusion of the work published in 2012 (Di et al., 2012), implying that certain inter-regional relationships could only be obtained using temporal readouts, leading sPET-rsFC, as well as GMV, to miss certain aspects of rsFC.

Recently, a number of papers have used dynamic [^{18}F]FDG PET datasets to compute rsFC. Employing a bolus protocol, Wehrl et al. identified three metabolic RSNs comparable to simultaneously-acquired BOLD-derived RSNs (Wehrl et al., 2013). For both modalities, the RSNs were sensitive to whisker stimulation. In the first human bdPET-rsFC study, Passow et al. identified the default-mode network using seed-based analysis of dynamic [^{18}F]FDG PET data following a bolus (Passow et al., 2015b). The similarity could not be confirmed by Tomasi et al. using ICA (Tomasi et al., 2017), emphasizing that comparing the two readouts strongly depends on the type of analysis used.

Since findings from previous publications indicated discrepancies in identifying RSNs depending on the applied analysis (Di and Biswal, 2012; Wu et al., 2009), RSNs were defined as being common for bdPET-rsFC and BOLD-rsFC if they were revealed by both ICA and seed-based analysis (Ionescu et al., 2021b). Using this approach, three common networks could be identified in the present work: the DMN, the basal ganglia network and a cerebellar-midbrain network. Nonetheless, the identified common RSNs also only overlapped partially between methods (Ionescu et al., 2021b). For instance, the DMN was split in two separate anterior and posterior components in the fMRI readout, as reported previously in rats (Hsu et

al., 2016a; Lu et al., 2012). In PET, the component found to comprise the midline regions reported as hubs of the DMN was more weighted towards posterior areas, but also exhibited signal in more anterior regions, such as the cingulate and prefrontal cortices. Interestingly, cerebellar contributions to the DMN were found for both fMRI and [^{18}F]FDG PET-derived components (Ionescu et al., 2021b). The role of the cerebellum in the DMN has only been sporadically investigated (Castellazzi et al., 2018; Habas et al., 2009b), partly due to its omission from many human studies. The basal ganglia network, previously found in rats using fMRI (Becerra et al., 2011; Hutchison et al., 2010), exhibited common signal for the two methods primarily in the striatum. The network involving cerebellum and midbrain showed higher integration between both regions in bdPET-rsFC, while the two areas appeared more segregated for BOLD-rsFC (Ionescu et al., 2021b).

Additionally, a number of modality-exclusive networks were identified in this work using ICA. For the BOLD data, these included mostly homotopic connections between the left and right hemispheres of the same regions – for instance the motor network or the auditory network (Ionescu et al., 2021b). The networks found in the BOLD-fMRI data have been previously reported (Hutchison et al., 2010). The [^{18}F]FDG PET dataset revealed three exclusive networks, the signal originating to a high extent from subcortical areas (Ionescu et al., 2021b). The networks have only been partially reported previously. The component including retrosplenial, hypothalamic and olfactory signal was already found by Wehrl et al. (Wehrl et al., 2013), while the connectivity between thalamus and hypothalamus was only found in awake rats using BOLD-rsFC (Becerra et al., 2011). The physiological meaning of these networks remains elusive.

More recently, the advances in [^{18}F]FDG tracer application paradigms have also been implemented in metabolic connectivity research. Specifically, Amend et al. employed simultaneous PET/fMRI to compare three different readouts using seed-based analyses: BOLD-rsFC, bdPET-rsFC and idPET-rsFC (Amend et al., 2019). The data demonstrated that the readout from dynamic [^{18}F]FDG PET data is dependent on the tracer application regarding both spatial and temporal properties of the readout. The authors suggested that the different kinetics of the two protocols determine the respective outputs. Specifically, the data after a bolus may be dominated by a high K_1/k_2 ratio at the beginning of the scan due to the large availability of tracer in the blood plasma. The K_1/k_2 ratio decreases over time, but never reaches a state of equilibrium, explaining the decreasing correlations observed when calculating bdPET-rsFC over later time-periods after the start of the scan. The data confirmed

a similar hypothesis suggested in earlier work by Tomasi et al. (Tomasi et al., 2017). In contrast, the work by Amend et al. showed the equilibrium ensured by a constant infusion after 20 to 30 minutes led to differing, but temporally stable idPET-rsFC patterns (Amend et al., 2019). Interestingly, both readouts indicated moderate correlations with BOLD-rsFC, albeit slightly higher for bdPET-rsFC. The postulated dominance of K_1 kinetics for bdPET-rsFC may explain this aspect, indicating that the bdPET-rsFC is physiologically more comparable to BOLD-rsFC, both being at least partially driven by blood flow kinetics. The increased influence of K_1 kinetics must be taken into account when interpreting the data in the first publication comprising the present thesis (Ionescu et al., 2021b).

Taken together, it becomes apparent that the interpretation of correlations inferred from [^{18}F]FDG PET data is intricate: sPET-rsFC, bdPET-rsFC and idPET-rsFC overlap to different extents with BOLD-rsFC. Therefore, it is likely that the different paradigms may shed light on distinct physiological phenomena. Unraveling the physiological meaning of each type of metabolic connectivity recently led to intense debates in the literature. The recent study by Jamadar et al. compared sPET-rsFC with idPET-rsFC and BOLD-rsFC (Jamadar et al., 2021). The authors found that sPET-rsFC and idPET-rsFC overlapped poorly, suggesting that sPET-rsFC is a poor predictor of subject-level metabolic connectivity acquired using idPET-rsFC and does not reflect functional relationships between brain regions due to the lack of temporal information (Jamadar et al., 2021). These statements triggered a direct response by Sala et al., arguing that connectivity in general is not dependent on temporal correlations, GMV and structural connectivity for instance being acquired without temporal information, similarly to sPET-rsFC (Sala et al., 2021). Most recently, the same group published work showing that sPET-rsFC overlaps strongly with structural connectivity (Yakushev et al., 2021). In general, the partly contrasting results, together with the debate on their physiological significance emphasize the acute need for further research to understand the different readouts. Apart from purely physiological aspects, technical aspects of the data have been largely neglected, especially for temporal PET correlation studies. As pointed out by Sala et al., the short frames used to compute metabolic connectivity from dynamic PET deliver the advantage of temporal resolution at the cost of poorer SNR (Sala et al., 2021). Factors such as frame length or applied radioactivity still have to be thoroughly investigated with regard to their impact on metabolic connectivity data. While constantly growing in recent years (Sala and Perani, 2019), the above passages emphasize that current research on metabolic connectivity has only scratched the surface on its significance, as well as its dependence on experimental or analytical paradigms.

3.1.2 Neurovascular Uncoupling: [^{18}F]FDG fPET/fMRI Unravels Acute MDMA Effects

In the third publication comprising this thesis, functional PET (fPET) using a constant infusion was applied along with BOLD-fMRI to investigate the effects of an acute MDMA challenge on hemodynamics and metabolism (Ionescu et al., 2022).

Our work indicated concurrent increases in glucose consumption, as indicated by [^{18}F]FDG fPET, and globally decreased hemodynamics, as shown by the BOLD-fMRI readout (Ionescu et al., 2022). The changes observed in fMRI mirrored the discussed decreases observed in the MRI-based publications described in the introduction (Carhart-Harris et al., 2012; Carhart-Harris et al., 2015). One of the strengths of the present work was the simultaneous acquisition of [^{18}F]FDG fPET data, enabling a precise temporal correlation between hemodynamic and metabolic effects of MDMA. Importantly, at the time of the challenge administration, [^{18}F]FDG uptake had reached K_1/k_2 equilibrium, as shown by the linear increase in the TACs and lack of change in the normalized TACs. Under these circumstances, significant increases in [^{18}F]FDG uptake over several regions were observed following the acute MDMA challenge. These increases accompany the decreases observed in the BOLD signal, albeit at regionally different magnitudes, across the entire brain (Ionescu et al., 2022). The simultaneous acquisition and tracer application protocol precluded temporal mismatches when investigating the effects of the compound. Taken together, the two datasets reveal not just a mismatch, but simultaneous changes in completely opposite directions in two measures which are both expected to map onto neuronal activity. Since both measures are only indirect measures of neuronal activity, this finding suggested that either hemodynamics or glucose consumption were sufficiently altered by an additional, simultaneously occurring phenomenon, to strongly disturb their relation to neuronal activity (Ionescu et al., 2022).

Further analyses provided strong evidence that hemodynamics are peripherally decreased under acute MDMA, disabling the neurovascular coupling. This was indicated by signals from extracerebral regions, comprised of tissues around the skull, where neuronal activity can be excluded. The data indicate similar changes in these areas to those observed within the brain, suggesting that hemodynamics are peripherally decreased after acute MDMA administration (Ionescu et al., 2022). This is in line with previous work describing direct vasoconstrictive effects of serotonin (Kim et al., 2018; Van Nueten et al., 1985). Therefore, taken together, the data seem to indicate a neurovascular uncoupling – increased activity, as mapped by [^{18}F]FDG-PET, accompanied by decreased hemodynamics. Generally, the concept

of MDMA having mostly excitatory, rather than inhibitory effects, appears to converge better with known subjective effects induced by this drug, including increased sociability, food seeking, sexual arousal, enthusiasm and general energy (Carhart-Harris et al., 2015; Sumnall et al., 2006). The limbic and frontal cortical regions showing the highest [^{18}F]FDG increases also appear to be functionally in line with the above hypotheses (Ionescu et al., 2022).

On the methodological side, the dataset emphasized different aspects. First, although fPET has only been used up to date for task-based studies (Hahn et al., 2016; Rischka et al., 2018; Villien et al., 2014), as demonstrated by the work in this thesis, the study of acute pharmacological effects offers another excellent application for this method (Ionescu et al., 2022). The ability to truly depict acute molecular effects *in vivo* using fPET opens new avenues in exploring acute metabolic effects of pharmacological compounds. Secondly, fPET is perfectly suited for simultaneous acquisitions with fMRI. This work (Ionescu et al., 2022) emphatically demonstrates the importance of investigating neuronal activity changes from different angles and sheds new light onto the conclusions drawn over the last years from methods relying solely on hemodynamic changes (Carhart-Harris et al., 2012; Carhart-Harris et al., 2015). The same holds true not only for activation studies, but also for studies on psychedelic effects on FC (Carhart-Harris et al., 2015; Roseman et al., 2014).

3.2 The Roles of Monoamines in Functional MRI Readouts

Neurotransmitters are essential actors in the transmission of signals across the brain. Especially modulatory neurotransmitters, such as monoamines, shape the brain in multiple ways, by affecting properties of synapses and neurons (Boto and Tomchik, 2019). Importantly, monoaminergic systems are targeted by drugs aiming to treat various disorders ranging from MDD to PD. Thus, it is important to elucidate the correlation between monoamines, along with their target receptors and transporters, and large-scale brain function. Therefore, as part of the final publication comprising the thesis, change induced by acute MDMA application in hemodynamics and SERT occupancy, one of the drug's main targets, were compared and correlated using simultaneous [^{11}C]DASB PET/fMRI (Ionescu et al., 2022). In the second publication part of the present work, interactions of monoaminergic systems with rsFC computed from simultaneously acquired datasets were evaluated (Ionescu et al., 2021a).

3.2.1 Direct Correlations of Serotonin and Hemodynamics

In the third manuscript part of the present thesis, investigating the acute effects of MDMA (Ionescu et al., 2022), we performed an additional study under the same experimental conditions as for the [^{18}F]FDG fPET/fMRI data described in the previous subchapter. [^{11}C]DASB PET was acquired simultaneously to BOLD-fMRI to correlate SERT occupancy with hemodynamic changes. The hemodynamic decreases observed in the first cohort were reproduced in the [^{11}C]DASB PET/fMRI dataset, demonstrating the reliability of the readout. As expected, since one of the main effects of MDMA is SERT blockage, [^{11}C]DASB bindings decreased across the brain following the MDMA challenge. Intriguingly, the regional magnitudes of [^{11}C]DASB reductions correlated very strongly with those of BOLD-fMRI decreases (Ionescu et al., 2022). Since SERT blockage by MDMA is expected to lead to increased extracellular serotonin concentrations, one could speculate that the finding supports the hypothesis that serotonin directly affects cerebral microvasculature (Cohen et al., 1996). Put differently, the readout implies that higher local extracellular serotonin leads to stronger decreases in hemodynamics. This effect is likely superimposed on the systemic decrease in hemodynamics evident in the extracerebral BOLD reductions discussed above (Ionescu et al., 2022). However, to further elucidate the direct effects of serotonin, further studies are necessary directly measuring *in vivo* concentrations of this neurotransmitter for example by microdialysis after MDMA application, ideally simultaneously with SERT occupancy and hemodynamics.

If the observed decreases of the BOLD signal were only due to systemic vascular suppression, it would appear feasible to retrieve neuronal information from BOLD by modeling the magnitude of the suppression. However, the data suggest that it is far from trivial to model the BOLD data to delineate neuronal activity, since magnitudes of the vascular effects of MDMA via serotonin appear to be regionally different (Ionescu et al., 2022). In addition, SERT is only one of the targets of MDMA, the drug also having high affinities to several serotonin receptors (Dipasquale et al., 2019), as well as affecting other monoaminergic systems (Gough et al., 1991). The same holds true for most psychedelic drugs. Therefore, the data acquired in the present works indicates the urgent need of combining molecular, hemodynamic and metabolic readouts to better understand the *in vivo* effects of these drugs. Novel analytical approaches including maps of several receptor and transporter distributions appear suited to delineate the effects of pharmacological compounds (Dipasquale et al., 2019). However, it becomes clear that simultaneous approaches such as those applied in this work are important, if not essential, to correlate acute drug effects at different levels.

3.2.2 Monoaminergic Transporter and Receptor Distributions Correlate with BOLD-Derived Resting-State Networks

In addition to the direct vascular effects which could affect neurovascular coupling, as shown in the previous subsection, monoaminergic systems can directly correlate with rsFC patterns. However, the relationship between monoamines and RSNs is poorly understood, few studies having performed correlations between the two. (Ionescu et al., 2021a), Therefore, this work aimed to investigate possible correlations between regional D2R and SERT availabilities, and prominent RSNs. To this end, we performed simultaneous [^{11}C]raclopride and [^{11}C]DASB PET/fMRI acquisitions at resting state in two separate cohorts (Ionescu et al., 2021a).

The readout indicated significant negative correlations between striatal D2R availability and the rsFC between and within all RSNs (Ionescu et al., 2021a). The data are consistent with the hypothesis that the indirect pathway, mediated by striatal D2Rs, inhibits thalamic and cortical activity (Calabresi et al., 2014). Also negative, albeit weaker negative correlations, were found between D2R availability in the mPFC and the three RSNs. The anti-correlation was strongest, and most significant, with DMN rsFC (Ionescu et al., 2021a). The finding complements suggestions that prefrontal dopamine receptors and particularly the balance between D1 and D2 receptors, are of importance in schizophrenia (Avery and Krichmar, 2015; Durstewitz and Seamans, 2008; Kahnt et al., 2015; Puig et al., 2014). Increased prefrontal D2R availability has been shown to generate cognitive flexibility by facilitating the transition between different network states, which would explain the negative correlation between prefrontal D2R availability and rsFC observed in the present work (Avery and Krichmar, 2015; Durstewitz and Seamans, 2008; Kahnt et al., 2015; Puig et al., 2014).

For striatal SERT availability, correlations with the investigated networks were weak. Only anti-correlations with parts of the salience network could be identified (Ionescu et al., 2021a). The data complements recent findings indicating that connectivity between the raphé nuclei and the striatum is negatively correlated with salience in schizophrenia (Han et al., 2020). Finally, prefrontal SERT availability exhibited network-specific correlation patterns with the investigated RSNs. In particular, rsFC was predominantly negatively correlated with prefrontal SERT availability (Ionescu et al., 2021a); however, it was accompanied by a positive correlation between prefrontal SERT availability and local prefrontal rsFC. This finding is of interest since the prefrontal cortex is the main hub of the anterior DMN, which has been proposed to be to a certain degree physiologically separatde from the posterior DMN in both rats and humans (Lu et al., 2012). A further analysis performed in the present work

investigated the balance between the connectivity within the anterior DMN and the connectivity between the anterior DMN and the posterior DMN, SN and SMN. Of note, this analysis revealed an even stronger correlation of SERT availability with the described balance between local and distant prefrontal rsFC (Ionescu et al., 2021a). This readout converges with several lines of evidence from the literature. In the study mentioned above, Conio et al. demonstrated that a shift in rsFC balance towards the DMN is associated with MDD, a pathology in which serotonin (Newberg et al., 2012; Parsey et al., 2006; Willeit et al., 2008) and specifically prefrontal SERT availabilities play essential roles (Celada et al., 2013; Conio et al., 2019; Puig and Gulledge, 2011). Several publications investigating the role of the DMN in MDD have delivered partly contradicting results (Yan et al., 2019); however, a recent meta-analysis revealed that the findings converge to the conclusion that specifically the anterior DMN is hyperconnected in MDD (Yan et al., 2019). Taken together, the data in the present work support the role of SERT in mediating prefrontal rsFC and potentially the relevance of this relationship in depressive phenotypes (Ionescu et al., 2021a).

A major strength of our study was the homogeneity of the cohorts and experimental conditions (Ionescu et al., 2021a). The few existing studies investigating similar relationships between neurotransmitter systems and rsFC were performed in humans (Hahn et al., 2012; McCutcheon et al., 2019; Nagano-Saito et al., 2017; Roffman et al., 2016; Vidal et al., 2018). The differences in gender, lifestyle, and age within the cohorts can affect both neurotransmitter systems and rsFC, therefore being major confounds when investigating relationships between the two parameters. The cohorts of animals used in this work were matched for strain, gender, age, diet, and living conditions, enabling a much better correlation between the two parameters of interest (Ionescu et al., 2021a).

However, it needs to be stressed that the PET acquired data for both tracers does not allow direct inferences on either local neurotransmitter concentrations or receptor/transporter densities. This is due to the fact that the binding potentials only indicate the availability of receptors or transporters. Especially for the D2 receptor, the binding potential has been shown to be determined both by the receptor density and the concentration of endogenous dopamine, since it competes with [^{11}C]raclopride for the same binding sites (Park and Park, 2000; Patel et al., 2008). Future studies directly measuring dopamine or serotonin concentrations may contribute to further elucidate the aspects discussed in this work (Venton and Cao, 2020). Finally, another drawback of the study was that the correlations were performed in two separate cohorts (Ionescu et al., 2021a). Investigating two or more types of receptors or

transporters in the same cohort would enable to decipher direct interactions between the investigated molecular targets.

In conclusion, the performed work emphasizes the role of simultaneously acquired PET/fMRI data in understanding the molecular basis of rsFC. The data both support and advance the understanding of the interactions between brain properties at different physiological levels potentially driving several disease phenotypes. The generated readout can contribute to the development of both diagnostic and therapeutic approaches for these pathologies (Ionescu et al., 2021a).

3.3 The Role of Anesthesia

A potential confound of the data which needs to be taken into account for both BOLD-fMRI and [^{18}F]FDG PET is the use of isoflurane. While kept at levels indicated previously to be suitable for rsFC measurements (Hutchison et al., 2014) and shown within the scope of the publication to enable temporally stable physiology (Ionescu et al., 2021b), other types of anesthesia have been reported to deliver more comparable data to the awake condition (Paasonen et al., 2018). For [^{18}F]FDG PET, the publication included in this thesis replicated earlier findings, indicating that isoflurane affects the relative uptake in different brain regions (Ionescu et al., 2021b; Park et al., 2017; Spangler-Bickell et al., 2016). For instance, the uptake in the cortex was shown to be decreased, while the metabolism in the cerebellum and midbrain were largely conserved (Ionescu et al., 2021b). This is of relevance in light of previous studies on bdPET-rsFC revealing dependencies of the correlation readout on regional CMRGlu (Tomasi et al., 2017) or [^{18}F]FDG uptake ratios (Amend et al., 2019). More work is required to elucidate the impact of different anesthesia protocols, especially for [^{18}F]FDG PET-derived correlations (Ionescu et al., 2021b). Importantly, anesthesia effects may not only affect hemodynamics and metabolism, but its effect on the [^{11}C]DASB and [^{11}C]raclopride data also cannot be excluded – more work is also required on this topic. Finally, for the MDMA study, although the acquisition of the control cohort injected with PBS instead of MDMA under the same anesthesia protocol validates much of the readout, direct interactions between isoflurane and MDMA cannot be ruled out (Ionescu et al., 2022; Jonckers et al., 2015) and must be investigated in future studies.

3.4 Conclusion: Functional MRI - Gold Standard but not Untouchable

Functional MRI is the method which led to the surge in interest for *in vivo* imaging of neuronal activity (Ogawa et al., 1990b), although other available methods exhibit important

advantages. For instance, EEG measures neuronal activity much more directly than fMRI, since it captures voltage changes induced by the activation itself, rather than the secondary hemodynamic changes accompanying neuronal activity, while also boasting a higher temporal resolution. However, it has a much lower spatial resolution, in addition to its inability to measure signal from deeper areas in the brain. In terms of spatial resolution, single electrodes measuring calcium currents or fast-scan cyclic voltammetry provide much higher spatial accuracy compared to EEG and fMRI. However, they are complicated to perform due to their invasiveness and therefore unsuitable for clinical translation. Furthermore, they only offer data on one location in the brain, precluding the inference of processes occurring in different brain areas simultaneously. Finally, despite the large number of mechanisms that can be imaged at the whole-brain level with the multitude of available tracers, PET exhibits both low spatial and temporal resolution compared to fMRI. In addition, the production of radioactive PET tracers is not trivial, requiring for instance a cyclotron and bears the disadvantage of having to administer radioactive substances to the subject.

Therefore, fMRI has probably emerged as the dominating method for neuronal activity studies since it performs well all-round compared to all other methods in terms of technical specifications and straightforward experimental implementation. Nonetheless, although being considered a gold standard method, it has a number of potential weaknesses. The present work emphasizes the value of simultaneous PET/fMRI acquisitions in understanding the metabolic and molecular substrate of hemodynamics and neurovascular coupling measured using BOLD-fMRI. The first publication comprising the thesis (Ionescu et al., 2021b) indicates that hemodynamics may not reveal the entire extent of the brain's rsFC. The networks revealed exclusively using the [^{18}F]FDG PET suggest that rsFC also occurs between regions which BOLD-fMRI does not detect as being functionally connected. Furthermore, the substantial inter-subject variability in the expression of rsFC and RSNs has hindered its translation to clinical routine. The second publication comprising the thesis (Ionescu et al., 2021a) demonstrates certain molecular targets correlating with RSN patterns and can help understand the factors driving inter-subject rsFC variability, even in healthy cohorts. Finally, the third paper part of this thesis (Ionescu et al., 2022) combines information on metabolism and SERT occupancy to characterize the effects of a drug which induces an uncoupling between hemodynamics and neuronal activity. In such cases, data acquired using fPET appear to be a lot more robust compared to fMRI. Additionally, PET can also indicate the molecular substrates of simultaneous hemodynamic changes – in this case, the data showed that SERT blockage appears to be strongly related with the vascular effects in the BOLD-fMRI signal.

Taken together, the present thesis demonstrates that through its potential to image complementary physiological aspects to BOLD-fMRI, the simultaneous acquisition of PET offers important, and in some cases essential, additional information which can strongly enhance our understanding of the BOLD signal, as well as the *in vivo* function of the brain.

4. Summary

The brain is one of the body's most multifaceted and complex organs, its function still being incompletely understood. The development of imaging methods has massively benefitted the research of brain function in recent years, enabling the *in vivo* monitoring of brain function on different physiological, spatial and temporal levels. Brain imaging can be used to delineate effects ranging from task-based stimuli to drugs and pathologies on brain activation and connectivity. However, all imaging methods have specific caveats and can only provide readout on one single physiological level, which may be insufficient for various applications. This work aimed to elucidate the complementary value positron emission tomography (PET) provides when acquired simultaneously to blood-oxygenation-level-dependent functional magnetic resonance imaging (BOLD-fMRI). Specifically, the readout generated using PET was used to delineate metabolic and molecular substrates of both neuronal activation and resting-state functional connectivity (rsFC) derived using BOLD-fMRI.

In the first study, rsFC derived from BOLD-fMRI and simultaneously acquired [^{18}F]fluorodeoxyglucose ([^{18}F]FDG) PET was compared on whole-brain and resting-state network (RSN) levels. While BOLD-fMRI is considered gold standard and is most widely used for the acquisition of rsFC, the generated readouts with this method suffer from the convoluted nature of the BOLD signal and its indirect reflection of neuronal activity. Calculating connectivity from [^{18}F]FDG PET may serve to validate but also complement readout generated from BOLD-fMRI. The data indicated similar organizations of the connectomes acquired using the two techniques, but only moderate correlations and overlaps at whole-brain and network levels between both outputs. Three common networks and several modality-specific networks were identified. The mismatch between the results indicates functional connectivity acquired using [^{18}F]FDG PET may offer significant complementary information and warrants further research into its substrate and physiological significance.

In the second study, the correlations between different distributions of D2 receptors (D2R) and serotonin transporters (SERT), on one side, and three prominent RSNs, on the other, were investigated. Although monoaminergic systems are postulated to be of paramount importance for brain function and dysfunction, their relation to RSNs is poorly elucidated. The study revealed that D2R and SERT availabilities in two prominent dopaminergic and serotonergic projection areas, the striatum and medial prefrontal cortex, correlated in differentiated manners with the default-mode network (DMN), sensorimotor network (SMN) and salience network (SN). Specifically, the data showed strong negative correlation between striatal D2R

availability and rsFC across all three RSNs. Additionally, prefrontal SERT correlated with prefrontal rsFC but negatively with rsFC across the rest of the networks and regions investigated. The generated data shed additional light into interactions between monoamines and RSNs and complement hypotheses regarding monoaminergic contributions to various pathologies, including Parkinson's disease, major depressive disorder, schizophrenia and bipolar disorder.

The third study aimed to delineate the acute effects of methylenedioxymethamphetamine (MDMA) on hemodynamics, metabolism and SERT availability, one of the main targets of this compound. Along with other psychedelic compounds, MDMA has received significant interest over the last decade due to its potential in the treatment of psychiatric disorders, such as major depressive disorder or post-traumatic stress disorder. To this extent, imaging studies have been previously performed to elucidate the mechanisms of action of MDMA and other psychedelics. However, most studies relied on hemodynamic MRI-based methods to detect neuronal activations or deactivations induced by acute administration of these compounds. The readout in this work mirrors decreases in BOLD signal reported previously in human studies. However, the global BOLD decreases were accompanied by increases in glucose consumption shown by simultaneously acquired [^{18}F]FDG PET data. Additionally, comparable BOLD signal decreases were seen in extracerebral regions. The data indicate global hemodynamic suppression of non-neuronal nature, accompanied by neuronal activation induced by MDMA. In the brain, the BOLD decreases correlated with the magnitudes of changes in SERT occupancy, hinting towards additional local vascular effects induced by SERT blockage. The study indicated that hemodynamic decreases observed after MDMA administration do not map onto neuronal activity, but are probably induced by the vascular effects of endogenous serotonin or direct effects of MDMA on vascular serotonin receptors. The readout therefore puts into perspective and warrants a reevaluation of most studies investigating the effects of psychedelic drugs on neuronal activity through indirect hemodynamic effects.

The strongly complementary readouts of both modalities used in this work recommend further use of PET/MRI to study brain function at rest and under activation. Elucidating the intricate connections between neurotransmitter systems, hemodynamics, metabolism and large-scale functional networks will help to more thoroughly understand *in vivo* brain function and dysfunction, thereby supporting the targeted development of diagnostic and therapeutic strategies.

5. German Summary

Das Gehirn ist eines der vielseitigsten und komplexesten Organe, dessen Funktion noch immer nicht vollständig verstanden ist. Die Entwicklung bildgebender Verfahren hat die Erforschung der Hirnfunktion in den letzten Jahren massiv begünstigt und eine *in vivo* Überwachung auf verschiedenen Ebenen ermöglicht. Mit Hilfe der Bildgebung des Gehirns lassen sich die Auswirkungen von einfachen Stimuli, Medikamenten oder Krankheiten auf die Aktivierung und Konnektivität des Gehirns darstellen. Alle bildgebenden Verfahren haben jedoch auch bestimmte Nachteile und können jeweils nur eine einzige physiologische Ebene erfassen, was für verschiedene Anwendungen unzureichend sein kann. Ziel dieser Arbeit war es, die Komplementarität der Positronenemissionstomographie (PET) und der „Blood-Oxygenation-Level-Dependent" funktionellen Magnetresonanztomographie (BOLD-fMRT) zu untersuchen. Insbesondere wurde PET dazu verwendet, die metabolischen und molekularen Substrate neuronaler Aktivierung und „resting-state" funktioneller Konnektivität (rsFC) zu beschreiben, die mit BOLD-fMRI abgeleitet wurden.

In der ersten Studie wurden die aus der BOLD-fMRI und der gleichzeitig durchgeführten [^{18}F]Fluordeoxyglucose ([^{18}F]FDG)-PET abgeleiteten rsFC auf Ganzhirnebene und Resting-State-Netzwerk (RSN) Ebene verglichen. Obwohl BOLD-fMRT als Goldstandard gilt und am häufigsten für die Erfassung von rsFC verwendet wird, sind die generierten Ergebnisse durch die komplexe Natur des BOLD-Signals und dessen indirekter Widerspiegelung neuronaler Aktivität nicht einfach zu interpretieren. Somit könnten aus [^{18}F]FDG-PET berechnete Konnektivitätsdaten zur Validierung, aber auch zur Ergänzung der aus der BOLD-fMRI gewonnenen Ergebnisse dienen. Die Ergebnisse dieser Studie deuteten auf vergleichbare Organisationen der mit beiden Techniken erfassten Konnektome hin, jedoch nur auf moderate direkte Korrelationen und Überlappungen beider Datensätze, sowohl auf Gesamthirn-, als auch auf Netzwerkebene. Es wurden drei gemeinsame Netzwerke und mehrere modalitätsspezifische Netzwerke identifiziert. Die Diskrepanz zwischen den beiden Datensätzen deutet darauf hin, dass die mit [^{18}F]FDG-PET erfasste funktionelle Konnektivität möglicherweise eine wichtige ergänzende Messgröße darstellt und weitere Forschung über ihr physiologisches Substrat gerechtfertigt ist.

In der zweiten Studie wurden Korrelationen zwischen den Verteilungen von D2 Rezeptoren (D2R) und Serotonin-Transportern (SERT), einerseits, und drei bekannten RSN, andererseits, untersucht. Obwohl monoaminergen Systemen eine große Bedeutung für die Funktion und Dysfunktions des Gehirns zugeschrieben wird, sind ihre Verhältnisse zu RSN nur

unzureichend geklärt. Die Studie ergab, dass die Verfügbarkeit von D2R und SERT in zwei wichtigen dopaminergen und serotonergen Projektionsarealen, dem Striatum und dem präfrontalen Kortex, unterschiedlich mit dem „Default-Mode“ Netzwerk (DMN), „Salience“ Netzwerk (SN) und „Sensorimotorischen“ Netzwerk (SMN) korrelieren. Insbesondere zeigten die Daten starke negative Korrelationen zwischen der D2R Verfügbarkeit im Striatum und allen untersuchten RSN. Zusätzlich wurde gezeigt, dass präfrontale SERT-Verfügbarkeit mit frontaler rsFC positiv korrelierte, jedoch negativ mit der rsFC der anderen untersuchten Regionen und Netzwerke. Die Ergebnisse werfen ein zusätzliches Licht auf Interaktionen zwischen monoaminergen Systemen und funktionellen Netzwerken und ergänzen Hypothesen zur Bedeutung monoaminerger Systeme für mehrere Pathologien, einschließlich der Parkinson Krankheit, Depression, Schizophrenie und Bipolarstörungen.

Die dritte Studie zielte darauf ab, akute Effekte von Methyldioxymethamphetamin (MDMA) auf Hämodynamik, Metabolismus und SERT Verfügbarkeit zu untersuchen. Zusammen mit anderen psychedelischen Substanzen hat MDMA im letzten Jahrzehnt aufgrund seines Potenzials zur Behandlung psychiatrischer Störungen wie Depression oder posttraumatischer Belastungsstörung großes Interesse erhalten. In diesem Zusammenhang wurden bildgebende Methoden ebenfalls vermehrt eingesetzt, um die Wirkmechanismen solcher psychedelischer Wirkstoffe besser zu verstehen. Die meisten Studien basierten jedoch auf MRT Methoden, die neuronale Aktivierungen oder Deaktivierungen, die durch die akute Verabreichung dieser Substanzen ausgelöst werden, über hämodynamische Änderungen erfassen. Das Ergebnis dieser Arbeit spiegelt die Verringerung des BOLD-Signals nach MDMA-Gabe wider, über die zuvor in Humanstudien berichtet wurde. Die globalen BOLD-Abnahmen gingen jedoch mit lokalen Anstiegen des Glukoseverbrauchs einher, wie die gleichzeitig erfassten [^{18}F]FDG-PET-Daten zeigten. Zusätzliche temporal vergleichbare BOLD Reduktionen wurden allerdings auch in extrazerebralem Gewebe festgestellt. Die Daten deuten auf eine globale hämodynamische Suppression nicht-neuronaler Natur hin, die mit einer durch MDMA induzierten neuronalen Aktivierung einhergeht. Weiterhin korrelierten die regionalen BOLD Reduktionen im Gehirn mit regionalen Änderungen in der SERT-Besetzung, was auf zusätzliche lokale vaskuläre Effekte hinweist. Zusammenfassend deutet die Studie darauf hin, dass hämodynamische Reduktionen nach MDMA Gabe durch vaskuläre Effekte von Serotonin oder direkt von MDMA an vaskulären Serotoninrezeptoren erzeugt werden. Die Ergebnisse relativieren somit frühere Studien, die die Auswirkungen psychedelischer Drogen auf die neuronale Aktivität indirekt mittels Hämodynamik untersuchten, und rechtfertigen eine neue Interpretation ihrer Ergebnisse.

Die stark komplementären Ergebnisse beider Modalitäten, die in dieser Arbeit eingesetzt wurden, empfehlen den weiteren Einsatz von PET/MRI zur Untersuchung der Hirnfunktion im Ruhezustand und unter Aktivierung. Die Aufklärung des komplexen Zwischenspiels zwischen Neurotransmittersystemen, Hämodynamik, Metabolismus und funktionellen Netzwerken wird dazu beitragen, die Funktion und Dysfunktion des Gehirns *in vivo* besser zu verstehen und damit die gezielte Entwicklung von diagnostischen und therapeutischen Strategien zu unterstützen.

6. References

Achard, S., Delon-Martin, C., Vértes, P.E., Renard, F., Schenck, M., Schneider, F., Heinrich, C., Kremer, S., Bullmore, E.T., 2012. Hubs of brain functional networks are radically reorganized in comatose patients. Proceedings of the National Academy of Sciences 109, 20608-20613.

Addis, D.R., Wong, A.T., Schacter, D.L., 2007. Remembering the past and imagining the future: common and distinct neural substrates during event construction and elaboration. Neuropsychologia 45, 1363-1377.

Aiello, M., Salvatore, E., Cachia, A., Pappata, S., Cavaliere, C., Prinster, A., Nicolai, E., Salvatore, M., Baron, J.C., Quarantelli, M., 2015. Relationship between simultaneously acquired resting-state regional cerebral glucose metabolism and functional MRI: a PET/MR hybrid scanner study. Neuroimage 113, 111-121.

Amend, M., 2019. Multifunctional PET/MR Imaging Decodes Brain Function on Hemodynamic and Metabolic Scales.

Amend, M., Ionescu, T.M., Di, X., Pichler, B.J., Biswal, B.B., Wehrl, H.F., 2019. Functional resting-state brain connectivity is accompanied by dynamic correlations of application-dependent [(18)F]FDG PET-tracer fluctuations. Neuroimage 196, 161-172.

An, J., Wang, L., Li, K., Zeng, Y., Su, Y., Jin, Z., Yu, X., Si, T., 2017. Differential effects of antidepressant treatment on long-range and short-range functional connectivity strength in patients with major depressive disorder. Scientific reports 7, 10214-10214.

Andersen, K.A.A., Carhart-Harris, R., Nutt, D.J., Erritzoe, D., 2021. Therapeutic effects of classic serotonergic psychedelics: A systematic review of modern-era clinical studies. Acta Psychiatr Scand 143, 101-118.

Andrade, R., 2011. Serotonergic regulation of neuronal excitability in the prefrontal cortex. Neuropharmacology 61, 382-386.

Andrade, R., Weber, E., 2010. Htr2a Gene and 5-HT2A Receptor Expression in the Cerebral Cortex Studied Using Genetically Modified Mice. Frontiers in neuroscience 4.

Andrews-Hanna, J.R., 2012. The brain's default network and its adaptive role in internal mentation. The Neuroscientist : a review journal bringing neurobiology, neurology and psychiatry 18, 251-270.

Andrews, P.W., Bharwani, A., Lee, K.R., Fox, M., Thomson, J.A., 2015. Is serotonin an upper or a downer? The evolution of the serotonergic system and its role in depression and the antidepressant response. Neuroscience & Biobehavioral Reviews 51, 164-188.

Arélin, K., Mueller, K., Barth, C., Rekkas, P.V., Kratzsch, J., Burmann, I., Villringer, A., Sacher, J., 2015. Progesterone mediates brain functional connectivity changes during the menstrual cycle—a pilot resting state MRI study. Frontiers in neuroscience 9.

Attwell, D., Laughlin, S.B., 2001. An energy budget for signaling in the grey matter of the brain. J Cereb Blood Flow Metab 21, 1133-1145.

Avery, M.C., Krichmar, J.L., 2015. Improper activation of D1 and D2 receptors leads to excess noise in prefrontal cortex. Frontiers in computational neuroscience 9, 31-31.

Azevedo, F.A., Carvalho, L.R., Grinberg, L.T., Farfel, J.M., Ferretti, R.E., Leite, R.E., Jacob Filho, W., Lent, R., Herculano-Houzel, S., 2009. Equal numbers of neuronal and nonneuronal cells make the human brain an isometrically scaled-up primate brain. J Comp Neurol 513, 532-541.

Azmitia, E.C., Segal, M., 1978. An autoradiographic analysis of the differential ascending projections of the dorsal and median raphe nuclei in the rat. J Comp Neurol 179, 641-667.

Badhwar, A., Tam, A., Dansereau, C., Orban, P., Hoffstaedter, F., Bellec, P., 2017. Resting-state network dysfunction in Alzheimer's disease: A systematic review and meta-analysis. Alzheimer's & dementia (Amsterdam, Netherlands) 8, 73-85.

Barkhof, F., Haller, S., Rombouts, S.A., 2014. Resting-state functional MR imaging: a new window to the brain. Radiology 272, 29-49.

Bartels, A.L., Leenders, K.L., 2009. Parkinson's disease: The syndrome, the pathogenesis and pathophysiology. Cortex 45, 915-921.

Basser, P.J., Pajevic, S., Pierpaoli, C., Duda, J., Aldroubi, A., 2000. In vivo fiber tractography using DT-MRI data. Magnetic Resonance in Medicine 44, 625-632.

Batson, M.A., Petridou, N., Klomp, D.W.J., Frens, M.A., Neggers, S.F.W., 2015. Single Session Imaging of Cerebellum at 7 Tesla: Obtaining Structure and Function of Multiple Motor Subsystems in Individual Subjects. PLoS One 10, e0134933.

Becerra, L., Pendse, G., Chang, P.C., Bishop, J., Borsook, D., 2011. Robust reproducible resting state networks in the awake rodent brain. PLoS One 6, e25701.

Bélanger, M., Allaman, I., Magistretti, Pierre J., 2011. Brain Energy Metabolism: Focus on Astrocyte-Neuron Metabolic Cooperation. Cell Metabolism 14, 724-738.

Bernal-Casas, D., Lee, H.J., Weitz, A.J., Lee, J.H., 2017. Studying Brain Circuit Function with Dynamic Causal Modeling for Optogenetic fMRI. Neuron 93, 522-532.e525.

Bhagwagar, Z., Whale, R., Cowen, P.J., 2018. State and trait abnormalities in serotonin function in major depression. British Journal of Psychiatry 180, 24-28.

Biswal, B., Yetkin, F.Z., Haughton, V.M., Hyde, J.S., 1995a. Functional connectivity in the motor cortex of resting human brain using echo-planar MRI. Magn Reson Med 34, 537-541.

Biswal, B., Zerrin Yetkin, F., Haughton, V.M., Hyde, J.S., 1995b. Functional connectivity in the motor cortex of resting human brain using echo-planar mri. Magnetic Resonance in Medicine 34, 537-541.

Bluhm, R.L., Miller, J., Lanius, R.A., Osuch, E.A., Boksman, K., Neufeld, R.W., Theberge, J., Schaefer, B., Williamson, P., 2007. Spontaneous low-frequency fluctuations in the BOLD signal in schizophrenic patients: anomalies in the default network. Schizophr Bull 33, 1004-1012.

Bostan, A.C., Strick, P.L., 2018. The basal ganglia and the cerebellum: nodes in an integrated network. Nat Rev Neurosci 19, 338-350.

Boto, T., Tomchik, S.M., 2019. The Excitatory, the Inhibitory, and the Modulatory: Mapping Chemical Neurotransmission in the Brain. Neuron 101, 763-765.

Bowyer, S.M., 2016. Coherence a measure of the brain networks: past and present. Neuropsychiatric Electrophysiology 2, 1.

Brodde, O.E., 1982. Vascular dopamine receptors: Demonstration and characterization by in vitro studies. Life Sci 31, 289-306.

Brodmann, K., 1909. Vergleichende Lokalisationslehre der Grosshirnrinde in ihren Prinzipien dargestellt auf Grund des Zellenbaues von Dr. K. Brodmann. J.A. Barth.

Brown, R.W., Cheng, Y.C.N., Haacke, E.M., Thompson, M.R., Venkatesan, R., 2014. Magnetic Resonance Imaging: Physical Principles and Sequence Design. Wiley.

Buchborn, T., Lyons, T., Song, C., Feilding, A., Knöpfel, T., 2020. The serotonin 2A receptor agonist 25CN-NBOH increases murine heart rate and neck-arterial blood flow in a temperature-dependent manner. J Psychopharmacol 34, 786-794.

Buckner, R.L., Andrews-Hanna, J.R., Schacter, D.L., 2008. The brain's default network: anatomy, function, and relevance to disease. Ann N Y Acad Sci 1124, 1-38.

Bullmore, E., Sporns, O., 2009. Complex brain networks: graph theoretical analysis of structural and functional systems. Nature reviews. Neuroscience 10, 186-198.

Buxton, R.B., 2009. Introduction to Functional Magnetic Resonance Imaging: Principles and Techniques. Cambridge University Press.

Buxton, R.B., 2012. Dynamic models of BOLD contrast. Neuroimage 62, 953-961.

Calabresi, P., Picconi, B., Tozzi, A., Ghiglieri, V., Di Filippo, M., 2014. Direct and indirect pathways of basal ganglia: a critical reappraisal. Nature Neuroscience 17, 1022-1030.

Carhart-Harris, R.L., Erritzoe, D., Williams, T., Stone, J.M., Reed, L.J., Colasanti, A., Tyacke, R.J., Leech, R., Malizia, A.L., Murphy, K., Hobden, P., Evans, J., Feilding, A., Wise, R.G., Nutt, D.J., 2012. Neural correlates of the psychedelic state as determined by fMRI studies with psilocybin. Proceedings of the National Academy of Sciences 109, 2138-2143.

Carhart-Harris, R.L., Goodwin, G.M., 2017. The Therapeutic Potential of Psychedelic Drugs: Past, Present, and Future. Neuropsychopharmacology : official publication of the American College of Neuropsychopharmacology 42, 2105-2113.

Carhart-Harris, R.L., Murphy, K., Leech, R., Erritzoe, D., Wall, M.B., Ferguson, B., Williams, L.T.J., Roseman, L., Brugger, S., De Meer, I., Tanner, M., Tyacke, R., Wolff, K., Sethi, A., Bloomfield, M.A.P., Williams, T.M., Bolstridge, M., Stewart, L., Morgan, C., Newbould, R.D., Feilding, A., Curran, H.V., Nutt, D.J., 2015. The Effects of Acutely Administered 3,4-Methylenedioxymethamphetamine on Spontaneous Brain Function in Healthy Volunteers Measured with Arterial Spin Labeling and Blood Oxygen Level–Dependent Resting State Functional Connectivity. Biological Psychiatry 78, 554-562.

Carson, R.E., Channing, M.A., Blasberg, R.G., Dunn, B.B., Cohen, R.M., Rice, K.C., Herscovitch, P., 1993. Comparison of Bolus and Infusion Methods for Receptor Quantitation: Application to [18F]Cyclofoxy and Positron Emission Tomography. Journal of Cerebral Blood Flow & Metabolism 13, 24-42.

Castellazzi, G., Bruno, S.D., Toosy, A.T., Casiraghi, L., Palesi, F., Savini, G., D'Angelo, E., Wheeler-Kingshott, C.A.M.G., 2018. Prominent Changes in Cerebro-Cerebellar Functional Connectivity During Continuous Cognitive Processing. Frontiers in Cellular Neuroscience 12.

Celada, P., Puig, M.V., Artigas, F., 2013. Serotonin modulation of cortical neurons and networks. Frontiers in integrative neuroscience 7, 25-25.

Challis, C., Berton, O., 2015. Top-Down Control of Serotonin Systems by the Prefrontal Cortex: A Path toward Restored Socioemotional Function in Depression. ACS chemical neuroscience 6, 1040-1054.

Cherry, S.R., Gambhir, S.S., 2001. Use of Positron Emission Tomography in Animal Research. ILAR Journal 42, 219-232.

Chou, Y.-h., Panych, L.P., Dickey, C.C., Petrella, J.R., Chen, N.-k., 2012. Investigation of Long-Term Reproducibility of Intrinsic Connectivity Network Mapping: A Resting-State fMRI Study. American Journal of Neuroradiology 33, 833-838.

Chuang, K.H., Lee, H.L., Li, Z., Chang, W.T., Nasrallah, F.A., Yeow, L.Y., Singh, K., 2019. Evaluation of nuisance removal for functional MRI of rodent brain. Neuroimage 188, 694-709.

Ciranna, L., 2006. Serotonin as a modulator of glutamate- and GABA-mediated neurotransmission: implications in physiological functions and in pathology. Current neuropharmacology 4, 101-114.

Cohen, Z.V.I., Bonvento, G., Lacombe, P., Hamel, E., 1996. SEROTONIN IN THE REGULATION OF BRAIN MICROCIRCULATION. Progress in Neurobiology 50, 335-362.

Cole, D.M., Beckmann, C.F., Oei, N.Y., Both, S., van Gerven, J.M., Rombouts, S.A., 2013a. Differential and distributed effects of dopamine neuromodulations on resting-state network connectivity. Neuroimage 78, 59-67.

Cole, D.M., Oei, N.Y., Soeter, R.P., Both, S., van Gerven, J.M., Rombouts, S.A., Beckmann, C.F., 2013b. Dopamine-dependent architecture of cortico-subcortical network connectivity. Cereb Cortex 23, 1509-1516.

Cole, M.W., Ito, T., Cocuzza, C., Sanchez-Romero, R., 2021. The Functional Relevance of Task-State Functional Connectivity. The Journal of Neuroscience 41, 2684-2702.

Cole, M.W., Pathak, S., Schneider, W., 2010. Identifying the brain's most globally connected regions. Neuroimage 49, 3132-3148.

Conio, B., Martino, M., Magioncalda, P., Escelsior, A., Inglese, M., Amore, M., Northoff, G., 2019. Opposite effects of dopamine and serotonin on resting-state networks: review and implications for psychiatric disorders. Mol Psychiatry.

Czoty, P.W., Riddick, N.V., Gage, H.D., Sandridge, M., Nader, S.H., Garg, S., Bounds, M., Garg, P.K., Nader, M.A., 2009. Effect of Menstrual Cycle Phase on Dopamine D2 Receptor Availability in Female Cynomolgus Monkeys. Neuropsychopharmacology : official publication of the American College of Neuropsychopharmacology 34, 548-554.

Damoiseaux, J.S., Rombouts, S.A., Barkhof, F., Scheltens, P., Stam, C.J., Smith, S.M., Beckmann, C.F., 2006. Consistent resting-state networks across healthy subjects. Proc Natl Acad Sci U S A 103, 13848-13853.

Daws, L.C., Gould, G.G., 2011. Ontogeny and regulation of the serotonin transporter: providing insights into human disorders. Pharmacol Ther 131, 61-79.

DeLong, M.R., Wichmann, T., 2007. Circuits and circuit disorders of the basal ganglia. Arch Neurol 64, 20-24.

Delso, G., Fürst, S., Jakoby, B., Ladebeck, R., Ganter, C., Nekolla, S.G., Schwaiger, M., Ziegler, S.I., 2011. Performance Measurements of the Siemens mMR Integrated Whole-Body PET/MR Scanner. Journal of Nuclear Medicine 52, 1914-1922.

Di, X., Biswal, B.B., 2012. Metabolic brain covariant networks as revealed by FDG-PET with reference to resting-state fMRI networks. Brain Connect 2, 275-283.

Di, X., Biswal, B.B., Alzheimer's Disease Neuroimaging, I., 2012. Metabolic brain covariant networks as revealed by FDG-PET with reference to resting-state fMRI networks. Brain Connect 2, 275-283.

Di, X., Gohel, S., Thielcke, A., Wehrl, H.F., Biswal, B.B., Alzheimer's Disease Neuroimaging, I., 2017. Do all roads lead to Rome? A comparison of brain networks derived from inter-subject volumetric and metabolic covariance and moment-to-moment hemodynamic correlations in old individuals. Brain Struct Funct 222, 3833-3845.

Dipasquale, O., Selvaggi, P., Veronese, M., Gabay, A.S., Turkheimer, F., Mehta, M.A., 2019. Receptor-Enriched Analysis of functional connectivity by targets (REACT): A novel, multimodal analytical approach informed by PET to study the pharmacodynamic response of the brain under MDMA. Neuroimage 195, 252-260.

Disselhorst, J.A., Newport, D.F., Schmid, A.M., Schmidt, F.P., Parl, C., Liu, C.C., Pichler, B.J., Mannheim, J.G., 2022. NEMA NU 4-2008 performance evaluation and MR compatibility tests of an APD-based small animal PET-insert for simultaneous PET/MR imaging. Phys Med Biol 67.

Drachman, D.A., 2005. Do we have brain to spare? Neurology 64, 2004-2005.

Durstewitz, D., Seamans, J.K., 2008. The Dual-State Theory of Prefrontal Cortex Dopamine Function with Relevance to Catechol-O-Methyltransferase Genotypes and Schizophrenia. Biological Psychiatry 64, 739-749.

Durstewitz, D., Seamans, J.K., Sejnowski, T.J., 2000. Dopamine-mediated stabilization of delay-period activity in a network model of prefrontal cortex. J Neurophysiol 83, 1733-1750.

Duvarci, S., Simpson, E.H., Schneider, G., Kandel, E.R., Roeper, J., Sigurdsson, T., 2018. Impaired recruitment of dopamine neurons during working memory in mice with striatal D2 receptor overexpression. Nature Communications 9, 2822.

Farde, L., Hall, H., Pauli, S., Halldin, C., 1995. Variability in D2-dopamine receptor density and affinity: a PET study with [11C]raclopride in man. Synapse 20, 200-208.

Ferrington, L., Kirilly, E., McBean, D.E., Olverman, H.J., Bagdy, G., Kelly, P.A.T., 2006. Persistent cerebrovascular effects of MDMA and acute responses to the drug. European Journal of Neuroscience 24, 509-519.

Filiano, A.J., Gadani, S.P., Kipnis, J., 2015. Interactions of innate and adaptive immunity in brain development and function. Brain Research 1617, 18-27.

Fischer, A.G., Ullsperger, M., 2017. An Update on the Role of Serotonin and its Interplay with Dopamine for Reward. Frontiers in Human Neuroscience 11.

Fox, M.D., Snyder, A.Z., Vincent, J.L., Corbetta, M., Van Essen, D.C., Raichle, M.E., 2005a. The human brain is intrinsically organized into dynamic, anticorrelated functional networks. Proceedings of the National Academy of Sciences of the United States of America 102, 9673-9678.

Fox, M.D., Snyder, A.Z., Vincent, J.L., Corbetta, M., Van Essen, D.C., Raichle, M.E., 2005b. The human brain is intrinsically organized into dynamic, anticorrelated functional networks. Proc Natl Acad Sci U S A 102, 9673-9678.

Gamoh, S., Hisa, H., Yamamoto, R., 2013. 5-Hydroxytryptamine Receptors as Targets for Drug Therapies of Vascular-Related Diseases. Biological and Pharmaceutical Bulletin 36, 1410-1415.

Gao, Y.R., Ma, Y., Zhang, Q., Winder, A.T., Liang, Z., Antinori, L., Drew, P.J., Zhang, N., 2017. Time to wake up: Studying neurovascular coupling and brain-wide circuit function in the un-anesthetized animal. Neuroimage 153, 382-398.

Gerfen, C.R., Surmeier, D.J., 2011. Modulation of striatal projection systems by dopamine. Annual review of neuroscience 34, 441-466.

Göttlich, M., Münte, T.F., Heldmann, M., Kasten, M., Hagenah, J., Krämer, U.M., 2013. Altered resting state brain networks in Parkinson's disease. PLoS One 8, e77336-e77336.

Gough, B., Ali, S.F., Slikker, W., Holson, R.R., 1991. Acute effects of 3,4-methylenedioxymethamphetamine (MDMA) on monoamines in rat caudate. Pharmacology Biochemistry and Behavior 39, 619-623.

Grandjean, J., Schroeter, A., Batata, I., Rudin, M., 2014. Optimization of anesthesia protocol for resting-state fMRI in mice based on differential effects of anesthetics on functional connectivity patterns. Neuroimage 102, 838-847.

Greicius, M.D., Krasnow, B., Reiss, A.L., Menon, V., 2003. Functional connectivity in the resting brain: a network analysis of the default mode hypothesis. Proc Natl Acad Sci U S A 100, 253-258.

Greicius, M.D., Srivastava, G., Reiss, A.L., Menon, V., 2004. Default-mode network activity distinguishes Alzheimer's disease from healthy aging: evidence from functional MRI. Proc Natl Acad Sci U S A 101, 4637-4642.

Gunn, R.N., Gunn, S.R., Turkheimer, F.E., Aston, J.A.D., Cunningham, V.J., 2002. Positron Emission Tomography Compartmental Models: A Basis Pursuit Strategy for Kinetic Modeling. Journal of Cerebral Blood Flow & Metabolism 22, 1425-1439.

Habas, C., Kamdar, N., Nguyen, D., Prater, K., Beckmann, C.F., Menon, V., Greicius, M.D., 2009a. Distinct cerebellar contributions to intrinsic connectivity networks. J Neurosci 29, 8586-8594.

Habas, C., Kamdar, N., Nguyen, D., Prater, K., Beckmann, C.F., Menon, V., Greicius, M.D., 2009b. Distinct cerebellar contributions to intrinsic connectivity networks. Journal of neuroscience 29, 8586-8594.

Hahn, A., Gryglewski, G., Nics, L., Hienert, M., Rischka, L., Vraka, C., Sigurdardottir, H., Vanicek, T., James, G.M., Seiger, R., Kautzky, A., Silberbauer, L., Wadsak, W., Mitterhauser, M., Hacker, M., Kasper, S., Lanzenberger, R., 2016. Quantification of Task-

Specific Glucose Metabolism with Constant Infusion of 18F-FDG. J Nucl Med 57, 1933-1940.

Hahn, A., Wadsak, W., Windischberger, C., Baldinger, P., Höflich, A.S., Losak, J., Nics, L., Philippe, C., Kranz, G.S., Kraus, C., Mitterhauser, M., Karanikas, G., Kasper, S., Lanzenberger, R., 2012. Differential modulation of the default mode network via serotonin-1A receptors. Proceedings of the National Academy of Sciences of the United States of America 109, 2619-2624.

Haken, H., Wolf, H.C., 2003. Atom- und Quantenphysik. Springer Berlin Heidelberg.

Hamacher, K., Coenen, H.H., Stocklin, G., 1986. Efficient stereospecific synthesis of no-carrier-added 2-[18F]-fluoro-2-deoxy-D-glucose using aminopolyether supported nucleophilic substitution. J Nucl Med 27, 235-238.

Han, S., Cui, Q., Guo, X., Fan, Y.-S., Guo, J., Zong, X., Hu, M., Lu, F., Chen, X., Chen, H., 2020. Disconnectivity between the raphe nucleus and subcortical dopamine-related regions contributes altered salience network in schizophrenia. Schizophrenia Research 216, 382-388.

Hansen, H.D., Mandeville, J.B., Sander, C.Y., Hooker, J.M., Catana, C., Rosen, B.R., Knudsen, G.M., 2017. Functional Characterization of 5-HT(1B) Receptor Drugs in Nonhuman Primates Using Simultaneous PET-MR. J Neurosci 37, 10671-10678.

Harte, M., O'Connor, W.T., 2004. Evidence for a differential medial prefrontal dopamine D1 and D2 receptor regulation of local and ventral tegmental glutamate and GABA release: A dual probe microdialysis study in the awake rat. Brain Research 1017, 120-129.

Hebb, D.O., 1950. The organization of behavior: A neuropsychological theory. New York: John Wiley and Sons, Inc., 1949. Science Education 34, 336-337.

Herfert, K., Mannheim, J.G., Kuebler, L., Marciano, S., Amend, M., Parl, C., Napieczynska, H., Maier, F.M., Vega, S.C., Pichler, B.J., 2020. Quantitative Rodent Brain Receptor Imaging. Molecular Imaging and Biology 22, 223-244.

Hevesy, G., 1923. The Absorption and Translocation of Lead by Plants: A Contribution to the Application of the Method of Radioactive Indicators in the Investigation of the Change of Substance in Plants. Biochem J 17, 439-445.

Hidalgo-Lopez, E., Mueller, K., Harris, T., Aichhorn, M., Sacher, J., Pletzer, B., 2020. Human menstrual cycle variation in subcortical functional brain connectivity: a multimodal analysis approach. Brain structure & function 225, 591-605.

Hidalgo-Lopez, E., Pletzer, B., 2017. Interactive Effects of Dopamine Baseline Levels and Cycle Phase on Executive Functions: The Role of Progesterone. Frontiers in neuroscience 11, 403-403.

Hjorth, O.R., Frick, A., Gingnell, M., Hoppe, J.M., Faria, V., Hultberg, S., Alaie, I., Månsson, K.N.T., Wahlstedt, K., Jonasson, M., Lubberink, M., Antoni, G., Fredrikson, M., Furmark, T., 2019. Expression and co-expression of serotonin and dopamine transporters in social anxiety disorder: a multitracer positron emission tomography study. Molecular Psychiatry.

Hodkinson, D.J., de Groote, C., McKie, S., Deakin, J.F.W., Williams, S.R., 2012. Differential Effects of Anaesthesia on the phMRI Response to Acute Ketamine Challenge. British journal of medicine and medical research 2, 373-385.

Honey, C.J., Sporns, O., Cammoun, L., Gigandet, X., Thiran, J.P., Meuli, R., Hagmann, P., 2009. Predicting human resting-state functional connectivity from structural connectivity. Proceedings of the National Academy of Sciences 106, 2035-2040.

Hornung, J.-P., 2010. The Neuronatomy of the Serotonergic System. Handbook of Behavioral Neuroscience 21, 51-64.

Horwitz, B., Duara, R., Rapoport, S.I., 1984. Intercorrelations of glucose metabolic rates between brain regions: application to healthy males in a state of reduced sensory input. J Cereb Blood Flow Metab 4, 484-499.

Houle, S., Ginovart, N., Hussey, D., Meyer, J.H., Wilson, A.A., 2000. Imaging the serotonin transporter with positron emission tomography: initial human studies with [11C]DAPP and [11C]DASB. European Journal of Nuclear Medicine 27, 1719-1722.

Howarth, C., Gleeson, P., Attwell, D., 2012. Updated energy budgets for neural computation in the neocortex and cerebellum. J Cereb Blood Flow Metab 32, 1222-1232.

Hsu, L.-M., Liang, X., Gu, H., Brynildsen, J.K., Stark, J.A., Ash, J.A., Lin, C.-P., Lu, H., Rapp, P.R., Stein, E.A., Yang, Y., 2016a. Constituents and functional implications of the rat default mode network. Proceedings of the National Academy of Sciences 113, E4541.

Hsu, L.-M., Liang, X., Gu, H., Brynildsen, J.K., Stark, J.A., Ash, J.A., Lin, C.-P., Lu, H., Rapp, P.R., Stein, E.A., Yang, Y., 2016b. Constituents and functional implications of the rat default mode network. Proceedings of the National Academy of Sciences 113, E4541-E4547.

Huang, H., Ding, M., 2016. Linking Functional Connectivity and Structural Connectivity Quantitatively: A Comparison of Methods. Brain connectivity 6, 99-108.

Huettel, S.A., Song, A.W., McCarthy, G., 2004a. Functional magnetic resonance imaging. Sinauer Associates Sunderland.

Huettel, S.A., Song, A.W., McCarthy, G., 2004b. Functional Magnetic Resonance Imaging. Sinauer Associates.

Hummerich, R., Reischl, G., Ehrlichmann, W., Machulla, H.-J., Heinz, A., Schloss, P., 2004. DASB –in vitro binding characteristics on human recombinant monoamine transporters with regard to its potential as positron emission tomography (PET) tracer. Journal of Neurochemistry 90, 1218-1226.

Humphries, M.D., Gurney, K., 2008. Network 'Small-World-Ness': A Quantitative Method for Determining Canonical Network Equivalence. PLoS One 3, e2051.

Hutchison, R.M., Hutchison, M., Manning, K.Y., Menon, R.S., Everling, S., 2014. Isoflurane induces dose-dependent alterations in the cortical connectivity profiles and dynamic properties of the brain's functional architecture. Human Brain Mapping 35, 5754-5775.

Hutchison, R.M., Mirsattari, S.M., Jones, C.K., Gati, J.S., Leung, L.S., 2010. Functional networks in the anesthetized rat brain revealed by independent component analysis of resting-state FMRI. J Neurophysiol 103, 3398-3406.

Iadecola, C., 2004. Neurovascular regulation in the normal brain and in Alzheimer's disease. Nature Reviews Neuroscience 5, 347-360.

Innis, R.B., Cunningham, V.J., Delforge, J., Fujita, M., Gjedde, A., Gunn, R.N., Holden, J., Houle, S., Huang, S.C., Ichise, M., Iida, H., Ito, H., Kimura, Y., Koeppe, R.A., Knudsen, G.M., Knuuti, J., Lammertsma, A.A., Laruelle, M., Logan, J., Maguire, R.P., Mintun, M.A., Morris, E.D., Parsey, R., Price, J.C., Slifstein, M., Sossi, V., Suhara, T., Votaw, J.R., Wong, D.F., Carson, R.E., 2007. Consensus nomenclature for in vivo imaging of reversibly binding radioligands. J Cereb Blood Flow Metab 27, 1533-1539.

Ionescu, T.M., Amend, M., Hafiz, R., Biswal, B.B., Maurer, A., Pichler, B.J., Wehrl, H.F., Herfert, K., 2021a. Striatal and prefrontal D2R and SERT distributions contrastingly correlate with default-mode connectivity. Neuroimage 243, 118501.

Ionescu, T.M., Amend, M., Hafiz, R., Biswal, B.B., Wehrl, H.F., Herfert, K., Pichler, B.J., 2021b. Elucidating the complementarity of resting-state networks derived from dynamic [18F]FDG and hemodynamic fluctuations using simultaneous small-animal PET/MRI. Neuroimage 236, 118045.

Ionescu, T.M., Amend, M., Watabe, T., Hatazawa, J., Maurer, A., Reischl, G., Pichler, B.J., Wehrl, H.F., Herfert, K., 2022. Neurovascular Uncoupling: Multimodal Imaging Delineates the Acute Effects of 3,4-Methylenedioxymethamphetamine. Journal of Nuclear Medicine, jnumed.122.264391.

Jakob, P., 2011. Small Animal Magnetic Resonance Imaging: Basic Principles, Instrumentation and Practical Issue. In: Kiessling, F., Pichler, B.J. (Eds.), Small Animal Imaging: Basics and Practical Guide. Springer Berlin Heidelberg, Berlin, Heidelberg, pp. 151-164.

Jamadar, S.D., Ward, P.G.D., Liang, E.X., Orchard, E.R., Chen, Z., Egan, G.F., 2021. Metabolic and Hemodynamic Resting-State Connectivity of the Human Brain: A High-Temporal Resolution Simultaneous BOLD-fMRI and FDG-fPET Multimodality Study. Cerebral Cortex 31, 2855-2867.

Joel, D., Weiner, I., 1994. The organization of the basal ganglia-thalamocortical circuits: open interconnected rather than closed segregated. Neuroscience 63, 363-379.

Jonckers, E., Delgado y Palacios, R., Shah, D., Guglielmetti, C., Verhoye, M., Van der Linden, A., 2014. Different anesthesia regimes modulate the functional connectivity outcome in mice. Magnetic Resonance in Medicine 72, 1103-1112.

Jonckers, E., Shah, D., Hamaide, J., Verhoye, M., Van der Linden, A., 2015. The power of using functional fMRI on small rodents to study brain pharmacology and disease. Frontiers in Pharmacology 6.

Judenhofer, M.S., Wehrl, H.F., Newport, D.F., Catana, C., Siegel, S.B., Becker, M., Thielscher, A., Kneilling, M., Lichy, M.P., Eichner, M., Klingel, K., Reischl, G., Widmaier, S., Rocken, M., Nutt, R.E., Machulla, H.J., Uludag, K., Cherry, S.R., Claussen, C.D., Pichler, B.J., 2008. Simultaneous PET-MRI: a new approach for functional and morphological imaging. Nat Med 14, 459-465.

Kahnt, T., Weber, S.C., Haker, H., Robbins, T.W., Tobler, P.N., 2015. Dopamine D2-Receptor Blockade Enhances Decoding of Prefrontal Signals in Humans. The Journal of Neuroscience 35, 4104-4111.

Kandel, E.R., Mack, S., Jessell, T.M., Schwartz, J.H., Siegelbaum, S.A., Hudspeth, A.J., 2013. Principles of Neural Science, Fifth Edition. McGraw-Hill Education.

Kellendonk, C., Simpson, E.H., Polan, H.J., Malleret, G., Vronskaya, S., Winiger, V., Moore, H., Kandel, E.R., 2006. Transient and Selective Overexpression of Dopamine D2 Receptors in the Striatum Causes Persistent Abnormalities in Prefrontal Cortex Functioning. Neuron 49, 603-615.

Kelly, C., de Zubicaray, G., Di Martino, A., Copland, D.A., Reiss, P.T., Klein, D.F., Castellanos, F.X., Milham, M.P., McMahon, K., 2009. L-dopa modulates functional connectivity in striatal cognitive and motor networks: a double-blind placebo-controlled study. J Neurosci 29, 7364-7378.

Kiessling, F., Pichler, B.J., 2011. Small animal imaging : basics and practical guide.

Kim, J.G., Leem, Y.-E., Kwon, I., Kang, J.-S., Bae, Y.M., Cho, H., 2018. Estrogen modulates serotonin effects on vasoconstriction through Src inhibition. Experimental & Molecular Medicine 50, 1-9.

Köhler, C., Hall, H., Ögren, S.-O., Gawell, L., 1985. Specific in vitro and in vivo binding of 3H-raclopride a potent substituted benzamide drug with high affinity for dopamine D-2 receptors in the rat brain. Biochemical Pharmacology 34, 2251-2259.

Krabbe, S., Duda, J., Schiemann, J., Poetschke, C., Schneider, G., Kandel, E.R., Liss, B., Roeper, J., Simpson, E.H., 2015. Increased dopamine D2 receptor activity in the striatum alters the firing pattern of dopamine neurons in the ventral tegmental area. Proceedings of the National Academy of Sciences 112, E1498-E1506.

Kupfermann, I., 1979. Modulatory actions of neurotransmitters. Annual review of neuroscience 2, 447-465.

Lammertsma, A.A., Hume, S.P., 1996. Simplified reference tissue model for PET receptor studies. Neuroimage 4, 153-158.

Langer, O., Någren, K., Dolle, F., Lundkvist, C., Sandell, J., Swahn, C.-G., Vaufrey, F., Crouzel, C., Maziere, B., Halldin, C., 1999. Precursor synthesis and radiolabelling of the dopamine D2 receptor ligand [11C]raclopride from [11C]methyl triflate. Journal of Labelled Compounds and Radiopharmaceuticals 42, 1183-1193.

Lanzenberger, R., Kranz, G.S., Haeusler, D., Akimova, E., Savli, M., Hahn, A., Mitterhauser, M., Spindelegger, C., Philippe, C., Fink, M., Wadsak, W., Karanikas, G., Kasper, S., 2012. Prediction of SSRI treatment response in major depression based on serotonin transporter interplay between median raphe nucleus and projection areas. Neuroimage 63, 874-881.

Lauterbur, P.C., 1973. Image Formation by Induced Local Interactions: Examples Employing Nuclear Magnetic Resonance. Nature 242, 190-191.

Lemogne, C., Delaveau, P., Freton, M., Guionnet, S., Fossati, P., 2012. Medial prefrontal cortex and the self in major depression. J Affect Disord 136, e1-e11.

Li, J., Kong, R., Liégeois, R., Orban, C., Tan, Y., Sun, N., Holmes, A.J., Sabuncu, M.R., Ge, T., Yeo, B.T.T., 2019. Global signal regression strengthens association between resting-state functional connectivity and behavior. Neuroimage 196, 126-141.

Liang, Z., King, J., Zhang, N., 2011. Uncovering intrinsic connectional architecture of functional networks in awake rat brain. J Neurosci 31, 3776-3783.

Lodish, H., Berk, A., Kaiser, C., Krieger, M., Bretscher, A., Ploegh, H., MARTIN, K., Yaffe, M., Amon, A., 2021. Molecular Cell Biology. Macmillan Learning.

Logan, J., Fowler, J.S., Volkow, N.D., Wolf, A.P., Dewey, S.L., Schlyer, D.J., MacGregor, R.R., Hitzemann, R., Bendriem, B., Gatley, S.J., et al., 1990. Graphical analysis of reversible radioligand binding from time-activity measurements applied to [N-11C-methyl]-(-)-cocaine PET studies in human subjects. J Cereb Blood Flow Metab 10, 740-747.

Logothetis, N.K., Pauls, J., Augath, M., Trinath, T., Oeltermann, A., 2001. Neurophysiological investigation of the basis of the fMRI signal. Nature 412, 150-157.

López-González, F.J., Silva-Rodríguez, J., Paredes-Pacheco, J., Niñerola-Baizán, A., Efthimiou, N., Martín-Martín, C., Moscoso, A., Ruibal, Á., Roé-Vellvé, N., Aguiar, P., 2020. Intensity normalization methods in brain FDG-PET quantification. Neuroimage 222, 117229.

Löwel, S., Singer, W., 1992. Selection of intrinsic horizontal connections in the visual cortex by correlated neuronal activity. Science 255, 209-212.

Lu, H., Zou, Q., Gu, H., Raichle, M.E., Stein, E.A., Yang, Y., 2012. Rat brains also have a default mode network. Proc Natl Acad Sci U S A 109, 3979-3984.

Magioncalda, P., Martino, M., 2021. A unified model of the pathophysiology of bipolar disorder. Molecular Psychiatry.

Magioncalda, P., Martino, M., Conio, B., Escelsior, A., Piaggio, N., Presta, A., Marozzi, V., Rocchi, G., Anastasio, L., Vassallo, L., Ferri, F., Huang, Z., Roccatagliata, L., Pardini, M., Northoff, G., Amore, M., 2015. Functional connectivity and neuronal variability of resting state activity in bipolar disorder--reduction and decoupling in anterior cortical midline structures. Hum Brain Mapp 36, 666-682.

Maguire, E.A., 2001. The retrosplenial contribution to human navigation: a review of lesion and neuroimaging findings. Scand J Psychol 42, 225-238.

Majeed, W., Magnuson, M., Hasenkamp, W., Schwarb, H., Schumacher, E.H., Barsalou, L., Keilholz, S.D., 2011. Spatiotemporal dynamics of low frequency BOLD fluctuations in rats and humans. Neuroimage 54, 1140-1150.

Mandeville, J.B., Marota, J.J., Ayata, C., Moskowitz, M.A., Weisskoff, R.M., Rosen, B.R., 1999. MRI measurement of the temporal evolution of relative CMRO(2) during rat forepaw stimulation. Magn Reson Med 42, 944-951.

Mandino, F., Cerri, D.H., Garin, C.M., Straathof, M., van Tilborg, G.A.F., Chakravarty, M.M., Dhenain, M., Dijkhuizen, R.M., Gozzi, A., Hess, A., Keilholz, S.D., Lerch, J.P., Shih, Y.-Y.I., Grandjean, J., 2020. Animal Functional Magnetic Resonance Imaging: Trends and Path Toward Standardization. Frontiers in Neuroinformatics 13.

Manoliu, A., Meng, C., Brandl, F., Doll, A., Tahmasian, M., Scherr, M., Schwerthöffer, D., Zimmer, C., Förstl, H., Bäuml, J., Riedl, V., Wohlschläger, A., Sorg, C., 2014. Insular dysfunction within the salience network is associated with severity of symptoms and aberrant inter-network connectivity in major depressive disorder. Frontiers in Human Neuroscience 7.

Marciano, S., Ionescu, T.M., Saw, R.S., Cheong, R.Y., Kirik, D., Maurer, A., Pichler, B., Herfert, K., 2021. Combining CRISPR/Cas9 and brain imaging: from genes to proteins to networks. bioRxiv, 2021.2009.2010.459766.

Marder, E., 2012. Neuromodulation of neuronal circuits: back to the future. Neuron 76, 1-11.

Martínez-Maestro, M., Labadie, C., Möller, H.E., 2019. Dynamic metabolic changes in human visual cortex in regions with positive and negative blood oxygenation level-dependent response. J Cereb Blood Flow Metab 39, 2295-2307.

Martino, M., Magioncalda, P., 2021. Tracing the psychopathology of bipolar disorder to the functional architecture of intrinsic brain activity and its neurotransmitter modulation: a three-dimensional model. Molecular Psychiatry.

Martino, M., Magioncalda, P., Huang, Z., Conio, B., Piaggio, N., Duncan, N.W., Rocchi, G., Escelsior, A., Marozzi, V., Wolff, A., Inglese, M., Amore, M., Northoff, G., 2016. Contrasting variability patterns in the default mode and sensorimotor networks balance in bipolar depression and mania. Proceedings of the National Academy of Sciences 113, 4824-4829.

Matthew Brett, J.-L.A., Romain Valabregue, Jean-Baptiste Poline, June 2-6, 2002. Region of interest analysis using an SPM toolbox. 8th Internation Conference on Functional Mapping of the Human Brain, Sendai, Japan.

McCormick, P.N., Ginovart, N., Wilson, A.A., 2011. Isoflurane anaesthesia differentially affects the amphetamine sensitivity of agonist and antagonist D2/D3 positron emission tomography radiotracers: implications for in vivo imaging of dopamine release. Mol Imaging Biol 13, 737-746.

McCutcheon, R.A., Nour, M.M., Dahoun, T., Jauhar, S., Pepper, F., Expert, P., Veronese, M., Adams, R.A., Turkheimer, F., Mehta, M.A., Howes, O.D., 2019. Mesolimbic Dopamine Function Is Related to Salience Network Connectivity: An Integrative Positron Emission Tomography and Magnetic Resonance Study. Biol Psychiatry 85, 368-378.

Menon, R.S., Ogawa, S., Hu, X., Strupp, J.P., Anderson, P., Uğurbil, K., 1995. BOLD based functional MRI at 4 Tesla includes a capillary bed contribution: echo-planar imaging correlates with previous optical imaging using intrinsic signals. Magn Reson Med 33, 453-459.

Millière, R., Carhart-Harris, R.L., Roseman, L., Trautwein, F.M., Berkovich-Ohana, A., 2018. Psychedelics, Meditation, and Self-Consciousness. Front Psychol 9, 1475.

Mitchell, J.M., Bogenschutz, M., Lilienstein, A., Harrison, C., Kleiman, S., Parker-Guilbert, K., Ot'alora G, M., Garas, W., Paleos, C., Gorman, I., Nicholas, C., Mithoefer, M., Carlin, S., Poulter, B., Mithoefer, A., Quevedo, S., Wells, G., Klaire, S.S., van der Kolk, B., Tzarfaty, K., Amiaz, R., Worthy, R., Shannon, S., Woolley, J.D., Marta, C., Gelfand, Y., Hapke, E., Amar, S., Wallach, Y., Brown, R., Hamilton, S., Wang, J.B., Coker, A., Matthews, R., de Boer, A., Yazar-Klosinski, B., Emerson, A., Doblin, R., 2021. MDMA-assisted therapy for severe PTSD: a randomized, double-blind, placebo-controlled phase 3 study. Nature Medicine 27, 1025-1033.

Morefield, K.M., Keane, M., Felgate, P., White, J.M., Irvine, R.J., 2011. Pill content, dose and resulting plasma concentrations of 3,4-methylendioxymethamphetamine (MDMA) in recreational 'ecstasy' users. Addiction 106, 1293-1300.

Murphy, K., Fox, M.D., 2017. Towards a consensus regarding global signal regression for resting state functional connectivity MRI. Neuroimage 154, 169-173.

Mwansisya, T.E., Hu, A., Li, Y., Chen, X., Wu, G., Huang, X., Lv, D., Li, Z., Liu, C., Xue, Z., Feng, J., Liu, Z., 2017. Task and resting-state fMRI studies in first-episode schizophrenia: A systematic review. Schizophrenia Research 189, 9-18.

Nagano-Saito, A., Lissemore, J.I., Gravel, P., Leyton, M., Carbonell, F., Benkelfat, C., 2017. Posterior dopamine D2/3 receptors and brain network functional connectivity. Synapse 71.

Navailles, S., De Deurwaerdère, P., 2011. Presynaptic control of serotonin on striatal dopamine function. Psychopharmacology 213, 213-242.

Nelson, A.J., Hindley, E.L., Haddon, J.E., Vann, S.D., Aggleton, J.P., 2014. A novel role for the rat retrosplenial cortex in cognitive control. Learn Mem 21, 90-97.

Newberg, A.B., Amsterdam, J.D., Wintering, N., Shults, J., 2012. Low brain serotonin transporter binding in major depressive disorder. Psychiatry research 202, 161-167.

Niedermeyer, E., da Silva, F.H.L., 2005. Electroencephalography: Basic Principles, Clinical Applications, and Related Fields. Lippincott Williams & Wilkins.

Ogawa, S., Lee, T.M., Kay, A.R., Tank, D.W., 1990a. Brain magnetic resonance imaging with contrast dependent on blood oxygenation. Proc Natl Acad Sci U S A 87, 9868-9872.

Ogawa, S., Lee, T.M., Kay, A.R., Tank, D.W., 1990b. Brain magnetic resonance imaging with contrast dependent on blood oxygenation. Proceedings of the National Academy of Sciences of the United States of America 87, 9868-9872.

Olsen, C.M., 2011. Natural rewards, neuroplasticity, and non-drug addictions. Neuropharmacology 61, 1109-1122.

Onnela, J.-P., Saramäki, J., Kertész, J., Kaski, K., 2005. Intensity and coherence of motifs in weighted complex networks. Physical Review E 71, 065103.

Paasonen, J., Stenroos, P., Salo, R.A., Kiviniemi, V., Gröhn, O., 2018. Functional connectivity under six anesthesia protocols and the awake condition in rat brain. Neuroimage 172, 9-20.

Park, M.-H., Park, E.-H., 2000. Synaptic concentration of dopamine in rat striatal slices in relationship to [3H]raclopride binding to the dopamine D2 receptor. Archives of Pharmacal Research 23, 360-366.

Park, T.Y., Nishida, K.S., Wilson, C.M., Jaiswal, S., Scott, J., Hoy, A.R., Selwyn, R.G., Dardzinski, B.J., Choi, K.H., 2017. Effects of isoflurane anesthesia and intravenous morphine self-administration on regional glucose metabolism ([18F]FDG-PET) of male Sprague-Dawley rats. European Journal of Neuroscience 45, 922-931.

Parsey, R.V., Hastings, R.S., Oquendo, M.A., Huang, Y.Y., Simpson, N., Arcement, J., Huang, Y., Ogden, R.T., Van Heertum, R.L., Arango, V., Mann, J.J., 2006. Lower serotonin transporter binding potential in the human brain during major depressive episodes. Am J Psychiatry 163, 52-58.

Passie, T., Seifert, J., Schneider, U., Emrich, H.M., 2002. The pharmacology of psilocybin. Addiction Biology 7, 357-364.

Passow, S., Specht, K., Adamsen, T.C., Biermann, M., Brekke, N., Craven, A.R., Ersland, L., Gruner, R., Kleven-Madsen, N., Kvernenes, O.H., Schwarzlmuller, T., Olesen, R., Hugdahl,

K., 2015a. A close link between metabolic activity and functional connectivity in the resting human brain. EJNMMI Phys 2, A78.

Passow, S., Specht, K., Adamsen, T.C., Biermann, M., Brekke, N., Craven, A.R., Ersland, L., Gruner, R., Kleven-Madsen, N., Kvernenes, O.H., Schwarzlmuller, T., Olesen, R.A., Hugdahl, K., 2015b. Default-mode network functional connectivity is closely related to metabolic activity. Hum Brain Mapp 36, 2027-2038.

Patel, V.D., Lee, D.E., Alexoff, D.L., Dewey, S.L., Schiffer, W.K., 2008. Imaging dopamine release with Positron Emission Tomography (PET) and (11)C-raclopride in freely moving animals. Neuroimage 41, 1051-1066.

Pauling, L., Coryell, C.D., 1936. The Magnetic Properties and Structure of Hemoglobin, Oxyhemoglobin and Carbonmonoxyhemoglobin. Proceedings of the National Academy of Sciences 22, 210-216.

Perani, D., 2013. FDG PET and cognitive symptoms of dementia. Clinical and Translational Imaging 1, 247-260.

Pessoa, L., 2013. The Cognitive-Emotional Brain: From Interactions to Integration. MIT Press.

Petersen, S.E., Sporns, O., 2015. Brain Networks and Cognitive Architectures. Neuron 88, 207-219.

Pfaus, J.G., Tse, T.L., Werk, C.M., Chanda, M.L., Leblonde, A., Harbour, V.L., Chapman, C.A., 2009. Enhanced synaptic responses in the piriform cortex associated with sexual stimulation in the male rat. Neuroscience 164, 1422-1430.

Phan, K.L., Wager, T., Taylor, S.F., Liberzon, I., 2002. Functional Neuroanatomy of Emotion: A Meta-Analysis of Emotion Activation Studies in PET and fMRI. Neuroimage 16, 331-348.

Phelps, M.E., 2004. PET: Molecular Imaging and Its Biological Applications. Springer.

Pichler, B.J., Wehrl, H.F., Judenhofer, M.S., 2008. Latest advances in molecular imaging instrumentation. J Nucl Med 49 Suppl 2, 5s-23s.

Price, P., 2001. PET as a potential tool for imaging molecular mechanisms of oncology in man. Trends in Molecular Medicine 7, 442-446.

Puig, M.V., Antzoulatos, E.G., Miller, E.K., 2014. Prefrontal dopamine in associative learning and memory. Neuroscience 282, 217-229.

Puig, M.V., Gulledge, A.T., 2011. Serotonin and prefrontal cortex function: neurons, networks, and circuits. Molecular neurobiology 44, 449-464.

Purves, D., Augustine, G., Fitzpatrick, D., Hall, W.C., LaMantia, A., Mooney, R., White, L.E., 2018. Neuroscience. Sinauer.

Quate, L., McBean, D.E., Ritchie, I.M., Olverman, H.J., Kelly, P.A.T., 2004. Acute methylenedioxymethamphetamine administration: effects on local cerebral blood flow and glucose utilisation in the dark agouti rat. Psychopharmacology 173, 287-295.

Raichle, M.E., Gusnard, D.A., 2002. Appraising the brain's energy budget. Proceedings of the National Academy of Sciences 99, 10237-10239.

Raichle, M.E., MacLeod, A.M., Snyder, A.Z., Powers, W.J., Gusnard, D.A., Shulman, G.L., 2001. A default mode of brain function. Proc Natl Acad Sci U S A 98, 676-682.

Rangaprakash, D., Tadayonnejad, R., Deshpande, G., O'Neill, J., Feusner, J.D., 2021. FMRI hemodynamic response function (HRF) as a novel marker of brain function: applications for understanding obsessive-compulsive disorder pathology and treatment response. Brain Imaging and Behavior 15, 1622-1640.

Reichardt, J., Bornholdt, S., 2006. Statistical mechanics of community detection. Physical Review E 74, 016110.

Reimold, M., Batra, A., Knobel, A., Smolka, M.N., Zimmer, A., Mann, K., Solbach, C., Reischl, G., Schwärzler, F., Gründer, G., Machulla, H.J., Bares, R., Heinz, A., 2008. Anxiety is associated with reduced central serotonin transporter availability in unmedicated patients with unipolar major depression: a [11C]DASB PET study. Molecular Psychiatry 13, 606-613.

Reimold, M., Smolka, M.N., Schumann, G., Zimmer, A., Wrase, J., Mann, K., Hu, X.Z., Goldman, D., Reischl, G., Solbach, C., Machulla, H.J., Bares, R., Heinz, A., 2007. Midbrain serotonin transporter binding potential measured with [11C]DASB is affected by serotonin transporter genotype. J Neural Transm (Vienna) 114, 635-639.

Ripp, I., Stadhouders, T., Savio, A., Goldhardt, O., Cabello, J., Calhoun, V., Riedl, V., Hedderich, D., Diehl-Schmid, J., Grimmer, T., Yakushev, I., 2020. Integrity of neurocognitive networks in dementing disorders as measured with simultaneous PET/fMRI. J Nucl Med.

Rischka, L., Gryglewski, G., Pfaff, S., Vanicek, T., Hienert, M., Klobl, M., Hartenbach, M., Haug, A., Wadsak, W., Mitterhauser, M., Hacker, M., Kasper, S., Lanzenberger, R., Hahn, A., 2018. Reduced task durations in functional PET imaging with [(18)F]FDG approaching that of functional MRI. Neuroimage 181, 323-330.

Roffman, J.L., Tanner, A.S., Eryilmaz, H., Rodriguez-Thompson, A., Silverstein, N.J., Ho, N.F., Nitenson, A.Z., Chonde, D.B., Greve, D.N., Abi-Dargham, A., Buckner, R.L., Manoach, D.S., Rosen, B.R., Hooker, J.M., Catana, C., 2016. Dopamine D1 signaling organizes network dynamics underlying working memory. Sci Adv 2, e1501672.

Rosazza, C., Minati, L., 2011. Resting-state brain networks: literature review and clinical applications. Neurological Sciences 32, 773-785.

Roseman, L., Leech, R., Feilding, A., Nutt, D.J., Carhart-Harris, R.L., 2014. The effects of psilocybin and MDMA on between-network resting state functional connectivity in healthy volunteers. Frontiers in Human Neuroscience 8, 204-204.

Roussakis, A.-A., Politis, M., Towey, D., Piccini, P., 2016. Serotonin-to-dopamine transporter ratios in Parkinson disease. Relevance for dyskinesias 86, 1152-1158.

Rubinov, M., Sporns, O., 2010. Complex network measures of brain connectivity: uses and interpretations. Neuroimage 52, 1059-1069.

Russo, D., Martino, M., Magioncalda, P., Inglese, M., Amore, M., Northoff, G., 2020. Opposing Changes in the Functional Architecture of Large-Scale Networks in Bipolar Mania and Depression. Schizophrenia Bulletin 46, 971-980.

Sala, A., Lizarraga, A., Ripp, I., Cumming, P., Yakushev, I., 2021. Static versus Functional PET: Making Sense of Metabolic Connectivity. Cerebral Cortex.

Sala, A., Perani, D., 2019. Brain Molecular Connectivity in Neurodegenerative Diseases: Recent Advances and New Perspectives Using Positron Emission Tomography. Frontiers in neuroscience 13.

Sanabria-Diaz, G., Martinez-Montes, E., Melie-Garcia, L., Alzheimer's Disease Neuroimaging, I., 2013. Glucose metabolism during resting state reveals abnormal brain networks organization in the Alzheimer's disease and mild cognitive impairment. PLoS One 8, e68860.

Sander, C.Y., Hooker, J.M., Catana, C., Normandin, M.D., Alpert, N.M., Knudsen, G.M., Vanduffel, W., Rosen, B.R., Mandeville, J.B., 2013. Neurovascular coupling to D2/D3 dopamine receptor occupancy using simultaneous PET/functional MRI. Proceedings of the National Academy of Sciences of the United States of America 110, 11169-11174.

Savini, G., Pardini, M., Castellazzi, G., Lascialfari, A., Chard, D., D'Angelo, E., Gandini Wheeler-Kingshott, C.A.M., 2019. Default Mode Network Structural Integrity and Cerebellar Connectivity Predict Information Processing Speed Deficit in Multiple Sclerosis. Frontiers in Cellular Neuroscience 13.

Savio, A., Funger, S., Tahmasian, M., Rachakonda, S., Manoliu, A., Sorg, C., Grimmer, T., Calhoun, V., Drzezga, A., Riedl, V., Yakushev, I., 2017. Resting-State Networks as Simultaneously Measured with Functional MRI and PET. J Nucl Med 58, 1314-1317.

Savitz, J., Drevets, W.C., 2009a. Bipolar and major depressive disorder: Neuroimaging the developmental-degenerative divide. Neuroscience & Biobehavioral Reviews 33, 699-771.

Savitz, J.B., Drevets, W.C., 2009b. Imaging phenotypes of major depressive disorder: genetic correlates. Neuroscience 164, 300-330.

Scarpetta, S., de Candia, A., 2014. Alternation of up and down states at a dynamical phase-transition of a neural network with spatiotemporal attractors. Frontiers in Systems Neuroscience 8.

Schaller, B., Mekle, R., Xin, L., Kunz, N., Gruetter, R., 2013. Net increase of lactate and glutamate concentration in activated human visual cortex detected with magnetic resonance spectroscopy at 7 tesla. Journal of Neuroscience Research 91, 1076-1083.

Scheinost, D., Sinha, R., Cross, S.N., Kwon, S.H., Sze, G., Constable, R.T., Ment, L.R., 2017. Does prenatal stress alter the developing connectome? Pediatric Research 81, 214-226.

Schiffer, W.K., Mirrione, M.M., Biegon, A., Alexoff, D.L., Patel, V., Dewey, S.L., 2006. Serial microPET measures of the metabolic reaction to a microdialysis probe implant. J Neurosci Methods 155, 272-284.

Schlemmer, H.-P.W., Pichler, B.J., Schmand, M., Burbar, Z., Michel, C., Ladebeck, R., Jattke, K., Townsend, D., Nahmias, C., Jacob, P.K., Heiss, W.-D., Claussen, C.D., 2008. Simultaneous MR/PET Imaging of the Human Brain: Feasibility Study. Radiology 248, 1028-1035.

Schroeter, M.L., Stein, T., Maslowski, N., Neumann, J., 2009. Neural correlates of Alzheimer's disease and mild cognitive impairment: a systematic and quantitative meta-analysis involving 1351 patients. Neuroimage 47, 1196-1206.

Seeley, W.W., 2019. The Salience Network: A Neural System for Perceiving and Responding to Homeostatic Demands. The Journal of Neuroscience 39, 9878-9882.

Seeley, W.W., Menon, V., Schatzberg, A.F., Keller, J., Glover, G.H., Kenna, H., Reiss, A.L., Greicius, M.D., 2007. Dissociable intrinsic connectivity networks for salience processing and executive control. J Neurosci 27, 2349-2356.

Seo, E.H., Lee, D.Y., Lee, J.-M., Park, J.-S., Sohn, B.K., Lee, D.S., Choe, Y.M., Woo, J.I., 2013a. Whole-brain Functional Networks in Cognitively Normal, Mild Cognitive Impairment, and Alzheimer's Disease. PLoS One 8, e53922.

Seo, E.H., Lee, D.Y., Lee, J.M., Park, J.S., Sohn, B.K., Lee, D.S., Choe, Y.M., Woo, J.I., 2013b. Whole-brain functional networks in cognitively normal, mild cognitive impairment, and Alzheimer's disease. PLoS One 8, e53922.

Shang, K., Wang, J., Fan, X., Cui, B., Ma, J., Yang, H., Zhou, Y., Zhao, G., Lu, J., 2018. Clinical Value of Hybrid TOF-PET/MR Imaging–Based Multiparametric Imaging in Localizing Seizure Focus in Patients with MRI-Negative Temporal Lobe Epilepsy. American Journal of Neuroradiology.

Sheth, S.A., Nemoto, M., Guiou, M., Walker, M., Pouratian, N., Toga, A.W., 2004. Linear and nonlinear relationships between neuronal activity, oxygen metabolism, and hemodynamic responses. Neuron 42, 347-355.

Sicard, K.M., Duong, T.Q., 2005. Effects of hypoxia, hyperoxia, and hypercapnia on baseline and stimulus-evoked BOLD, CBF, and CMRO2 in spontaneously breathing animals. Neuroimage 25, 850-858.

Silkis, I., 2001. The cortico-basal ganglia-thalamocortical circuit with synaptic plasticity. II. Mechanism of synergistic modulation of thalamic activity via the direct and indirect pathways through the basal ganglia. Biosystems 59, 7-14.

Smith, S.M., Fox, P.T., Miller, K.L., Glahn, D.C., Fox, P.M., Mackay, C.E., Filippini, N., Watkins, K.E., Toro, R., Laird, A.R., Beckmann, C.F., 2009. Correspondence of the brain's functional architecture during activation and rest. Proceedings of the National Academy of Sciences 106, 13040-13045.

Smith, Y., Bevan, M.D., Shink, E., Bolam, J.P., 1998. Microcircuitry of the direct and indirect pathways of the basal ganglia. Neuroscience 86, 353-387.

Solbach, C., Reischl, G., Machulla, H.-J., 2004. Determination of reaction parameters for the synthesis of the serotonin transporter ligand [11C]DASB: Application to a remotely controlled high yield synthesis. Radiochimica Acta 92, 341-344.

Sorg, C., Manoliu, A., Neufang, S., Myers, N., Peters, H., Schwerthöffer, D., Scherr, M., Mühlau, M., Zimmer, C., Drzezga, A., Förstl, H., Bäuml, J., Eichele, T., Wohlschläger, A.M., Riedl, V., 2013. Increased Intrinsic Brain Activity in the Striatum Reflects Symptom Dimensions in Schizophrenia. Schizophrenia Bulletin 39, 387-395.

Soto-Montenegro, M.L., Vaquero, J.J., Arango, C., Ricaurte, G., García-Barreno, P., Desco, M., 2007. Effects of MDMA on blood glucose levels and brain glucose metabolism. European Journal of Nuclear Medicine and Molecular Imaging 34, 916-925.

Spangler-Bickell, M.G., de Laat, B., Fulton, R., Bormans, G., Nuyts, J., 2016. The effect of isoflurane on 18F-FDG uptake in the rat brain: a fully conscious dynamic PET study using motion compensation. EJNMMI research 6, 86.

Sporns, O., 2010. Networks of the Brain. The MIT Press.

Sporns, O., Tononi, G., Kotter, R., 2005. The human connectome: A structural description of the human brain. PLoS Comput Biol 1, e42.

Su Lui, M.D., Ph.D. ,, Qizhu Wu, Ph.D. ,, Lihua Qiu, M.D. ,, Xun Yang, Ph.D. ,, Weihong Kuang, M.D. ,, Raymond C.K. Chan, Ph.D. ,, Xiaoqi Huang, M.D. ,, Graham J. Kemp, M.A., D.M. ,, Andrea Mechelli, Ph.D. , and, Qiyong Gong, M.D., Ph.D., 2011. Resting-State Functional Connectivity in Treatment-Resistant Depression. American Journal of Psychiatry 168, 642-648.

Sumnall, H.R., Cole, J.C., Jerome, L., 2006. The varieties of ecstatic experience: an exploration of the subjective experiences of ecstasy. J Psychopharmacol 20, 670-682.

Tang, Y., Liow, J.-S., Zhang, Z., Li, J., Long, T., Li, Y., Tang, B., Hu, S., 2019. The Evaluation of Dynamic FDG-PET for Detecting Epileptic Foci and Analyzing Reduced Glucose Phosphorylation in Refractory Epilepsy. Frontiers in neuroscience 12, 993-993.

Ter-Pogossian, M.M., Phelps, M.E., Hoffman, E.J., Mullani, N.A., 1975. A Positron-Emission Transaxial Tomograph for Nuclear Imaging (PETT). Radiology 114, 89-98.

Thanos, P.K., Robison, L., Nestler, E.J., Kim, R., Michaelides, M., Lobo, M.K., Volkow, N.D., 2013. Mapping brain metabolic connectivity in awake rats with μPET and optogenetic stimulation. J Neurosci 33, 6343-6349.

Thulborn, K.R., Waterton, J.C., Matthews, P.M., Radda, G.K., 1982. Oxygenation dependence of the transverse relaxation time of water protons in whole blood at high field. Biochim Biophys Acta 714, 265-270.

Tomasi, D., Wang, G.-J., Volkow, N.D., 2013. Energetic cost of brain functional connectivity. Proceedings of the National Academy of Sciences 110, 13642-13647.

Tomasi, D.G., Shokri-Kojori, E., Wiers, C.E., Kim, S.W., Demiral, S.B., Cabrera, E.A., Lindgren, E., Miller, G., Wang, G.J., Volkow, N.D., 2017. Dynamic brain glucose metabolism identifies anti-correlated cortical-cerebellar networks at rest. J Cereb Blood Flow Metab 37, 3659-3670.

Tong, S., Alessio, A.M., Kinahan, P.E., 2010. Image reconstruction for PET/CT scanners: past achievements and future challenges. Imaging in medicine 2, 529-545.

Toni, R., Malaguti, A., Benfenati, F., Martini, L., 2004. The human hypothalamus: a morpho-functional perspective. J Endocrinol Invest 27, 73-94.

Tsurugizawa, T., Djemai, B., Zalesky, A., 2019. The impact of fasting on resting state brain networks in mice. Scientific reports 9, 2976.

Turkheimer, F.E., Selvaraj, S., Hinz, R., Murthy, V., Bhagwagar, Z., Grasby, P., Howes, O., Rosso, L., Bose, S.K., 2012. Quantification of ligand PET studies using a reference region with a displaceable fraction: application to occupancy studies with [(11)C]-DASB as an example. J Cereb Blood Flow Metab 32, 70-80.

Uddin, L.Q., 2013. Complex relationships between structural and functional brain connectivity. Trends in Cognitive Sciences 17, 600-602.

Uddin, L.Q., Yeo, B.T.T., Spreng, R.N., 2019. Towards a Universal Taxonomy of Macro-scale Functional Human Brain Networks. Brain topography 32, 926-942.

Ullmer, C., Schmuck, K., Kalkman, H.O., Lübbert, H., 1995. Expression of serotonin receptor mRNAs in blood vessels. FEBS Letters 370, 215-221.

Upadhyay, J., Baker, S.J., Chandran, P., Miller, L., Lee, Y., Marek, G.J., Sakoglu, U., Chin, C.L., Luo, F., Fox, G.B., Day, M., 2011. Default-mode-like network activation in awake rodents. PLoS One 6, e27839.

van den Heuvel, M.P., Sporns, O., 2013. Network hubs in the human brain. Trends in Cognitive Sciences 17, 683-696.

Van Laeken, N., Kersemans, K., De Meestere, D., Goethals, I., De Vos, F., 2013. Improved HPLC purification strategy for [11C]raclopride and [11C]DASB leading to high radiochemical yields and more practical high quality radiopharmaceutical formulations. Applied Radiation and Isotopes 78, 62-67.

Van Nueten, J.M., Janssens, W.J., Vanhoutte, P.M., 1985. Serotonin and vascular reactivity. Pharmacol Res Commun 17, 585-608.

van Sluis, J., de Jong, J., Schaar, J., Noordzij, W., van Snick, P., Dierckx, R., Borra, R., Willemsen, A., Boellaard, R., 2019. Performance Characteristics of the Digital Biograph Vision PET/CT System. J Nucl Med 60, 1031-1036.

Vandenberghe, S., Marsden, P.K., 2015. PET-MRI: a review of challenges and solutions in the development of integrated multimodality imaging. Physics in Medicine and Biology 60, R115-R154.

Vann, S.D., Aggleton, J.P., Maguire, E.A., 2009. What does the retrosplenial cortex do? Nat Rev Neurosci 10, 792-802.

Vazquez-Borsetti, P., Cortes, R., Artigas, F., 2009. Pyramidal neurons in rat prefrontal cortex projecting to ventral tegmental area and dorsal raphe nucleus express 5-HT2A receptors. Cereb Cortex 19, 1678-1686.

Venton, B.J., Cao, Q., 2020. Fundamentals of fast-scan cyclic voltammetry for dopamine detection. Analyst 145, 1158-1168.

Vidal, B., Fieux, S., Redouté, J., Villien, M., Bonnefoi, F., Le Bars, D., Newman-Tancredi, A., Costes, N., Zimmer, L., 2018. In vivo biased agonism at 5-HT(1A) receptors: characterisation by simultaneous PET/MR imaging. Neuropsychopharmacology : official publication of the American College of Neuropsychopharmacology 43, 2310-2319.

Villien, M., Wey, H.-Y., Mandeville, J.B., Catana, C., Polimeni, J.R., Sander, C.Y., Zürcher, N.R., Chonde, D.B., Fowler, J.S., Rosen, B.R., Hooker, J.M., 2014. Dynamic functional imaging of brain glucose utilization using fPET-FDG. Neuroimage 100, 192-199.

Vollenweider, F.X., Leenders, K.L., Scharfetter, C., Maguire, P., Stadelmann, O., Angst, J., 1997. Positron emission tomography and fluorodeoxyglucose studies of metabolic hyperfrontality and psychopathology in the psilocybin model of psychosis. Neuropsychopharmacology : official publication of the American College of Neuropsychopharmacology 16, 357-372.

Walker, M., Ehrlichmann, W., Stahlschmidt, A., Pichler, B.J., Fischer, K., 2016. In Vivo Evaluation of 11C-DASB for Quantitative SERT Imaging in Rats and Mice. J Nucl Med 57, 115-121.

Wang, H.-L., Zhang, S., Qi, J., Wang, H., Cachope, R., Mejias-Aponte, C.A., Gomez, J.A., Mateo-Semidey, G.E., Beaudoin, G.M.J., Paladini, C.A., Cheer, J.F., Morales, M., 2019. Dorsal Raphe Dual Serotonin-Glutamate Neurons Drive Reward by Establishing Excitatory Synapses on VTA Mesoaccumbens Dopamine Neurons. Cell reports 26, 1128-1142.e1127.

Wehrl, H.F., 2013. Möglichkeiten und Grenzen der kombinierten PET/MR-Bildgebung in der onkologischen und neurologischen Grundlagenforschung.

Wehrl, H.F., Hossain, M., Lankes, K., Liu, C.C., Bezrukov, I., Martirosian, P., Schick, F., Reischl, G., Pichler, B.J., 2013. Simultaneous PET-MRI reveals brain function in activated and resting state on metabolic, hemodynamic and multiple temporal scales. Nat Med 19, 1184-1189.

Wehrl, H.F., Judenhofer, M.S., Thielscher, A., Martirosian, P., Schick, F., Pichler, B.J., 2011. Assessment of MR compatibility of a PET insert developed for simultaneous multiparametric PET/MR imaging on an animal system operating at 7 T. Magn Reson Med 65, 269-279.

Wehrl, H.F., Wiehr, S., Divine, M.R., Gatidis, S., Gullberg, G.T., Maier, F.C., Rolle, A.-M., Schwenck, J., Thaiss, W.M., Pichler, B.J., 2014. Preclinical and Translational PET/MR Imaging. Journal of Nuclear Medicine 55, 11S-18S.

Weishaupt, D., Köchli, V.D., Marincek, B., 2013. Wie funktioniert MRI?: Eine Einführung in Physik und Funktionsweise der Magnetresonanzbildgebung. Springer Berlin Heidelberg.

Whittington, R.A., Virag, L., 2006. Isoflurane decreases extracellular serotonin in the mouse hippocampus. Anesth Analg 103, 92-98, table of contents.

Wihlbäck, A.C., Sundström Poromaa, I., Bixo, M., Allard, P., Mjörndal, T., Spigset, O., 2004. Influence of menstrual cycle on platelet serotonin uptake site and serotonin2A receptor binding. Psychoneuroendocrinology 29, 757-766.

Wilkerson, G., London, E.D., 1989. Effects of methylenedioxymethamphetamine on local cerebral glucose utilization in the rat. Neuropharmacology 28, 1129-1138.

Willeit, M., Sitte, H.H., Thierry, N., Michalek, K., Praschak-Rieder, N., Zill, P., Winkler, D., Brannath, W., Fischer, M.B., Bondy, B., Kasper, S., Singer, E.A., 2008. Enhanced serotonin transporter function during depression in seasonal affective disorder. Neuropsychopharmacology : official publication of the American College of Neuropsychopharmacology 33, 1503-1513.

Williams, K.A., Magnuson, M., Majeed, W., LaConte, S.M., Peltier, S.J., Hu, X., Keilholz, S.D., 2010. Comparison of α-chloralose, medetomidine and isoflurane anesthesia for functional connectivity mapping in the rat. Magnetic Resonance Imaging 28, 995-1003.

Wilson, A.A., Ginovart, N., Schmidt, M., Meyer, J.H., Threlkeld, P.G., Houle, S., 2000. Novel Radiotracers for Imaging the Serotonin Transporter by Positron Emission Tomography: Synthesis, Radiosynthesis, and in Vitro and ex Vivo Evaluation of 11C-Labeled 2-(Phenylthio)araalkylamines. Journal of Medicinal Chemistry 43, 3103-3110.

Wu, C.W., Gu, H., Lu, H., Stein, E.A., Chen, J.-H., Yang, Y., 2009. Mapping functional connectivity based on synchronized CMRO2 fluctuations during the resting state. Neuroimage 45, 694-701.

Xia, M., Wang, J., He, Y., 2013. BrainNet Viewer: a network visualization tool for human brain connectomics. PLoS One 8, e68910.

Yakovlev, D.S., Spasov, A.A., Mal'tsev, D.V., Anisimova, V.A., 2014. Effect of 5-HT(2A) receptor antagonists on blood flow in the carotid vessels upon elevation of serotonin level. Bull Exp Biol Med 157, 350-352.

Yakushev, I., Ripp, I., Wang, M., Savio, A., Schutte, M., Lizarraga, A., Bogdanovic, B., Diehl-Schmid, J., Hedderich, D.M., Grimmer, T., Shi, K., 2021. Mapping covariance in brain FDG uptake to structural connectivity. European Journal of Nuclear Medicine and Molecular Imaging.

Yan, C.-G., Chen, X., Li, L., Castellanos, F.X., Bai, T.-J., Bo, Q.-J., Cao, J., Chen, G.-M., Chen, N.-X., Chen, W., Cheng, C., Cheng, Y.-Q., Cui, X.-L., Duan, J., Fang, Y.-R., Gong, Q.-Y., Guo, W.-B., Hou, Z.-H., Hu, L., Kuang, L., Li, F., Li, K.-M., Li, T., Liu, Y.-S., Liu, Z.-N., Long, Y.-C., Luo, Q.-H., Meng, H.-Q., Peng, D.-H., Qiu, H.-T., Qiu, J., Shen, Y.-D., Shi, Y.-S., Wang, C.-Y., Wang, F., Wang, K., Wang, L., Wang, X., Wang, Y., Wu, X.-P., Wu, X.-R., Xie, C.-M., Xie, G.-R., Xie, H.-Y., Xie, P., Xu, X.-F., Yang, H., Yang, J., Yao, J.-S., Yao, S.-Q., Yin, Y.-Y., Yuan, Y.-G., Zhang, A.-X., Zhang, H., Zhang, K.-R., Zhang, L., Zhang, Z.-J., Zhou, R.-B., Zhou, Y.-T., Zhu, J.-J., Zou, C.-J., Si, T.-M., Zuo, X.-N., Zhao, J.-P., Zang, Y.-F., 2019. Reduced default mode network functional connectivity in patients with recurrent major depressive disorder. Proceedings of the National Academy of Sciences of the United States of America 116, 9078-9083.

Yancey, S.E., Rotenberg, D.J., Tam, F., Chiew, M., Ranieri, S., Biswas, L., Anderson, K.J.T., Nicole Baker, S., Wright, G.A., Graham, S.J., 2011. Spin-history artifact during functional MRI: Potential for adaptive correction. Medical Physics 38, 4634-4646.

Yoon, H.S., Ko, G.B., Kwon, S.I., Lee, C.M., Ito, M., Chan Song, I., Lee, D.S., Hong, S.J., Lee, J.S., 2012. Initial Results of Simultaneous PET/MRI Experiments with an MRI-Compatible Silicon Photomultiplier PET Scanner. Journal of Nuclear Medicine 53, 608-614.

Zhang, J., Magioncalda, P., Huang, Z., Tan, Z., Hu, X., Hu, Z., Conio, B., Amore, M., Inglese, M., Martino, M., Northoff, G., 2019. Altered Global Signal Topography and Its Different Regional Localization in Motor Cortex and Hippocampus in Mania and Depression. Schizophr Bull 45, 902-910.

Zhang, N., Rane, P., Huang, W., Liang, Z., Kennedy, D., Frazier, J.A., King, J., 2010. Mapping resting-state brain networks in conscious animals. J Neurosci Methods 189, 186-196.

7. Declaration of Contribution

The projects comprising this work were designed by Dr. Hans Wehrl, Prof. Dr. Bernd Pichler and Prof. Bharat Biswal.

The experimental work comprising the present thesis was performed by Tudor Ionescu, Dr. Mario Amend, André Thielke, Linda Schramm and Sandro Aidone. The experiments comprising the first publication were performed by André Thielke (9 experiments), Mario Amend (6 experiments) and Tudor Ionescu together with Mario Amend (15 experiments). The scans comprising the second publication were performed by Tudor Ionescu with support for each scan by Linda Schramm, Sandro Aidone or Mario Amend. The experiments comprising the final publication were performed by Mario Amend. The tracers used in the experiments were provided by the Radiopharmacy department of the Werner Siemens Imaging Center under the supervision of Prof. Dr. Gerald Reisch and Dr. Andreas Maurer.

Tudor Ionescu processed and analyzed all datasets comprising this work. The preprocessing pipeline was designed by Tudor Ionescu and Rakibul Hafiz from the New Jersey Institute of Technology. The entire analysis was designed and performed by Tudor Ionescu.

Tudor Ionescu interpreted the data, wrote the manuscripts comprising this work, as well as the PhD thesis independently. Dr. Mario Amend, Dr. Hans Wehrl, Prof. Dr. Kristina Herfert, Prof. Dr. Bernd Pichler, Rakibul Hafiz, Prof. Dr. Bharat Biswal, Dr. Andreas Maurer and Dr. Tadashi Watabe supported the interpretation of the data and corrected the manuscripts.

Prof. Dr. Bernd Pichler, Prof. Dr. Kristina Herfert, Dr. Hans Wehrl, Dr. Mario Amend and Prof. Bharat Biswal supervised the projects.

The percent contributions of all authors to the papers published as part of this thesis can be in the tables provided as an annex to this thesis, approved and signed by all respective authors.

Tudor Ionescu, Tuebingen, October 1st 2022

8. Acknowledgements

Ich möchte mich gerne bei allen Personen bedanken, die mich auf dem Weg bis zur Entstehung dieser Thesis begleitet und unterstützt haben. Als erstes gilt mein Dank Prof. Dr. Bernd Pichler, der mir die Möglichkeit gab, die Arbeit in seiner Abteilung durchzuführen und mich durchgehend unterstützt hat. Sehr herzlich bedanke ich mich auch bei Prof. Dr. Kristina Herfert, die die Betreuung und Begutachtung dieser Arbeit übernommen hat, mir bei der Erstellung der Publikationen sehr geholfen hat und mich bei der Arbeit immer sehr unterstützte. Ebenfalls möchte ich mich bei Dr. Hans Wehrl und Dr. Mario Amend, die auch am Anfang meiner Thesis mich betreut haben und auch im Anschluss ebenfalls maßgeblich meine Arbeit mit wertvollen Ratschlägen begleitet haben.

Mein Dank gilt auch dem gesamten Werner Siemens Imaging Center und allen Kollegen. Ohne die technische Assistenz durch Dr. Julia Mannheim, Dr. Rebecca Rock, Dr. Neele Hübner, Dr. Andreas Dieterich, Linda Schramm und Sandro Aidone wäre die Erstellung dieser Dissertation nicht möglich gewesen. Ebenso haben mir die Ideen, die aus Diskussionen mit der Neurologie-Gruppe entstanden sind, sowie die ausgezeichnete Atmosphäre der Gruppe sehr geholfen, meine Arbeit durchzuführen und zu verbessern. Allgemein hat die exzellente Arbeitsatmosphäre in der gesamten Abteilung mir eine sehr produktive und schöne Zeit ermöglicht. Zahlreiche Freundschaften auch außerhalb der Arbeit sind entstanden, aus Kollegen sind Freunde geworden und diese standen mir durchgehend zur Seite und halfen mir maßgeblich, meine Arbeit erfolgreich zu gestalten. Hier möchte ich besonders Adrian, Adriana, Anaïs, Barbara, Chamba, Dimitri, Fabian, Greg, JC, Kristin, Laura, Lucas, Marilena, Paul, Remy, Roman, Sabina, Sabrina und Stef hervorheben, aber bei jedem und jeder Mitarbeiter(in) und Freund(in) möchte ich mich herzlich für die tolle Zeit und die lustigen Momente bedanken. Thank you, gracias, grazie, merci!

Nicht zuletzt gilt mein Dank meinen Eltern. meiner Familie und meinen Freunden und besonders meiner Mutter und meiner Freundin, ohne mich nicht nur bei der Thesis, sondern mir bei jedem Aspekt meines Lebens ständig unterstützen und zur Seite stehen, Euch gilt mein ganz besonderer Dank, denn ohne Euch wäre nichts möglich gewesen.